Investigation of a DNA Damage Response Protein Targeted Meitner-Auger Electron Emitting Theranostic for Ovarian Cancer

By

Sabrina L. V. Hoffman

A dissertation submitted in partial fulfillment of
the requirements for the degree of

Doctor of Philosophy

(Medical Physics)

at the

UNIVERSITY OF WISCONSIN–MADISON

2023

Date of final oral examination: March 29, 2023

The dissertation is approved by the following members of the Final Oral Committee:

Paul A. Ellison, Co-advisor, Assistant Professor, Medical Physics
Bryan P. Bednarz, Co-advisor, Associate Professor, Medical Physics & Human Oncology
Jonathan W. Engle, Associate Professor, Medical Physics & Radiology
Reinier Hernandez, Assistant Professor, Medical Physics
Tod W. Speer, Radiation Oncologist, Centra Care
Bruce R. Thomadsen, Professor Emeritus, Medical Physics

ABSTRACT

Metastatic ovarian cancer currently has a 5-year survival rate of 30% and limited therapeutic options. The FDA-approved targeted therapeutic, rucaparib, is a poly(ADP-ribose) polymerase inhibitor (PARPi) that limits single-strand DNA damage response and can trap the PARP-drug complex nanometers from DNA. Radiolabeled PARPi with Meitner-Auger electron (MAe^-) emitting radionuclides such as ^{77}Br ($t_{1/2}$ = 57 h, 6–7 MAe^- per decay) can exploit this biological mechanism to target the DNA with short-range, high linear energy transfer radiation. Its theranostic pair, ^{76}Br ($t_{1/2}$=16.2 h, 55% β^+), has the potential to be used for diagnostic and patient specific dosimetry with PET imaging. This work investigates the therapeutic and diagnostic potential of $^{77/76}Br$ labeled rucaparib derivative, called [$^{77/76}Br$]RD1.

Radiopharmacological and cytotoxic response of various ovarian cancer cell lines *in vitro* were investigated with [^{77}Br]RD1. The goal of this objective was to characterize the radiopharmaceutical as a therapeutic agent, including its binding properties and cytotoxic effects. Dosimetric calculations were conducted with the goal of converting the cytotoxic response *in vitro* measured as a function of activity concentrations into dose. Further experiments characterizing the ovarian cancer cell characteristics were done to properly inform assumptions to calculate the dose using MIRDcell.

The potential of [^{76}Br]RD1 as a diagnostic PET imager was also investigated through preclinical animal studies measuring the radiopharmaceutical's *in vivo* and *ex vivo* organ and tumor uptake. RAPID and OLINDA dosimetry platforms were used to calculate the dose to organs using [^{76}Br]RD1 organ uptake measured by PET. These calculations were done for both radiobromine MAe^- emitter ^{77}Br and positron emitter ^{76}Br.

This work describes preclinical experiments used to characterize a MAe^- and PET emitting theranostic radiopharmaceutical targeting PARP. It contributes to the understanding of the radiochemistry and radiation biology of MAe^-–emitting radiopharmaceuticals and will inform experimental design for future studies of this and other PARP-targeted agents for the treatment and diagnosis of metastatic cancers.

To my late father, whose eccentric and beloved spirit continues to inspire me.

ACKNOWLEDGEMENTS

Many thanks to the following people who helped make this work possible. Thank you to Jason Mixdorf for your expertise and answering my chemistry questions. Thank you to Eduardo Aluicio Sarduy for your advice, guidance and expertise with cell work. Thank you to Justin Jeffery and Ashley Weichmann of the Small Animal Imaging facility. A huge thank you to my fellow graduate students, Taylor Johnson and Ohyun Kwon, for your camaraderie. Taylor, I sincerely appreciate your help on those long days. I can't begin to tell you how much I appreciated it. Ohyun, thank you for all your help with the dosimetry work.

I would like to express my sincere gratitude to the members of my committee—Jonathon Engle, Reiner Hernandez, and Tod Speer—for your time and support throughout my academic journey. Your guidance and feedback during the development and completion of my research have been invaluable in shaping my academic and professional growth. My graduate school path has been a long and unconventional one. Thank you for your patience and understanding when I left graduate school for residency, and thank you for being a part of the process when I came back two years later to finish.

Thank you to Bruce Thomadsen for your mentorship and support during the first portion of my graduate studies. I so appreciated our conversations, and you helped me grow into the person I am today. I can't thank you enough for your support of me and your role in my T32 training grant funding. Thank you, from the bottom of my heart.

Thank you to my co-advisors, Bryan Bednarz and Paul Ellison, for taking me as your student after I had already left for residency. Bryan, thank you for your mentorship, advice and understanding when I felt especially unsure of myself. I can't thank you enough for the way you supported me in those moments. A tremendous thank you, Paul, for your mentorship and guidance the past two years. I am immensely grateful for the opportunity to work under your leadership, and appreciate the chance you took in accepting me as your student. Your enthusiasm, support, and expert knowledge have been a constant source of inspiration, and I appreciate the way you gave me space to figure things out on my own while providing the right amount of guidance and support. Your availability and willingness to answer my questions have made a significant difference in my research. I will be eternally grateful for your mentorship and feel lucky to be your first graduating student.

Thank you to my family for your patience, support, and love throughout my academic journey. I miss you terribly, and I am excited for the future. Mom, thank you for always believing in me and for being so proud of me. I hope you know I am the person I am today because of you. To my Tia Yoly, thank you for being a wonderful role model all my life. Thank you to my sisters, Adita,

Karina, and Maria, for your continued belief in me. I was always so excited for December to come because I knew we would all be together again. Nick, thank you for being so patient with me always crashing during the holidays.

Thank you so much to Jane Villa for your hospitality and support while I was in Madison. I appreciated our conversations and hangouts, especially on the days I had hardly said anything out loud after spending all day in the basement with only my cells to keep me company. That you opened your home to me during the time in your life that you did—words will not be able to describe the depth of my gratitude to you. Truly, thank you so much.

Thank you to the Carpenter-Graffy family for your support and understanding when I spent all my energy focusing on being a scientist and started to struggle to carry normal conversations. I appreciate you taking care of my soul while I was in Madison away from my sisters, aunt and mother. Thank you, Adam and Audrey, for welcoming and opening your home to me. Thank you, Elisa and Cris, for all your support and love, and for letting me carry odd hours and hang out with you late at night, even if it was just to stop by and have a quick meal with you. I hope you can understand how much I needed those moments and how much they mean and meant to me. Cris, we miss you so much.

To Peter, thank you for believing in me always, being patient with me as I go through my moments of imposter syndrome and doubt, and allowing me the room to be frustrated before you push back to remind me how much I've accomplished and how much I've learned and grown. Thank you for your unwavering support throughout my atypical academic journey, from our time in Madison the first time, moving to Oak Park for my residency, doing long distance when I came back to Madison a second time, and all the long nights and early mornings as I finally wrap this thing up. Thank you for pushing me to be my best version, to reach my full potential, for instilling confidence in me, and for offering your support even when I felt like I couldn't do it. My life changed when I met you, and I am so excited to see where we go next.

This research is supported by the U.S. Department of Energy Isotope Program, managed by the Office of Science for Isotope R&D and Production, grant number DE-SC0020960 and the U.S. Department of Defense Ovarian Cancer Research Program Pilot Award, grant number W81XWH2110351. J.C.M. is supported by the National Cancer Institute of the National Institutes of Health under Award Number T32CA009206. The project was supported by the Clinical and Translational Science Award (CTSA) program, through the NIH National Center for Advancing Translational Sciences (NCATS), grant UL1TR002373. The content is solely the responsibility of the authors and does not necessarily represent the official views of the NIH.

TABLE OF CONTENTS

Abstract i

Acknowledgments iii

List of Tables ix

List of Figures xii

List of Abbreviations xx

Chapter 1: Introduction and Outline 1
1.1 Overview 1
1.2 Aims 1
1.3 Thesis Outline 2

Chapter 2: Background 4
2.1 Ovarian Metastatic Cancer 4
2.1.1 DNA Repair Pathways 5
2.1.1.1 Breast Cancer Type 1/2 (*BRCA1/2*) Gene 7
2.1.1.2 Poly(ADP-Ribose) Polymerase 1 Protein 7
2.1.2 Therapies 8
2.1.2.1 PARP Inhibitors 8
2.1.2.2 Rucaparib 12
2.2 Positron Emission Tomography Imaging of PARP 13
2.3 Radiopharmaceutical Therapy 13
2.3.1 Meitner-Auger Emitters 15
2.3.2 Radiobromine 18
2.3.3 Production of Radiobromine 21
2.4 Internal Dosimetry 22
2.4.1 Monte Carlo Methods 23
2.4.2 Medical Internal Radiation Dose Cellular S Values 24

Chapter 3: Cellular Pharmacokinetics and Cytotoxicity Studies with Radiobrominated PARP1 Inhibitor 27
3.1 Ovarian Cancer Cell Lines 27
3.2 Cellular Dose Response Assays 28
3.3 Methods 30

3.3.1 Radiopharmaceutical Production and Quality Control . . . 30
3.3.1.1 Cyclotron Production and Distillation of Radiobromide . . . 30
3.3.1.2 [^{77}Br]RD1 Synthesis and Purification . . . 31
3.3.1.3 Analytical High-Performance Liquid Chromatography . . . 32
3.3.1.4 Preparing Radiopharmaceutical Solutions . . . 34
3.3.1.5 Thin-Layer Chromatography . . . 35
3.3.1.6 Gamma Counter Calibration . . . 35
3.3.2 Cell Culture and Growth . . . 36
3.3.2.1 Cell Culture . . . 36
3.3.2.2 Doubling Time . . . 37
3.3.3 Cellular Pharmacokinetics . . . 37
3.3.3.1 Total and Nonspecific Binding . . . 38
3.3.3.2 Association and Dissociation . . . 39
3.3.4 Radiotoxicology . . . 42
3.3.4.1 Viability Assay . . . 42
3.3.4.2 Viability Assay Optimization . . . 43
3.3.4.3 Viability Assay Validation . . . 44
3.4 Results . . . 47
3.4.1 Radiopharmaceutical Production and Quality Control . . . 47
3.4.2 Gamma Counter Calibration . . . 47
3.4.3 Cell Doubling Time . . . 49
3.4.4 Cellular Pharmacokinetics . . . 51
3.4.4.1 Total, Specific and Nonspecific Binding . . . 51
3.4.4.2 Association and Dissociation . . . 52
3.4.5 Radiotoxicology . . . 55
3.4.5.1 Viability Assay Optimization . . . 55
3.4.5.2 Viability Assay Validation . . . 56
3.4.5.3 Radiopharmaceutical Cytotoxicity . . . 60
3.5 Discussion . . . 62
3.5.1 Radiopharmaceutical Production and Quality Control . . . 62
3.5.2 Gamma Counter Calibration . . . 62
3.5.3 Cell Doubling Time . . . 63
3.5.4 Pharmacokinetics . . . 63
3.5.5 Radiotoxicology . . . 65
3.5.5.1 Viability Assay Optimization . . . 65
3.5.5.2 Viability Assay Validation . . . 66
3.5.5.3 Radiopharmaceutical Cytotoxicity . . . 66
3.6 Conclusion . . . 68

Chapter 4: Preclinical Dosimetric Investigation of a Radiobromine PARP1 Inhibitor . . 69
4.1 MIRDcell Software . . . 69
4.2 Cellular Characterization . . . 74
4.2.1 Methods . . . 74
4.2.1.1 Nuclear Staining . . . 75
4.2.1.2 Radiopharmaceutical Cellular Distribution . . . 75

4.2.2 Results . . . 77
4.2.2.1 Cell Characterization . . . 77
4.2.2.2 Radiopharmaceutical Nuclear Distribution . . . 79
4.3 Cellular Dosimetry . . . 80
4.3.1 Methods . . . 80
4.3.1.1 Cellular Geometry . . . 80
4.3.1.2 MIRDCell Calculations and Validation . . . 81
4.3.1.3 *In Vitro* Dosimetry . . . 83
4.3.2 Results . . . 84
4.3.2.1 Cellular Dosimetry and MIRDcell Validation . . . 84
4.3.2.2 *In Vitro* Dosimetry . . . 87
4.4 Discussion . . . 88
4.5 Conclusion . . . 91

Chapter 5: PET Imaging Potential of Radiobrominated PARP1 Inhibitor and Murine Biodistribution Studies . . . 93
5.1 Tumor Models . . . 93
5.2 Positron Emission Tomography . . . 94
5.3 RAPID and OLINDA Dosimetry Platforms . . . 96
5.4 Methods . . . 99
5.4.1 Radiopharmaceutical Production . . . 99
5.4.2 Radiobromine PET Calibration . . . 99
5.4.3 Animal Cancer Cell Inoculation . . . 100
5.4.4 Imaging . . . 101
5.4.4.1 Ultrasound . . . 101
5.4.4.2 MicroPET/CT *In Vivo* Biodistribution . . . 104
5.4.4.3 Regions of Interest and Organ Contouring . . . 105
5.4.5 *Ex Vivo* Biodistribution . . . 106
5.4.6 Statistics . . . 107
5.4.7 Dosimetry . . . 107
5.5 Results . . . 108
5.5.1 Radiopharmaceutical Production . . . 108
5.5.2 Radiobromine PET Calibrations . . . 109
5.5.3 Tumor Models . . . 109
5.5.4 MicroPET/CT Imaging . . . 111
5.5.5 Biodistribution . . . 114
5.5.6 Dosimetry . . . 121
5.6 Discussion . . . 121
5.7 Conclusion . . . 128

Chapter 6: Conclusions and Future Work . . . 130
6.1 Conclusions . . . 130
6.2 Recommendations For Future Work . . . 131

Appendix A: Protocols . . . 135

A.1 Cell Line Handling . . . 135
A.1.1 Thawing . . . 135
A.1.2 Subculturing . . . 136
A.1.3 Freezing . . . 137
A.2 Preparing Concentration Stock Vials . . . 138
A.3 Total, Nonspecific and Specific Binding . . . 141
A.4 Timed Uptake Studies . . . 144
A.5 Luminescence Assay . . . 147
A.6 Clonogenic Assay . . . 148
A.6.1 Cell Plating and Staining . . . 148
A.6.2 ImageJ Colony Counting . . . 150
A.6.2.1 Lawn Forming Cells . . . 152
A.7 External Beam Radiotherapy Treatment . . . 154
A.8 Nuclear Extraction . . . 155
A.9 Subcutaneous Injections . . . 157

Appendix B: Supplemental Data . . . 160
B.1 Chapter 3: Cellular Pharmacokinetics and Cytotoxicity Studies with Radiobrominated PARP1 Inhibitor . . . 160
B.2 Chapter 4: Preclinical Dosimetric Investigation of a Radiobromine PARP1 Inhibitor 162
B.2.1 Radiopharmaceutical Cellular Distribution . . . 162
B.3 Chapter 5: PET Imaging Potential of Radiobrominated PARP1 Inhibitor and Murine Biodistribution Studies . . . 166

References . . . 178

LIST OF TABLES

2.1 Clinical PARP inhibitors (PARPi) and ovarian cancer. 11

2.2 General characteristics of therapeutic radionuclide decay particles [73]. 15

2.3 Radioisotopes of bromine with potential medical applications. Decay information is from the Online Nuclear Data Service [103] and the number of MAe^- per decay is from ICRP Publication 107 [104]. 19

3.1 Ovarian cancer cell lines investigated in this work. 28

3.2 Gradient method for analytical HPLC (aHPLC). 33

3.3 The [^{77}Br]RD1 pharmacological characteristics calculated from total and nonspecific binding studies in the various ovarian cancer cell lines and their corresponding 95% confidence intervals (CI). These values were calculated using the data summarized in Figure 3.14. 52

3.4 The dissociation rate constant (k_{off}) and nonspecific binding percent (NS) calculated from the association and competitive dissociation (1 μM BrRD1) assay with 0.13–0.44 nM [^{77}Br]RD1 (ID8 n=3, OVCAR8 n=3 and OVCAR8 PARP1-KO n=1). The calculated association rate constant (k_{on}) was calculated from the K_D calculated from the binding studies. 55

3.5 The dose to reduce the surviving fraction to 37% (D_{37}) as measured by viability assay over a range of 3–9 days post external beam radiotherapy treatment. These values were fit using the data shown in Figure 3.17. 56

3.6 The D_{37} calculated from the viability and clonogenic assays for various ovarian cancer cell lines (OVCAR8 PARP1-KO n=1 for the cytotoxic assay, otherwise n=2). 58

3.7 The EC_{50} values of the various ovarian cancer cell lines and their corresponding 95% CI for [^{77}Br]RD1. 60

4.1 Doubling time of ovarian cancer cell lines. 75

4.2 Cell and nuclear radii of various ovarian cancer cells. 78

4.3 [^{77}Br]RD1 cellular uptake for PARP expressing cell lines, PARP1(+) (n=6) and PARP1-KO, PARP1(-) (n=3) cell lines. 79

4.4 The assumptions used for calculations converting activity distribution to dose of various ovarian cancer cell lines. 84

4.5 A comparison of the nuclear self-dose for various cellular activity distributions normalized to the nuclear self-dose from PARP1(+) cellular activity distribution. . . 87

4.6 The D_{50} (Gy) nuclear doses measured from external beam radiotherapy (EBRT) and viability assay with [^{77}Br]RD1 and the relative biological effectiveness (RBE). 87

5.1 Procedure information for inoculation of ID8-based ovarian cancer cell lines in C57B6/J mice from literature. These studies informed the orthotopic and heterotopic inoculation scheduling in our study. 95

5.2 Listed energies and their associated characteristics of β^+ particles emitted from ^{76}Br and ^{18}F for comparison [78, 105, 164]. 97

5.3 *In vivo* [^{76}Br]RD1 uptake for the liver and liver section ROI. The difference between each ROI for each scan was measured and averaged. Percent difference between the liver section and liver is included. 112

5.4 *In vivo* and *ex vivo* [^{76}Br]RD1 organ uptake measurements in all animal models at 48 p.i. (n=16). 114

A.1 Cancer cell line plating characteristics and specific media. Seeding ratio is from an approximately 80% confluent plate. Doubling time for both UWB1.289 is from the ATCC website. Roby, *et al.* reported them as 15 h and 20 h for UWB1.289 and UWB1.289+BRCA1, respectively [130]. 135

A.2 The step in the protocol when each fraction is collected and the container used for gamma counting. SCV: scintillation vial; SN: supernatant. 156

B.1 Mass of the radioinert BrRD1 and the corresponding area under the curve (AUC) of the milli absorbance unit measured at 8.86 min. 161

B.2 Radiopharmaceutical [^{77}Br]RD1 activity measured for each fraction and the corresponding percent uptake. OVCAR8 PARP1-KO cells were dosed with the radiopharmaceutical with 2 μM radioinert BrRD1 (blocked) or without (nonblocked). . . 165

B.3 The *ex vivo* and *in vivo* [^{76}Br]RD1 organ uptake (%ID/g) at 4 time points p.i. in the nondiseased models (n=4). 166

B.4 The *ex vivo* and *in vivo* [^{76}Br]RD1 organ uptake (%ID/g) at 4 time points p.i. in the diseased models (n=12). 166

B.5 The [^{76}Br]RD1 organ uptake 48 post injection (p.i.) of the diseased and nondiseased models measured *in vivo* with microPET/CT. 171

B.6 The [^{76}Br]RD1 organ uptake in the diseased models measured *in vivo* with microPET/CT 48 h p.i. grouped by radiopharmaceutical administration method. . . . 171

B.7 The [^{76}Br]RD1 organ uptake in the diseased models measured *in vivo* with microPET/CT 48 h p.i. grouped by tumor model with administration method. 172

B.8 The [^{76}Br]RD1 organ uptake measured *ex vivo* of the diseased and nondiseased models. 172

B.9 The [^{76}Br]RD1 organ uptake in the diseased models measured *ex vivo* grouped by radiopharmaceutical administration method. 173

B.10 The [^{76}Br]RD1 organ uptake in the diseased models measured *ex vivo*, grouped by tumor model with administration method. 174

B.11 The tumor-to-muscle ratio (T:M) and tumor-to-contralateral-to-tumor control volume ratio (T:CTCV) for the three disease models measured *in vivo* at 48 h p.i. . . . 175

B.12 The [$^{76/77}$Br]RD1 estimated organ dose from Monte Carlo calculations using RAPID for murines and OLINDA for humans. 177

LIST OF FIGURES

2.1 Four repair pathways for a DNA double-strand break (DSB). Non-homologous end joining (NHEJ) uses proteins in complex to reconnect the broken ends. Single-strand annealing (SSA) undergoes end resection until encountering homologous repeats (shown in orange). The complimentary longer strand forms a tail that will eventually be cleaved. Alternative end joining (altEJ) is similar to SSA, except the annealing process does not need to occur at a homologous repeat location. Homologous recombination (HR) uses a sister chromatid or homologous chromosome to form a displacement loop (D-loop) to use as a template for DSB repair. Of all the pathways, HR gives an accurate repair, where NHEJ gives an error-prone repair and altEJ and SSA have deletions. 6

2.2 PARP1 protein (green) in complex with a DNA single-strand break (SSB) and PARP inhibitor, rucaparib (magenta) [36–38]. Olaparib, niraparib, talazoparib and veliparib also bind to this location. 10

2.3 Chemical structures of clinically used PARP inhibitors. 10

2.4 Simplified schematic of electron capture (EC) and internal conversion (IC) which can then produce Meitner-Auger electrons (MAe^-). In EC, the nucleus absorbs an inner orbital electron. In IC, the excited and unstable nucleus releases energy that ejects an inner orbital electron. In both instances, the hole left in the inner shell will be filled by an outer electron. When this happens, a characteristic x-ray can be emitted or an electron is ejected, called the MAe^-. 16

2.5 A PARP1 protein attached to a SSB is 600$\times$ smaller than the nucleus in an ovarian cancer cell. 17

2.6 Bromine isotopes with possible medical applications and the relevant stable isotopes that could be used for low-energy cyclotron production. Decay information is from the Online Nuclear Data Service [103]. 19

2.7 Simplified decay schemes of (**A**) positron-emitting ^{76}Br and (**B**) Meitner-Auger electron-emitting ^{77}Br [105, 106]. 20

2.8 Excitation functions for (**A**) ^{77}Br and (**B**) ^{76}Br [107, 108]. 21

2.9 Cell model consisting of two concentric spheres that make up the nuclear, cytoplasmic, and cell surface compartments. 26

3.1 Dry distillation of radiobromine using a vertical tube furnace assembly. The irradiated CoSe target (a) was placed in a flat-bottomed quartz tube (b) and sealed inside the assembly. Argon was flowed over the target through quartz (c) and PTFE tubing (d) and bubbled through a water trap (e) [138]. 31

3.2 Radiosynthesis of $^{76/77}$Br-labeled PARP1 inhibitor rucaparib derivative, [$^{76/77}$Br]RD1. 32

3.3 The binding study workflow conducted on ovarian cancer cells. Cell lines were plated at a density of 7,000–50,000 cells/well for 24 hours. After contacting in triplicate with [^{77}Br]RD1 (total binding) or [^{77}Br]RD1+1 μM BrRD1 (nonspecific binding) for 2 h at 37ºC, media and cells were collected in individual cluster tubes and the activity counted on a gamma counter (PerkinElmer). These measurements were used to plot the total and nonspecific binding curves. 40

3.4 The viability study workflow for all ovarian cancer cells. Ovarian cancer cells were plated at a density of 200 cells/well for 2 hours before contacting with [^{77}Br]RD1 in triplicate to wells for 7 days. Bioluminescent ATP assay (CellTiter-Glo 2.0) was used to measure the cell viability to generate surviving fraction (SF) curves. 40

3.5 Oxidative decarboxylation of luciferin is catalyzed by luciferase in the presence of ATP, oxygen and Mg^{2+} and emits light that can be measured [140]. This signal is directly proportional to the amount of ATP which is also directly proportional to the number of viable cells. 43

3.6 Cell growth after 7 days in a volume of 1.5 mL and a well area of 9.5 cm^2 for (**A**) ID8 colony forming cancer cells plated at a seeding of 40 cells and (**B**) UWB1.289 lawn forming cancer cells plated at a seeding of 5,000 cells. Cells were fixed and stained with 25% glutaraldehyde and 1% crystal violet. 44

3.7 The ColonyArea plugin for ImageJ crops the picture of the 6-well plate, converts the image to (**A**) an 8-bit image and then (**B**) uses a lookup table (LUT) to convert the pixel intensity to a corresponding color value. The arrow points to a stain smudge that indicates too large of a threshold value was used, but if the circularity function is used, these pixels would be excluded from the automatic colony tally function. . 46

3.8 Distillation of ^{77}Br for production number 7. 48

3.9 Radiochemical yield of [^{77}Br]RD1 after seven separate radiolabeling reactions. . . 48

3.10 Stability of [^{77}Br]RD1 after 72 hours in PBS. The radiopharmaceutical was greater than 95% stable for activity concentrations less than 2 MBq/mL. For activity concentrations larger than 4 MBq/mL, breakdown after 24 h occurred, with greater than 90% stability after 72 hours. 49

3.11 Bromine-77 gamma counter calibration factors for vials of various activity volumes. Larger volumes show less stability between measurements compared to smaller volume vials due to the geometric dependence of the gamma counter. 50

3.12 Calibration of the Wizard^2 gamma counter for ^{76}Br and ^{77}Br. The calibration coefficient was 1.85±0.02 Bq/CPS and 3.42±0.02 Bq/CPS for ^{76}Br and ^{77}Br, respectively. 50

3.13 ID8 cells were plated at a concentration between 100–4,800 cells/well in sextuplicate. The resulting cell density per well was counted by a hemocytometer as a function of time. 52

3.14 Total (closed symbols, solid lines) and nonspecific (open symbols, dotted lines) binding of (**A**) UWB1.289 (gold, n=3), UWB1.289 +BRCA1 (gray, n=3), ID8 (red, n=2) (**B**) OVCAR8 (green, n=4), and OVCAR8 PARP1-KO (blue, n=4) and (C) the specific binding (dashed lines) of [^{77}Br]RD1 as a function of radiopharmaceutical molar concentration. 53

3.15 The fractional activity bound to the cells as a function of time for ID8 and OVCAR8 (n=1) ovarian cancer cell between 2 minutes and 21 hours. The dissociation was measured by removing the radiopharmaceutical containing media and adding fresh media. 56

3.16 The association and dissociation of [^{77}Br]RD1 for the ID8 (n=3, 0.216 nM), OVCAR8 (n=3, 0.113–0.408 nM), and OVCAR8 PARP1-KO (n=1, 0.271 nM) cell lines. Each curve represents a single experiment. The kinetic dissociation was measured with competing 1 μM BrRD1 at 1 hour. 57

3.17 The viability assay was performed 3 (n=1), 5 (n=2), 6 (n=1),7 (n=2) and 9 (n=1) days after EBRT of (**A**) OVCAR8 and (**B**) ID8 ovarian cancer cells. 58

3.18 Validation of the ImageJ area calculation method. (**A**) The colony forming cell line, ID8, shows a manual count of 15 colonies (excluding 3 small colonies less than 25 cells). The measuring tool can report the ROI (red circle) area and the percentage of pixels within the green mask. Knowing the average size of a colony, the number of colonies can be calculated. (**B**) A comparison of the average surviving fraction as a function of dose for the area calculation method to the manual count for 6 wells at each dose level. 59

3.19 Validation of the viability assay (open symbols) was done with clonogenic assay (shaded symbols) using EBRT as the treatment for (**A**) ID8 (red), OVCAR8 (green), (**B**) UWB1.289 (gold) and UWB1.289+BRCA1 (grey). 59

3.20 The D_{37} calculated from the viability and clonogenic assays for various ovarian cancer cell lines (n=2). 60

3.21 (**A**) The cell survival of ID8 (red, n=2), OVCAR8 (green, n=4), OVCAR8 PARP1-KO (blue, n=3), UWB1.289 (gold, n=3), and UWB1.289+BRCA1 (gray, n=3) cell lines as a function of radiopharmaceutical activity concentration (**B**) and the same data presented without data points to clearly compare the trendlines. (**C**) The same data as a function of molar concentration. (**D**) The radiopharmaceutical activity concentration was converted to specific uptake (Bq/cell) inherent to the cell lines. The gray region in (**B**) and (**D**) show how the spread changes with the conversion. . 61

4.1 Radiation source tab allows the user to choose the radionuclide and full or average β energy spectrum. The user can also choose a monoenergetic particle emitter or manually enter radionuclide information. For predefined MIRD radionuclides, the input data for calculation is shown in the bottom left box. 71

4.2 Defining the target regions for output calculations, the radius of the nucleus and cell and the radiopharmaceutical cellular distribution within the cell surface, cytoplasm or nucleus. 72

4.3 The cell labeling and multicellular geometry configuration for a 2D example. . . . 73

4.4 An example of the output given for a 2D configuration. 73

4.5 The time it takes a single cell from various cell lines with varying doubling times to create 9, 25, 45, 69 and 109 cell colonies is shown. Two cell lines reach confluency before a 7-day treatment time and are shown in solid red circles. UWB1.289+BRCA1 finishes a 7-day treatment time with approximately 350 cells in a colony. [a]OVCAR8 PARP1-KO is assumed to have the same doubling time as OVCAR8. 77

4.6 Fluorescence and bright field microscopic imaging of various ovarian cancer cell lines. Scale bar: 10 μm (×40). 78

4.7 [^{77}Br]RD1 cellular uptake for OVCAR8 (n=6) and OVCAR8 PARP1-KO (n=3) cell lines. Uptake in ID8 and both UWB1.289 lines were assumed to have the same radiopharmaceutical distribution as the OVCAR8 cell line. 79

4.8 Examples of multicellular geometry configurations in 2D, with the first 5 examples showing an increase in the colony size for a spherical colony. The last example shows 200 cells with 400 μm distance between cells in a 3.2 mm radius area like that in a 96-well plate well. Images were taken from MIRDcell v3.12 and are not to scale. 81

4.9 (**A**) The cellular dimensions used for nuclear dose calculations. Two activity distributions were used for calculations, (**B**) a uniform activity distribution of 67.5% and 32.5% in the nucleus and cytoplasm, respectively, and (**C**) 44.3% and 55.7% in the nucleus and cytoplasm, respectively. 82

4.10 Nuclear self-dose calculations of various cell sizes for cellular activity distributions corresponding to PARP1(+) and PARP1(-) expression. 84

4.11 The dose to the cytoplasm or nucleus from radiobromine as a percentage of (**A**) particle type contribution and (**B**) self- or cross-dose contribution averaged from a 9-cell colony and confluent 96-well plate for cell with radii sizes of 8, 10 and 12 μm. IE: internal conversion electron. 85

4.12 A comparison of the calculated nucleus dose between the reference (no adjacent cells) and either a 9-, 25-, 145-cell colony or a confluent 96-well plate well for (**A**) ^{76}Br, (**B**) ^{77}Br and (**C**) ^{80m}Br. Differences for cellular dose distributions corresponding to PARP1(+) and PARP1(-) are summarized. 86

4.13 Nuclear dose as a function of the specific uptake calculated from MIRDcell for various ovarian cancer cell lines for ^{76}Br, ^{77}Br, ^{80m}Br. The cell line labeled OVCAR8-KO is PARP1-KO. 87

4.14 (**A**) Viability assays (Fig. 3.21D) conducted for several ovarian cancer cell lines, with cell survival plotted as a function of specific uptake (Bq/cell). (**B**) The specific uptake was converted to absorbed dose for ^{77}Br. 88

5.1 Study design for control (blue), heterotopic (green) and orthotopic (black) models. Orthotopic models underwent transabdominal ultrasound (TAUS) monitoring for disease progression and staging. The mice were ranked for disease burden based on TAUS imaging and the 8 mice with the highest burden were chosen for PET/CT and biodistribution studies. For intravenous drug administration, control models had a 1-hour dynamic scan and heterotopic and orthotopic models had a 20-minute dynamic scan. For IP drug administration in orthotopic models, a static microPET/CT was conducted at 1 hour. 102

5.2 Study timeline for orthotopically diseased mice with ID8 ovarian cancer. 103

5.3 X-ray CT images showing contours of masses at tumor-injection-sites (TIS, in pink) and contralateral-to-tumor control volumes (CTCV, in navy) in (**A-B**) two orthotopic models shown here in the coronal plane and (**C-D**) two heterotopic models shown in the axial plane. Mice were imaged in the prone position. 106

5.4 Derenzo phantoms with 1.0–1.5 mm and 1.6–2.6 mm sized rods filled with ^{76}Br. Images were acquired on a Siemens Inveon microPET. 109

5.5 (**A**) The computed maximum intensity projection (MIP) for a partial volume (PV) correction phantom injected with ^{76}Br. The recovery coefficient (RC) (**B**) as a function of sphere volume and (**C**) as a function of sphere diameter. 110

5.6 Tumors located on the left gracillis or adductor muscle on the left side of the mice. Intraperitoneal (IP) injection occurred in the lower left quadrant of the abdomen, approximately 0.5–1 cm superior to these two tumors. 110

5.7 (**A**) Anatomy of mouse liver, including right medial (RM) lobe, left medial (LM) lobe, and left lateral (LL) lobe. The gallbladder is located posterior and between the RM and LM lobes. (**B**) Registered PET/CT image at 4 h post injection (p.i.) showing gallbladder uptake. (**C**) Registered PET/CT image at 24 h p.i. showing liver uptake. 111

5.8 PET MIP images of a representative heterotopic mouse injected intravenously with [^{76}Br]RD1. Red arrow: heart; brown arrow: liver; green arrow: intestines; blue arrow: gallbladder; white arrow: stomach contents. 113

5.9 PET/CT axial slice at 4 h p.i. of two heterotopic mouse models with masses at the tumorinjection-site (TIS) on the right flank and corresponding CTCV on the left side. 113

5.10 The *in vivo* [^{76}Br]RD1 organ uptakes at 4 time points p.i. and the *ex vivo* measurement in the (**A**) nondiseased models (n=4) and (**B**) diseased models (n=12). 115

5.11 *In vivo* and *ex vivo* [^{76}Br]RD1 organ uptake measurements 48 h p.i. (n=16). †*In vivo* organ contour compared to *ex vivo* organ and organ contents separately, i.e., blood for heart, and enteric contents (EC) for stomach. $^{*}P<0.05$. 116

5.12 The [^{76}Br]RD1 uptake *in vivo* at 48 h of the 16 mice grouped into various cohorts. (**A**) Diseased (n=12) vs nondiseased (n=4), (**B**) IP injected (n=4) vs IV injected (n=8) in diseased models and (**C**) the diseased mice split into disease models and injection method (n=4 for all). $^{*}P<0.05$. CTCV:Contralateral-to-tumor control volume. 117

5.13 The *ex vivo* biodistribution of the 16 mice grouped into various cohorts. (**A**) Diseased (n=12) vs nondiseased (n=4), (**B**) IP injected (n=4) vs IV injected (n=8) in diseased models and (**C**) the diseased mice split into disease models and injection method (n=4 for all). $^{*}P<0.05$. Gb=gallbladder, LI=large intestine, SI=small intestine, EC=enteric contents. 118

5.14 Timed uptake of [^{76}Br]RD1 in all the mice (n=16) for various organs measured *in vivo*. TIS: tumor-injection-site 119

5.15 Timed activity curves of [^{76}Br]RD1 in the (**A**) normal tissues liver, heart bladder, kidney, (**B**) tumor-injection-site (TIS) and contralateral-to-tumor control volume (CTCV) for each model measured *in vivo* (n=4). 120

5.16 Dosimetry analysis showing estimated integrated organ-level absorbed doses following [^{76}Br]RD1 administration for (**A**) each disease model using RAPID, (**B**) all diseased mice using RAPID, (**C**) in nondiseased mice using RAPID and (**D**) equivalent dose in female humans using OLINDA. SI: small intestine; ULI: upper large intestine; LLI: lower large intestine. 122

A.1 Excel spreadsheet to calculate volumes and concentrations depending on type and number of assays to perform after production of [^{77}Br]RD1. 138

A.2 (**A**) Radiopharmaceutical concentration orientation of wells. Series Uc and UBc are the control wells with no radiopharmaceutical added, just 20 µL of PBS. Wells with cells and radiopharmaceutical are surrounded by wells with 200 µL of PBS to avoid edge effects on dosed wells. (**B**) A ten-sample rack orientation for the gamma counter. The first 3 slots are empty, the 4th slot has an empty sample holder for a rack background count, and the next 6 slots have samples from the same radiopharmaceutical concentration level. 142

A.3 (**A**) Timed uptake orientation of wells. The k_{off} series had the radiopharmaceutical added to it 60 minutes before beginning the timed series. The labels on the left-hand side corresponds to the plotted time in minutes (add 60 to each label for the k_{off} data). At each time point, starting at time point labeled 60 minutes, radiopharmaceutical was added to the k_{on} series and antagonist was added to the k_{off} series. This was repeated for subsequent rows at the corresponding time. (**B**) A ten-sample rack orientation for gamma counter measurements. The first slot has an empty sample holder for a background count, and the next 9 slots have samples with increasing activity levels, starting with k_{on} at time point label 1. Repeat the same order for the k_{off} vials. 145

A.4 Hemocytometer dimensions and example. If counting the 1.0×1.0 mm^2 boxes marked in green and choosing to count the outside edges of the hemocytometer, the upper left-hand corner has 8 cells, the lower corner has 9 cells, and the average count is 8.5×10^4 cells/mL. 148

A.5 Use the rectangle selection tool to outline the wells to analyze. The box should encompass the wells themselves (yellow line) instead of the edges of the well as to not throw an error. You can see here that I used a blank page of Word to have the computer screen fill with white to get a clean picture of my plate. 151

A.6 The LUT image stack is shown in the top right (showing well 1 of 6). The gray scale images processed into binary images are shown in the middle box. It also has the Overlay (shown in blue) from Analyze Particles and a count marker over each counted colony. The Results box summarizing the characteristics of each colony is shown on the right, and the Summary box for all images in the stack is shown in the lower left box. 152

A.7 The left image is after converting the image stack to binary images. The *Oval* selection was used to place an ROI over the well. The shadow from the well edge is excluded from the ROI selection. The Results box on the right shows measurements for individual colonies as the first 8 entries. The final six measurements are of the entire well. 153

B.1 Calibration curve of radioinert BrRD1 on analytical high-performance liquid chromatography (aHPLC). 160

B.2 (**A**) Comparison between radiopharmaceutical distribution when OVCAR8 cells are dosed for 2 h or 24 h. (**B**) Comparison between radiopharmaceutical distribution of OVCAR8 and OVCAR8 PARP1-KO ovarian cancer cells with and without a blocking dose (2 μM radioinert BrRD1) was added to the OVCAR8 PARP1-KO cell lines to see effects of radiopharmaceutical cellular distribution. SN: supernatant; CF: cytosolic fraction; NE: nuclear extract; NM: nuclear membrane. 164

B.3 Serial maximum intensity projection (MIP) PET/CT images of nondiseased models (mice labeled N1-N4) IV injected with [^{76}Br]RD1. Dynamic scans were acquired at t=0–60 minutes in 1 minute bins from 0–5 minutes, 5 minute bins between 5–20 minutes, and a 10 minute bin from 50–60 min. Static scans were acquired at t=4, 24 and 48 h. Scales are in %ID/g. 167

B.4 Serial maximum intensity projection (MIP) PET/CT images of heterotopic models (mice labeled H1-H4) IV injected with [^{76}Br]RD1. Dynamic scans were acquired at t=0–20 minutes in 1 minute bins from 0–5 minutes and 5 minute bins between 5–20 minutes. Static scans were acquired at t=4, 24 and 48 h. Scales are in %ID/g. 168

B.5 Serial maximum intensity projection (MIP) PET/CT images of orthotopic models (mice labeled O1-O4) injected with [^{76}Br]RD1 via IV administration. Dynamic scans were acquired at t=0–20 minutes in 1 minute bins from 0–5 minutes and 5 minute bins between 5–20 minutes. Static scans were acquired at t=4, 24 and 48 h. Scales are in %ID/g. 169

B.6 Serial maximum intensity projection (MIP) PET/CT images of orthotopic models (mice labeled O5-O8) injected with [^{76}Br]RD1 via IP administration. Static scans were acquired at t= 1, 4, 24 and 48 h. Scales are in %ID/g. 170

B.7 (**A**) Tumor-to-muscle ratios (T:M) *in vivo* at various time points compared to the *ex vivo* and tumor-to-contralateral-to-tumor control volume ratios (T:CTCV) *in vivo* at 48 h p.i. of 9.2 MBq (250 μCi) [^{76}Br]RD1 in the various diseased models (heterotopic, orthotopic (IV or IP)) in tumor-bearing mice. (**B**) Heterotopic T:M *ex vivo*, *in vivo* and partial volume (PV) corrected using the recovery coefficient based off caliper measurements of the tumors before imaging at 48 h p.i. [a]Recovery coefficient (RC) corrected. (**C**) The tumor-to-organ ratios for the organs measured *ex vivo* after the 48 h p.i. PET scan for all diseased models. 176

LIST OF ABBREVIATIONS

*	$P \leq 0.05$
**	$P \leq 0.001$
%ID/g	Percent injected dose per gram
aHPLC	Analytical high-performance liquid chromatography
ATP	Adenosine triphosphate
B_{max}	Maximum specific binding
AUC	Area under the curve
BG	Background
BRCA1/2	Breast cancer type 1 and 2
CI	Confidence interval
CPM	Counts per minute
CPS	Counts per second
CsI(Tl)	Cesium iodide (thallium)
CT	Computed tomography
CTCV	Contralateral-to-tumor control volume
D_{37}	Dose corresponding to a surviving fraction of 37% of the original
DAPI	4',6-diamidino-2-phenylindole
DSB	Double-strand break
DTT	Dithiothreitol
EBRT	External beam radiotherapy
EC_{50}	Half maximal effective concentration
EOC	Epithelial ovarian cancer
FBS	Fetal bovine serum
Geant4	Geometry and Tracking Generation 4
Gy	Gray
HGSC	High-grade serous carcinoma
HPGe	High purity germanium
HR	Homologous recombination
HU	Hounsfield unit
IP	Intraperitoneal
IV	Intravenous
K_D	Equilibrium dissociation constant
KO	Knock-out
LET	Linear energy transfer
MA	Molar activity

MAe$^-$	Meitner-Auger electron
MAPi	Meitner-Auger PARP1 inhibitor
mAU	Milliabsorbance unit
MC	Monte Carlo
MIP	Maximum intensity projection
MIRD	Medical Internal Radiation Dose
NS	Nonspecific
OTf	Trifluoromethanesulfonate
p.i.	Post injection
PARP	Poly [ADP-ribose] polymerase
PARPi	PARP inhibitor
PBS	Phosphate-buffered saline
PDB	Protein data bank
PET	Positron emission tomography
pHPLC	Preparative high-performance liquid chromatography
PTFE	Polytetrafluoroethylene
PV	Partial volume
QMA	Quaternary methyl ammonium
RAPID	Radiopharmaceutical Assessment Platform for Internal Dosimetry
R_C	Cell radius
RC	Recovery coefficient
RCC	Radiochemical conversion
rcf	Relative centrifugal force
rpm	Rotations per minute
RCP	Radiochemical purity
RCY	Radiochemical yield
RD1	Rucaparib derivative 1
R_N	Nucleus radius
ROI	Region of interest
RPT	Radiopharmaceutical therapy
SCV	Scintillation vial
SN	Supernatant
SPECT	Single-photon emission computed tomography
SSB	Single-strand break
T:M	Tumor to muscle ratio
TAC	Time activity curve
TC	Tissue culture
TLC	Thin layer chromatography

CHAPTER 1
INTRODUCTION AND OUTLINE

1.1 Overview

A Meitner-Auger electron (MAe^-) emitting radionuclide-labeled poly [ADP-ribose] polymerase inhibitor (PARPi) was investigated to explore the fundamental radiation biology of low-energy electron emitters in ovarian cancer. The high linear energy transfer (LET) capabilities and short range of MAe^- make them a promising tool for inducing lethal damage in the target area while minimizing harm to surrounding tissue. By binding to DNA, PARPis enable targeted damage by the short-range MAe^-. This potential combination therapy may increase the damage to ovarian cancer cells with fewer side effects than traditional radiotherapy or PARPi targeted therapy.

Radiobromine was chosen as the radionuclide because of its favorable characteristics, including its ability to radiolabel small molecule biological targeting vectors, such as PARPis, the production routes via a (p,n) reaction, the half-life of the isotope that is favorable for therapy, diagnostics and commercial use, and its capability as a theranostic with ^{76}Br as the diagnostic radionuclide and ^{77}Br as the therapeutic radionuclide.

1.2 Aims

The goal of this project is to investigate the potential of [$^{76/77}$Br]RD1 as a theranostic for metastatic ovarian cancer. The aims of this work were to (1) characterize the cellular pharmacokinetics and cytotoxicity of a PARPi, [^{77}Br]RD1, in various ovarian cancer cell lines *in vitro*, (2) characterize the cellular properties and activity distribution of [$^{76/77}$Br]RD1 to perform cellular dosimetric calculations and (3) characterize the biodistribution *in vivo* and *ex vivo* of [^{76}Br]RD1 in animal models and estimate the dosimetry in murine and human models.

1.3 Thesis Outline

This thesis will start with a background chapter before going into the aims. Each chapter that covers an aim (Chapter 3–5) will have an additional introduction/background section at the beginning of the chapter to cover aim-specific concepts before going into the methods, results, discussion and conclusion. The specific chapter and appendices descriptions are listed below.

Chapter 2: *Background*

This chapter describes background information on fundamental concepts pertinent to this work. It will add context and go further in depth on topics that are present throughout this thesis. When going through the rest of the chapters, this chapter can always be used as reference to go back to. It will discuss ovarian cancer, PARP inhibitors, radiobromine production and chemistry and dosimetry concepts.

Chapter 3: *Cellular Pharmacokinetics and Cytotoxicity Studies with Radiobrominated PARP1 Inhibitor*

This chapter will cover the first aim of this work. It describes the ovarian cancer cell lines chosen for this work and the pharmacokinetics and radiotoxicology of [^{77}Br]RD1.

Chapter 4: *Preclinical Dosimetric Investigation of a Radiobromine PARP1 Inhibitor*

This chapter will have a different organization compared to Chapter 3 and Chapter 5. Instead of having a "Methods" and "Results" section, this chapter is broken up into two subsections, one describing *in vitro* studies characterizing the cell lines and the second describing the cellular dosimetry calculations. In each subsection, methods and results are described. This organization is necessary because the cell characterization results directly inform the methods used in the dosimetry calculations. After reporting the results of the dosimetry calculations, the discussion and conclusions pertain to the contents of the entire chapter.

Chapter 5: *PET Imaging Potential of Radiobrominated PARP1 Inhibitor and Murine Biodistribution Studies*

Covering the third aim, Chapter 5 will explore the feasibility of [^{76}Br]RD1 as a PET radiotracer. It will report the biodistribution of [^{76}Br]RD1 in mice *in vivo* over 2 days and compare that to the measured *ex vivo* organ uptake. *In vivo* PET measurements will be used to calculate murine doses and estimate human organ doses.

Chapter 6: *Conclusions and Future Work*

Chapter 6 will summarize the work provided in this thesis and provide recommendations for future directions.

Appendices

The appendices will provide protocols for many of the assays discussed in this work. They are provided in stepwise form for future investigators to reference, with personal recommendations sprinkled throughout. Additionally, some chapters have supplemental materials. Those contents can be found here. Most of the supplemental information are tables for data that have already been presented in graph form in their respective chapters, but are provided here for completeness.

CHAPTER 2
BACKGROUND

2.1 Ovarian Metastatic Cancer

An estimated 19,710 new cases of ovarian cancer will be diagnosed in 2023 [1]. Approximately 19% of those will be caught at the local site, while more than 75% of patients diagnosed will present with distant-staged disease. Symptoms for ovarian cancer usually do not manifest until the advanced stage of the disease, when tumor cells disseminate through peritoneal fluid within the abdominal cavity and cause ascites [2]. Once ovarian cancer has metastasized, patients have a 5-year relative survival rate of 30%, a rate that has only increased 1–3% over the last 20 years [3].

Epithelial ovarian cancer (EOC) accounts for 90% of all new ovarian cancer diagnoses, making it the most common type of ovarian cancer [4]. There are four different subgroups of EOC, with one being serous ovarian cancer. This subtype is further divided into two groups—low-grade and high-grade serous ovarian cancer (HGSC). HGSC comprises approximately 75% of all EOCs and is defined by the poorly differentiated cells with a pattern of invasion and rapid growth [5].

Currently, the standard of care for advanced ovarian cancer includes cytoreductive surgery and platinum-based chemotherapy with curative intent [6, 7]. Platinum-based chemotherapy drugs are known for their lack of selectivity, high systemic toxicity and drug resistance [8]. Patients may have good initial response to this treatment, but approximately 75% of women in the advanced stage of the disease will relapse, requiring further chemotherapy treatments. Furthermore, 30% of these patients will develop chemotherapy drug resistance, at which point, treatment intent shifts from curative intent to maintaining an acceptable quality of life [9].

The Cancer Genome Atlas in 2016 provided comprehensive molecular characterization of EOC and HGSCs, which demonstrated an over-representation of breast cancer type 1/2 *BRCA1/2* pathogenic variants [10]. This demonstrated the importance of double strand DNA repair pathways,

such as the homologous recombination (HR) repair pathway, with further studies confirming that dysfunction in this pathway lead to a higher risk of development of EOC. Drugs targeting the HR dysfunction in patients who have relapsed provide another way to target the advanced disease for patients who have poor prognosis and few options.

2.1.1 DNA Repair Pathways

A single-strand break (SSB) or double-strand break (DSB) of DNA compromises the genetic integrity of the cell. This needs to be addressed through cell signaling, either for repair or induction of cell death. When incorrect repair occurs, this can lead to mutations. For SSB repair, the complementary DNA strand can be used as a template for the broken strand. For most DSB repair pathways, this is not possible, and so the DNA is more vulnerable to repair errors.

There are several distinct pathways for repair of DNA DSBs, including non-homologous end joining (NHEJ), alternative end joining (altEJ, also known as microhomology-mediated end joining), single-strand annealing (SSA) and homologous recombination (HR) (Fig. 2.1, [11–13]). In NHEJ, the DNA ends next to the break are engaged by proteins aiding in the repair, forming a complex that aid in trimming the DNA ends [14]. This is then followed by DNA gap filling and ligation. These can cause deletion or insertion of a few nucleotides, which result in error-prone repair. In altEJ and SSA, the 3' end undergoes annealing to form intermediate 3' DNA tails. These tails are then trimmed, and the DNA joint is sealed through ligation. AltEJ and SSA join the DNA at different locations, with altEJ repair joining by microhomology-mediated DNA and the SSA repair joining at homologous repeats. Both of these processes result in deletions.

HR repair is the only pathway that gives an accurate repair without deletion or errors. It uses a sister chromatid or homologous chromosome DNA strand as a template to repair the DSB. It unzips the sister chromatid at the section of the break to create a displacement loop (D-loop) [14]. Synthesis of the broken strand then occurs within the D-loop to aid in the repair. When there is a decrease or dysfunction in this pathway, it can lead to inefficient repair of DNA, which may then lead to mutations that can lead to cancers.

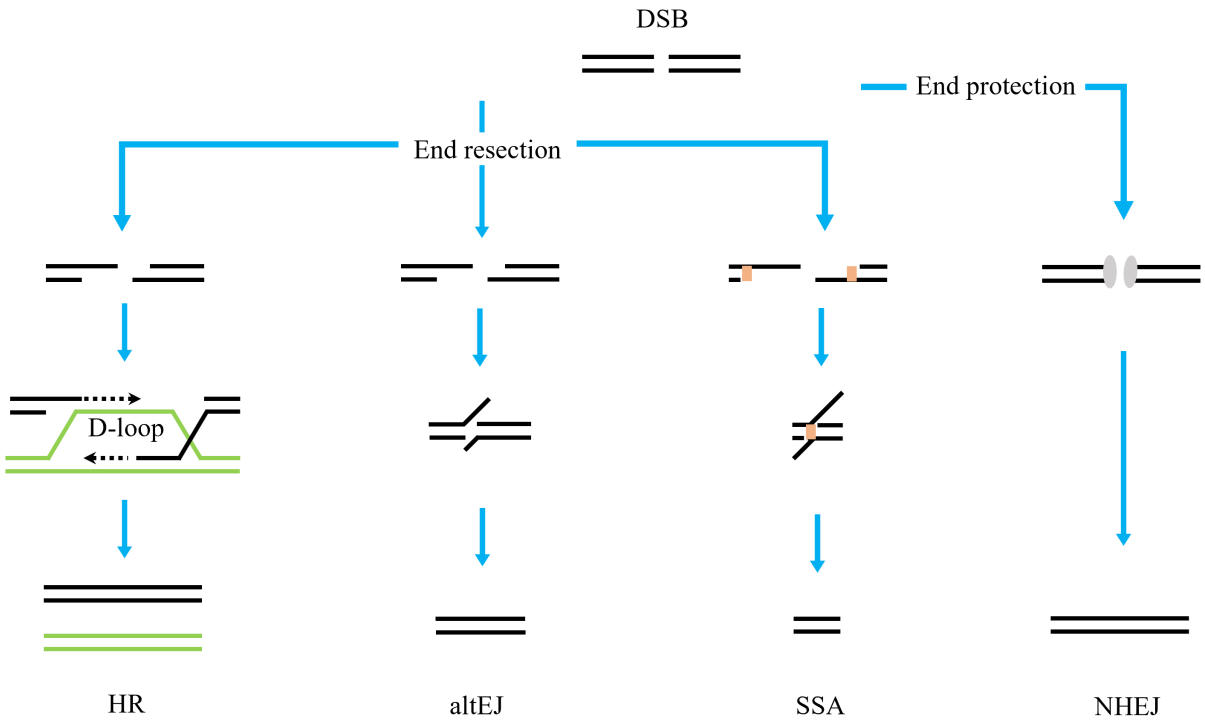

Figure 2.1: Four repair pathways for a DNA double-strand break (DSB). Non-homologous end joining (NHEJ) uses proteins in complex to reconnect the broken ends. Single-strand annealing (SSA) undergoes end resection until encountering homologous repeats (shown in orange). The complimentary longer strand forms a tail that will eventually be cleaved. Alternative end joining (altEJ) is similar to SSA, except the annealing process does not need to occur at a homologous repeat location. Homologous recombination (HR) uses a sister chromatid or homologous chromosome to form a displacement loop (D-loop) to use as a template for DSB repair. Of all the pathways, HR gives an accurate repair, where NHEJ gives an error-prone repair and altEJ and SSA have deletions.

2.1.1.1 Breast Cancer Type 1/2 (BRCA1/2) Gene

Genes like breast cancer type 1 (*BRCA1*) are essential in the HR repair pathway. *BRCA1* is a human tumor suppressor gene that aids in DNA repair, transcription and tumor suppression. *BRCA1* may act as a higher-order mediator for HR by recruiting proteins necessary for DSBs [15]. The BRCA1 protein also has a role in the nucleolytic resection of DSB ends, indicating that *BRCA1* influences the efficiency of DNA end resection [14]. BRCA2 has a role downstream of BRCA1, involving the regulation of protein RAD51. Although unclear, BRCA2 may transport RAD51 into the nucleus of the cell to the site of DNA damage for repair [16].

BRCA1/2 deficiency can be acquired through spontaneous deleterious mutations, epigenetic silencing of *BRCA1/2* through DNA methylation, or the presence of germline *BRCA1/2* mutations, i.e., hereditary mutations that are passed on from parent to offspring, [14]. Patients with germline mutations of *BRCA1/2* are at a higher risk of cancer due to the HR repair pathway deficiencies, with these cancers developing most commonly as breast or ovarian cancers [17, 18]. The general population at the age of 70 has a risk of developing ovarian cancer 1–2%, increasing to 39% (95% confidence interval (CI): 18–54%) and 11% (95% CI: 4–18%) for *BRCA1* and *BRCA2* mutations, respectively [1, 19].

Although these mutations cause problems, BRCA1/2 deficiency can be exploited for therapeutic approaches. Mutant cells are sensitive to DNA damage since the HR pathway is deficient, so approaches that causes SSBs and DSBs, like ionizing radiation, can lead to cell death. *BRCA1/2* germline mutations are associated with tumor response to platinum-based therapies and PARP inhibitors [20–24], discussed in Section 2.1.2.1.

2.1.1.2 Poly(ADP-Ribose) Polymerase 1 Protein

Poly(ADP-Ribose) polymerase 1 (PARP1) is a nuclear DNA damage response protein that binds to single- and double-strand breaks in DNA. Following this binding, using nicotinamide adenine dinucleotide as a substrate, PARP1 catalyzes the formation of poly(ADP-ribose) (PAR) polymers on itself and other target proteins, such as nearby histones, a process called PARylation [25]. The

PARP1 protein consists of three domains—the N-terminal DNA-binding domain (containing zinc finger motifs), the C-terminal catalytic domain, and the central automodification domain (containing the BRCA1 C-terminal (BRCT) domain). These domains help mediate PARP1 in the DNA damage response processes, with a high binding affinity to DNA breaks [25]. PARP1 recognizes breaks quickly, making it a first responder to DNA repair. It also functions, through PARylation, as a recruiter for other proteins to help in repair. In the DSB repair process, it has a role in end resection by recruiting enzyme MRE11 and then binding to a single strand at the break site. This occurs in HR and altEJ during the end resection portion of the repair pathway.

2.1.2 Therapies

The recurrence rate for EOC is very high, with approximately 75% of patients experiencing relapse [8]. First-line therapy after cytoreductive surgery is platinum-based chemotherapy with curative intent [26]. However, most patients present with advanced disease and will relapse. Secondary therapy options will depend on platinum-free interval, i.e., the time between the last platinum dose and the relapse diagnosis, and the side effects incurred during the first round of therapy. If relapse occurs within six months of the last dose of platinum-based therapy, then the EOC will generally be classified as platinum resistant [27]. When a secondary therapy is required due to platinum resistance, several approaches can be utilized to improve efficacy: improving drug delivery, re-sensitizing the tumor to platinum, enhancing immune responses, modulating the cell cycle, or exploiting synthetic lethality, i.e., the induction of cell death caused by simultaneously inactivating two different genes or biological pathways, neither of which affect viability when inactivated alone [28].

2.1.2.1 PARP Inhibitors

Specific, high affinity small molecule PARP inhibitors (PARPi) were discovered in the mid-2000s [29, 30]. These PARPi are nicotinamide mimics, binding to the NAD+-substrate binding pocket in the C-terminal catalytic domain of PARP and inhibiting the enzymatic function of

PARylation. PARPi exploit synthetic lethality through SSB and DSB repair pathways, specifically the HR impaired pathway. The PARPi limits the control of the MRE11 protein, which results in excessive DNA degradation [31]. A SSB bound to an inhibited PARP protein has a higher chance of becoming a DSB during DNA replication, which can then be repaired by HR. In mouse models with normal working HR pathways, inhibition of PARP, either through genetic ablation or PARPi, does not increase the development of tumors or onset of cancer [32]. However, when the HR pathway is deficient, like in the case of a deleterious *BRCA1/2* mutations, PARPi can cause cellular lethality through synthetic lethality [28]. With *BRCA1/2* mutated, PARP inhibition causes chromosomal instability, cell-cycle arrest and apoptosis [33].

PARPi trap PARP1 protein on the DNA [34, 35]. In Figure 2.2, the PARPi is shown bound to the PARP1 protein in complex with a SSB of DNA using files obtained from the Protein Data Bank (PDB). Three x-ray crystal structures, one with the complete PARP1 protein [36], one with the two N-terminal zinc finger motifs F1 and F2 bound to a DNA SSB [37], and one with the catalytic domain bound to PARPi, rucaparib [38], were superimposed over each other in PyMOL v2.4.0 to estimate the geometry of the inhibitor-protein-DNA complex the complex. When PARP1 is bound to a DNA SSB, the PARPi are approximately 50 Å from the DNA.

Olaparib and rucaparib are FDA approved PARPi that are used for both treatment and maintenance therapy of *BRCA* mutated ovarian cancer. Olaparib was approved in 2014 as the first PARPi used for the treatment of BRCA-mutated metastatic ovarian cancer. Rucaparib was approved in 2016 for advanced stage ovarian cancer with somatic or germline *BRCA1/2* mutations. Olaparib, rucaparib and niraparib were approved in 2017 for maintenance therapy in recurrent cases, regardless of *BRCA1/2* mutation [39]. Rucaparib and olaparib were also approved for prostate cancer in 2020. PARPi used clinically are summarized in Table 2.1. The chemical structures are summarized in Fig. 2.3.

PARPi can be used as a monotherapy or in combination with other therapies, including chemotherapy, immunotherapy, or targeted therapy, to overcome PARPi resistance. Unfortunately, whether as a monotherapy or combination therapy, although PARPi have increased progression-free

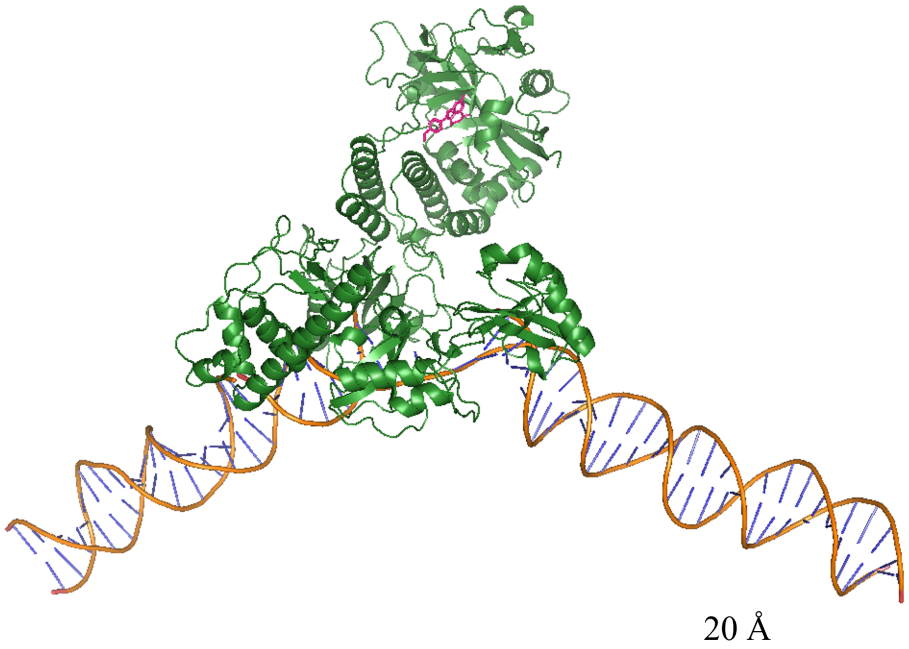

Figure 2.2: PARP1 protein (green) in complex with a DNA single-strand break (SSB) and PARP inhibitor, rucaparib (magenta) [36–38]. Olaparib, niraparib, talazoparib and veliparib also bind to this location.

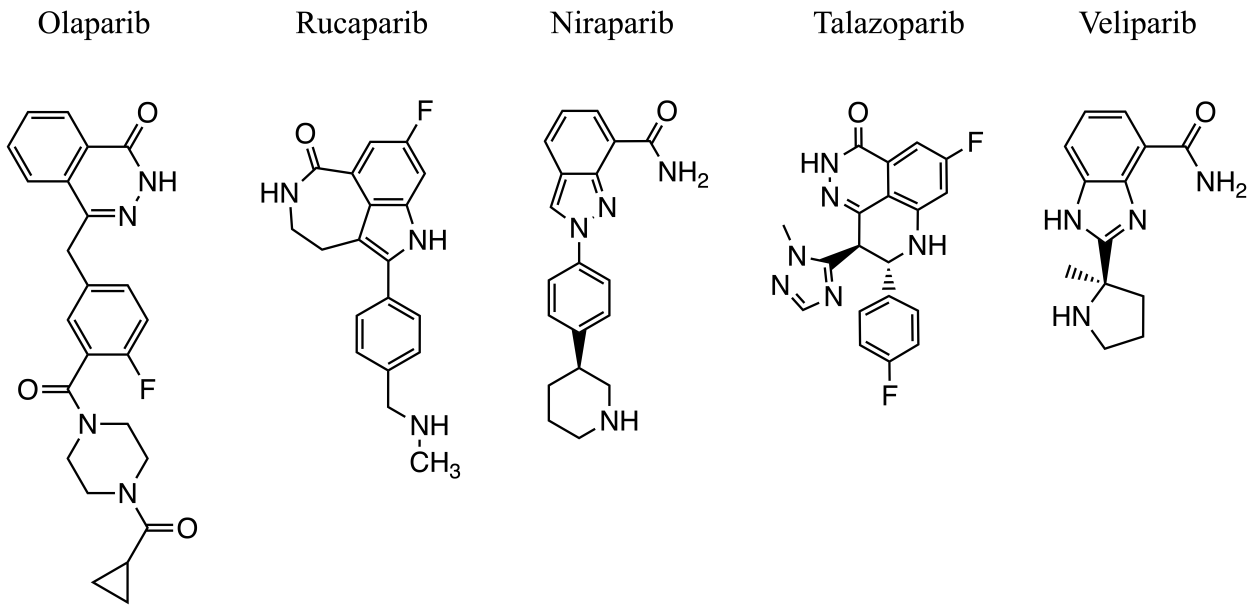

Figure 2.3: Chemical structures of clinically used PARP inhibitors.

Table 2.1: Clinical PARP inhibitors (PARPi) and ovarian cancer.

PARP inhibitor	**Olaparib**	**Rucaparib**	**Niraparib**	**Veliparib**	**Talazoparib**[a]
Manufacturer	AstraZeneca	Clovis Oncology	Tesaro	AbbVie	Pfizer
FDA Approval Year	2014	2016	2017	NA[b]	2018
PARP trapping potency	Average	Average	Average	Low	High
Monotherapy[c]	• Germline BRCA1/2 mutations • Following ≥3 rounds of chemotherapy	• Germline BRCA 1/2 mutations • Following ≥2 rounds of chemotherapy	• HR deficient by BRCA mutation or genomic instability • Advanced cancer following ≥3 rounds of chemotherapy	-	• Germline BRCA 1/2 mutations • HER2(-) metastatic cancer
Maintenance Therapy	• Germline or somatic BRCA1/2 mutations • Recurrent cancer without BRCA mutations	• Regardless of BRCA mutation • Recurrent cancer w/complete or partial response to PB chemotherapy	• Regardless of BRCA mutation • Recurrent cancer w/complete or partial response to PB chemotherapy	-	-

[a]Talazoparib is not usually used for ovarian cancer, but is included here as an FDA approved PARPi for breast cancer.
[b]Currently undergoing clinical trials for epithelial ovarian cancer.
[c]Ovarian cancer for olaparib, rucaparib and niraparib and breast cancer for talazoparib.
HR: homologous repair; PB: Platinum-based

survival, it is not apparent that they have increased overall survival [40]. They may also increase the risk of severe adverse side effects. These side effects include nausea, fatigue and myelosuppression that can lead to increased risk of infection or bleeding problems. PARPi were associated with a statistically significant higher risk of hematologic events, including anemia, thrombocytopenia and neutropenia [41]. Furthermore, for ovarian cancer patients with functioning *BRCA1/2*, other methods of therapy are considered because of a lack of synthetic lethality.

2.1.2.2 Rucaparib

Studies have shown that rucaparib (also known as PF-01367338 and AG-014699) has a higher PARP inhibitory activity compared to olaparib or niraparib, with maximum inhibition reported at 92%, 60% and 65% for rucaparib, olaparib and niraparib, respectively [42]. The drug accumulated in tumors after a single dose in mice and was retained for 7 days [43]. It also slowed and reduced the growth of tumors in BRCA1/2 deficient allograft and xenograft mouse models [44]. It also showed that rucaparib sensitivity was not restricted to BRCA1/2 mutations, although it is more cytotoxic in cancers with *BRCA1/2* mutated genes [45].

Two clinical trials in humans, Study 10 and ARIEL2, established that rucaparib is a well-tolerated monotherapy with antitumor response [46, 47]. These Phase I/II studies established the recommended starting dose and assessed the safety and efficacy of rucaparib in EOC. In ARIEL2 (Phase II) and ARIEL3 (Phase III), 20% of patients experienced anemia, 11% experienced elevated AST/ALT (liver damage indicator) and 22% had a serious adverse event [48]. The phase III trial reported a median progression-free survival in patients with a *BRCA* mutation as 16.6 months (95% CI 13.4–22.9; 35% of patients) with rucaparib versus 5.4 months (3.4–6.7; 35% of patients) with placebo. Patients in the study had platinum-sensitive, HGSC with at least 2 previous platinum-based chemotherapy regimens.

ARIEL4 is a phase III clinical trial comparing rucaparib to chemotherapy for women with *BRCA1/2* mutations and at least two previous lines of platinum-based chemotherapy. The progression-free survival was reported as 7.4 months (95% CI 7.3–9.1) for the rucaparib cohort and 5.7 months

(95% CI 5.5–7.3) [49]. Serious adverse events occurred in 27% of the patients receiving rucaparib versus 12% in the chemotherapy arm, with the most common being anemia.

2.2 Positron Emission Tomography Imaging of PARP

The use of positron emission tomography (PET) imaging to assess physiologic PARP1 levels in patients has been established as a successful noninvasive imaging tool [50]. [^{18}F]-labeled PARPi are in the process of being translated from preclinical research to clinical applications for PET imaging [51–53]. The first agent, [^{18}F]FTT, has been shown to have potential for imaging PARP1 and PARP2, two proteins involved in DNA repair that have implications in cancer treatment [54]. Multiple studies have demonstrated [^{18}F]FTT's effectiveness in preclinical models, and human trials are currently underway [52, 55]. The second agent, [^{18}F]PARPi, has been shown to target PARP1 and PARP2 as well as other PARP family members, and has shown promise in imaging breast, ovarian and brain cancers [56, 57]. [^{18}F]PARPi is currently undergoing clinical trials to further investigate its potential as a diagnostic tool for cancer. [^{18}F]PARPi has also been shown to have potential in imaging other DNA damage response pathways, including DNA-PK, ATR, and ATM [58]. Additional ^{18}F-labeled isotopologues that have been preclinically investigated include [^{18}F]rucaparib [59, 60], [^{18}F]talazoparib [61, 62], and [^{18}F]olaparib [63, 64].

2.3 Radiopharmaceutical Therapy

Radiopharmaceutical therapy (RPT) is a form of radiation therapy that uses a radioactively tagged targeting molecule to deliver radiation directly to a target. In oncology, the target is in the cancer microenvironment, which could be on the cell membrane, cytoplasm, nuclear membrane, or nucleus. The targeting vector can take the form of a simple ion or a radiochemically labeled small molecule, peptide, nanoparticle or antibody. For example, radioactive [^{131}I]iodide is an effective treatment for thyroid disease because the thyroid uses iodine to produce thyroid hormones, resulting in the organ's high and selective uptake of [^{131}I]iodide [65]. Ibritumomab tiuxetan, commercially known as Zevalin, uses beta emitter yttrium-90 bonded to a monoclonal antibody to target a specific

antigen found on the cell surface of malignant B cells [66]. In this case, the radionuclide yttrium has no affinity for cellular uptake. However, chemically attaching it to an antibody with tumor cell specificity—malignant B cells that cause non-Hodgkin's lymphoma—allows radioyttrium to deposit the dose locally.

RPT is often paired with a biologically matched radiopharmaceutical labeled with a diagnostic radionuclide, in what is termed the theranostic approach. The FDA recently approved two radiopharmaceuticals that use the radionuclide ^{177}Lu, which emits a beta-particle that can deliver dose locally. The first, ^{177}Lu-DOTATATE, commercially known as Lutathera [67], was approved for neuroendocrine tumors, and has a diagnostic analogs, ^{68}Ga-DOTATATE [68] and ^{68}Ga-DOTA-TOC [69][1]. Neuroendocrine tumor cells overexpress somatostatin receptor (SSTR) is specifically targeted by the radionuclide-conjugated peptide tetraazacyclododecane tetraacetic acid octreotate (DOTATATE).

The second, ^{177}Lu-PSMA-617, commercially known as Pluvicto [70], targets prostate-specific membrane antigen (PSMA), a protein found on the membrane of prostate cells, with an over expression on prostate cancer cells [71]. Its diagnostic analog, ^{68}Ga-PSMA-11, is used for PET imaging for patient selection [72].

When designing theranostic radiopharmaceuticals, a practical consideration is the chemistry to attach the radionuclide to the targeting molecule. Although the above theranostic pairs, targeting the same receptors, are biologically matched, each have different pharmacokinetic profiles due to the varying radioelements and surrogate vectors. It makes the diagnostic pair suitable for patient selection, but lacking for patient-specific dosimetry. When the diagnostic and therapeutic analogs incorporate different isotopes of the same element, not only will the radiolabeling chemistry stay the same[2], the pharmacokinetics will be identical, and thus, imaging with the diagnostic agent could be used for dosimetry of the therapeutic.

A radionuclide's role in radiopharmaceuticals is significantly influenced by several physical properties. The half-life, production pathway, and radiochemistry are important. Likewise, the decay properties, including emitted particle type, energy, intensity, range, and linear energy transfer

[1] ^{68}Ga-DOTATATE was approved as a kit preparation

[2] The difference in production and radiochemical yields will need to be considered.

Table 2.2: General characteristics of therapeutic radionuclide decay particles [73].

Decay Particle	Energy	Range in Tissue	LET (keV/μm)
α	5–9 MeV*	50–100 μm	50–230
β^-	0.05–2.3 MeV	2–12 mm	0.1–0.3
MAe^-	eV–keV*	0.001–100 μm	1–23

*Monoenergetic

(LET). For imaging purposes, isotopes with appropriate gamma emissions can be used for single-photon emission computed tomography (SPECT) and positron emitters can be used for PET. For therapeutic purposes, alpha emitters, beta electron emitters and low-energy electron emitters that produce Meitner-Auger electrons (MAe^-), can be utilized. The characteristics of the emitted particles are summarized in Table 2.2 [73].

2.3.1 Meitner-Auger Emitters

In the electron capture radioactive decay mode and the internal conversion nuclear deexcitation process, an electron is removed from an inner shell of an atom. When an outer shell electron fills that vacancy, a characteristic x-ray is emitted equal in energy to the difference in binding energies of the two shells. Alternatively, the deexcitation energy is transferred to a bound orbital electron. This electron, ejected in place of an x-ray, is termed a Meitner-Auger, Auger-Meitner, or Auger electron and was first observed in 1922 by Lise Meitner and 1923 by Pierre Auger [74–77]. The notation for MAe^- identifies where the vacancies come from, defining the shell with the initial vacancy, the shell that the electron dropped from to fill the shell, and the shell the ejected electron came from, respectively. A schematic is shown in Figure 2.4, in which the MAe^- would have a notation of KLM. The energy of the MAe^- emitted in Figure 2.4 is described in Eq. 2.1:

$$E_{MAe^-} = BE_K - BE_L - BE_M, \qquad \text{(Eq. 2.1)}$$

where BE_K is the binding energy of shell K and BE_L is the binding energy of shell L.

The schematic represents a basic case, but orbital vacancies can be filled with other outer shell

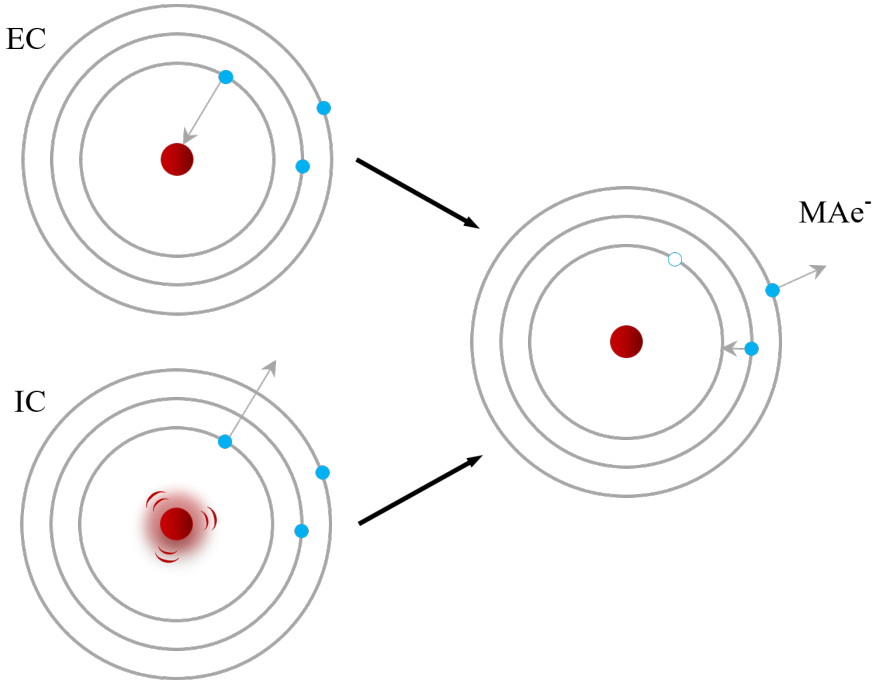

Figure 2.4: Simplified schematic of electron capture (EC) and internal conversion (IC) which can then produce Meitner-Auger electrons (MAe^-). In EC, the nucleus absorbs an inner orbital electron. In IC, the excited and unstable nucleus releases energy that ejects an inner orbital electron. In both instances, the hole left in the inner shell will be filled by an outer electron. When this happens, a characteristic x-ray can be emitted or an electron is ejected, called the MAe^-.

electrons, initiating a cascade of events which can then cause the emission of more characteristic x-rays or MAe^-. The probability that a characteristic x-ray or an MAe^- is emitted is dependent on the specific element and orbital shell involved. Elements with high Z are more likely to yield characteristic x-rays, while elements with a lower Z are more likely to yield MAe^-.

MAe^- originating from K-shell transitions can have energies up to 80 keV, although the majority of MAe^- have energies below 25 keV [73]. In tissue, their range varies from approximately 1 nm to 15 µm for most electrons, but can extend up to around 90 µm for the 80 keV electrons [78]. Meanwhile, the mammalian nucleus diameter is between 5–20 µm [79], with the DNA double helix having a diameter of 2 nm. Therefore, it may be important for the targeting molecule to deliver the radiopharmaceutical to the nucleus of the cancer cell, especially for low range MAe^-, to impart energy to the DNA to cause strand breaks. A schematic showing the PARP protein bound to a SSB in the cell nucleus of an ovarian cancer cell, with average diameters of 10 µm and 20 µm for the

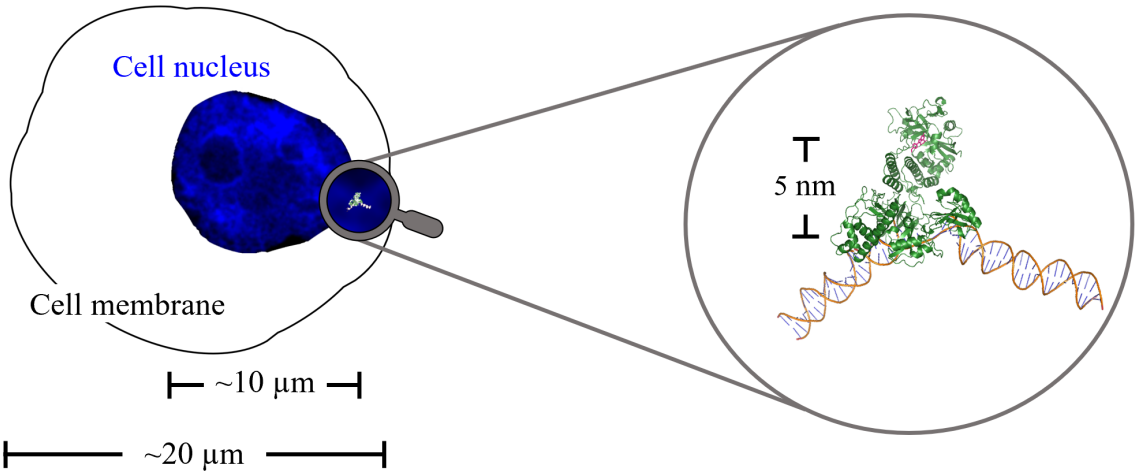

Figure 2.5: A PARP1 protein attached to a SSB is 600× smaller than the nucleus in an ovarian cancer cell.

nucleus and cell, respectively, is summarized in Fig. 2.5.

DNA can be damaged directly by MAe^-. Alternatively, indirect damage can occur when reactive oxygen species (ROS) are generated as a result of the interaction between water and the MAe^-, producing free radicals, which can cause a concentrated area of harm to macromolecules [73]. Cross-dose effects from neighboring cells may dose directly adjacent targeted cells, and longer range cells may be affected by the bystander effect, perhaps due to the mediators released by the DNA damage response [80]. Although many studies indicate the importance of MAe^- being delivered to the nucleus of the cell [81–85], cytotoxicity effects have been observed for cell membrane targeting vectors, perhaps due to the indirect damage [86, 87].

MAe^- have been attached to PARPi (MAPi) in preclinical studies for cancer therapy in glioblastoma (^{123}I and β^- emitter ^{131}I) [88, 89], neuroblastoma (^{125}I) [90], colon (^{125}I) [63], breast (^{125}I) [91], prostate (^{77}Br) [92] and ovarian ($^{123/125}$I) cancers [93]. *In vitro* cell cytotoxicity studies showed MAPi to be highly cytotoxic across several cancer cell lines. For the studies that conducted animal studies, prolonged survival in mice treated with MAPi were observed [63, 88, 92]. Higher cytotoxicity was observed compared to radioinert PARPi, with no dependence on *BRCA1* expression [93]. These results show promising radiotherapeutic potential that warrants further preclinical and clinical investigation across a multitude of cancers.

2.3.2 Radiobromine

Radiobromine has isotopes that can be used for therapeutic or diagnostic applications. As a radiohalogen, it can be readily incorporated into small organic molecules through covalent carbon-bromine bonds in either alkyl (sp3-hybridized) or aryl (sp2-hybridized) systems [94]. Compared to radioiodine, which is used in FDA approved small molecule radiopharmacueticals like [^{123}I]ioflupane [95] and [$^{123/131}$I]iobenguane [96], the C–Br bond is 10–15 kcal/mol stronger than the C–I bond, which will result in less dehalogenation [97]. Furthermore, unlike radioiodine, free radiobromine does not accumulate in the thyroid and has a biological half-life in humans of 9–12 days [98]. Small molecule labeling with radiobromine can proceed via oxidative electrophilic radiobrominations using alkyl tin precursors [51] and nucleophilic aromatic radiobrominations using diaryliodonium salt [99] and aryl boron [100] precursors.

Figure 2.6 and Table 2.3 summarize radioisotopes of bromine with potential medical applications. Although ^{76}Br (Fig. 2.7) has the lowest positron branching ratio (56%, Table 2.3), it has a practical production route via the ^{76}Se(p,n) nuclear reaction at low energy. The longer half-life also allows for PET scans at longer time points to further investigate the *in vivo* radiopharmaceutical pharmacokinetics and allows for regional distribution of the radionuclide. Comparatively, even though ^{74}Br and ^{78}Br have the highest positron emission intensities, 94% and 92%, respectively, they also have the shortest half-lives, making their commercial use nonviable. ^{75}Br has a 1.6 h half-life, with a relatively high positron emission rate (75%). Unfortunately, the daughter isotope, ^{75}Se, has a half-life of 120 days, which contributes to patient dose with no imaging upside.

Stability of the compound is important to check and measure, and dehalogenation can occur through self-radiolysis, where ionizing radiation interacts with molecules in the material to generate free radicals. The free radicals can undergo chemical reactions that alter the chemical composition of the material and cause degradation. Alternatively, MAe$^-$ can cause Meitner-Auger charging, in which the compound gains or loses electrons due to the inner-shell vacancy of the MAe$^-$ emitting radioisotope, causing subsequent molecular fragmentation [101]. Furthermore, debromination through nucleophilic substitution or through elimination type reactions can occur in alkyl bromide

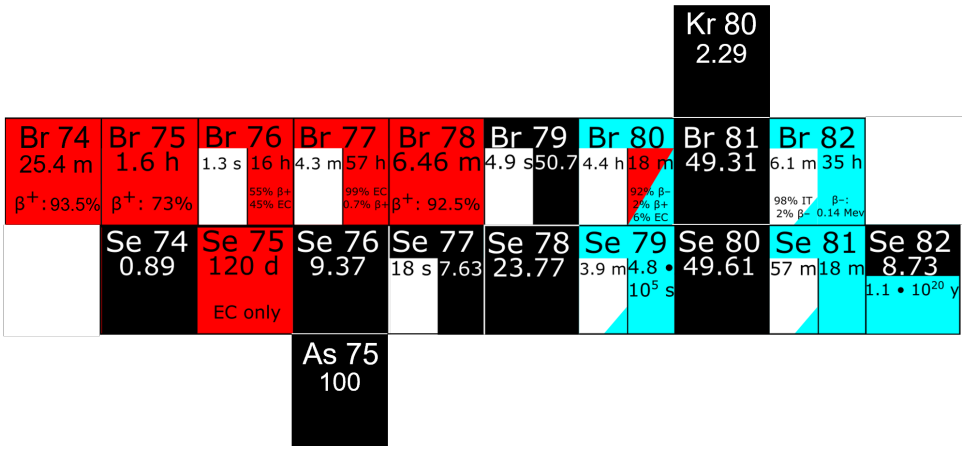

Figure 2.6: Bromine isotopes with possible medical applications and the relevant stable isotopes that could be used for low-energy cyclotron production. Decay information is from the Online Nuclear Data Service [103].

molecules, such as 7α-[^{76,77,82}Br]bromo-5α-dihydrotestosterone [102]. Whether through radiolysis, Meitner-Auger charging, or debromination reactions, poorer radiochemical stability at high concentrations can be observed compared to low concentrations. Dry storage can ameliorate the instability.

Table 2.3: Radioisotopes of bromine with potential medical applications. Decay information is from the Online Nuclear Data Service [103] and the number of MAe$^-$ per decay is from ICRP Publication 107 [104].

Isotope	$t_{1/2}$	Decay Mode	Average Energy (keV, % intensity)	MAe$^-$ per decay
^{74}Br	25.4 m	EC, β^+ (94%)	1,182 (18%)	0.8
^{75}Br	96.7 m	EC, β^+ (75%)	773 (53%)	2.1
^{76}Br	16.2 h	EC, β^+ (56%)	1,532 (26%)	2.9
^{77}Br	57.0 h	EC, β^+ (0.73%)	152 (0.73%)	6.6
^{78}Br	6.45 m	EC, β^+ (92%)	1,143 (81%)	0.5
^{80}Br	17.7 m	EC, β^- (92%), β^+ (2.2%)	804 (85%)[a]	0.4
^{80m}Br	4.4 h	IT	368 (2%)	9.6
^{82}Br	35.3 h	β^- (103%)	138 (99%)[a]	0.03

EC: Electron Capture; IT: Isomeric transition

[a]β^- emission

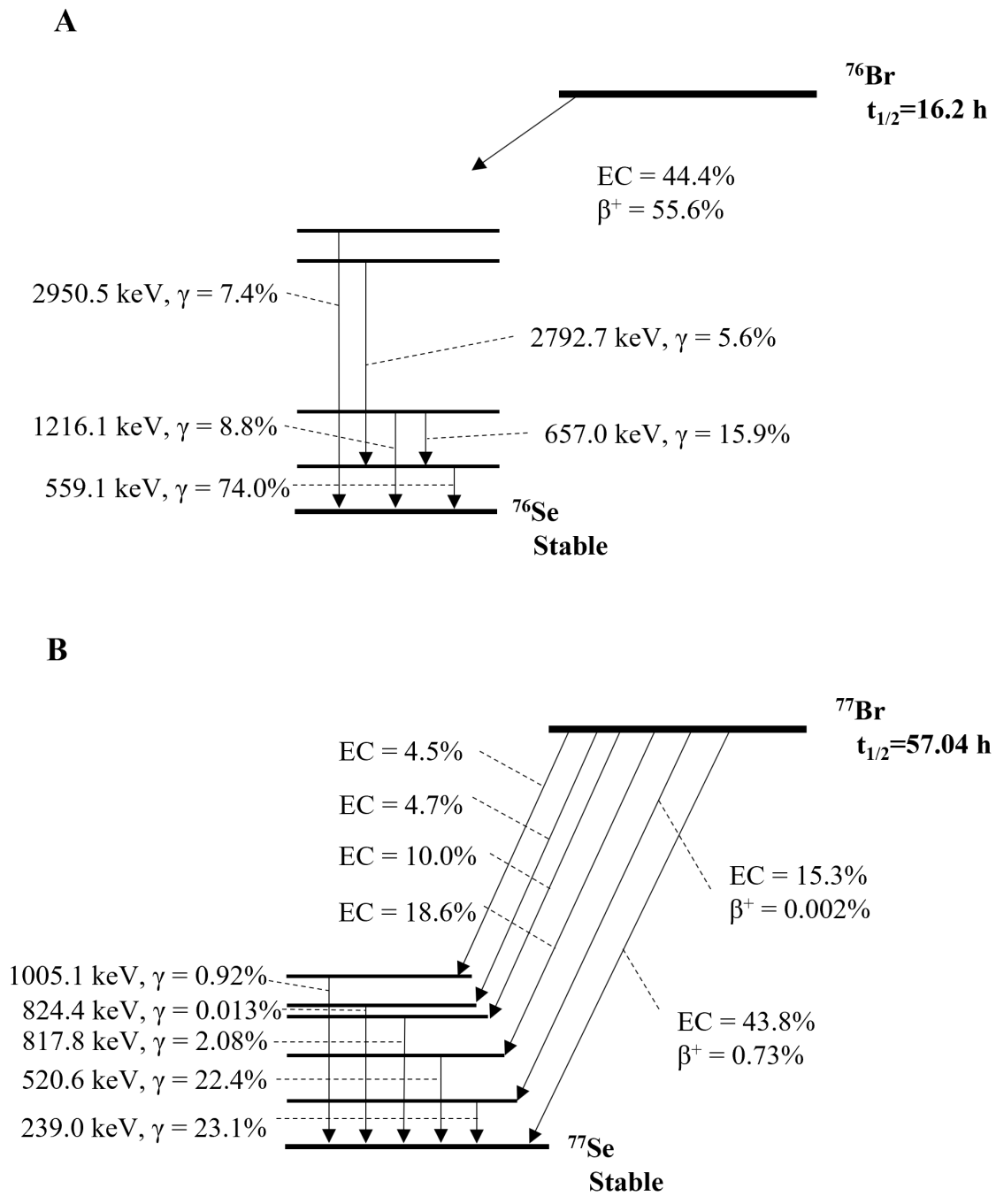

Figure 2.7: Simplified decay schemes of (**A**) positron-emitting ^{76}Br and (**B**) Meitner-Auger electron-emitting ^{77}Br [105, 106].

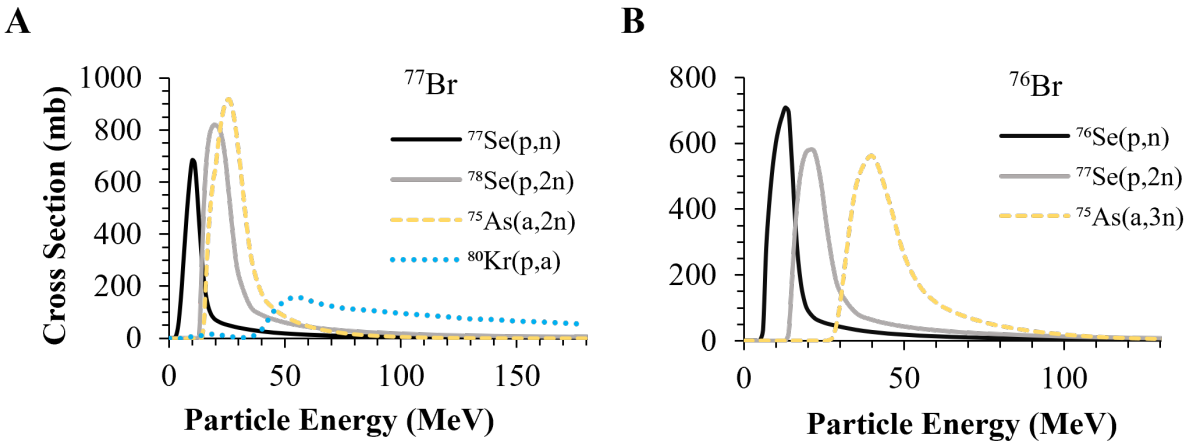

Figure 2.8: Excitation functions for (**A**) ^{77}Br and (**B**) ^{76}Br [107, 108].

2.3.3 Production of Radiobromine

The most medically relevant radionuclides of bromine can be produced through 5–30 MeV proton irradiation of selenium target via (p,n) or (p,2n) nuclear reactions. Excitation functions for various production pathways are shown in Figure 2.8 [107, 108]. However, selenium has a relatively low melting point of 221°C, boiling point of 685°C, thermal conductivity of 0.02 W/cm^{-1}K^{-1}, and heat of vaporization of 95.5 kJ/mol [109]. This makes a metallic selenium cyclotron target sensitive to heat and thus limits its tolerance to high intensity proton irradiation. To allow for moderate intensity (20–40 μA) proton irradiations, and therefore larger quantities of produced ^{76,77}Br, intermetallic compounds of selenium with transition metals are used as robust cyclotron targets.

Cyclotron irradiation of binary intermetallic compounds of transition metals with selenium was done initially with copper [110]. Enriched $Cu_2{}^{76}Se$ has been used to produce radionuclidically pure ^{76}Br [111, 112], and enriched $Cu_2{}^{77}Se$ for ^{77}Br [112]. NiSe [113, 114] and ZnSe [115] have also been investigated for producing $^{76/77}$Br with naturally abundant selenium. For all studies, $^{76/77}$Br production capacity was limited to less than that needed for clinical studies. Selenium's thermal limitations result in a maximum proton irradiation intensity of 15–20 μA, which is only a fraction of a modern cyclotron's capabilities of over 100 μA. Furthermore, proton activation of

naturally abundant copper or nickel yields large amounts of gamma-emitting ^{63}Zn and ^{60}Cu with half-lives of 38.1 min and 23.7 min, respectively. These radioisotopes must decay away before handling of the target to isolate bromine, which lowers the amount of bromine collected at the end of production. Isotopically enriched copper/zinc could be used, with the downside of increasing cost. Cobalt, a naturally monoisotopic element, was developed as a selenium target intermetallic additive at UW–Madison by the Cyclotron Group for its properties to combat selenium's thermal limitations, with a proton intensity tolerance of 40 μA [116]. Proton activation of cobalt only produces minimal amounts of long-lived waste streams, ^{59}Ni ($t_{1/2}$ = 76,000 y) and ^{58g}Co ($t_{1/2}$ = 70.9 d). This allows for isolation of bromine immediately after the end of bombardment, rather than waiting for the ^{63}Zn/^{60}Cu to decay away, and with it, the wanted $^{76/77}$Br product. Irradiation of Co^{77}Se with 13 MeV protons resulted in 99.6% radionuclidic purity (RNP) of ^{77}Br with a physical yield of 17±1 MBq/μAh and irradiation of Co^{76}Se with 16 MeV protons resulted in 99.9% RNP of ^{76}Br with a physical yield of 88±10 MBq/μAh [116].

Radiobromine can be chemically isolated from proton irradiated metal selenide targets using thermochromatographic distillation [111–113, 116]. Furthermore, individual CoSe targets have been reused in over 20 radiobromine productions [116], proving the robustness of these targets in the irradiation/distillation process.

2.4 Internal Dosimetry

Internal dosimetry is the quantification of dose from ionizing radiation from radionuclides inside the body. Normal tissue and tumor quantification can be done through absorbed dose calculations. The absorbed dose, or the amount of energy from ionizing radiation deposited per unit mass [J/kg=Gy], is dependent on the activity distribution, biokinetics, and particle type [117]. A general formalism using Monte Carlo methods was developed by the Medical Internal Radiation Dose (MIRD) committee of the Society of Nuclear Medicine and Molecular Imaging (SNMMI) [118].

2.4.1 Monte Carlo Methods

Monte Carlo (MC) techniques utilize statistical methods with random sampling to calculate numerical integrations. This can be used to calculate radiation transport that is stochastic in nature. The probability density function, *p(x)*, can be used to describe the likelihood of a given value of *x*, and integrating *x* weighted by *p(x)* over the whole domain gives us the mean, or expectation value, *f(x)* [119, 120]. Using random variables can help compute radiation transport in which a particle has discrete outcomes with varying probabilities.

In MC methods, millions of particles, or histories, are recorded as they travel through the medium in a geometry that is defined by the user [121]. An energy threshold is set in which at some minimum, the particle is no longer recorded and is absorbed at that location. Particles and their trajectories are tracked, and corresponding scattering events are stochastically simulated. The particle has a probability of interacting with the medium after a certain path length. Cross-sections for the various photon interactions, including coherent scattering, photoelectric effect, Compton scattering, and pair production, are used to calculate the probability of that type of interaction. Once the interaction type is modeled, the parameters of all secondary particles can be determined, like the energy and scattering angles, using appropriate probability distributions. The cross-section is dependent on the particle energy and medium composition. After an interaction, the particle will then terminate if it meets the energy minimum or leaves the defined geometry. As these particles travel and interact with the medium, the contributions of each interaction are summed to calculate the dose [119, 120].

MC is subject to statistical uncertainty, where increasing the number of histories gives better accuracy. However, because so many particles must be run to give an accurate calculation, this process can be slow. With the advancement of CPUs, these calculations can be done more quickly [122]. Well established direct Monte Carlo platforms and codes include Geometry and Tracking (Geant4) [123], Monte Carlo N-Particle Transport Code (MCNP) [124] and Electron Gamma Shower maintained by the National Research Council Canada (EGSnrc) [125]. Geant4 is open source and allows the user flexibility and control of the physics toolkits available. For dosimetry

calculations with MAe$^-$ that may be at energies below the minimum energy threshold to track the particle, this user control can be especially important. Additional softwares that use Monte Carlo methods for radiation dose calculations include Organ Level INternal Dose Assessment (OLINDA/EXM) [126] and MIRDcell [127] which will be further discussed in Chapter 4 and 5.

2.4.2 Medical Internal Radiation Dose Cellular S Values

The committee of Medical Internal Radiation Dose (MIRD) developed a framework for internal dosimetry of radionuclides in organ compartments and cellular compartments. This was done specifically for radionuclides with emitted radiation on the order of cellular dimensions [128], such as MAe$^-$-emitters like ^{77}Br. The cellular absorbed dose is calculated using the cellular S values (absorbed dose per unit cumulated activity).

The cellular model used by MIRD consists of two concentric homogeneous spheres of density 1 g/cm^3 where each sphere has a radius designated by R_C for the cell and R_N for the nucleus. This basic model makes up the two compartments of the cytoplasm and nucleus and is summarized in Figure 2.9. For simple models, the radioactive distribution can be assumed to be uniformly distributed in various compartments of the cell, including the entirety of the cell (C), the cell surface (CS), the cytoplasm (Cy), or the cell nucleus (N).

The mean absorbed dose $\overline{D}_k$ to target r_k from source region r_h as defined by MIRD is shown in Eq. 2.2:

$$\overline{D}(r_k \leftarrow r_h) = \tilde{A}_h S(r_k \leftarrow r_h), \qquad \text{(Eq. 2.2)}$$

where $\tilde{A}_h$ (Bq h) is the cumulated activity, or the sum of all radioactive decays over a time of measurement, in the source region r_h defined as:

$$\tilde{A}_h = \int_0^{t_d} A_h dt, \qquad \text{(Eq. 2.3)}$$

where t_d is the time-integration period in the source region r_h, which is usually the time of administration of the radiopharmaceutical to the biological end point. To calculate the cumulative number

of nuclear transformations over a dose-integration period (h) per unit administered activity (Bq) gives the time-integrated activity coefficient ã (h):

$$\tilde{a} = \frac{\tilde{A}_h}{A_0}, \qquad \text{(Eq. 2.4)}$$

where A_0 is the initial activity in the source region at t=0. The S value in Eq. 2.2 is the dose to the target region per unit cumulated activity in the source region, defined by Eq. 2.5:

$$S(r_k \leftarrow r_h) = \sum_i \frac{\Delta_i \varphi_i(r_k \leftarrow r_h)}{m_k}, \qquad \text{(Eq. 2.5)}$$

where m_k is the mass of the target region, Δ_i is the mean energy emitted per nuclear transition, and φ_i is the absorbed fraction of energy emitted from the source region that is absorbed in the target region for the i^{th} radiation component. The absorbed fraction $\varphi_i(r_k \leftarrow r_h)$ is shown in Eq. 2.6

$$\varphi_i(r_k \leftarrow r_h) = \int_0^\infty \Psi_{r_k \leftarrow r_h}(x) \frac{1}{E_i} \frac{dE}{dX}\bigg|_{X(E_i)-x} dx, \qquad \text{(Eq. 2.6)}$$

where E_i is the initial energy of the i^{th} particle, $\Psi_{(r_k \leftarrow r_h)}x$ is the geometric reduction factor, and $dE/dX\big|_{X(E_i)\text{-}x}$ is the stopping power evaluated at $X(E_i)$, the residual range of a particle with initial energy E_i after passing a distance of x through the medium. The geometric reduction factor $\Psi_{(r_k \leftarrow r_h)}x$ is the mean probability that a randomly directed vector of length x starting at a random point in source region r_h ends in target region r_k.

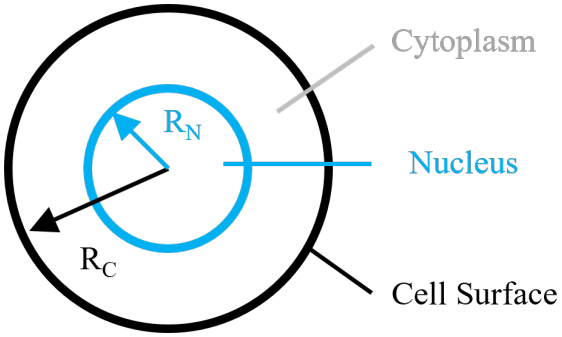

Figure 2.9: Cell model consisting of two concentric spheres that make up the nuclear, cytoplasmic, and cell surface compartments.

CHAPTER 3
CELLULAR PHARMACOKINETICS AND CYTOTOXICITY STUDIES WITH RADIOBROMINATED PARP1 INHIBITOR

3.1 Ovarian Cancer Cell Lines

Ovarian cancer cell lines were selected for *PARP1* expression, *BRCA1* expression, and human or murine species origin. A murine ovarian cancer was selected to characterize it for future animal studies. *PARP1* expression was considered since it is the target for the targeting vector, PARP1 inhibitor (PARPi). PARPis have also shown synthetic lethality—in which mutations in two genes cause cell death, but a mutation in either gene alone does not—with *BRCA1* deficient cell lines, so *BRCA1* expression was also considered [129]. The cell lines chosen were ID8, OVCAR8 and UWB1.289.

ID8 is a clonal line established from late passaged C57BL/6 murine ovarian surface epithelial cells that causes peritoneal tumors and ascites [130]. This cancer cell line is often used in syngeneic mouse models for ovarian cancer, and has been heavily investigated, making it a good candidate for non-immunocompromised animal studies. It is important to note that it does not have *BRCA1/2* mutations that are characteristic of many human ovarian high-grade serous carcinoma (HGSC) [131].

The OVCAR8 cell line was established from a patient with progressive disease after high-dose treatment with the chemotherapeutic drug, carboplatin [132]. This adenocarcinoma has reduced BRCA1 expression attributed to methylation in the promoter region [133, 134]. To obtain an isogenic cell line with significantly reduced PARP1 expression, the *PARP1* gene in OVCAR8 was deleted through CRISPR/Cas9 gene editing, yielding the cell line OVCAR8 PARP1-KO with more than 90% reduction of PARP1 expression [135].

UWB1.289 is an ovarian carcinoma taken from a tumor of papillary serous histology with a

germline *BRCA1* mutation and a wild-type allele deletion, making it fully deficient of functioning BRCA1 protein (*BRCA1* negative) [136]. To generate an isogenic cell line with normal *BRCA* function, the wild-type *BRCA1* gene was stably transfected into the UWB1.289 cell line, yielding the cell line UWB1.289+BRCA1, with high level BRCA1 protein expression (*BRCA1* positive) [136]. The cells and their gene expressions are summarized in Table 3.1.

Table 3.1: Ovarian cancer cell lines investigated in this work.

		Gene Expression	
Ovarian Cancer Cell Line	**Species**	***BRCA1***	***PARP1***
ID8	Murine	WT	WT
OVCAR8	Human	Methylated	WT
OVCAR8 PARP1-KO	Human	Methylated	KO
UWB1.289	Human	Null	WT
UWB1.289+BRCA1	Human	Restored	WT

3.2 Cellular Dose Response Assays

Clonogenic assays, or colony formation assays, are the gold standard for measuring cell survival after radiation dosing. The clonogenic assay measures the ability of a single cell to not only survive but to retain the capability of replication by treating cells at low seeding density and allowing the cells to grow over a period of time to form colonies [137]. Clonogenic assays can be used to measure the surviving fraction (SF), in which the linear quadratic formula can be used to model the effect of radiation on cancer cells and normal tissues:

$$SF = e^{-\alpha D - \beta D^2} \qquad \text{(Eq. 3.1)}$$

where D is the dose of radiation, α is the linear coefficient and β is the quadratic coefficient. The linear term (αD) describes the cell-killing effect of low-dose radiation and the quadratic term (βD^2) accounts for the effect of high-dose radiation, with the α term often thought of as lethal damage caused by a single incident particle, and the β term representing cell death caused by the interaction of more than one radiation track, which scales with D^2. The dose required to reduce the population

to a survival fraction of 37% is called the D_{37} and is used to quantify the radiosensitivity of cells.

Clonogenic assays require single cell suspension at an optimized plating density that may not be assessed without first running optimization studies. Cells plated at lower densities to count unique colonies at low doses may have different growth characteristics compared to non-dosed cells, like doubling time or plating efficiency, which may lead to an inaccurate assessment of counted colonies. Clonogenic assays also take several weeks to obtain results, which may be futile if the cells were not plated at the appropriate density to begin with. This assay is also done under large volumes, which may present problems for small-scale production of radiopharmaceuticals. For example, the minimum volume of media using a clonogenic assay is approximately 1 mL, which is 5$\times$ larger than alternative cell-health assays that could be performed in 96-well format in only 200 µL.

Viability assays use biomarkers as a surrogate to measure cell survival. In our methods, we use measurements of adenosine triphosphate (ATP), the principal cellular energy carrier, to indicate the health of a cell. However, unlike colony forming assays, the results may be obscured by cell senescence and cell cycle arrest, in which the cell is still producing ATP, but does not have replication abilities. For that reason, an ATP-based viability assay can result in higher D_{37} values compared to clonogenic assays.

Assays of this type may suffer from poor reproducibility, potentially due to non-uniform cell growth and edge effects. To mitigate this, experiments were typically conducted on central wells of the plate, with peripheral wells filled with PBS to account for evaporation. Additionally, experiments were performed in triplicate to address any variability in cell growth. Optimization studies for ATP-based viability assays can also help to establish best practices. Finally, comparison of the viability assay to the clonogenic assay using external beam radiotherapy can provide valuable insights into the strengths and limitations of the viability assay.

3.3 Methods

3.3.1 Radiopharmaceutical Production and Quality Control

3.3.1.1 Cyclotron Production and Distillation of Radiobromide

Bromine-77[1] was produced by proton irradiation of enriched $Co^{77}Se$ according to published methods [116]. Briefly, the UW–Madison GE PETtrace cyclotron (GE Healthcare) irradiated $Co^{77}Se$ ($\sim$300 mg) on niobium backings (35–40 μA, 12.5 MeV protons) for 1 hour. An ARTMS QIS solid target system (Vancouver, CA) water jet cooled the niobium backing and produced 520±70 MBq ^{77}Br (n=8) at the end of bombardment.

The cobalt selenide target releases radiobromine when it is heated to 1050°C allowing for the collection of the radionuclide via thermal chromatographic distillation. Furthermore, the selenium intermetallic target can be used multiple times before being depleted, with measured losses of 0.9±0.5% (n=20) of CoSe mass per irradiation and distillation cycle [116]. A vertical distillation assembly was used for these studies. The CoSe target was placed in a flat-bottomed quartz tube and the entire assembly was sealed. As shown in Figure 3.1, the quartz tube was placed in the furnace (Carbolite TF1 11/32/150) with argon (80 mL/min) flowing over the target (a) in the outer quartz tube (b), out a bell-shaped inner quartz tube (c), through the PTFE tubing (d) and bubbled through a water trap (e). After 5 min of heating, the quartz tube was transferred to a room temperature water bath for cooling, still with argon flow. The assembly was cooled for up to 10 min and then vented to atmospheric pressure using valves V1 and V3. A 60 mL syringe attached to the inlet vent was used to apply vacuum to the system to rinse the PTFE tubing and quartz tube of radiobromide with the water from the water trap. This was done 5 times to ensure a full rinse.

Using valves V2 and V4, the contents of the water trap were then passed through a quaternary methylammonium-(QMA-)functionalized solid phase extraction light cartridge (Sep-Pak Accell Plus QMA Plus Light Cartridge, 130 mg/cart, 37–55 μm, Waters Corp.) pre-equilibrated with 10

[1] Br-76 was produced for imaging experiments in mice models described in Chapter 5. The differences are outlined in the Chapter 5 Methods section, but the production and synthesis was the same using a $Co^{76}Se$ target.

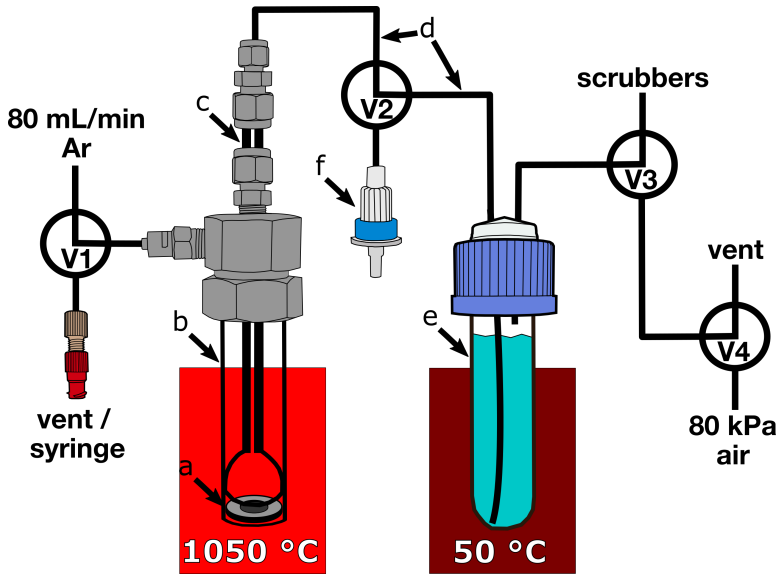

Figure 3.1: Dry distillation of radiobromine using a vertical tube furnace assembly. The irradiated CoSe target (a) was placed in a flat-bottomed quartz tube (b) and sealed inside the assembly. Argon was flowed over the target through quartz (c) and PTFE tubing (d) and bubbled through a water trap (e) [138].

mL of 0.5 M Na_2SO_4 or $NaHCO_3$ and H_2O. This was eluted with 0.1 M NH_4OH or Me_2NH in MeCN/H_2O (1:1, 600–1,200 µL). Before subsequent radiopharmaceutical synthesis, the solvent was evaporated until dryness under a constant stream of argon at 110ºC.

3.3.1.2 [^{77}Br]RD1 Synthesis and Purification

[^{77}Br]RD1 was synthesized via copper-mediated radiobromodeborylation chemistry according to published procedures [138]. Briefly, dried radiobromine was reconstituted in a solution of 1-(4-(4,4,5,5-tetramethyl-1,3,2-dioxaborolan-2-yl)phenyl)-8,9-dihydro-2,7,9a-triazabenzo[cd]azulen-6(7H)-one (pre-RD1, 1 µmol), [$Cu(py)_4OTf_2$] (0.5 µmol), and 3,4,7,8-tetramethyl-1,10-phenanthroline (0.5 µmol) in MeOH/H_2O (9:1, 100 µL) and reacted at room temperature for 30 minutes with stirring (Fig. 3.2). Radiopharmaceutical purification was performed using C18 solid-phase extraction and preparative high-performance liquid chromatography (pHPLC). The octadecyl-(C18-)functionalized SPE cartridges (Sep-Pak C18 Plus Light Cartridge, 130 mg/cart, 55–105 µm, Waters Corp.) were preconditioned with 5 mL EtOH and 10 mL water before use. The reaction was diluted into 10 mL of water and loaded onto the C18 light cartridge and rinsed with 10

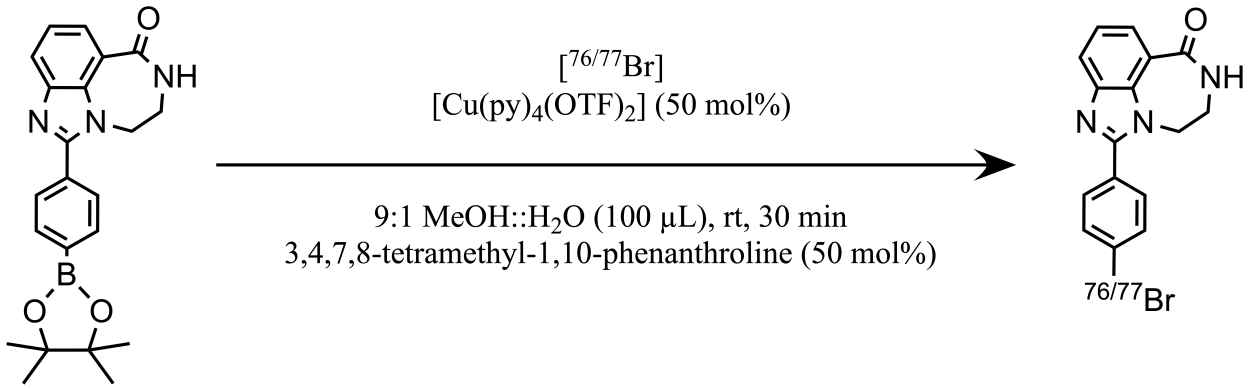

Figure 3.2: Radiosynthesis of $^{76/77}$Br-labeled PARP1 inhibitor rucaparib derivative, [$^{76/77}$Br]RD1.

mL of water to trap the radiolabeled compound. Crude product was then eluted slowly with 0.5 mL of EtOH followed by 0.5 mL of water. The eluted solution was injected onto a pHPLC (Kinetix XB-C18, 5 µm, 100 Å, 10×250 mm) in 40:60 MeCN/0.1 M NH_4HCO_2 (aq – 4 mL/min) monitored by 254 nm absorbance (Knauer, Smartline 200) and radioactivity (Carroll & Ramsey Instruments, Model 105) detectors. The [^{77}Br]RD1 radiopeak (approximately 12.9 min) was collected from the pHPLC, diluted into 50 mL of water, passed through a prepped C18 light cartridge and rinsed with 10 mL of water. Purified [^{77}Br]RD1 was then eluted slowly with 0.5 mL of EtOH. [^{77}Br]RD1 in EtOH was dried under Ar flow and reconstituted in phosphate buffered saline (PBS) for *in vitro* and 10% EtOH in saline for *in vivo* experiments. Radioactivity was measured using Capintec CRC 15R (Pittsburgh, PA) with a setting of #120.

Radiochemical conversion (RCC) was calculated by dividing the radioactivity of crude [^{77}Br]RD1 by the activity loaded onto the intermediate C18 cartridge). Non-decay corrected radiochemical yield (n.d.c. RCY) was calculated by dividing the isolated radiolabeled product collected from the pHPLC by the starting activity in the reaction. Average RCC and n.d.c. RCY (n=12) was 63±43% and 54±29%, respectively.

3.3.1.3 Analytical High-Performance Liquid Chromatography

Analytic high-performance liquid chromatography (aHPLC, Agilent 1260 Diode-Array Detector HS) was performed with a CsI(Tl) scintillator (1×1 cm, Hilger Crystals Ltd., Kent, UK) coupled

to a photomultiplier tube (E849-35, Hamamatsu Photonics, Hamamatsu City, Japan) powered and processed with bench-top electronics (925-SCINT, Ortec, Oak Ridge, TN, USA) with the electronic analog pulse converted to voltage (Model 106, Lawson Labs Inc., Malvern, PA, USA) and logged using an Agilent 1200 universal interface box. Injections of the [^{77}Br]RD1 radiopharmaceuticals were done on a 1260 Infinity II Quaternary System (Agilent) with 00D-4462-EO Kinetex (2.6 µM, 100 Å, 100×4.6 mm) column and 20 µL injection volume. A linear gradient method with aqueous 0.1 M triethylamine (TEA) and MeCN was used as described in Table 3.2, with a flow rate of 1.0 mL/min.

Solutions of 0.05–50 µM radioinert BrRD1 standard in 5% acetonitrile were assayed in triplicate to establish the BrRD1 mass response of the UV absorbance detector. The area under the BrRD1 peak (retention time = 8.94±0.02 min, 254 nm absorbance), measured in milli-absorbance units (mAU), for each molar concentration was quantified and used to make a calibration curve. The data was fitted with a least squares regression line and the resulting equation used to convert the aHPLC areas under the peaks to BrRD1 mass (pmol, Appx. B.1). The slope and intercept were calculated as 0.3694±0.0003 pmol/mAU and -0.576±0.411 pmol, respectively. Using this calibration curve, the milli-absorbance units (mAU) were converted to molar mass.

Table 3.2: Gradient method for analytical HPLC (aHPLC).

Time (min)	**0.1 M TEA (%)**	**MeCN (%)**
0	95	5
2	95	5
10	50	50
15	50	50
16	95	5
22	95	5

On the day of experiments with [^{77}Br]RD1, a 100 pmol BrRD1 standard injection analytic system suitability test was done to validate the retention time and absorbance calibration on the aHPLC system. The activity and volume of the radiopharmaceutical were then measured and injected on the column. The free radiobromide had a retention time of 50±1 s and the radiopharmaceutical

had a retention time of 8.94±0.02 min (254 nm absorbance). The peak areas of these two radiation peaks were used to calculate the radiochemical purity (RCP) using Eq. 3.2:

$$\mathrm{RCP} = \frac{A_{\mathrm{R_P}}}{A_{\mathrm{R_P}} + A_{\mathrm{F_P}}}. \qquad \text{(Eq. 3.2)}$$

where $A_{\mathrm{R_P}}$ is the area under the radiopharmaceutical peak and $A_{\mathrm{F_P}}$ is the area under the free radiobromide peak. The RCP was 99.0±1.9% (n=11).

The molar activity (MA) of the radiopharmaceutical was calculated using Eq. 3.3:

$$\mathrm{MA} = \frac{A \cdot A_{\mathrm{R_P}}}{\mathrm{M} \cdot (A_{\mathrm{R_P}} + A_{\mathrm{F_P}})}, \qquad \text{(Eq. 3.3)}$$

where A is the activity per 20 µL and M is the mass corresponding to the $A_{\mathrm{R_P}}$ molar mass. The MA was then decay corrected to the time of dosing.

3.3.1.4 Preparing Radiopharmaceutical Solutions

The radiopharmaceutical was split into two vials, one for the viability assay and one for the total and nonspecific binding assay. The radiopharmaceutical was diluted seven-fold five times for the viability assays, with the highest activity concentrations being 17–75 MBq/mL (50–430 nM, n=10). For the binding studies, the activity from the radiopharmaceutical made it possible to assess the uptake in the cells. However, the objective was to have a high enough molar concentration to more accurately assess the maximum binding unique to a cell line (Section 3.3.3.1), not necessarily a high MA. Therefore, radioinert BrRD1 was added to the second vial for the binding studies before undergoing four-fold dilutions five times, with the highest concentrations being 9–128 nM (0.74–49 MBq/mL, n=16[2]).

[2]For n=4, radioinert BrRD1 was not added to increase the molar concentration. The range for the highest concentrations for these experiments was 9–111 nM (11–49 MBq/mL). Excluding these values, the highest concentrations for the binding studies range from 93–128 nM (0.74–2.6 MBq/mL, n=12).

3.3.1.5 Thin-Layer Chromatography

Thin layer chromatography (TLC) was used to measure the stability of the radiopharmaceutical in liquid over time. For experiments performed using radiopharmaceutical solutions aged more than 24 hours later with high radioactivity concentration (>700 kBq/mL), TLC was performed using aluminum-backed SiO_2 plates (Merck KGaA) developed with 3:1 EtOAc:CH_3CN mobile phase and visualized by storage phosphor autoradiography (Perkin Elmer Cyclone Plus). The retention factor (R_f) was 0.6 for [^{77}Br]RD1 and 0.1 for free [^{77}Br]bromide.

3.3.1.6 Gamma Counter Calibration

Vials with various activities in various volumes were measured by efficiency- and energy-calibrated high purity germanium (HPGe, Canberra C1519) gamma spectroscopy and used as ground truth for both ^{76}Br[3] and ^{77}Br. For ^{76}Br, activity was calculated using the peak area measured at 559 keV with a gamma-ray intensity of 74% [105]. For ^{77}Br, peaks measured at 239 and 521 keV with gamma-ray intensities of 23.1% and 22.4%, respectively, were used [106]. The calibrated vials were then measured on the Wizard^2 2480 gamma counter (PerkinElmer) for 1–2 minutes. For ^{76}Br, the counting window on the gamma counter was 400–1,500 keV. For ^{77}Br, the counting window was 150–700 keV.

The user can set the real time (t_r) on the gamma counter. The gamma counter then reports the following—the real time, total counts measured (C_m), counts per minute (CPM), and the percent error associated with the count. The gamma counter does not report the dead time (t_d), live time (t_l) or background. If the user divides the total measured counts by the real time, it does not equal the gamma counter reported CPM. This indicates that when the gamma counter is calculating the CPM, it is accounting for the detector dead time, the background, or both. If we ignore the background, we can calculate the live time in minutes of the detector for each measurement using Eq. 3.4:

$$t_l = \frac{C_m}{CPM}, \qquad \text{(Eq. 3.4)}$$

[3]To avoid repetition in Chapter 5, the methods and results for ^{76}Br will be presented in this chapter.

which can give us the dead time:

$$t_d = t_r - t_l. \quad \text{(Eq. 3.5)}$$

Vials were placed on racks that could hold a maximum of 10 samples. Vials on the same rack contribute the most to the background. For this reason, vials with activities of the same order of magnitude were placed on the same rack with an empty sample. If the empty vial had higher than 5% CPM of the vials on the same rack, the rack was remeasured 24 h later after additional decay had occurred. If necessary, to reduce the background, the assembly conveyor and rack were kept empty of additional samples. Figure A.2B in Appendix A.3 shows an example of a filled rack.

The dead time was calculated for each measurement. If the dead time was higher than 10%, the measurement was retaken. Using Eq. 3.4, some samples had negative dead times. This happened for low count and background measurements, indicating that the gamma counter had an internal background measurement and subtraction from the CPM measurement. Since our equation does not have a background subtraction, this discrepancy is expected.

As the HPGe calibrated samples' activity decayed, the vials were remeasured on the gamma counter to get a range from 1.8×10^4 to 1×10^6 CPM for ^{76}Br and 90 to 9×10^6 CPM for ^{77}Br. These measurements were converted to counts per second (CPS). The known activity as measured by the HPGe in Bq was plotted as a function of the gamma counter measured CPS. The slope [Bq/CPS] was calculated for both ^{76}Br and ^{77}Br and used as the gamma counter calibration coefficient.

3.3.2 Cell Culture and Growth

3.3.2.1 Cell Culture

Murine ID8 ovarian cancer cells were gifted from Dr. Katherine Roby (University of Kansas, KS) and were maintained in Dulbecco's modified Eagle's medium with 4.5 g/L glucose, L-glutamine and sodium pyruvate (Corning) supplemented with 5% fetal bovine serum (FBS, Corning), 1% penicillin-streptomycin (Corning) and 0.2% 500X insulin-transferrin-selenium (ITS) supplement (BioWhittiker) in a 5% CO_2 atmosphere at 37°C.

Human OVCAR8 and OVCAR8 PARP1-KO G1 [135] ovarian cancer cells were gifted from Dr. Mehran Makvandi (University of Pennsylvania, PA) and were maintained in RPMI-1640 medium (Gibco) supplemented with 10% FBS and 1% penicillin-streptomycin in a 5% CO_2 atmosphere at 37°C. OVCAR8 PARP1-KO G1 had an additional 2 µg/mL puromycin (Gibco) added to the medium.

Human UWB1.289 and UWB1.289+BRCA1 ovarian cancer cells were purchased from American Type Culture Collection (ATCC) and were maintained in media composed of 1:1 RPMI-1640 (Gibco) and mammary epithelial growth medium (MEGM, Lonza) supplemented with 3% FBS in a 5% CO_2 atmosphere at 37°C. UWB1.289+BRCA1 had an additional 200 µg/mL Geneticin selective antibiotic (G418 Sulfate, Gibco) added to the medium. The ovarian cancer cell lines and characteristics, including doubling time, medium, seeding ratio and passing rate are summarized in Table A.1 in Appendix A.1.

3.3.2.2 Doubling Time

The doubling time of ID8 cells was measured in clear tissue-culture (TC)-treated sterile 96-well plates (Corning) with well area of 0.32 cm^2. Various seeding cell densities in sextuplicate were used to measure the impact of cell doubling time from 100–48,000 cells/well in a volume of 200 µL cell medium. After various growth periods (3.5 –96 hours), the media was aspirated and the adhered cells dispersed with 50 µL 0.25% trypsin-EDTA (Corning) for approximately 5 minutes at 37°C and then 50 µL cell media was added to neutralize the trypsin. The cell concentration was then measured using a hemocytometer (Appx. A.6.1).

3.3.3 Cellular Pharmacokinetics

Cells were grown in clear, sterile, TC-treated 96-well plates (Corning) at a seeding density between 5,000–50,000 cells/well in a volume of 180 µL cell medium for 15–24 hours. The cells were then treated in triplicate with varying molar concentrations of [^{77}Br]RD1 for varying amounts of time depending on the assay, and further described in the relevant sections. The radiopharmaceutical

in phosphate buffered saline (PBS, BioWhittaker) without calcium or magnesium was added to the wells in a volume of 20 µL for a total volume in wells of 200 µL for the assays described in Section 3.3.3.1 and 3.3.3.2.

After the radiopharmaceutical dosed the cells for the set amount of time established by the specific protocol, the radiopharmaceutical containing medium was removed and placed in corresponding polypropylene cluster tubes (Corning). The wells were rinsed with 100 µL of PBS and this was removed and placed in the same corresponding cluster tubes. The cells were then dispersed with 50 µL of 0.25% trypsin-EDTA (Corning) for 20 minutes at 5% CO_2 and 37°C. This volume was then removed and placed in separate corresponding cluster tubes. The wells were again rinsed with 100 µL of PBS, and this was removed and placed in the trypsin-EDTA containing corresponding cluster tubes. Control wells with no activity were used to measure the cell density per well using a hemocytometer (Appx. A.6.1).

The cluster tubes were capped and labeled, and placed in empty scintillation vials. Vials were measured for 1–3 minutes with the Wizard^2 2480 gamma counter using the ^{77}Br setting as described in Section 3.3.1.6, with lower activities measured for 3 minutes, and high activities measured for 1–2 minutes. Empty vials were measured to approximate the background for each rack. If the empty sample accounted for more than 5% CPM of any vial measurement, the vial's activity was remeasured. If the dead time (Section 3.3.1.6) was larger than 10%, the vial was remeasured. CPM were decay corrected to the time of dosing and converted to Bq using the gamma counter calibration coefficient calculated from Section 3.3.1.6.

3.3.3.1 Total and Nonspecific Binding

Cells were treated in triplicate with varying concentrations of radiopharmaceutical to achieve a final concentration ranging from 0.0086 to 128 nM (0.81 kBq/mL to 49 MBq/mL, n=4 for OVCAR8 and n=3 for all other cell lines) for six concentrations in four-fold dilutions with and without a blocking dose of 1 µM radioinert Br-rucaparib derivative 1 (BrRD1) (Fig. 3.3, Appx. A.3). For the activity measured by the gamma counter on the vials that contained cells, the molar activity

measured with aHPLC and the measured number of cells/well by hemocytometer were used to calculate the cellular molar uptake, U_{M}, or the number of moles of radiopharmaceutical per cell:

$$U_{\mathrm{M}} = \frac{A}{A_{\mathrm{M}} \cdot N_{\mathrm{C}}}, \tag{Eq. 3.6}$$

where A is the measured activity of the cells, N_{C} is the counted number of cells/well by hemocytometer and A_{M} is the molar activity. Nonlinear regression analyses for a one-site, total and nonspecific binding ($\mathrm{NS_B}$) option were done with GraphPad Prism v9.3.1 (Dotmatics). The specific binding ($\mathrm{S_B}$) can be calculated using the total binding ($\mathrm{T_B}$) and $\mathrm{NS_B}$:

$$\mathrm{S_B} = \mathrm{T_B} - \mathrm{NS_B}, \tag{Eq. 3.7}$$

$$\mathrm{S_B} = \frac{B_{\mathrm{max}} \cdot [L]}{[L] + K_{\mathrm{D}}}, \tag{Eq. 3.8}$$

$$\mathrm{NS_B} = \mathrm{NS}[L] + \mathrm{BG}, \tag{Eq. 3.9}$$

where B_{max} is the maximum specific binding, $[L]$ is the radioligand concentration, K_{D} is the equilibrium dissociation constant, NS is the slope of the $\mathrm{NS_B}$, and BG is the background, or amount of nonspecific binding with no added radioligand.

The activity in vials containing media were added to the corresponding vials with cells from the same well for quality check of the measured activity values compared to the expected activity values. The molar uptake per cell as a function of radiopharmaceutical molar concentration was plotted and the B_{max}, K_{D}, NS and corresponding 95% confidence intervals were calculated.

3.3.3.2 Association and Dissociation

The number of cells plated in each well of a 96-well plate was kept constant for each individual assay, with 25,000–50,000 cells seeded in 180 µl volumes 24 hours before the assay (n=3 for ID8 and OVCAR8, n=1 for OVCAR8 PARP1-KO). Half the cells were used to determine the

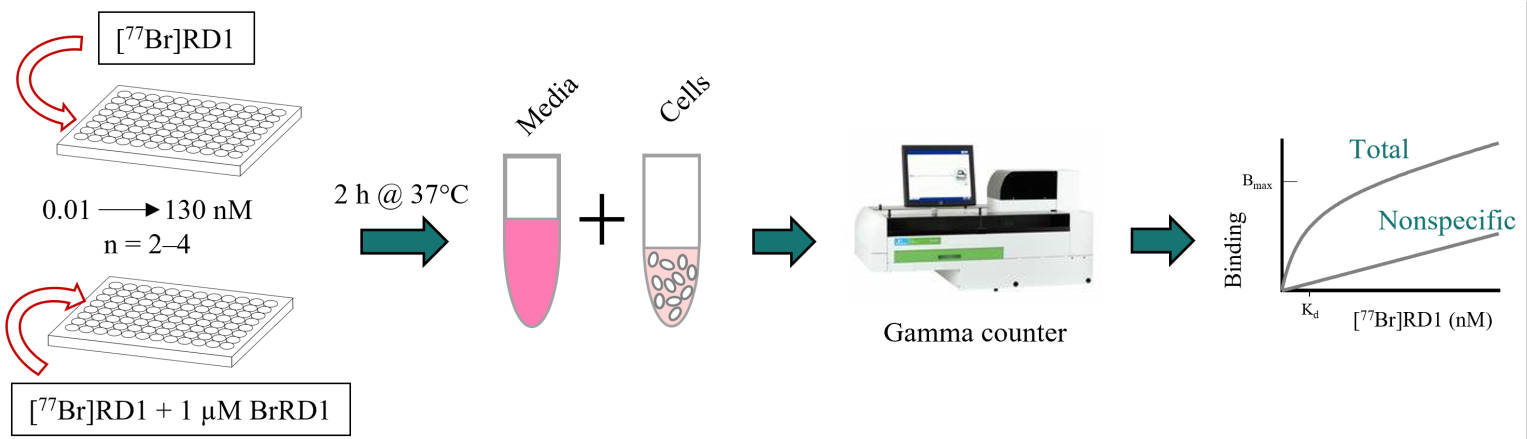

Figure 3.3: The binding study workflow conducted on ovarian cancer cells. Cell lines were plated at a density of 7,000–50,000 cells/well for 24 hours. After contacting in triplicate with [^{77}Br]RD1 (total binding) or [^{77}Br]RD1+1 µM BrRD1 (nonspecific binding) for 2 h at 37ºC, media and cells were collected in individual cluster tubes and the activity counted on a gamma counter (PerkinElmer). These measurements were used to plot the total and nonspecific binding curves.

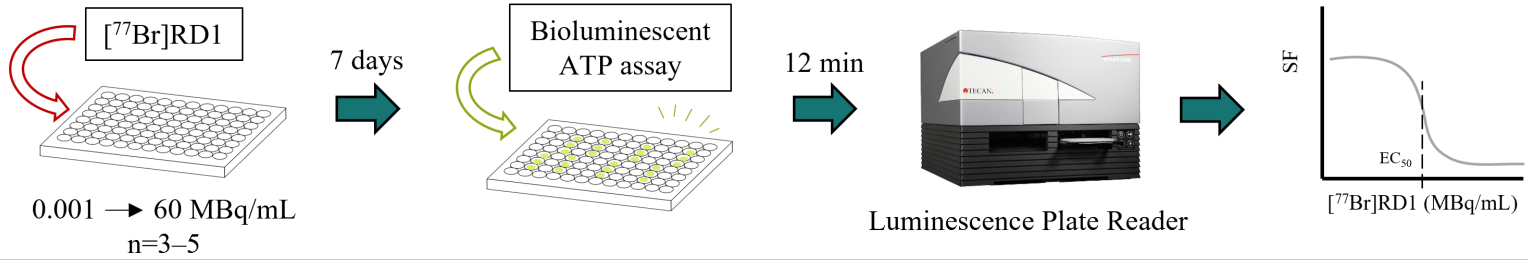

Figure 3.4: The viability study workflow for all ovarian cancer cells. Ovarian cancer cells were plated at a density of 200 cells/well for 2 hours before contacting with [^{77}Br]RD1 in triplicate to wells for 7 days. Bioluminescent ATP assay (CellTiter-Glo 2.0) was used to measure the cell viability to generate surviving fraction (SF) curves.

association rate constant, and the other half were used to determine the dissociation rate constant (Appx A.4). To determine the dissociation rate constant, half the cells were treated with 0.1–0.4 nM [^{77}Br]RD1 (40–100 kBq/mL, 100–370 MBq/nmol) at time point 0 minutes and then 1 μM radioinert BrRD1 at multiple time points from 60–120 minutes in triplicate. To determine the association rate constant, the other half of the cells were treated with 0.1–0.5 nM [^{77}Br]RD1 (40–100 kBq/mL, 100–370 MBq/nmol) at multiple time points from 60–120 minutes in triplicate. When the plate was outside the incubator, a heat pad was used to keep the cells at 37°C. After the final time point, cells and media were collected in cluster tubes and their activity measured using the Wizard^2 2480 gamma counter as described in Section 3.3.3.

The measurements collected by gamma counter were used to calculate the percent uptake of [^{77}Br]RD1 in the cells compared to the amount of [^{77}Br]RD1 in the medium. The fractional uptake as a function of time was plotted in GraphPad Prism and the nonlinear regression for an association-then-dissociation analyses was done. The association rate constant (k_{on}), dissociation rate constant (k_{off}), B_{max}, K_D, NS and corresponding 95% confidence intervals were calculated.

The dissociation rate constant was also measured a second way. Cells were plated at a constant seeding density per well, with a seeding 25,000–50,000 cells across experiments (n=2) 24 hours before assay in a 96-well plate at 180 μl. Approximately 0.1 nM (270–440 MBq/μmol) of [^{77}Br]RD1 in PBS (exact concentration was measured for each assay) in a 20 μl volume was added to the cells and let to sit for 1 hour. After 60 min, the media with radiopharmaceutical was removed and fresh media (37ºC) was added to the wells. This was labeled t=0. At multiple time points from 2 minutes to 21 hours, the radiopharmaceutical containing media and cells were collected in cluster tubes as described at the beginning of this section. After the final time point, the cluster tubes containing the cells and media were measured with the Wizard^2 gamma counter (Section 3.3.1.6). The fractional uptake in the cells was calculated from the known activity added to each well and from the measured activity in the collected media.

3.3.4 Radiotoxicology

Cell viability was measured using the ATP-based luminescent assay protocol summarized in Section 3.3.4.1. Cells were treated with the radiopharmaceutical at activity concentrations of 0.001–60 MBq/mL (0.001–250 nM) at the time of dosing for 7 days. The luminescence signal was normalized to the sham treated control readings (Fig. 3.4).

The activity concentration was converted to molar concentration by dividing by the aHPLC measured molar activity. The B_{max} and K_D values calculated from the total and nonspecific binding assays were used to convert the activity concentration [MBq/mL] to specific uptake, A_S [Bq/cell] using Eq. 3.10:

$$A_S = \frac{B_{max} \cdot [A]}{K_D + [A]/A_M}, \qquad \text{(Eq. 3.10)}$$

where A_M is the molar activity and $[A]$ is the activity concentration.

The normalized luminescence signal, or surviving fraction, as a function of radiopharmaceutical concentration and as a function of activity uptake per cell was plotted in GraphPad Prism. The data was fit using a nonlinear regression for a sigmoidal dose-response with a variable slope analyses. The bottom and top value were manually set to 0 and 1, respectively, and the half maximal effective concentration (Log(EC_{50}) and EC_{50}), hill slope of the curve and corresponding 95% confidence intervals were calculated.

3.3.4.1 Viability Assay

The CellTiter-Glo® 2.0 Assay (Promega) was used to determine the number of viable cells in culture by quantifying the amount of ATP present. Briefly, the number of metabolically active cells is proportional to the ATP present [139]. CellTiter-Glo lyses the cell and introduces Ultra-Glo™ Luciferase and luciferin in the presence of Mg^{2+} to produce light that can be quantified. The reaction is summarized in Figure 3.5.

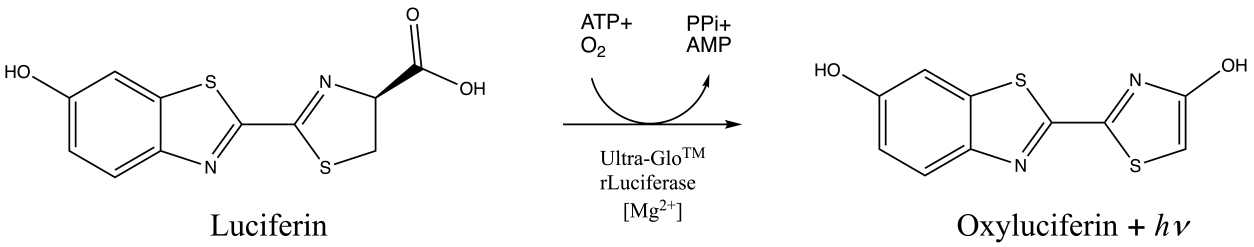

Figure 3.5: Oxidative decarboxylation of luciferin is catalyzed by luciferase in the presence of ATP, oxygen and Mg^{2+} and emits light that can be measured [140]. This signal is directly proportional to the amount of ATP which is also directly proportional to the number of viable cells.

Cells were plated in sterile 96-well white/opaque, tissue-culture treated plates (Falcon). Cell seeding density was optimized for experimental conditions, with 200 cells/well at a 7-day reading giving consistent results (further discussed in Section 3.3.4.2). Cells were plated in 180 µL media 2 hours before dosing with radiopharmaceutical. For radiopharmaceutical studies, 20 µL of the drug was added to triplicate wells. Plates were then incubated at 37°C at 5% CO_2 for 7 days in humid conditions. To avoid evaporation of peripheral wells and thus changing the radiopharmaceutical concentration, neighboring empty wells were filled with 200 µL phosphate buffered saline (PBS).

After 7 days, well volumes were measured and the amount exceeding 100 µL was removed, approximately 60–80 µL. CellTiter-Glo 2.0 was stored at -70°C and thawed to room temperature before use. Equal parts of room temperature CellTiter-Glo (100 µL) was added to each well. The plate was then manually shaken for 2 minutes at approximately 300 revolutions per minute (rpm) and then incubated at room temperature for 10 minutes to stabilize the luminescent signal. A Spark 10M Plate Reader (Tecan) with an integration time of 1 second was used to measure the luminescence. Measurements were normalized to sham dosed wells (20 µL PBS) to give the percent viable as a function of dose.

3.3.4.2 Viability Assay Optimization

To determine how many days after dosing were optimal for luminescent viability assay performance, studies measuring the viability with CellTiter-Glo 2.0 were performed at 3, 5, 6, 7 and 9 days after dosing. Plates were seeded at a density of 200 cells/well and irradiated with external

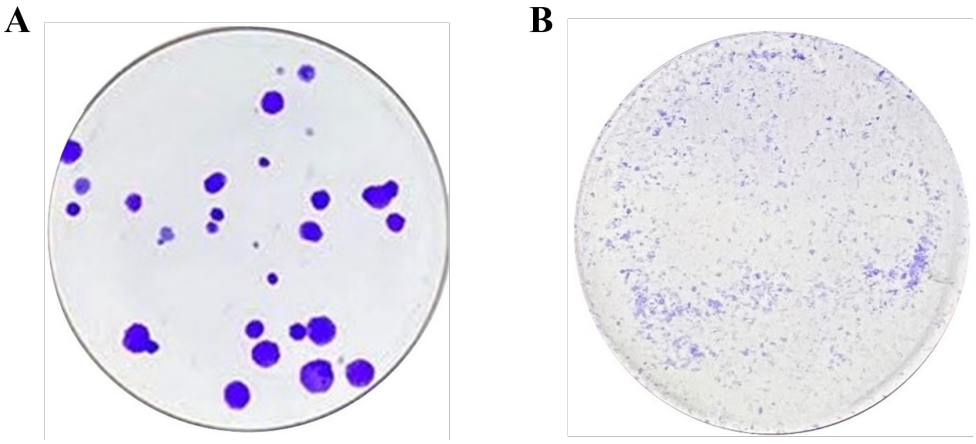

Figure 3.6: Cell growth after 7 days in a volume of 1.5 mL and a well area of 9.5 cm^2 for (**A**) ID8 colony forming cancer cells plated at a seeding of 40 cells and (**B**) UWB1.289 lawn forming cancer cells plated at a seeding of 5,000 cells. Cells were fixed and stained with 25% glutaraldehyde and 1% crystal violet.

beam (Xstrahl CIX3 Cabinet Irradiator) in triplicate with doses of 1, 2, 5, 10, 20 and 50 Gy for OVCAR8 and ID8 ovarian cancer cells.

3.3.4.3 Viability Assay Validation

The viability assay was validated using the clonogenic, or colony forming assay. The cancer cell lines used in this study have two different colony growth characteristics. The murine ovarian cancer cell line, ID8, grows in a colony formation with clearly defined margins (Figure 3.6A). The human ovarian cancer cell lines, OVCAR8 and UWB1.289, grow in lawn formation without clear colony formations (Figure 3.6B). If lawn forming cells were plated at too sparse a density, it was observed that the cells would not reach confluency even with extended time and extended feedings. This indicated that the doubling time was not constant below a certain threshold. This needed to be accounted for in the clonogenic assay.

For the clonogenic assay ([137], Appx. A.6) cells were grown in clear TC-treated sterile 6-well plates (Corning) with a volume of 1.5 mL of growth media and a well area of 9.6 cm^2 and dosed with external beam radiotherapy (EBRT) in sextuplicate.[4] For colony forming cell lines, cells were

[4]Two cell densities were used and treated by EBRT in triplicate. After many experiments of having chosen a seeding density that was too low (no colonies formed) or too high (individual colonies could not be counted), this method

plated at a density of 20–4,000 cells per well. For lawn forming cell lines, cells were grown at a density of 1,000–1×10^5 cells per well. The density was increased for increasing radiotherapeutic dose delivered by EBRT. ID8 cells were irradiated with an Xstrahl CIX3 Cabinet Irradiator and OVCAR8, UWB1.289 and UWB1.289+BRCA1 cells were irradiated with an Xstrahl RS225 Cell Irradiator. Both orthovoltage units had a nominal energy of 150 kV using a 3 mm aluminum filter with focal source distances (FSD) of 30 cm. This gave a field size diameter of 19 cm and corresponded to a dose rate of 3.3 Gy/min.

Plates were irradiated at various doses from 1–40 Gy for the murine cancer cell line (ID8) and 1–20 Gy for the human cancer cell lines (OVCAR8, UWB1.289 and UWB1.289+BRCA1). The plates were kept warm using Styrofoam boxes with 37°C heat packs during transit and between dosing. After dosing, plates were kept in a 5% CO_2 atmosphere at 37°C for 7 days. On the 7th day, the medium was removed and the wells were rinsed with 2 mL of PBS. The PBS was removed and the cells were stained with 1.5 mL of colony fixation-staining solution, which consisted of 25% glutaraldehyde (Crescent Chemical) and 1% crystal violet (Electron Microscopy Sciences) in distilled water.

The stain was left in the wells for 30 minutes and then removed. The plates were rinsed in water to remove excess stain and the plates were turned upside down and left to dry for 24 hours. Plates were photographed with a light box $\sim$1 meter behind the plates and the images were processed with ImageJ (National Institutes of Health). Figure 3.6 shows two cell lines after using the colony fixation-staining solution for the control plates.

The ColonyArea plugin [141] (University of Turku) was used to process the pictures of the plates. This plugin automatically detects and crops around each well and calculates a threshold value to remove the background. It then creates two stacks of images. The first stack has each well converted to 8-bit images (Figure 3.7A). The second stack uses the automatically calculated threshold value to remove the background, and converts the remaining pixels into a color value produced by a lookup table (LUT) (Figure 3.7B). The threshold value was manually checked to

allowed for more flexibility in the seeding density since two were chosen for each dose level.

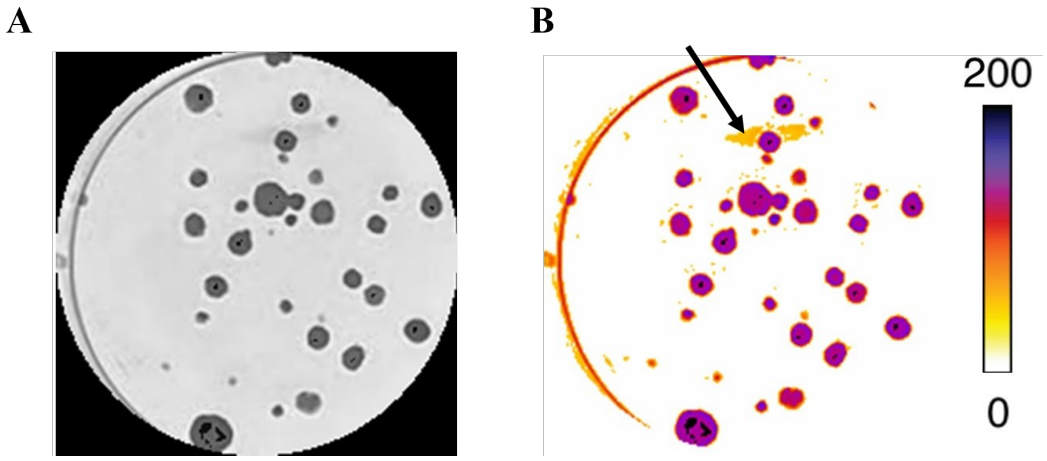

Figure 3.7: The ColonyArea plugin for ImageJ crops the picture of the 6-well plate, converts the image to (**A**) an 8-bit image and then (**B**) uses a lookup table (LUT) to convert the pixel intensity to a corresponding color value. The arrow points to a stain smudge that indicates too large of a threshold value was used, but if the circularity function is used, these pixels would be excluded from the automatic colony tally function.

make sure that pixels corresponding to colonies were included and any shadows or well edges were excluded. When the plugin calculated an inappropriate threshold value—usually by mistakenly increasing the threshold value to include pixels corresponding to stain smudges—the threshold value was manually chosen, instead. The threshold value varied between 185–205 in ImageJ.

The image scale was changed using the known well diameter of the 6-well plates. The Analyze Particles feature in ImageJ was used to automatically count colonies. The circularity and minimum and maximum size of a colony features were selected to exclude any pixels that did not correspond to a colony. For colony forming cells, colonies smaller than 25 cells were excluded. This was done using measurements of 25 cell colonies from a microscope as the minimum size threshold. The circularity threshold was used to exclude leftover smudges, especially those at the edge of the plate. The Analyze Particles feature also has a tally and outline output that the user can use to validate the colony count. The Analyze Particles feature on ImageJ was then validated by comparing the automatic count with a manual count.

For lawn forming cells, a region of interest (ROI) was drawn to encompass a single colony. This was repeated eight times to get an average colony size for the lawn growing cells. An ROI

encompassing the entire well was used to measure the percent area covered by stained cells using the ImageJ Measure tool. To calculate the number of colonies, the area of the plate covered in colonies was divided by the single average colony size. This method was validated by comparing manual and automated colony counts in the colony forming cell line, ID8.

The surviving fraction after dosing by EBRT for the clonogenic and viability assay were fit to a linear quadratic equation (Eq. Eq. 3.1) and the D_{37} average value and standard deviation were calculated for ID8, OVCAR8, UWB1.289 and UWB1.289+BRCA1 (n=2). The 95% CI were calculated for OVCAR8 PARP1-KO (n=1).

3.4 Results

3.4.1 Radiopharmaceutical Production and Quality Control

For ^{77}Br production, the average physical yield was 15±2 MBq/μAh and the distillation yield was 70±13%. During distillation, two CsI(Tl) radiation detectors were used to measure the activity. One of the detectors was collimated on the furnace where the CoSe target was located, and the other on the water trap. Figure 3.8 shows the radioactivity profile in these detectors as a function of time across the distillation, apparatus rinsing, and QMA loading. After labeling, the radiochemical yield (RCY) of [^{77}Br]RD1 for seven radiochemical reactions are summarized in Figure 3.9 for all the productions.

TLC showed [^{77}Br]RD1 was greater than 95% stable after 72 hours for activity concentrations less than 2 MBq/mL and greater than 90% stable for activity concentrations of 10 and 70 MBq/mL (Fig. 3.10). For activity concentrations larger than 4 MBq/mL and stored in solvent for longer than same day use, TLC was used to measure the stability of the radiopharmaceutical.

3.4.2 Gamma Counter Calibration

The Wizard^2 gamma counter exhibited a geometric dependence, as evidenced by 13 readings taken over 32 days. After the first reading, vials were inverted upon removal from the rack after

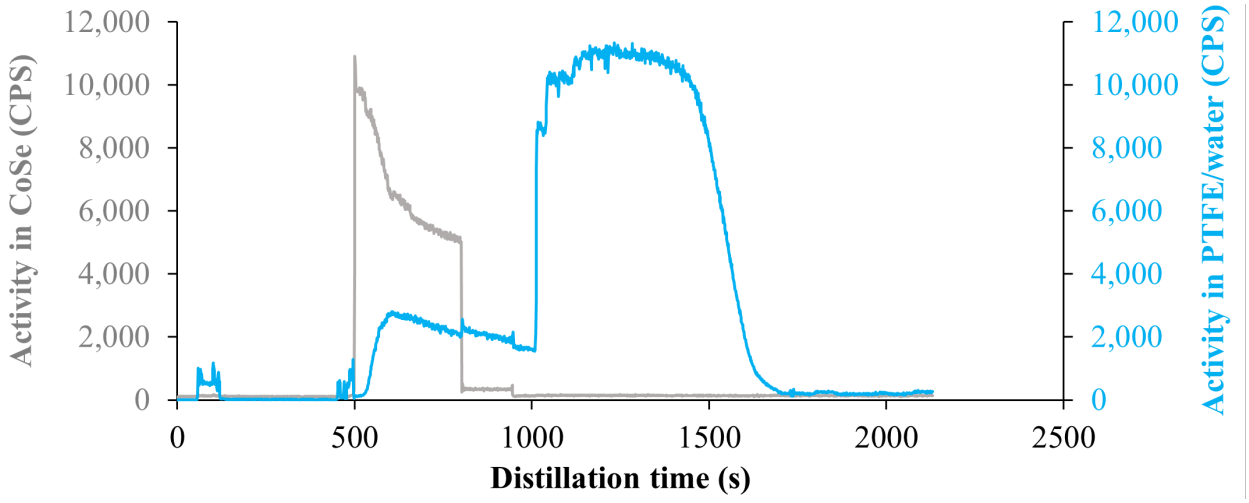

Figure 3.8: Distillation of ^{77}Br for production number 7.

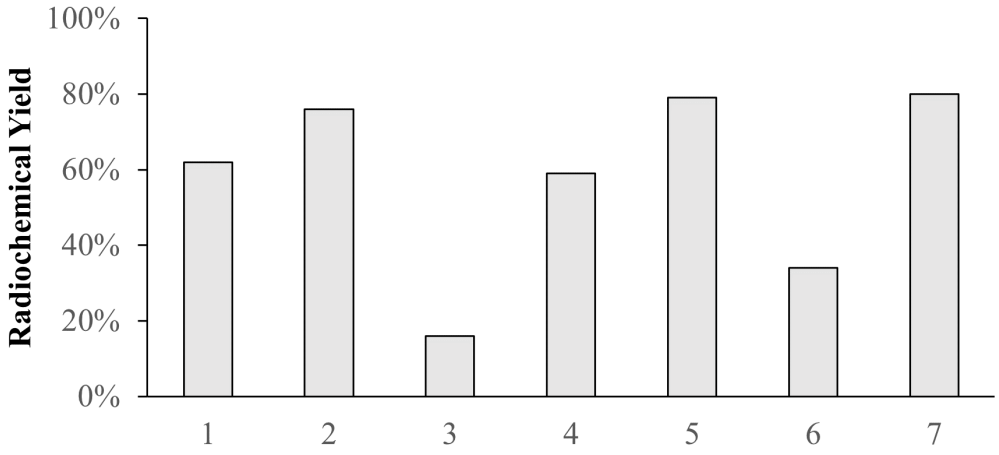

Figure 3.9: Radiochemical yield of [^{77}Br]RD1 after seven separate radiolabeling reactions.

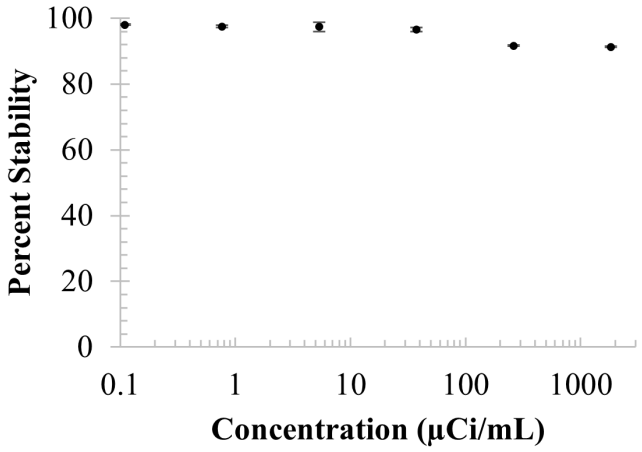

Figure 3.10: Stability of [^{77}Br]RD1 after 72 hours in PBS. The radiopharmaceutical was greater than 95% stable for activity concentrations less than 2 MBq/mL. For activity concentrations larger than 4 MBq/mL, breakdown after 24 h occurred, with greater than 90% stability after 72 hours.

each measurement for the next four subsequent measurements.[5] Vials with volumes greater than 25 µL displayed less stable calibration factors (the ratio between HPGe and Gamma Counter activity readings) between measurements as the activity decayed (Fig. 3.11). This instability may be attributed to the volume and activity spread across the height of the 4 cm vial when it was tipped. Further details are provided in the discussion section.

For calibration, only the vials with volumes less than 5 µL were used to characterize the gamma counter. The calibration coefficient was calculated as 1.85±0.02 Bq/CPS with a counting window of 400–1,500 keV and 3.42±0.02 Bq/CPS with a counting window of 150–700 keV for ^{76}Br and ^{77}Br, respectively. The measurements are summarized in Figure 3.12.

3.4.3 Cell Doubling Time

ID8 cells were shown to reach confluency at about 100,000 cells/well for a 96-well plate with a plate area of 0.32 mm^2 (Fig. 3.13). At that point, the cell growth slows as it reaches capacity due to the limited space. If the slowdown in growth due to confluency is ignored, the data can be fitted

[5]After the fifth reading, the vials were stored upright in the rack between measurements.

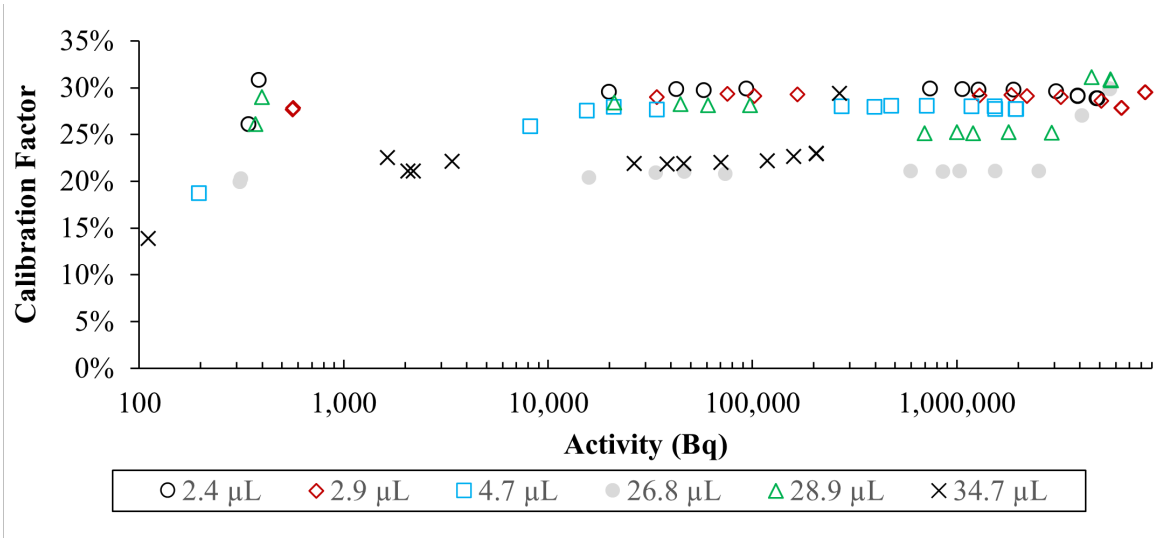

Figure 3.11: Bromine-77 gamma counter calibration factors for vials of various activity volumes. Larger volumes show less stability between measurements compared to smaller volume vials due to the geometric dependence of the gamma counter.

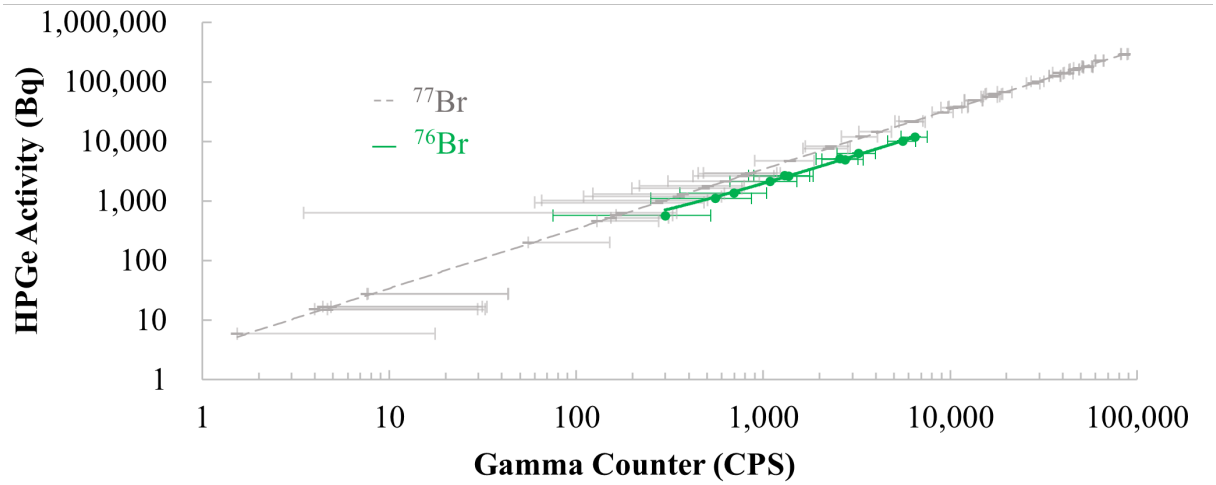

Figure 3.12: Calibration of the Wizard[2] gamma counter for ^{76}Br and ^{77}Br. The calibration coefficient was 1.85±0.02 Bq/CPS and 3.42±0.02 Bq/CPS for ^{76}Br and ^{77}Br, respectively.

with the exponential growth equation:

$$N = logN_0 + kt, \qquad \text{(Eq. 3.11)}$$

where N_0 is the starting population and k is the rate constant. The doubling time is calculated using $ln(2)/k$. Using Eq. 3.11, the doubling time is 14±4 h, with the minimum doubling time of 10±2 h for the lowest density (100 cells/well) and the maximum doubling time of 20±2 for the highest density (4,800 cells/well). The highest plated density reached confluency fastest, at around hour 56. At that point, the graph shows a plateau until the final time at 96 h. Doubling of the cells would not occur between 56–92 hours due to limited space in the well. This falsely increases the doubling time calculation. If, instead, the logistic growth equation:

$$N = \frac{N_M \cdot N_0}{N_M - N_0} \cdot e^{-kt} + N_0, \qquad \text{(Eq. 3.12)}$$

is used, where N_M is the maximum population, and the starting population, N_0, is set to the measured value by hemocytometer, disregarding plating efficiency, the calculated doubling time is 12±2 hours with a maximum population of 156,000 cells per well (95% CI: (131–192)$\times 10^3$ cells).

3.4.4 Cellular Pharmacokinetics

3.4.4.1 Total, Specific and Nonspecific Binding

The total binding and nonspecific binding curves (Fig. 3.14A–B) and the resulting B_{max}, K_D and NS values were calculated using GraphPad Prism v9.4.1 and are summarized in Table 3.3. These values were used to calculate the specific binding curves with Eq. 3.7 (Fig. 3.14C).

For the OVCAR8 PARP1-KO cell line, there was no statistical difference between the nonspecific and total binding measurements for molar concentrations above 25 nM (n=4). This indicated a low number of specific binding sites that were small compared with nonspecific binding above 25 nM. Thus, values measured above 25 nM were excluded from the B_{max}, K_D and NS fitting analysis for

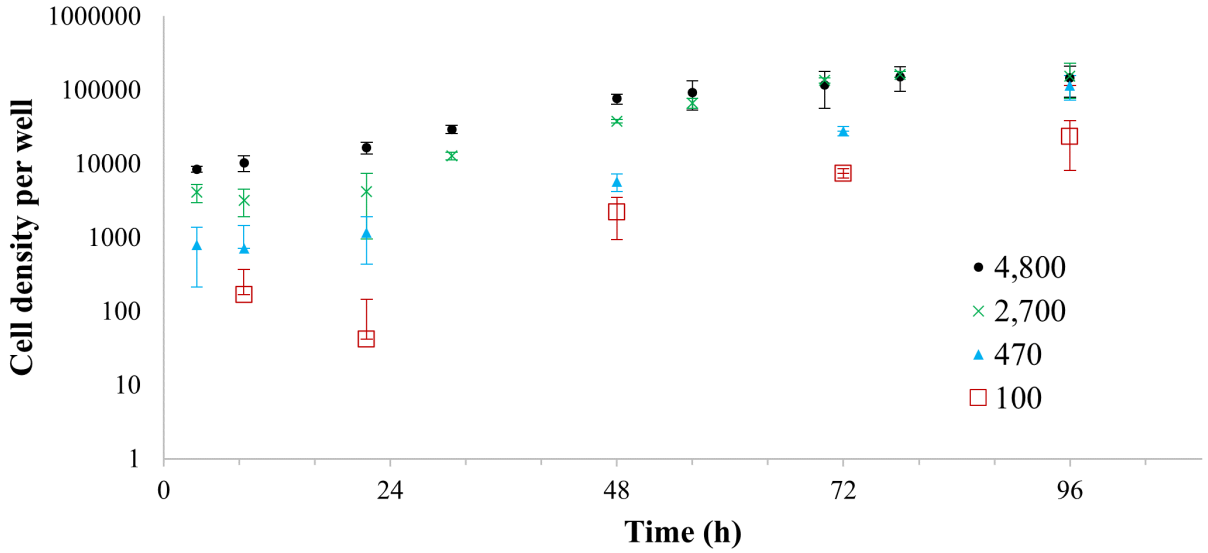

Figure 3.13: ID8 cells were plated at a concentration between 100–4,800 cells/well in sextuplicate. The resulting cell density per well was counted by a hemocytometer as a function of time.

Table 3.3: The [^{77}Br]RD1 pharmacological characteristics calculated from total and nonspecific binding studies in the various ovarian cancer cell lines and their corresponding 95% confidence intervals (CI). These values were calculated using the data summarized in Figure 3.14.

Ovarian Cancer Cell Line	B_{max} (95% CI) (attomol/cell)		K_D (95% CI) (nM)		NS (95% CI) (attomol/cell/nM)	
ID8	3.0	(2.4–3.9)	31	(20–49)	0.049	(0.047–0.052)
OVCAR8	1.6	(1.4–1.8)	6.0	(4.2–8.2)	0.050	(0.048–0.052)
OVCAR8 PARP1-KO	0.83	(0.50–1.5)	7.5	(2.7–20)	0.039	(0.033–0.046)
UWB1.289	11	(7.9–16)	24	(10–57)	0.20	(0.19–0.21)
UWB1.289+BRCA1	8.6	(6.6–11)	25	(13–48)	0.26	(0.25–0.26)

this cell line.

3.4.4.2 Association and Dissociation

For the dissociation assay in which the cells were washed with non-radioligand-containing media (Fig. 3.15), the data were fitted with a nonlinear regression model using one phase exponential decay that is summarized in Eq. 3.13:

$$R_t = (R_0 - \mathrm{NS}) \cdot \mathrm{e}^{-k_{\mathrm{off}} t} + \mathrm{NS}, \qquad \text{(Eq. 3.13)}$$

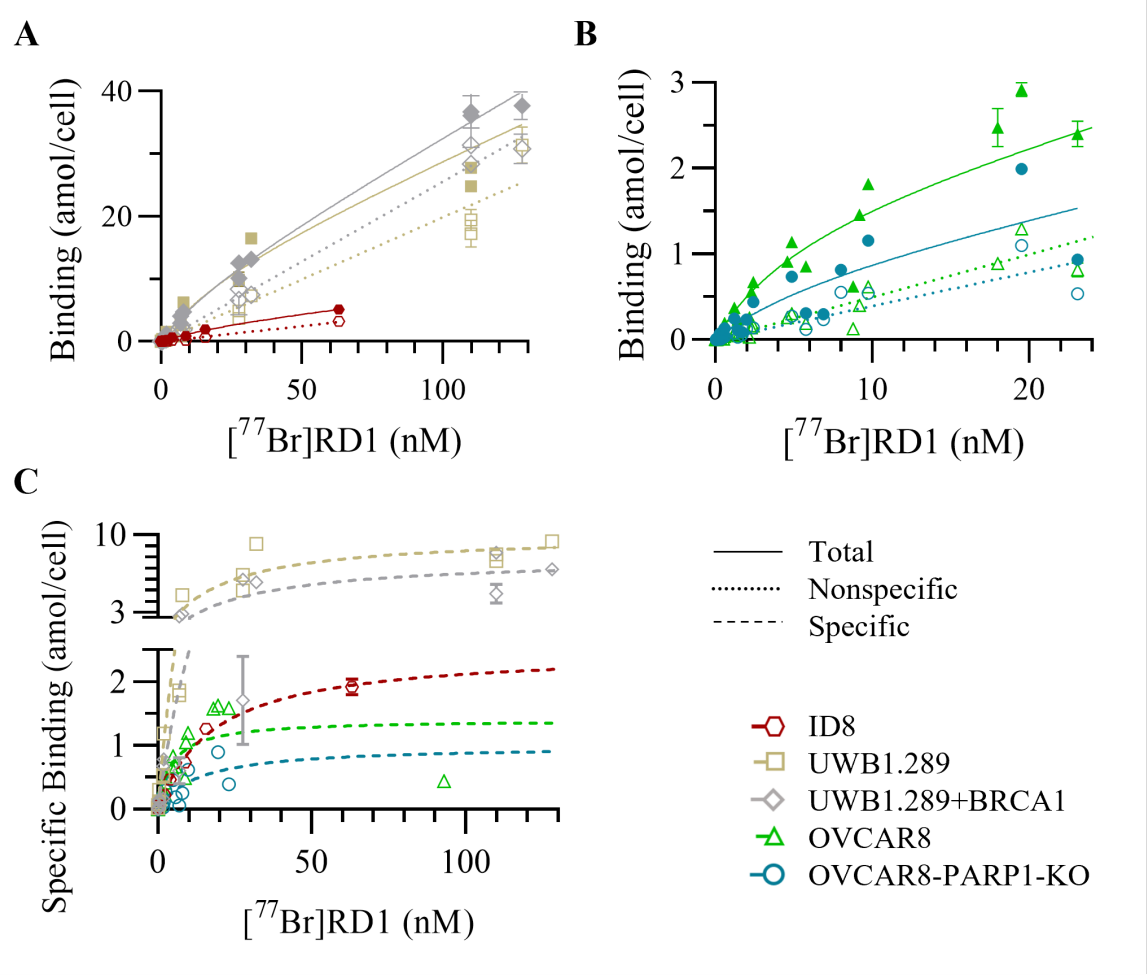

Figure 3.14: Total (closed symbols, solid lines) and nonspecific (open symbols, dotted lines) binding of (**A**) UWB1.289 (gold, n=3), UWB1.289 +BRCA1 (gray, n=3), ID8 (red, n=2) (**B**) OVCAR8 (green, n=4), and OVCAR8 PARP1-KO (blue, n=4) and (C) the specific binding (dashed lines) of [^{77}Br]RD1 as a function of radiopharmaceutical molar concentration.

where R_0 is the percent bound at time zero, NS is the nonspecific binding at infinite time, k_{off} is the dissociation rate constant and t is the time. This study showed how the radioligand dissociated from the cells to nonspecific binding levels by 30 minutes. This informed the time points for the association and competitive dissociation assay summarized in Fig. 3.16. The ID8 cells (n=1) were conducted first, and the time points chosen missed the dissociation rate. For the OVCAR8 study (n=2), increasing the number of time points before 30 minutes yielded a k_{off} value of 0.132 min^{-1} (95% CI: 0.112–0.156 min^{-1}), which was approximately 20% higher than the k_{off} value calculated from the competitive dissociation assay (0.112±0.076 min^{-1}, see below).

For the competitive dissociation and association assay (Fig. 3.16), the dissociation data were fitted with Eq. 3.13, and the association data were fitted with a nonlinear regression model using the kinetics binding equations summarized in Eq. 3.14:

$$R_{t,\,\text{association}} = \frac{R_{\max}[L]}{K_D + [L]}\left(1 - e^{-(k_{on}[L]+k_{off})t}\right), \qquad \text{(Eq. 3.14)}$$

where R_t is the response at time t, R_{max} is the response at the maximum of the association phase and $[L]$ is the radioligand concentration [142]. The association response time was calculated using the k_{off} fit from the competitive dissociation assay and the K_D values from the binding assays (Section 3.3.3.1). The radioligand concentration was measured using the aHPLC and was between 0.113–0.408 nM for the various experiments. The calculated variables k_{off} and NS are summarized in Table 3.4.

From Figure 3.16, the nonlinear regression fits used to calculate k_{off} are more robust compared to the association assays used to calculate k_{on}. Therefore, the k_{on} values were calculated using the following equation:

$$k_{on} = \frac{k_{off}}{K_D} \qquad \text{(Eq. 3.15)}$$

where k_{off} values from the dissociation assays were used and the K_D values from the binding studies

were used. The 95% CIs for the K_D values were converted to standard errors (SE)[6] [143]:

$$SE = \frac{CI_{upperlimit} - CI_{lowerlimit}}{2 \cdot t_{(n-1),C}} \quad \text{(Eq. 3.16)}$$

where $CI_{upper\ limit}$ is the upper limit of the 95% CI, $CI_{lower\ limit}$ is the lower limit of the 95% CI and $t_{(n-1),C}$[7] is the critical value of the t statistic that depends on the chosen value of the confidence level. The standard error was assumed to be equal to the standard deviation (SD).[8] The SD for K_D and k_{off} were used to calculate the SD for k_{on}.

Table 3.4: The dissociation rate constant (k_{off}) and nonspecific binding percent (NS) calculated from the association and competitive dissociation (1 μM BrRD1) assay with 0.13–0.44 nM [^{77}Br]RD1 (ID8 n=3, OVCAR8 n=3 and OVCAR8 PARP1-KO n=1). The calculated association rate constant (k_{on}) was calculated from the K_D calculated from the binding studies.

Constants	ID8	OVCAR8	OVCAR8 PARP1-KO
k_{off} (min^{-1})	0.19±0.09	0.11±0.08	0.112 (0.067–0.176)
NS (%)	1.2±0.5	1.5±0.4[a]	2.02 (1.68–2.33)
k_{on} ($min^{-1}nM^{-1}$)[b]	(6.1±4.9)×10^{-3}	(1.8±1.7)×10^{-2}	(1.5±3.3)×10^{-2}

[a]Excluded experiment n_3.

[b]Calculated using K_D from the binding assays fit.

3.4.5 Radiotoxicology

3.4.5.1 Viability Assay Optimization

The viability of cells were measured with an ATP-based luminescent assay for ID8 and OVCAR8 cells between 3–9 days after treatment with external beam radiotherapy. The measurements taken at 3 days after dosing showed higher surviving fraction values for all measurements compared to those taken at 5–9 days post-treatment (Fig. 3.17). The study was done once for days 3, 6 and 9

[6]This assumes that the CI is based on a normal distribution with a known standard deviation (SD). Although that may not be the case for this nonlinear regression model, using this assumption allows an estimate for the SD to use for error propagation purposes.

[7]This value can be found in appendices of many statistical textbooks or put into Excel as equation "=tinv(1-0.95, *df*)", for a 95% confidence level, where *df* is the degrees of freedom, or the sample size minus 1.

[8]The standard error (SE) can be assumed to equal the SD when the sample size is large. The SE was calculated from CI calculated from nonlinear regression modeling using GraphPad, which did not estimate the SD. This assumption was made in order to calculate the error for k_{on}.

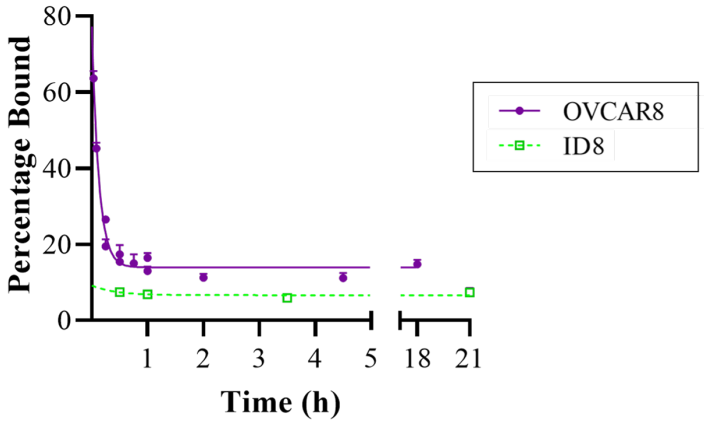

Figure 3.15: The fractional activity bound to the cells as a function of time for ID8 and OVCAR8 (n=1) ovarian cancer cell between 2 minutes and 21 hours. The dissociation was measured by removing the radiopharmaceutical containing media and adding fresh media.

Table 3.5: The dose to reduce the surviving fraction to 37% (D_{37}) as measured by viability assay over a range of 3–9 days post external beam radiotherapy treatment. These values were fit using the data shown in Figure 3.17.

Days after treatment	**D_{37} (Gy, 95% CI)**	
	OVC8	**ID8**
3	42[a]	14[a]
5	4.0 (3.0–5.5)	7.6 (7.1–8.4)
6	1.9[a]	8.9 (8.2–9.8)
7	2.7 (2.3–3.3)	8.8 (8.2–9.8)
9	2.4 (2.2–2.7)	11.7 (10.8–12.8)

[a]Unstable fit.

days post radiation and twice for 5 and 7 days post radiation. Readings between 5–9 days showed overlapping standard deviations in the ID8 cells (Fig. 3.17B). The dose corresponding to 37% survival is summarized in Table 3.5. Since the readings were stable between 5–9 days, luminescent viability assays were performed at 7 days after dosing for the radiopharmaceutical studies.

3.4.5.2 Viability Assay Validation

Counting the number of colonies was done manually for ID8 cells. For the lawn forming cell lines, the area calculation method with ImageJ was used. We validated this method with the ID8 cells (Fig. 3.18A, n=1) and the results are summarized in Figure. 3.18B. The calculated D_{37} was

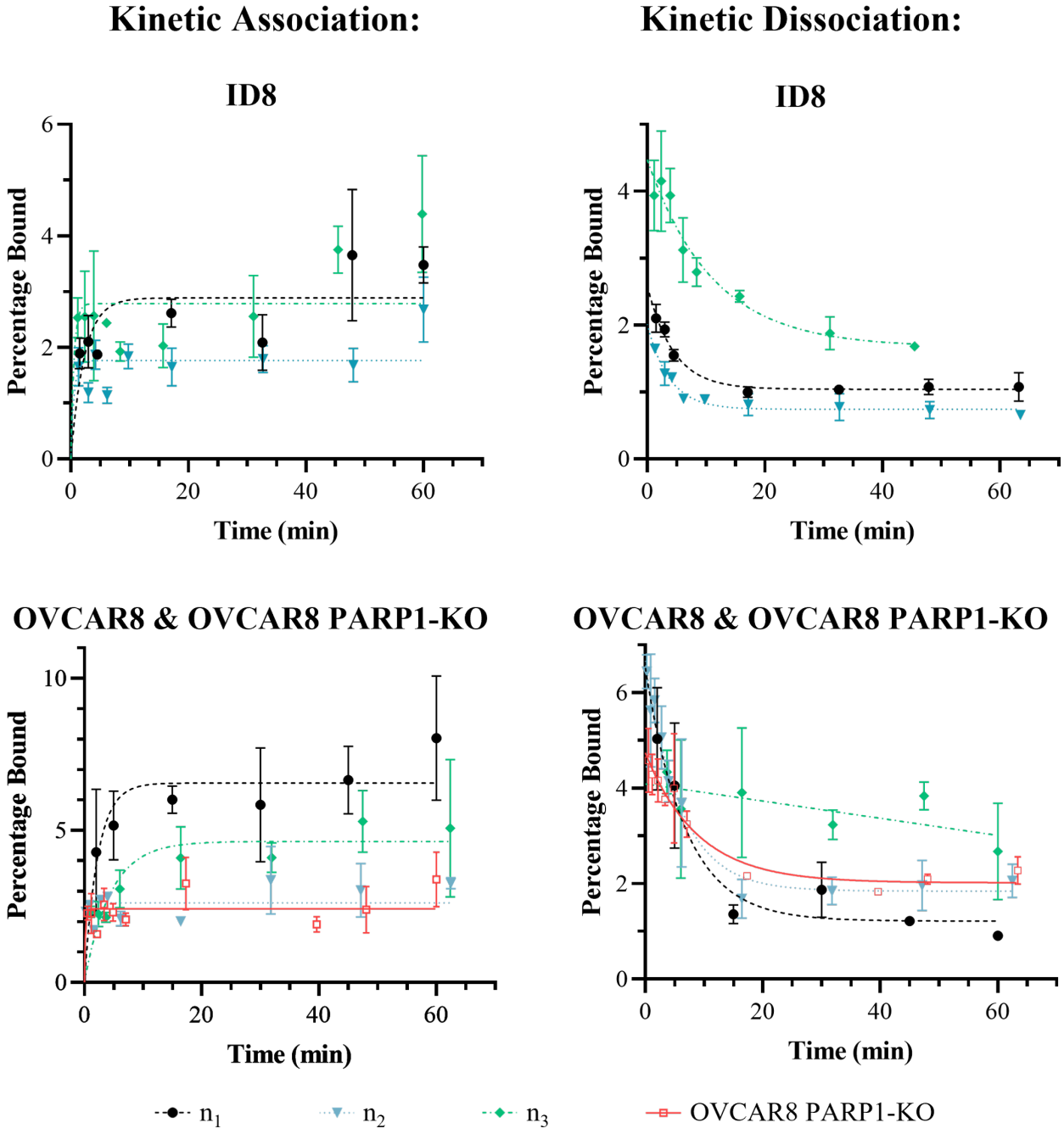

Figure 3.16: The association and dissociation of [^{77}Br]RD1 for the ID8 (n=3, 0.216 nM), OVCAR8 (n=3, 0.113–0.408 nM), and OVCAR8 PARP1-KO (n=1, 0.271 nM) cell lines. Each curve represents a single experiment. The kinetic dissociation was measured with competing 1 μM BrRD1 at 1 hour.

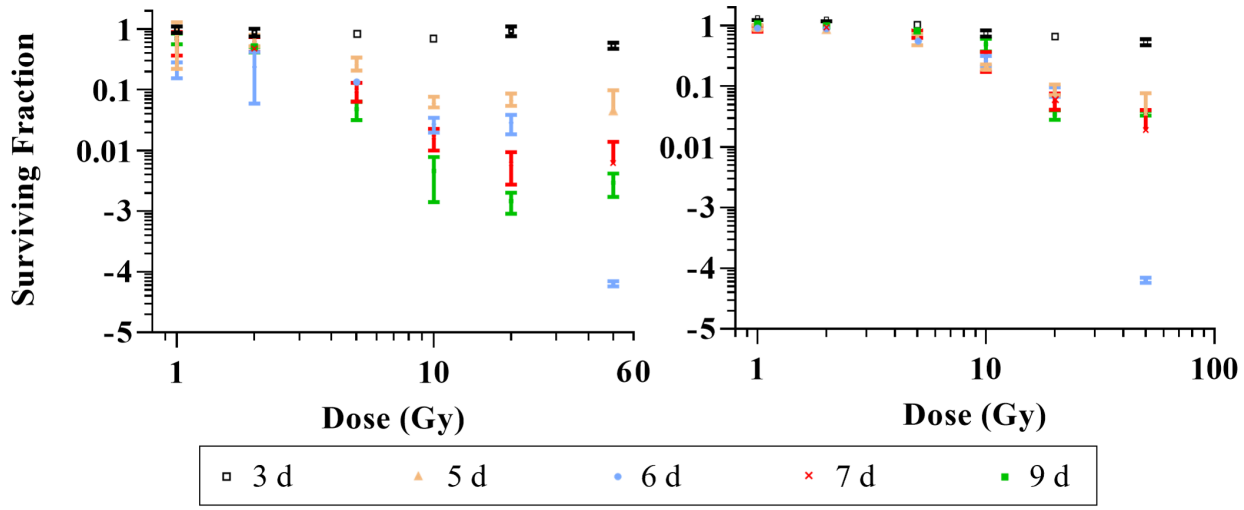

Figure 3.17: The viability assay was performed 3 (n=1), 5 (n=2), 6 (n=1),7 (n=2) and 9 (n=1) days after EBRT of (**A**) OVCAR8 and (**B**) ID8 ovarian cancer cells.

Table 3.6: The D_{37} calculated from the viability and clonogenic assays for various ovarian cancer cell lines (OVCAR8 PARP1-KO n=1 for the cytotoxic assay, otherwise n=2).

Ovarian Cancer Cell Line	**D_{37} (Gy)**	
	Viability	**Clonogenic**
ID8	8.8 ± 1.2	6.2 ± 0.7
OVCAR8	2.6 ± 1.0	2.0 ± 0.2
OVCAR8 PARP1-KO	1.9 (1.8–2.1)[a]	–
UWB1.289	4.9 ± 3.6	3.7 ± 0.9
UWB1.289+BRCA1	2.5 ± 0.6	1.3 ± 0.4

[a]95% confidence interval

4.5 Gy (95% CI: 3.7–5.6) and 5.7 Gy (95% CI: 4.8–6.9) for the area calculation method and the manual count method, respectively. The results from the clonogenic and viability assays of cell lines are summarized in Figure 3.19. The data were fitted with the linear quadratic formula (Eq. 3.1) and the dose corresponding to a surviving fraction of 37% (D_{37}) was calculated (Fig. 3.20, Table 3.6). For the ID8 cells, the highest dose for each experiment was done at two different doses, 40 Gy and 50 Gy. All other doses and cell lines were done twice. We conducted the experiment once with the OVCAR8 PARP1-KO cell line using only the viability assay. The D_{37} result is reported in Table 3.6.

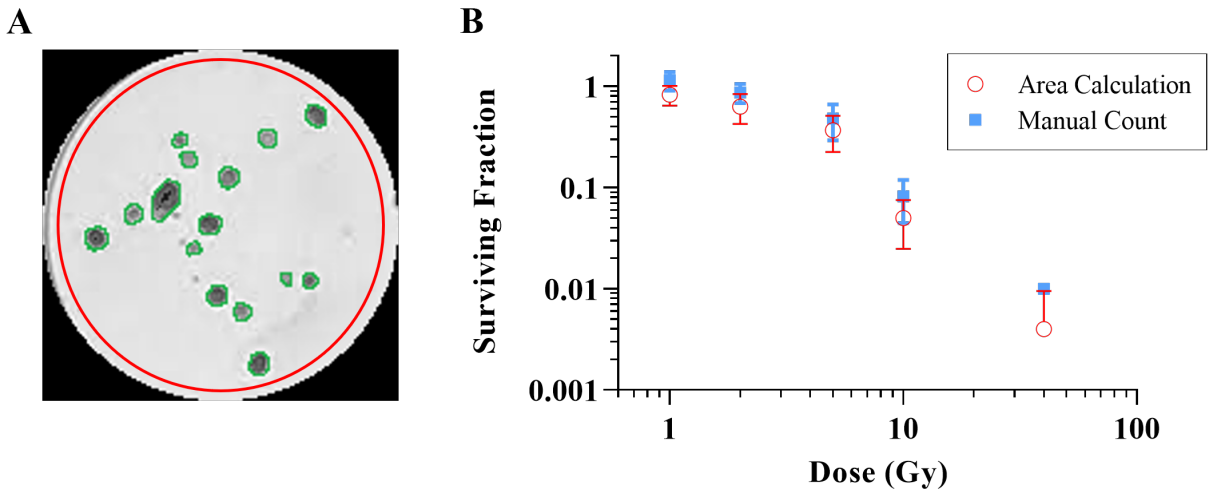

Figure 3.18: Validation of the ImageJ area calculation method. (**A**) The colony forming cell line, ID8, shows a manual count of 15 colonies (excluding 3 small colonies less than 25 cells). The measuring tool can report the ROI (red circle) area and the percentage of pixels within the green mask. Knowing the average size of a colony, the number of colonies can be calculated. (**B**) A comparison of the average surviving fraction as a function of dose for the area calculation method to the manual count for 6 wells at each dose level.

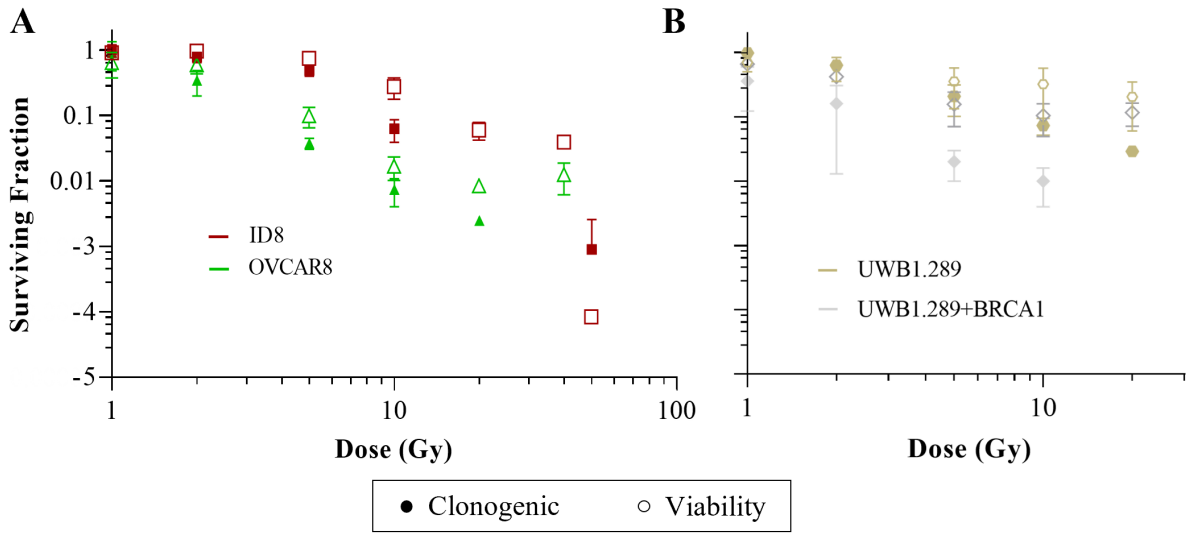

Figure 3.19: Validation of the viability assay (open symbols) was done with clonogenic assay (shaded symbols) using EBRT as the treatment for (**A**) ID8 (red), OVCAR8 (green), (**B**) UWB1.289 (gold) and UWB1.289+BRCA1 (grey).

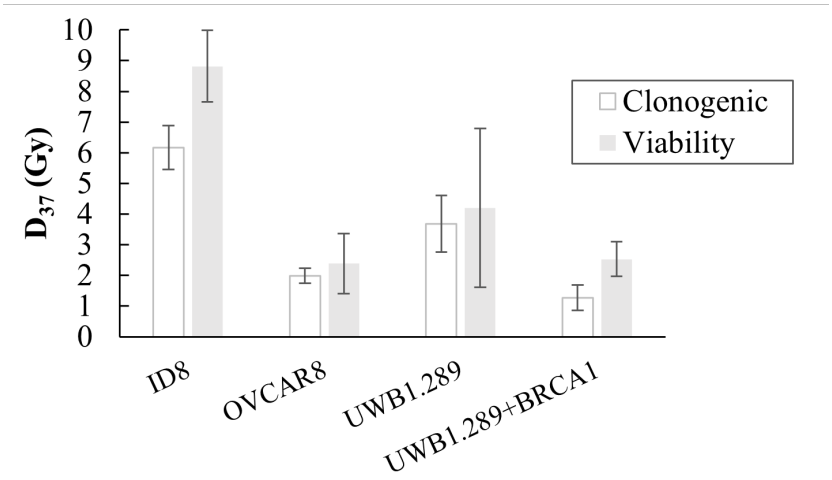

Figure 3.20: The D_{37} calculated from the viability and clonogenic assays for various ovarian cancer cell lines (n=2).

Table 3.7: The EC_{50} values of the various ovarian cancer cell lines and their corresponding 95% CI for [^{77}Br]RD1.

Ovarian Cancer Cell Line	Molar Concentration (nM)		Activity Concentration (10^{-2} MBq/mL)		Cellular Activity Uptake (10^{-2} Bq/cell)	
	EC_{50}	95% CI	EC_{50}	95% CI	EC_{50}	95% CI
ID8	2.3	(1.8–2.9)	44	(36–53)	3.9	(3.3–4.6)
OVCAR8	0.17	(0.13–0.24)	7.0	(6.2–8.0)	1.8	(1.6–2.0)
OVCAR8 PARP1-KO	0.46	(0.34–0.62)	20	(15–28)	2.0	(1.5–2.7)
UWB1.289	0.27	(0.21–0.36)	6.1	(4.4–8.6)	2.7	(2.0–3.7)
UWB1.289+BRCA1	0.30	(0.22–0.41)	6.8	(5.5–8.3)	2.3	(1.9–2.8)

3.4.5.3 Radiopharmaceutical Cytotoxicity

The cell survival curves of the various ovarian cancer cell lines are summarized in Figure 3.21 as a function of activity concentration (Fig. 3.21A–B), molar concentration (Fig. 3.21C) and specific uptake (Fig. 3.21D). The EC_{50} and the corresponding 95% confidence intervals (CI) are summarized in Table 3.7.

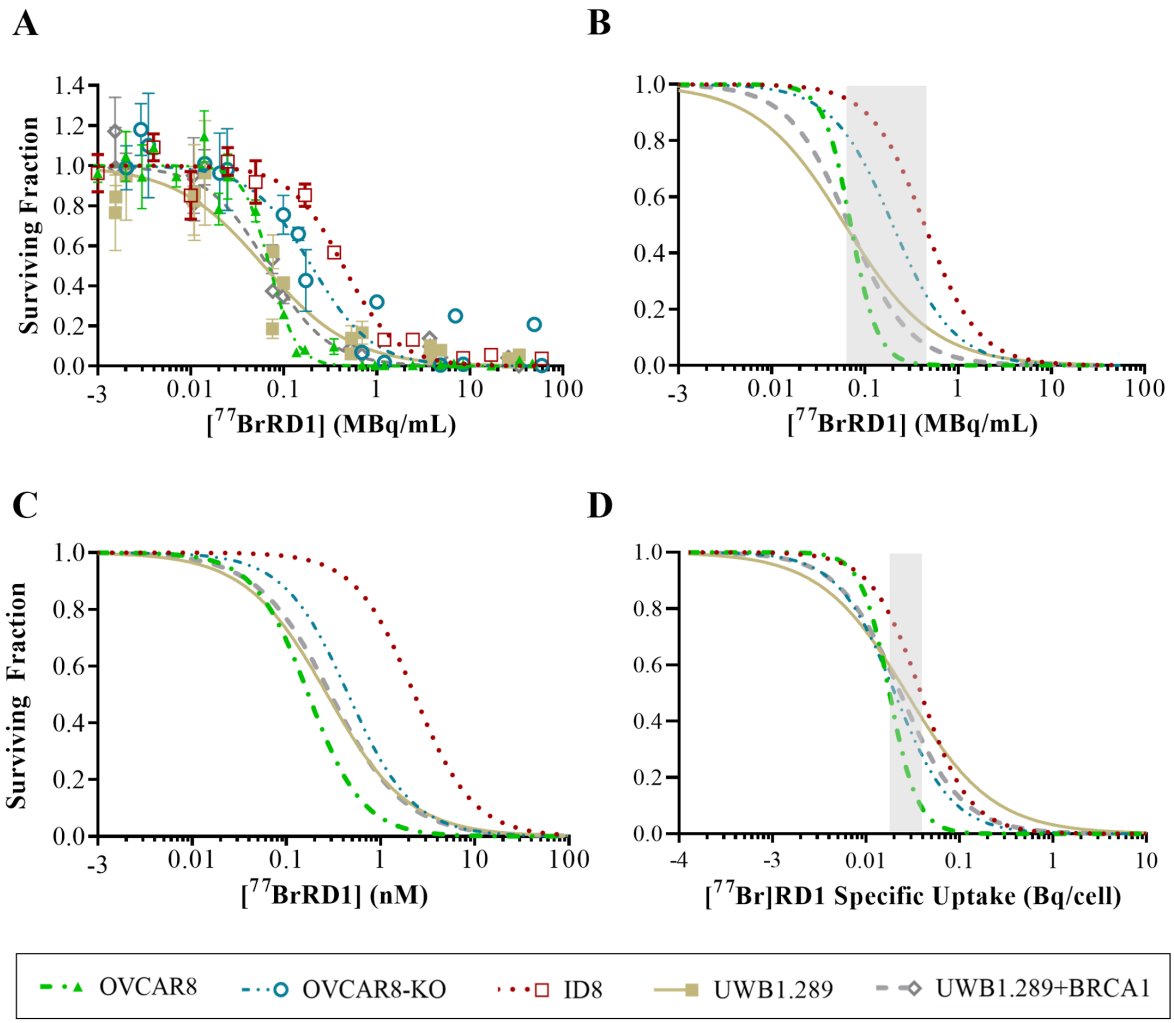

Figure 3.21: (**A**) The cell survival of ID8 (red, n=2), OVCAR8 (green, n=4), OVCAR8 PARP1-KO (blue, n=3), UWB1.289 (gold, n=3), and UWB1.289+BRCA1 (gray, n=3) cell lines as a function of radiopharmaceutical activity concentration (**B**) and the same data presented without data points to clearly compare the trendlines. (**C**) The same data as a function of molar concentration. (**D**) The radiopharmaceutical activity concentration was converted to specific uptake (Bq/cell) inherent to the cell lines. The gray region in (**B**) and (**D**) show how the spread changes with the conversion.

3.5 Discussion

3.5.1 Radiopharmaceutical Production and Quality Control

The radiopharmaceutical showed greater than 90% stability for high concentrations in PBS after 72 hours (Fig. 3.10). For the pharmacokinetic and radiotoxicology studies, experiments were usually conducted within 24 hours of [^{77}Br]RD1 production, with the majority of the storage time in dried state to keep the radiopharmaceutical stable.

For production run number 3 and number 6, radiochemical yield (RCY) of ^{77}Br was 16% and 34%, respectively (Fig. 3.9). The rest of the productions had yields of 59–80%. Production number 3 used 1.6 mL of 0.1 NMe_2H that had been stored in a polypropylene plastic tube. After dry down, the product was brown when it is typically white, and the radiochemical conversion (RCC) was only 1%. This may be attributed to plastic leeching into the 0.1 NMe_2H. The reaction was performed again with the recycled ^{77}Br after trapping on a QMA cartridge, giving 24% RCC to give a final 16% RCY. For production number 6, the [^{77}Br]bromide was stored 19 h in 1.2 mL 0.1 M NMe_2H prior to radiochemistry. The low RCY may have been due to radiolytic effects at the high activity concentration (220 MBq/mL).

3.5.2 Gamma Counter Calibration

Since the cluster tubes were turned upside down to remove them from the racks, the contents could spread across the height of the tube. Tubes with smaller volumes (less than 5 µL) were more likely to stick to the bottom of the tube, even when the tube was inverted. Volumes on the order of 30 µL would have had the contents smear across the tube and not necessarily return to the bottom of the 4 cm tube when turned right side up. The tubes with larger volume samples showed changes in calibration factors from readings performed on different days. For example, all the highest readings for each of the tubes with volumes over 26 µL had calibration factors above 27%. After being inverted, they each dropped 6% (Fig. 3.11). For this reason, we excluded larger volume containing tubes from the calibration calculations (Fig. 3.12).

3.5.3 Cell Doubling Time

This study measured the doubling time of ID8 cells in a 96-well plate at a high passage rate (greater than 42). This study was also used to inform how many cells to plate in a well for the binding studies and viability studies. The binding studies benefit from having as many cells in a well as possible to have a large enough signal to measure the activity in a cluster tube with the gamma counter. Knowing that confluency was reached with approximately 100,000 cells/well, we could use the doubling time inherent to the specific cell line to calculate how many cells to plate 24 h in advance of adding the radiopharmaceutical.

For the viability experiments, the endpoint was 7 days post plating, as informed by the viability assay optimization study. If the cells will be growing for 7 days post seeding, a low seeding density is required. For ID8 cells, confluency was reached before 96 h for wells plated at 470 cells/well. Confluency was not reached by 96 h for the cells seeded at 100 cells/well. However, the errors in the doubling time and y-intercept calculation compared to the other cell densities show that plating at such a low density did not give consistent cell measurements. This may be due to the dilution errors and plating efficiency at that seeding density. Using an initial seeding density of 200 cells/well increases the reproducibility compared to 100 cells/well and allows for the cells to reach confluency after 5 days for ID8 cells and 7 days for cell lines with doubling times greater than 24 hours.

3.5.4 Pharmacokinetics

The OVCAR8 cell line had significantly more PARP1 binding sites ($B_{\max}$) compared to OVCAR8 PARP1-KO, as expected (Table 3.3). ID8, UWB1.289 and UWB1.289+BRCA1 had significantly more binding sites compared to OVCAR8. The UWB1.289+BRCA1 restored cell line had similar binding sites compared to UWB1.289 with *BRCA1* null expression. We measured the binding sites as a number of attomoles per cell. Makvandi, et al. reported $B_{\max}$ as a number of picomoles per Lowry-assay-quantified protein mass using the PARPi [^{125}I]KX1, a highly related iodo-for-bromo-exchange analog of BrRD1 [135, 144]. They reported more PARP1 sites in the UWB1.289 compared to the UWB1.289+BRCA1 by approximately 1.5–1.6 times (9.204±0.0144

pmol/mg and 5.910±0.0314 pmol/mg, respectively). We saw an increase of 1.3 times. They also reported higher binding sites in OVCAR8 compared to the PARP1-KO line of approximately 9 times (5.666±0.0408 pmol/mg and 0.6197±0.0157 pmol/mg, respectively) [135]. Our findings showed an increase of approximately 2-fold.

The ID8, UWB1.289 and UWB1.289+BRCA cell lines had equilibrium dissociation constants (K_D) on the same order of magnitude, with both the OVCAR8 and OVCAR8 PARP1-KO cell lines approximately 3–5 times lower. Makvandi reported values between 1.5–5.1 nM for all the cell lines. Our range was 6.0–25 nM for the same cell lines.

From the pure dissociation assay, it was apparent the dissociation of the radiopharmaceutical happened rapidly. The assay requires removal of the media, washing of the cells with PBS followed by tryspinization. The washing of the cells with PBS occurred in approximately 10±5 s, but if we see disassociation fall approximately 20% between 2–5 min, dissociation could be occurring during the washing phase. Furthermore, the washing step is inconsistent in time, that could cause problems with reproducibility. If we remove the washing phase, we may be counting radiopharmaceutical that was not bound to receptors, also giving inconsistent results. If the washing step can be standardized between experiments and for all wells, that may solve the reproducibility problem.

The association and dissociation assay was performed three times for OVCAR8 and ID8 cells. However, reproducibility was not achieved between experiments. Even when experiments used the same molar concentration of radiopharmaceutical, the results were inconsistent. The pipette tips were not dipped into the wells, perhaps causing variability in the molar concentration if the drop did not fully disperse into the well. Furthermore, the nonspecific and specific binding (total binding) was only observed to be a factor of 2–6 times higher than the nonspecific binding. Together with the inter-replicate variability, fitting the data using an “association then dissociation” equation was not possible. Improving the experiment with a higher molar concentration of the radiopharmaceutical on the order of 1–10 nM rather than 0.1–0.4 nM may address this issue.

3.5.5 Radiotoxicology

3.5.5.1 Viability Assay Optimization

The results for the luminescent viability assay taken 5–9 days after EBRT treatment show the cells receiving the highest dose decreasing to between 0.1–10% survival, compared to the measurements taken 3 days after treatment, in which the higher dosed cells had surviving fractions on the same order as the lower doses (Fig. 3.17). This may be due to control sham treated cells needing to undergo additional replication, increasing the luminescence signal and effectively decreasing the measured survival, since the measurements were normalized to the control sham treated cells. If the time between treatment and measurement is too short, the signals from the sham-treated and treated cells can be similar. However, allowing for more time to elapse enables cellular processes like cell senescence and apoptosis to occur, leading to a decrease in signal from the treated cells and an increase in signal from the sham-treated cells that have undergone normal replication.

The ID8 cells showed higher than 100% surviving fraction for low doses. This may be due to an increase in amount of ATP present after cellular response to lower amounts of DNA damage. Cells may undergo transient transcription arrest, which can lead to ATP surplus in defective DNA repair cells [145]. The higher dosed cells may experience cell cycle arrest, leading to apoptosis. After 5 days, this transient cell cycle arrest may be resolved, and the ATP levels decrease compared to the non-dosed cells.

The OVCAR8 cell line (Fig. 3.17A) gave less reproducible results compared to the ID8 cells (Fig. 3.17B). For the low dose values, the standard deviations of the ID8 cells were much smaller compared to the OVCAR8 low dose measurements. The measurements at 1 Gy and 2 Gy across all days have an average surviving fraction of 103±18% and 100±15%, respectively, compared to 50±36% and 47±27%, respectively, for the OVCAR8 cells. However, the D_{37} values between 6–9 days post treatment show less variability, with a range of 0.8 Gy between the three measurements

(Table 3.5).[9] For the ID8 cells, the difference in the D_{37} calculated on days 5, 6 or 7 showed minimal differences (1.3 Gy), with overlapping 95% CI (Table 3.5). Due to these results, running the luminescent assay 7 days post treatment was established for protocols with this assay.

3.5.5.2 Viability Assay Validation

Although the clonogenic and viability assays did not give overlapping survival curves (Fig. 3.19), the D_{37} values were of the same magnitude (Fig. 3.20). The OVCAR8 and UWB1.289 both had D_{37} values with overlapping standard deviations, albeit the UWB1.289 had a considerable standard deviation for the viability assay. This may be due to the reproducibility issues of the viability assay. The results at 1 Gy and 2 Gy gave overlapping readings for all cell lines, but above 5 Gy, the viability and clonogenic assays started to deviate from each other. The doses at the highest range gave the highest deviation between the two assays, although the ID8 cells showed a massive drop in the surviving fraction between 40 and 50 Gy.

Since the clonogenic assay is measuring the replication abilities of dosed cells, and the viability assay is measuring the ATP, it is expected that the cell survival may not be equal between the two assays. However, since the D_{37} were on the same order of magnitude, it seemed possible to use the viability assay as a substitute for clonogenic assays for the radiopharmaceutical studies. Although the viability assay gave less reproducible results as shown in the large variability of the UWB1.289 D_{37} value (Table 3.6), the variability in individual readings with the large error bars (Fig. 3.17) and the variability on D_{37} depending on what day post treatment the measurements were taken, the convenience and scalability of the assay makes it a much more viable assay to conduct compared to the clonogenic assay.

3.5.5.3 Radiopharmaceutical Cytotoxicity

The toxicological EC_{50} (in nM) of [^{77}Br]RD1 was thousands of times smaller compared to rucaparib for OVCAR8 (2,400×), OVCAR8 PARP1-KO (6,700×) and UWB1.289+BRCA1 (3,000×),

[9] Although, the D_{37} CI at 6 days post treatment was not calculated due to the unstable fit from the large error bars for the low dose values.

and 70× smaller for UWB1.289 [135]. These results show the radiotoxicity of [^{77}Br]RD1 is significantly greater than the chemotoxicity of structurally-related rucaparib in ovarian cancer. Compared to the radioiodinated MAe$^-$-emitting analog, ^{125}I-KX1, the EC_{50} (in MBq/mL) of [^{77}Br]RD1 is 5× and 4× larger for OVCAR8 and OVCAR8 PARP1-KO, respectively [93]. This difference may be due to the smaller average number of MAe$^-$s emitted with ^{77}Br (6-7 MAe$^-$/decay) compared with ^{125}I (∼23 MAe$^-$/decay) [104]. When measured in terms of activity concentration, the OVCAR8 PARP1-KO cell line was significantly more [^{77}Br]RD1-tolerant (P=0.0140) compared to OVCAR8 (Fig. 3.21A–B), with EC_{50} of 0.20 (95% CI: 0.15–0.28) MBq/mL and 0.070 (0.062–0.080) MBq/mL (Table 3.7), respectively. However, after accounting for the cell line's lower number of specific binding sites, this differential sensitivity was no longer observed (P=0.6228), with EC_{50} of 0.020 (0.015–0.027) Bq/cell and 0.018 (0.016–0.020) Bq/cell for OVCAR8 PARP1-KO and OVCAR8 cell lines, respectively (Fig. 3.21D, Table 3.7). These results indicate that the PARP-expression dependence of [^{77}Br]RD1 radiotoxicity is driven by differences in specific binding site expression, instead of differences in DNA repair capacity of the cell lines.

[^{77}Br]RD1 had similar cytotoxic effects regardless of *BRCA1* gene expression. The chemotherapeutic effect of PARPi, like rucaparib, results in increased cytotoxicity in homologous recombination deficient *BRCA1* mutated cells [33]. In studies showing the chemotherapeutic effects of rucaparib on UWB1.289 compared to UWB1.289+BRCA1, the *BRCA1* null cell line UWB1.289 had an EC_{50} value that was 46 times smaller compared to the *BRCA1* restored cell line [135]. When adding the radiotherapeutic effect of the MAe$^-$ emitting isotope ^{77}Br, this biomarker-dependency was no longer apparent—the [^{77}Br]RD1 shows similar cytotoxicity in UWB1.238 cells even with upregulated *BRCA1* expression. This indicates the [^{77}Br]RD1 radiotherapeutic effect was not dependent on the synthetic lethality that drives unlabeled PARPi chemotherapeutic effects.

The cytotoxicity of [^{77}Br]RD1 was found to be *PARP1* expression dependent and *BRCA1* status independent. These results together indicate the radiotherapeutic effect of the MAe$^-$ emitting radionuclide was driving the cytotoxicity of [^{77}Br]RD1 beyond the PARPi chemotherapeutic effect.

The EC_{50} value for OVCAR8 PARP1-KO was 2.9 times larger than OVCAR8, indicating

that radiosensitivity to [^{77}Br]RD1 was dependent on *PARP1* expression (Fig. 3.21A and Table 3.21). UWB1.289 and UWB1.289+BRCA1 had overlapping 95% CI (Fig. 3.21B and Table 3.7), suggesting no evident cytotoxic dependence on *BRCA1* expression.

Figure 3.21C summarizes the fitted curves of all the cell lines, showing ID8 and OVCAR8 PARP1-KO had a higher EC_{50} compared to the other cell lines. When converting to specific uptake by using Eq. 3.10 to account for the number of receptor cells for each cell line and the A_M for each replicate (Fig. 3.21D), all the cell lines have overlapping 95% CI except OVCAR8 PARP1-KO with cell lines other than OVCAR8 (Table 3.7). The EC_{50} for the OVCAR8 PARP1-KO becomes 1.6 times smaller compared with OVCAR8 when accounting for specific uptake (Fig. 3.21D and Table 3.7) when it had been 2.9 times larger when measuring in radiopharmaceutical concentration (Fig. 3.21C and Table 3.7).

3.6 Conclusion

The methodology provided in this chapter is intended to provide instructions and rationale for future experiments aimed at probing the fundamental radiation biology of targeted radionuclide therapeutic agents. Validation of established assays provides uncertainty to the user in these types of experiments, with the hope that results can be properly evaluated and the limitations not only understood, but also measured.

The pharmacokinetics of [^{77}Br]RD1 were measured in various ovarian cancer cell lines with and without PARP1 and BRCA1 expression. We observed specific uptake of [^{77}Br]RD1 in human and murine ovarian cancer cells that was dependent on PARP expression. We also evaluated the cytotoxicity of the radiopharmaceutical and found potent cytotoxicity at concentrations 2–4 orders of magnitude lower than chemotherapeutic concentrations. The observed PARP-dependent, BRCA-agnostic efficacy in cell lines suggests potential for treating BRCA-positive ovarian cancer, a group that is currently ineffectively treated with approved PARP inhibitors. These preclinical studies demonstrate translational potential and provide insights into the fundamental radiation biology of this low-energy electron emitter.

CHAPTER 4
PRECLINICAL DOSIMETRIC INVESTIGATION OF A RADIOBROMINE PARP1 INHIBITOR

The previous chapter provided crucial information on the cellular pharmacokinetics, biodistribution, and cytotoxicity of [$^{76/77}$Br]RD1, laying the foundation for the current aim of *in vitro* dosimetry calculations. Accurate dosimetry is essential for the successful translation of radiopharmaceuticals into clinical practice. Therefore, we have taken extra care to ensure that our dosimetry calculations are based on the most reliable and comprehensive data available. Wherever possible, we have supplemented our existing data with additional measurements to reduce uncertainties and improve the accuracy of our results. Ultimately, this chapter aims to provide a detailed analysis of the doses delivered to cancer cells *in vitro*, thereby providing a critical step towards the development of effective and safe radiopharmaceutical therapies for cancer with Meitner-Auger electron emitting radiobromine.

4.1 MIRDcell Software

Rutgers University together with the Committee on Medical Internal Radiation Dose (MIRD) of the Society of Nuclear Medicine and Molecular Imaging (SNMMI) made a multicellular dosimetry and biological response calculation software [127][1] that was used for dosimetric calculations in this aim. MIRDcell is briefly summarized here before discussing its use in the methods section.

The user controls various inputs, including the radiation or radionuclide source, cellular dimensions, radiopharmaceutical distribution, source and target definitions for dose calculations and 1D-, 2D- or 3D-multicellular configuration. The output from the software includes S-value, i.e., the absorbed dose per unit cumulated activity, to each cellular region from each region. This is given

[1]This article is published for v2.0. In this work, we used v3.12. Rutgers updated to v3.13 on March 20, 2023. Spot checks of the output for v3.13 were compared to v3.12 for all three radionuclides (R_C=8 μm and R_N=5 μm) for a colony size of 350 μm (1,489 cells). No differences were reported.

in tabulated form to give the self-dose, i.e., the dose given to the cell from activity within the cell, and the cross-dose, i.e., the dose given to the cell from activity from neighboring cells or areas, as a function of distance from the cell in micrometer steps starting a distance of the radius of the cell (R_C) away. For 2D- and 3D-multicellular setups, the output also includes dose calculations in tabulated form as a function of mean activity per cell.

The user-modifiable inputs are split into various tabs in the software. The first tab (Fig. 4.1) allows the user to choose the radionuclide and the full or average β energy spectrum [146]. The continuous β spectra is logarithmically binned, giving a more accurate calculation compared to the average β spectra. However, using the full β spectra can significantly increase the computation time. Additionally, the user can manually enter the radionuclide information or choose a monoenergetic particle emitter. For predefined MIRD radionuclides, the input data is shown in the bottom right box.

In the second tab, the user can define the target and source regions (Fig. 4.2) for dose calculations. The cell radius (R_C) and nucleus radius (R_N) can be set, along with the percent activity on the cell surface, in the cytoplasm or in the nucleus. On the fourth tab, the user can choose the 1D-, 2D- or 3D-multicellular geometry. For the 1D configuration, the user can set the distance between two cells. The number inputted will be the maximum number the tabulated output table will calculate for the S-value cross-dose, with the minimum number being the distance between two abutting cells. For the 2D configuration, the multicell geometry can be defined, including the shape of the 2D region of interest and its dimensions. This region can be thought of as setting the colony size when cells are abutting each other, or as the plate dimensions when the distance between cells is larger than a cell diameter. This will be further explained in Section 4.3.1.1.

For the 2D configuration, the user can also input the cell labeling information (Fig. 4.3). The max mean activity per cell will be the maximum value (A_{mean}) in the tabulated dose table, with additional outputs in increments of $0.01 \cdot A_{\text{mean}}$. The time integrated activity coefficient (ã) described in Chapter 2.4 in Eq. 2.4 is automatically set to an infinite amount of time, but can be

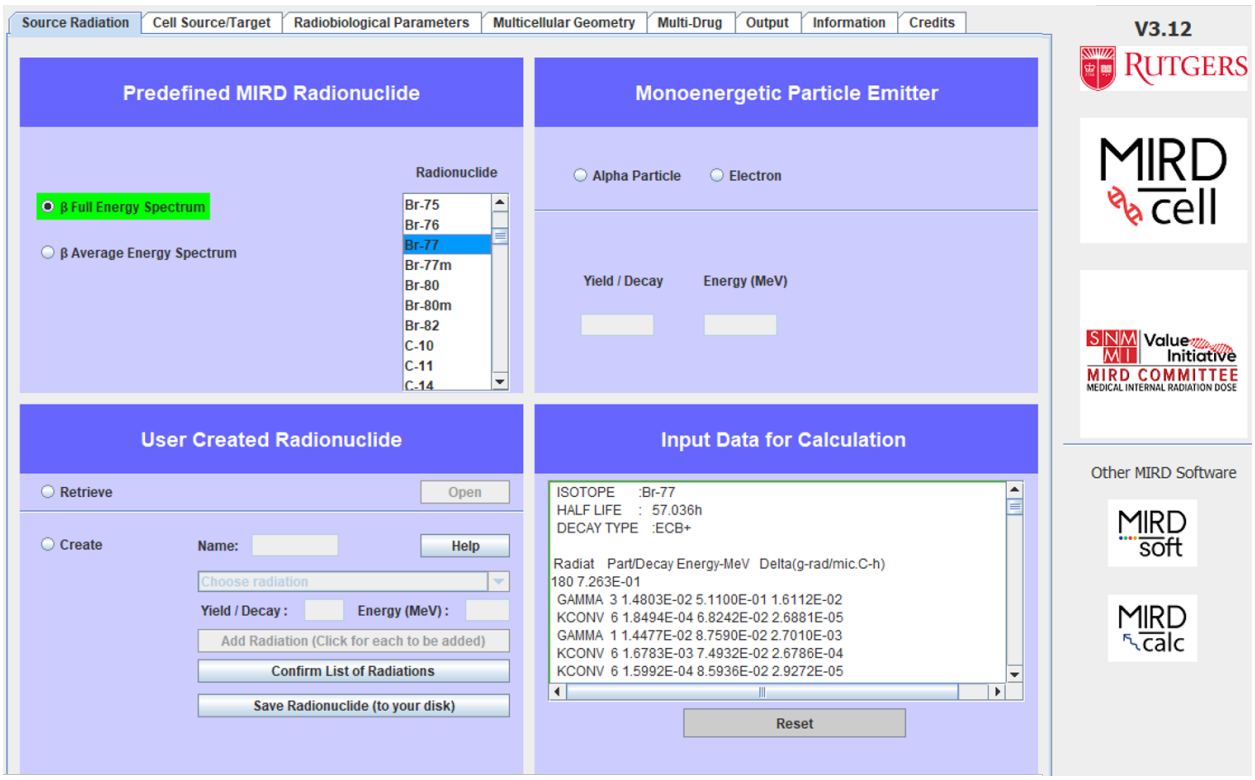

Figure 4.1: Radiation source tab allows the user to choose the radionuclide and full or average β energy spectrum. The user can also choose a monoenergetic particle emitter or manually enter radionuclide information. For predefined MIRD radionuclides, the input data for calculation is shown in the bottom left box.

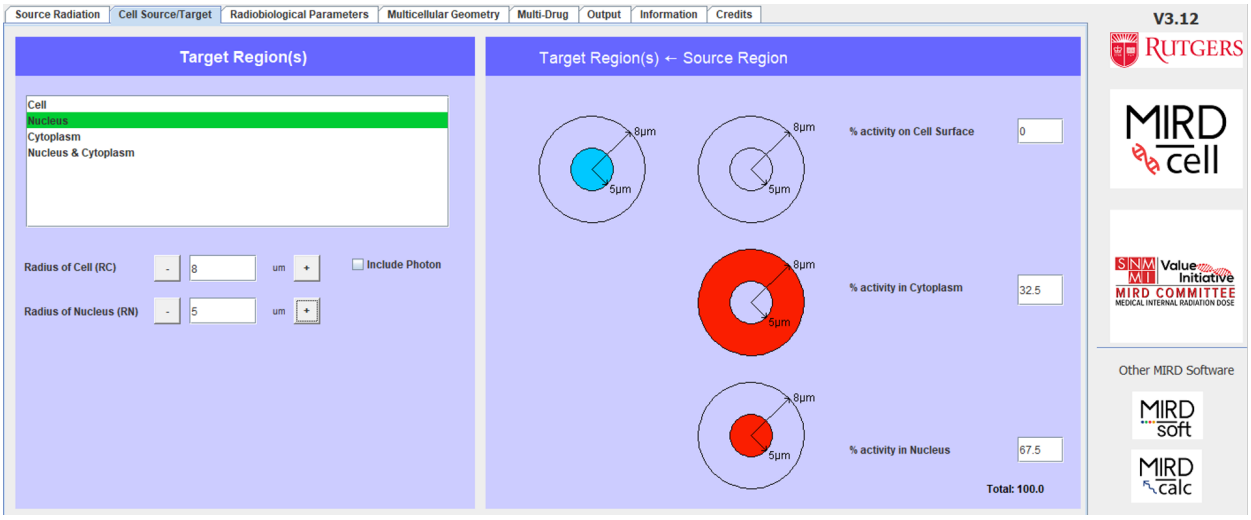

Figure 4.2: Defining the target regions for output calculations, the radius of the nucleus and cell and the radiopharmaceutical cellular distribution within the cell surface, cytoplasm or nucleus.

manually inputted using the following equation:

$$\tilde{a} = \frac{t_{1/2}}{ln2} \cdot (1 - e^{-ln2 \cdot t/t_{1/2}}) \qquad \text{(Eq. 4.1)}$$

where $t_{1/2}$ is the radionuclide half-life and t is the treatment time.

The labeling method drop-down allows the user to choose the labeling distribution between uniform, normal and log-normal distributions within the colony or plate. The user can also set the percentage of cells that are labeled. Like for the 1D configuration, the output will provide the tables for the S-values up to the input radius distance. Additionally, the mean absorbed dose to the selected target region is tabulated (Fig. 4.4). If the 'Nucleus and Cytoplasm' option is selected as the target region, the output will give the absorbed dose to both the nucleus and cytoplasm, as well as the self-dose and cross-dose separately. It can also separate the mean absorbed dose as given by particle type, e.g., β^+, internal conversion electron and MAe$^-$ when both the nucleus and cytoplasm are selected. If only the cell, nucleus or cytoplasm are selected, only the dose to the target region is given in the output[2].

[2]Although, if the Nucleus & Cytoplasm option is chosen as the target first and then cell, nucleus, or cytoplasm are chosen after, the mean absorbed dose by particle type will be reported. The software will have to be restarted in order for the output to not report those values.

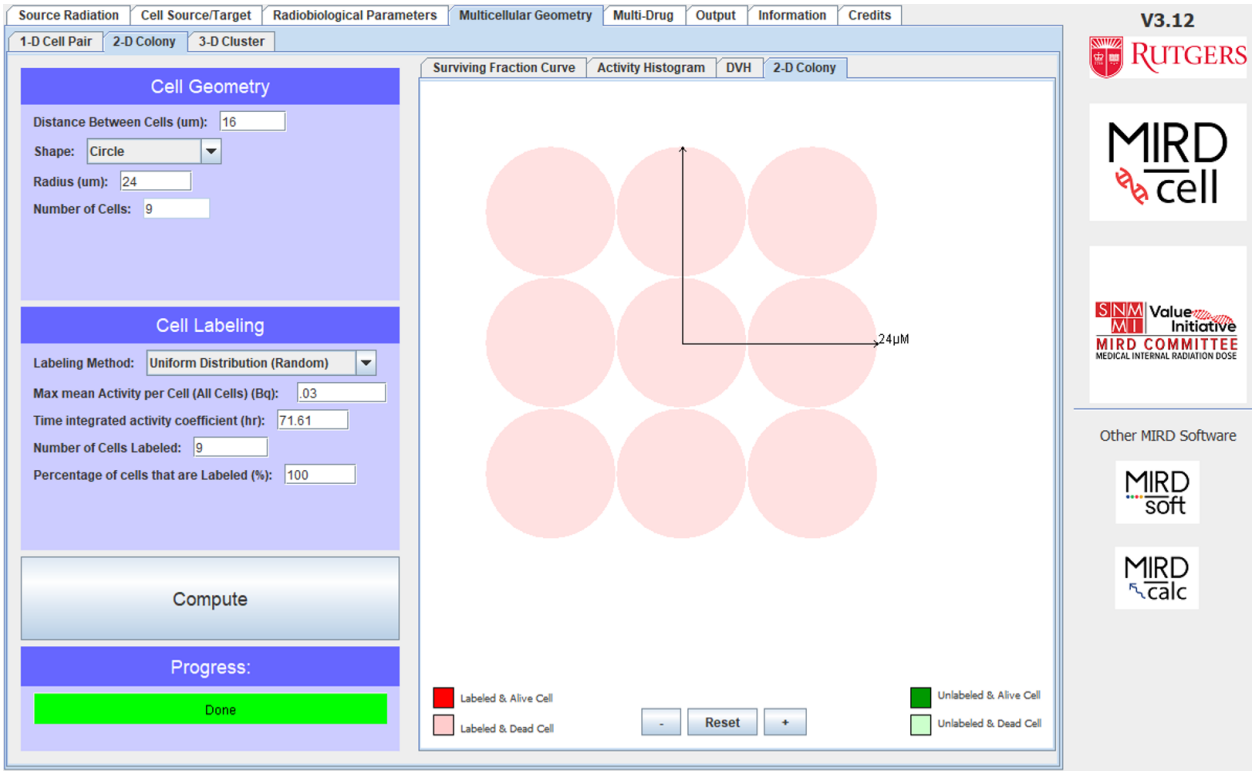

Figure 4.3: The cell labeling and multicellular geometry configuration for a 2D example.

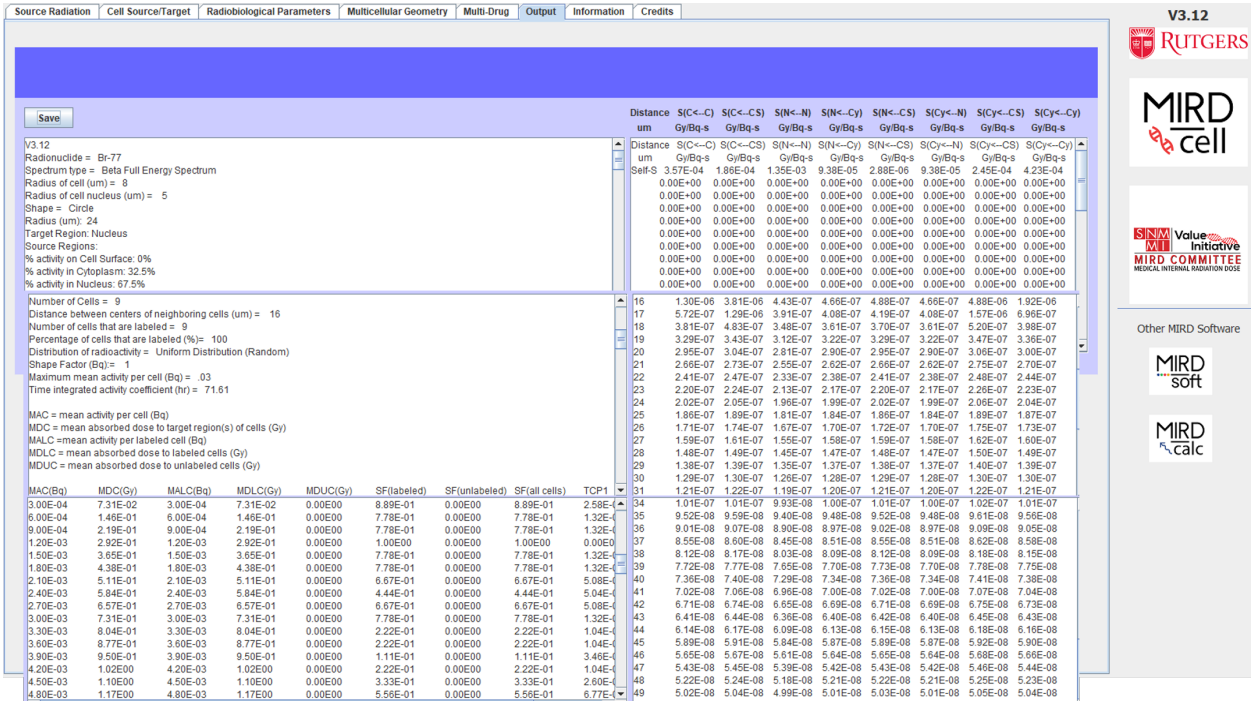

Figure 4.4: An example of the output given for a 2D configuration.

4.2 Cellular Characterization

Due to the short range of the MAe$^-$, characterization of the geometry of the individual cells and the neighboring cell configuration is important for accurate dosimetry calculations. The following section aims to characterize the cellular and nuclear sizes, cellular growth rate, and radiopharmaceutical cellular distribution of [^{77}Br]RD1 in ovarian cancer cell lines.

4.2.1 Methods

The ovarian cancer cell lines ID8, OVCAR8, OVCAR8 PARP1-KO, UWB1.289 and UWB1.289+BRCA1 were characterized. The cells were cultured and grown as described in Chapter 3.3.2. The cell doubling time (t) was measured for ID8 in a 96-well plate. The doubling times for OVCAR8, UWB1.289 and UWB1.289+BRCA1 were taken from the literature [136, 147]. The doubling time for OVCAR8 PARP1-KO was assumed to be the same as OVCAR8. Doubling times are summarized in Table 4.1. Colonies that grew approximately one radial layer adjacent to the cell in a square-grid were of interest in this work. The doubling times (t_2) were used to calculate the time it took for a cell to grow into colony sizes of 9, 25, 45, 69 and 145 cells using the following equation:

$$t = t_2 \cdot ln(N/N_0)/ln(2) \qquad \text{(Eq. 4.2)}$$

where N is the number of cells in the colony, and N_0 is the initial cell number. Timelines for the cell lines were then made spanning a time of 7 days, the treatment time for the cytotoxicity assays. For cell lines that did not reach a colony size of 145 cells by treatment day 7, the time it took them to reach confluency with a seeding of 200 cells (approximately 100,000 cells in a 96-well plate well) was calculated. If the cell line did not reach confluency, then the size of the colony at day 7 was calculated.

Table 4.1: Doubling time of ovarian cancer cell lines.

Ovarian Cancer Cell Line	Doubling Time (h)
ID8	12±2
OVCAR8	24±4
OVCAR8 PARP1-KO	24±4
UWB1.289	15
UWB1.289+BRCA1	20

4.2.1.1 Nuclear Staining

Cells were grown in a 35 mm diameter glass bottom culture dishes with a 14 mm microwell number 1.5 coverglass that was poly-d-lysine coated (MatTek, MA) at a seeding of 50,000 cells/plate for 24 hours in 2 mL of cell medium. The medium was then removed and the plate rinsed with 2 mL of phosphate buffered saline 1X (PBS, Corning). After removing PBS, 1 mL of 10% buffered formalin phosphate (Fisher Chemical) was added to the plate for 5 minutes, removed, and the plate rinsed with 2 mL of PBS. After removing PBS, 1 mL of 300 nM nuclear stain 4',6-diamidino-2-phenylindole (DAPI) was added to the plate for 5 minutes and then removed and rinsed with 2 mL of PBS. The cells were then imaged with a digital Keyence BZ-X810 microscope (Keyence Corporation, IL) at 40× magnification. Bright field images and fluorescent images were captured with a 40× objective lens (PlanApo NA = 0.95, WD = 0.25–0.17 mm) with the DAPI filter cube with an excitation wavelength of 360 nm (FWHM=40 nm), emission wavelength of 460 nm (FWHM=50 nm) and dichroic mirror wavelength of 400 nm. The average cell diameters were measured for 15 cells for all cell lines. If the cell was elliptic, the length and width were measured. This was repeated for measurements of the nucleus.

4.2.1.2 Radiopharmaceutical Cellular Distribution

A nuclear extraction kit (Chemicon, Cat. No. 2900) was used to isolate cytoplasmic and nuclear samples in both OVCAR8 and OVCAR8 PARP1-KO ovarian cancer cell lines. Plates were grown in tissue-culture treated T75 flasks (Corning) in triplicate for 24–48 hours to get 70–90% confluency. Cells were treated with 30–50 kBq/mL (0.02–5 nM) [^{77}Br]RD1 for 2 or 24 hours in the T75 flask

in a 7 mL volume. OVCAR8 PARP1-KO cells were treated with or without blocking dose (2 μM radioinert BrRD1) at the same time as dosing of the radiopharmaceutical. After dosing, the radioactive media was removed and plates were rinsed with 3 mL of ice-cold PBS for 10 seconds. The rinse was collected in a 20 mL scintillation vial (SCV) for gamma counting. A total of 5 mL of ice-cold PBS was added to the plates and scraped off the cells from the plate with a sterilized cell scraper (Nunc) and transferred them to a sterile centrifuge tube. The culture flask was rinsed with 3 mL of ice-cold PBS and added to the same vial as the cells in the centrifuge tube. The cells were then centrifuged (VWR International) at 250 relative centrifugal force (rcf) at room temperature.

The supernatant (SN1) was removed and collected in a new SCV and 800 μL of ice-cold PBS was added to the cell pellet and dispersed. This was transferred to a 5 mL centrifuge tube (Eppendorf AG) and placed in a 4ºC centrifuge (Beckman Coulter) at 200 rcf for 5 min. The supernatant (SN2) was collected in an Eppendorf tube and 70 μL of 1x cytoplasmic lysis buffer (CLB) (Chemicon) was used to disperse the pellet. This was chilled on ice for 15 min and then centrifuged at 4ºC at 200 rcf for 5 min. The supernatant (1st lysis) was collected in an Eppendorf tube and 50 μL of 1x CLB was added to the tube with the cell pellet. The cells were gently dispersed with a 1 mL syringe with a 26 gauge blunt needle, drawing and ejecting the contents 5 times, and then this was centrifuged at 8,000 rcf for 20 min at 4ºC. The supernatant, containing the cytosolic portion of the cell lysate, was transferred to a new Eppendorf tube.

The cell pellet was resuspended in 50 μL of ice-cold nuclear extraction buffer (NEB, Chemicon) containing 0.5 mM DTT and 1/1,000 protease inhibitor cocktail (PIC, Chemicon). A fresh syringe was used to disperse the pellet, drawing and ejecting the contents 5 times. It was then placed on an orbital shaker (Eppendorf) at 300 rpm on ice for 30 min followed by centrifugation at 16,000 rcf for 5 min at 4ºC. The supernatant, containing the nuclear extract, was placed in a new Eppendorf tube. The pellet, containing the nuclear membrane debris, was washed with 50 μL of PBS and transferred to a fresh Eppendorf tube. The empty Eppendorf tube that had contained the pellet was also saved.

All SCV and Eppendorf tubes were measured on the gamma counter (PerkinElmer) calibrated by HPGe as described in Chapter 3.3.1.6. The counts were converted to activity and measurements

were background and decay corrected to the time of dosing. Each plate had the activity from each fraction summed and the percent of each fraction was reported.

4.2.2 Results

4.2.2.1 Cell Characterization

The doubling time was used to calculate the time it took for colonies of various sizes to grow from a single cell. Those results are summarized in Figure 4.5 and were used to inform the plate geometry that should be used for dosimetry calculations.

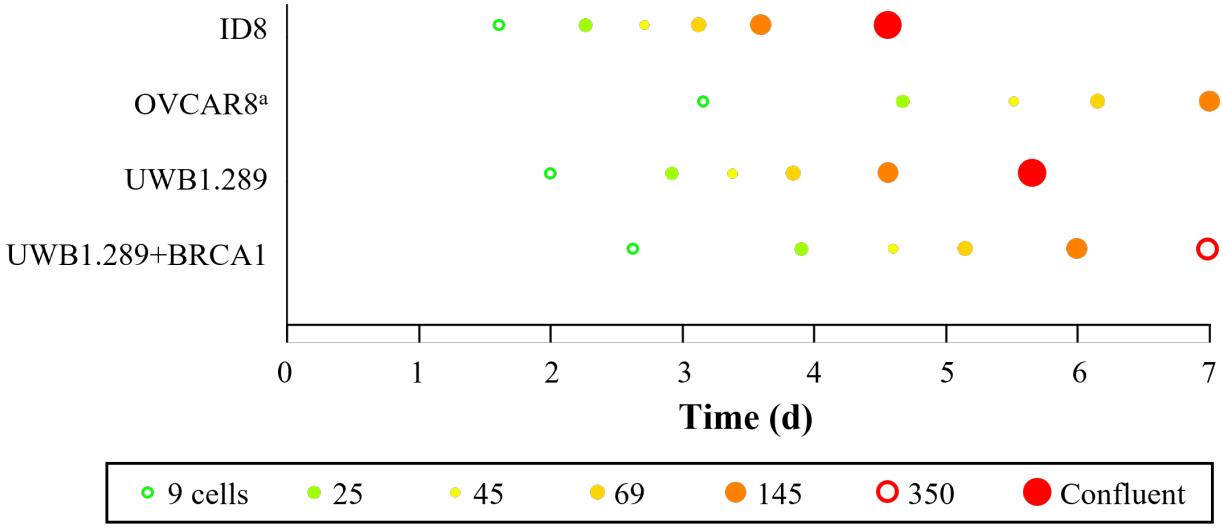

Figure 4.5: The time it takes a single cell from various cell lines with varying doubling times to create 9, 25, 45, 69 and 109 cell colonies is shown. Two cell lines reach confluency before a 7-day treatment time and are shown in solid red circles. UWB1.289+BRCA1 finishes a 7-day treatment time with approximately 350 cells in a colony. [a]OVCAR8 PARP1-KO is assumed to have the same doubling time as OVCAR8.

Figure 4.6 shows microscopy images of the various cancer cells with DAPI staining. Most cells were spherical, although both UWB1.289 lines presented ellipsoidal cells for approximately 15% of the population. Most nuclei appeared spherical. The radii of the cells and nuclei of each cell line are summarized in Table 4.2. These results informed the cellular geometry to be used for dosimetry calculations.

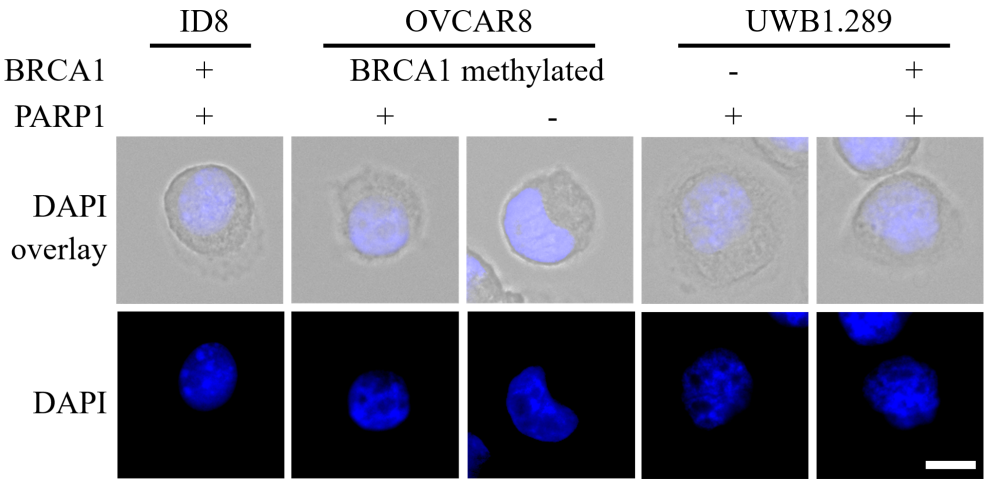

Figure 4.6: Fluorescence and bright field microscopic imaging of various ovarian cancer cell lines. Scale bar: 10 µm (×40).

Table 4.2: Cell and nuclear radii of various ovarian cancer cells.

Ovarian Cancer Cell Line	**Cell Radius (µm)**	**Nucleus Radius (µm)**
ID8	9±2	5±1
OVCAR8	10±2	5±1
OVCAR8 PARP1-KO	8±1	5±1
UWB1.289	12±2	6±1
UWB1.289+BRCA1	12±3	6±1
Total	10±2	5±1

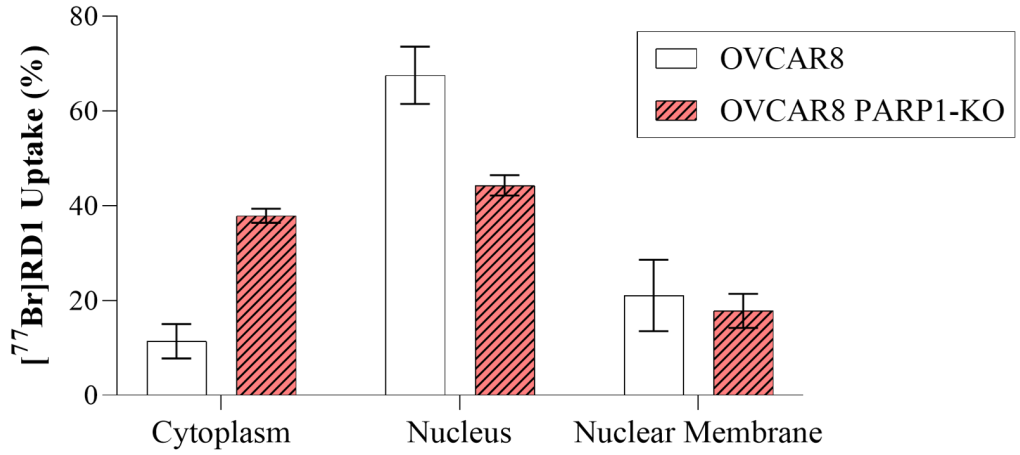

Figure 4.7: [^{77}Br]RD1 cellular uptake for OVCAR8 (n=6) and OVCAR8 PARP1-KO (n=3) cell lines. Uptake in ID8 and both UWB1.289 lines were assumed to have the same radiopharmaceutical distribution as the OVCAR8 cell line.

Table 4.3: [^{77}Br]RD1 cellular uptake for PARP expressing cell lines, PARP1(+) (n=6) and PARP1-KO, PARP1(-) (n=3) cell lines.

Fraction	PARP1 (+)	PARP1 (-)
Cytoplasm	11.4±3.6%	37.9±1.5%
Nucleus	67.5±6.0%	44.3±2.1%
Nuclear Membrane	21.1±7.5%	17.8±3.6%

4.2.2.2 Radiopharmaceutical Nuclear Distribution

All fraction contributions are summarized in the Appendix B.2. The amount of time the cells were in contact with the radiopharmaceutical (2 h or 24 h) did not significantly alter the amount of radiopharmaceutical found in any of the collected fractions (Appx. Fig. B.2A), so all measurements with OVCAR8 were used for cellular distribution calculations. Furthermore, for dosimetry calculations, the cytosolic fraction, nuclear fraction and nuclear membrane were the fractions of interest. Those fractions were summed, and the cellular fractional contribution calculated for OVCAR8 (n=6) and OVCAR8 PARP1-KO (n=3). Those results are summarized in Figure 4.7 and then in Table 4.3 as PARP1(+) and PARP1(-) cells.

4.3 Cellular Dosimetry

4.3.1 Methods

4.3.1.1 Cellular Geometry

For MIRDcell calculations, choosing the right geometry was important to get an accurate dose calculation. For cytotoxicity experiments, 200 cells per well were placed in a 96-well plate 2 h before exposure to [^{77}Br]RD1 for seven days. The number of 200 cells per well was chosen because it represented the minimum count of cells that could be consistently replicated in each well (Fig. Ch3Fig:ID8doublingGraph, Section 3.5.3). At higher seeding densities, confluency would be reached much faster than 7 days. Untreated cells were used to normalize cell survival data and if they have been in confluence for a significant portion of the treatment, it may not provide an accurate normalization for treated cells.

The initial state of the culture plate, i.e., 200 cells in a 3.2 mm radius well, assumed to be evenly spaced apart[3] with a distance of 400 μm between cells, will be called the reference geometry. These cells can then be assumed to adhere to the bottom of the well, at which point they will behave as single colonies. From the colony growth timeline summarized in Figure 4.5, it is seen that the intercellular geometry in the well is changing with time. The timeline summarizes healthy cells with their normal doubling time. However, when a toxic radiopharmaceutical is added, the growth rate is going to change, and that rate will change depending on the amount of radiopharmaceutical present in the well.

This work aims to compare the dose calculated in our reference geometry and the dose to colonies of various sizes, summarized in Figure 4.8. The dose was also calculated when the 3.2 mm radius well was filled tightly on a square grid with cells, i.e., the confluent case. Since the ovarian cancer cells had different sizes, the dose was also measured for cells of different cell and nucleus sizes. Additionally, two different activity cellular activity distributions were measured in different

[3] Although this is the assumption made for calculation purposes, when looking at cells through the microscope, one can find that the cells like to clump together, often in groups of 2–5 cells.

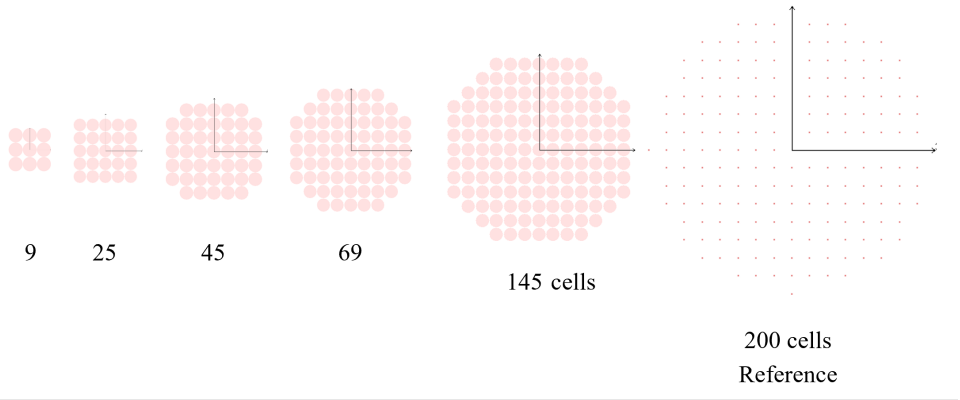

Figure 4.8: Examples of multicellular geometry configurations in 2D, with the first 5 examples showing an increase in the colony size for a spherical colony. The last example shows 200 cells with 400 μm distance between cells in a 3.2 mm radius area like that in a 96-well plate well. Images were taken from MIRDcell v3.12 and are not to scale.

cell lines with the nuclear extraction kit. Since MIRDcell does not have a nuclear membrane region, the activity measured in the nuclear membrane fraction was assumed to be activity in the cytoplasm. The activity distribution in the cytoplasm and nucleus were assumed to be uniform. From the measurements, the assumed activity distribution was 67.5% and 32.5% in the nucleus and cytoplasm, respectively, for PARP1(+) cell lines and 44.3% and 55.7% in the nucleus and cytoplasm, respectively, for PARP1(-) cell lines. These distributions are summarized in Figure 4.9B-C.

4.3.1.2 MIRDCell Calculations and Validation

MIRDcell v3.12 was used for dose calculations for MAe^{-} emitters ^{77}Br and ^{80m}Br and positron emitter ^{76}Br. The full β energy spectrum was selected for calculations. The geometries summarized in Section 4.3.1.1 were employed for calculations. The PARP1(+) cellular activity distribution was used when calculating the dose by particle type. Both PARP1(+) and PARP1(-) cellular activity distribution were used when calculating the dose to the nucleus. The time integrated activity coefficient used for each radionuclide was 71.61, 6.378 and 23.33 h for ^{77}Br, ^{80m}Br and ^{76}Br, respectively, to match the 7-day contact period for the viability assay in Chapter 3.

The dose delivered to the cytoplasm and nucleus by particle type were calculated for the confluent case and the reference case for the 8 μm and 12 μm cell radii cells (the two extreme

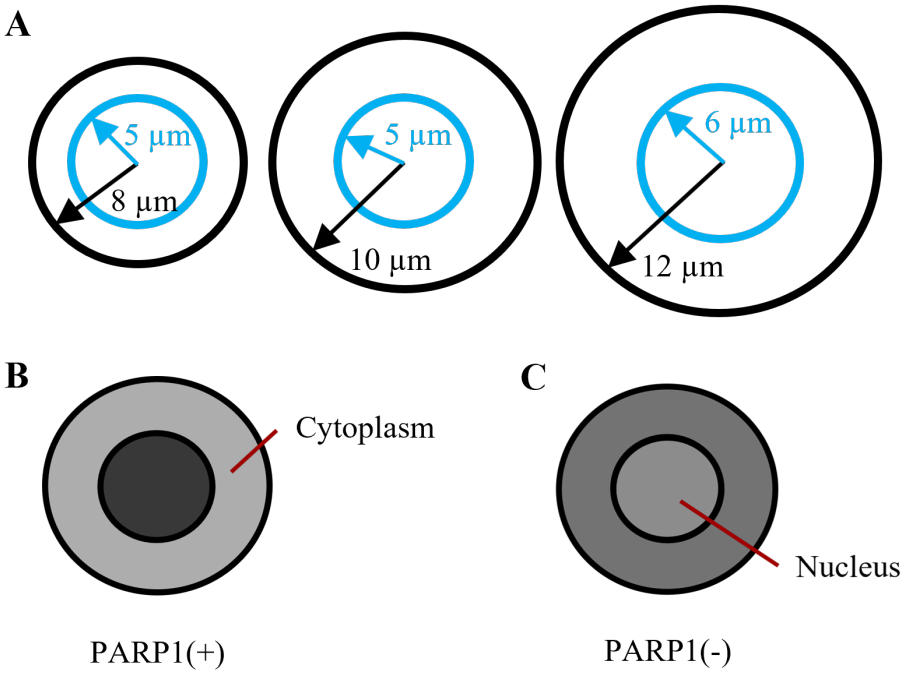

Figure 4.9: (**A**) The cellular dimensions used for nuclear dose calculations. Two activity distributions were used for calculations, (**B**) a uniform activity distribution of 67.5% and 32.5% in the nucleus and cytoplasm, respectively, and (**C**) 44.3% and 55.7% in the nucleus and cytoplasm, respectively.

cellular size and plate geometries), and all four measurements were averaged. The self-dose and the cross-dose to the nucleus and cytoplasm were calculated for the confluent and 9-cell colony size for the 8 μm and 12 μm cell radii cells, and averaged[4]. The dose contribution by particle type and cross- vs. self-dose were plotted.

The nuclear dose for cells of size 8, 10 and 12 μm cell radii were calculated for colony sizes of 9-, 25-, 45-, 69-, 109-, 145-cells and the confluent and reference geometries. The doses were compared to the reference geometry and the differences were calculated for intracellular activity distributions measured from PARP1(+) (62.5% activity in the nucleus and 37.5% in the cytoplasm) and PARP1(-) (44.3% activity in the nucleus and 55.7% in the cytoplasm) cells.

Nuclear dose was calculated assuming a 100% nuclear activity distribution, a 100% cytoplasmic activity distribution, and 44.3% nuclear activity distribution (the PARP1(-) case) and normalized to the nuclear dose assuming a 62.5% nuclear activity distribution (the PARP1(+) case). These calculations were repeated for the three cell sizes and with 9-cell and 145-cell colony sizes and these values averaged.

4.3.1.3 In Vitro Dosimetry

The measured radius of the cell and nucleus for each cell line was used. The cellular distribution of [^{77}Br]RD1 was assumed to be the distribution measured from the nuclear distribution assay described in Section 4.2.1.2. The number of neighboring cells to calculate the cross-dose was estimated as the colony size at approximately 4 days, rounding down to the nearest full-ringed colony number. The assumptions for each cell line are summarized in Table 4.4.

The nuclear dose was calculated by MIRDcell for activity uptake between 3×10^{-4} – 3.0 Bq/cell. These values were plotted on GraphPad Prism v9.3.1 and a simple linear regression model was calculated. The viability assay results (Chapter 3.4.5.3) were then converted from specific uptake to dose for all radiobromide isotopes. The data were fitted with a nonlinear regression sigmoidal dose-response curve to calculate the D_{50} in terms of absorbed dose. The D_{50} and 95% CI were

[4]The reference case calculated zero cross-dose, presumably because the nearest neighbors were 400 μm away.

Table 4.4: The assumptions used for calculations converting activity distribution to dose of various ovarian cancer cell lines.

Ovarian Cancer Cell Line	R_C (µm)	R_N (µm)	Colony Size	Nuclear Distribution (%)
ID8	10	5	145	62.5
OVCAR8	10	5	9	62.5
OVCAR8 PARP1-KO	8	5	9	44.3
UWB1.289	12	6	69	62.5
UWB1.289+BRCA1	12	6	25	62.5

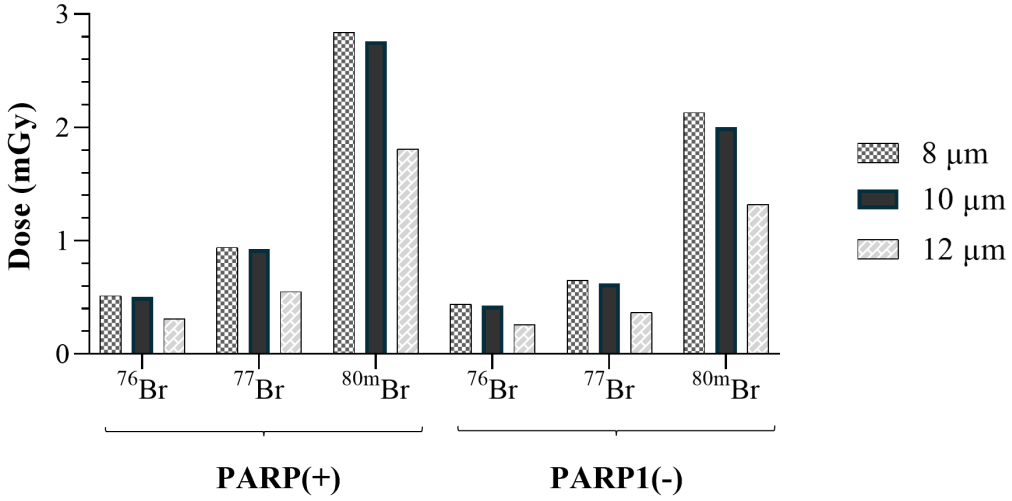

Figure 4.10: Nuclear self-dose calculations of various cell sizes for cellular activity distributions corresponding to PARP1(+) and PARP1(-) expression.

calculated and compared to D_{50} values obtained from EBRT studies (Chapter 3.4.5.2). The EBRT D_{50} was divided by the [^{77}Br]RD1 D_{50} to calculate the relative biological effectiveness (RBE).

4.3.2 Results

4.3.2.1 Cellular Dosimetry and MIRDcell Validation

The nuclear self-dose was calculated for 3 cell sizes with PARP1(+) and PARP1(-) activity distributions. Those results are summarized in Figure 4.10. Comparing the results for the cell radii of 8 and 12 µm to the 10 µm radius gave an increased dose of 1.8–6.5% and a decreased dose of 34–41%, respectively. The dose to the cytoplasm and nucleus from the MAe$^-$, internal conversion

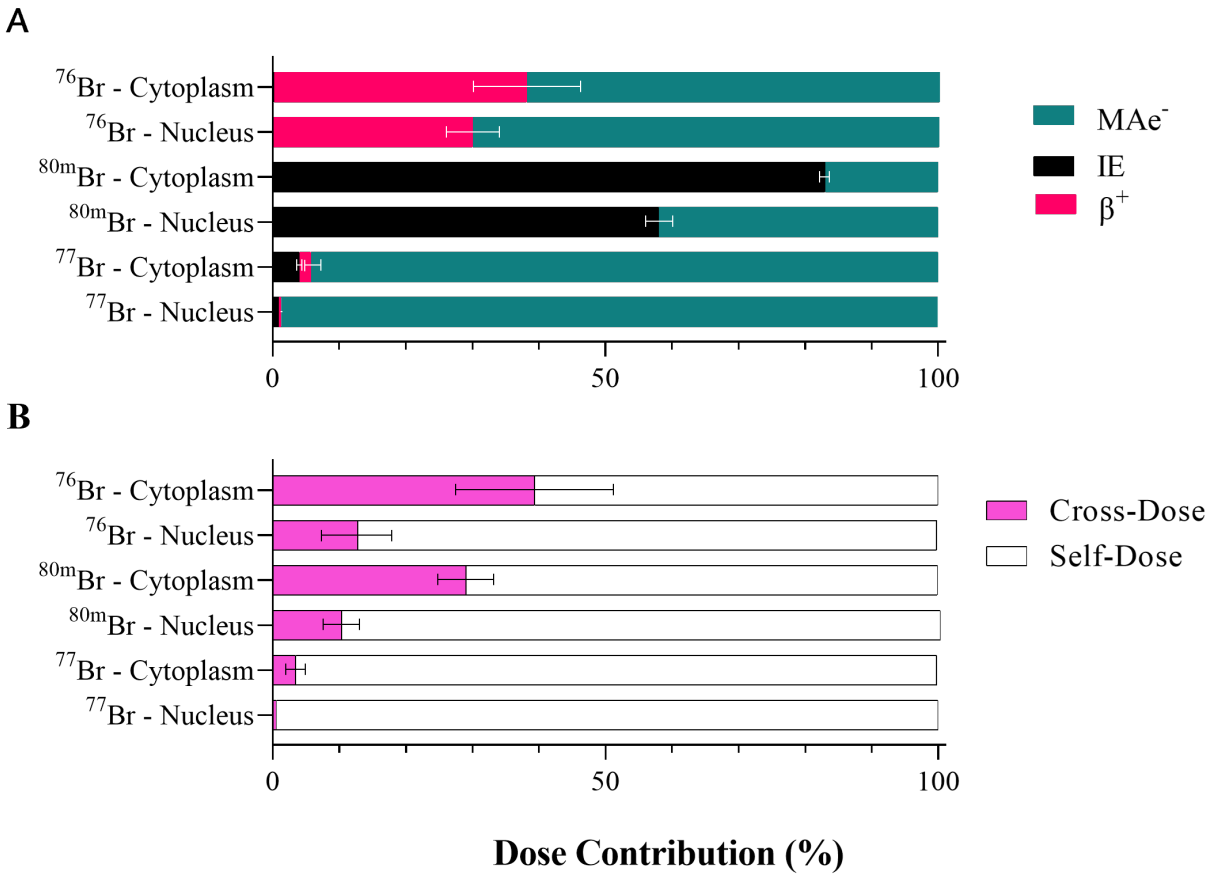

Figure 4.11: The dose to the cytoplasm or nucleus from radiobromine as a percentage of (**A**) particle type contribution and (**B**) self- or cross-dose contribution averaged from a 9-cell colony and confluent 96-well plate for cell with radii sizes of 8, 10 and 12 μm. IE: internal conversion electron.

electrons (IE) and β^+ particles for various radiobromide isotopes are summarized in Figure 4.11A. The dose to the cytoplasm and nucleus from cross- or self-dose from the various radiobromides is summarized in Figure 4.11B.

The dose difference between the reference geometry and a 9-, 25-, 145-cell colony and a confluent well for cell radii of 8, 10 and 12 μm for various radiobromide isotopes is summarized in Figure 4.12 for the two cellular distributions—PARP1(+) with 62.5% uptake in the nucleus, and PARP1(-) with 44.3% uptake in the nucleus. The comparison of the nuclear dose resulting from different cellular activity distributions normalized to the PARP1(+) activity distribution are summarized in Table 4.5.

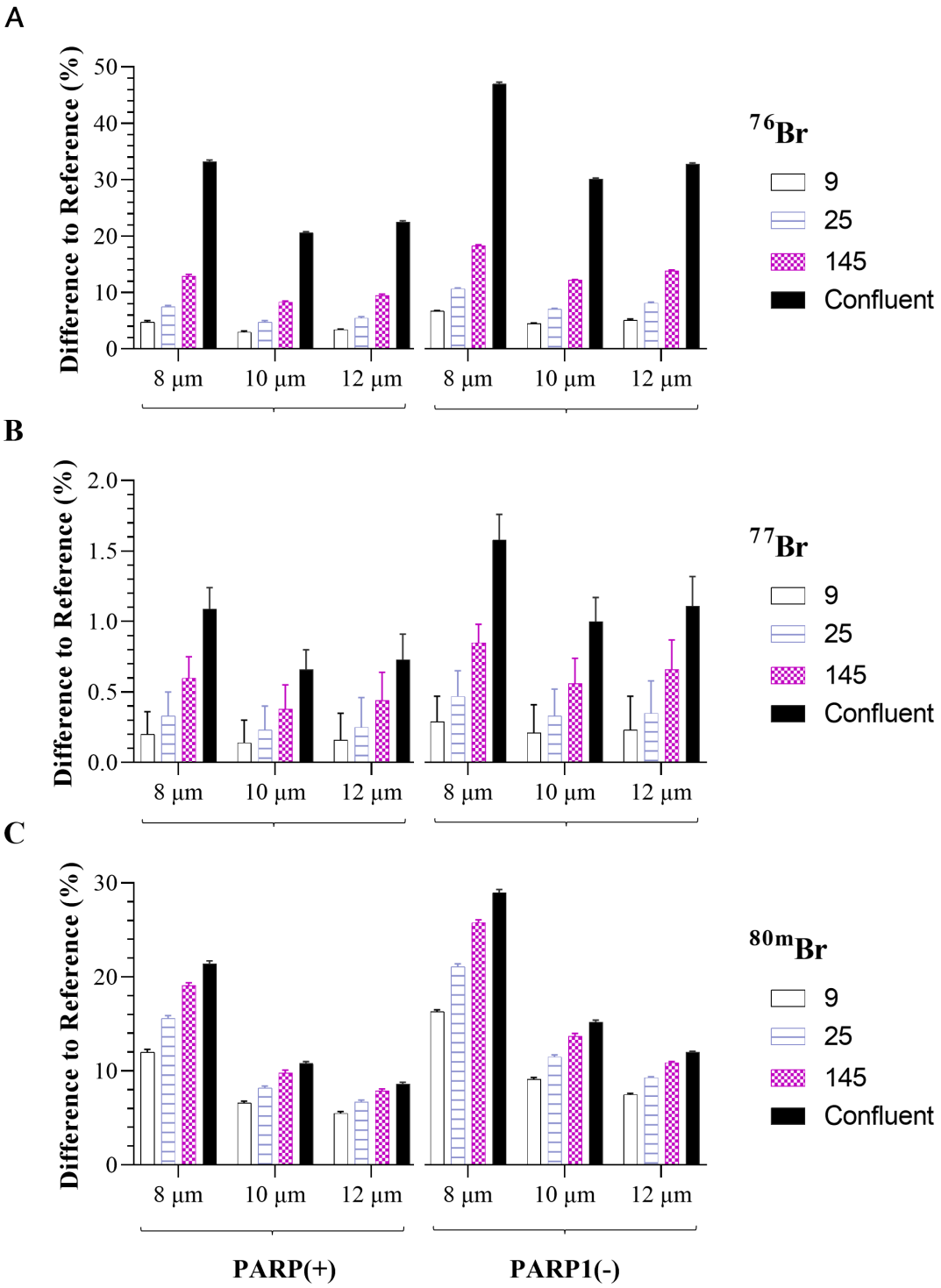

Figure 4.12: A comparison of the calculated nucleus dose between the reference (no adjacent cells) and either a 9-, 25-, 145-cell colony or a confluent 96-well plate well for (**A**) ^{76}Br, (**B**) ^{77}Br and (**C**) ^{80m}Br. Differences for cellular dose distributions corresponding to PARP1(+) and PARP1(-) are summarized.

Table 4.5: A comparison of the nuclear self-dose for various cellular activity distributions normalized to the nuclear self-dose from PARP1(+) cellular activity distribution.

Isotope	Nucleus	Cytoplasm	PARP1(-)
^{76}Br	1.40±0.02	0.17±0.05	0.72±0.02
^{77}Br	1.45±0.02	0.06±0.03	0.68±0.01
^{80m}Br	1.33±0.04	0.32±0.08	0.77±0.03

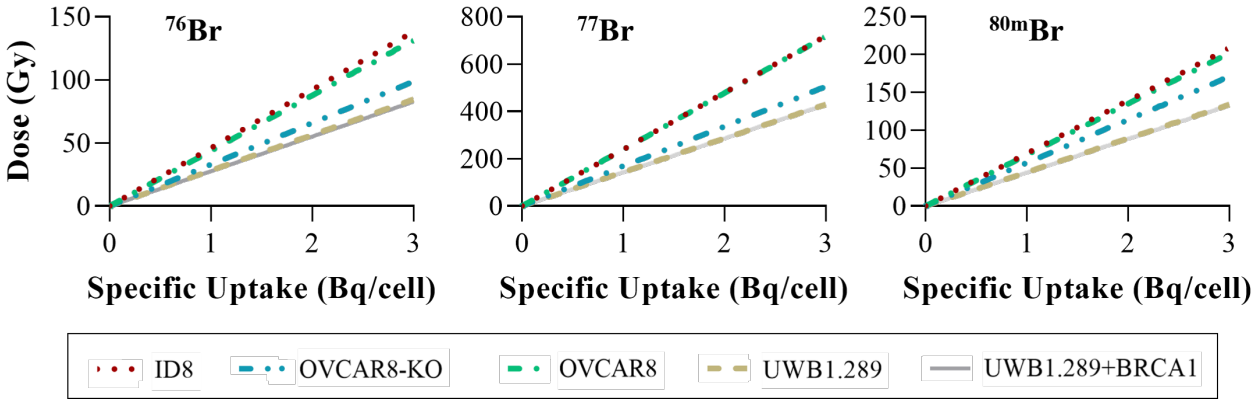

Figure 4.13: Nuclear dose as a function of the specific uptake calculated from MIRDcell for various ovarian cancer cell lines for ^{76}Br, ^{77}Br, ^{80m}Br. The cell line labeled OVCAR8-KO is PARP1-KO.

4.3.2.2 In Vitro Dosimetry

The nuclear dose as a function of specific uptake was plotted for the various radiobromide isotopes, summarized in Figure 4.13. The viability assay results (Chapter 3.4.5.3) were converted from specific uptake to dose for all radiobromide isotopes. Those values are summarized in Fig. 4.14. The resulting D_{50} values were calculated and compared to the EBRT D_{50} values to get the RBE. Those values are summarized in Table 4.6.

Table 4.6: The D_{50} (Gy) nuclear doses measured from external beam radiotherapy (EBRT) and viability assay with [^{77}Br]RD1 and the relative biological effectiveness (RBE).

Ovarian Cancer Cell Line	EBRT D_{50}	[^{77}Br]RD1 D_{50}	[^{77}Br]RD1 RBE
ID8	7.2±1.3	9.2±1.0	0.78±0.17
OVCAR8	1.8±0.9	4.3±0.3	0.42±0.22
OVCAR8 PARP1-KO	1.4±0.2	3.4±0.6	0.41±0.09
UWB1.289	2.6±1.4	3.9±0.8	0.67±0.39
UWB1.289+BRCA1	1.7±0.4	3.3±0.4	0.52±0.13

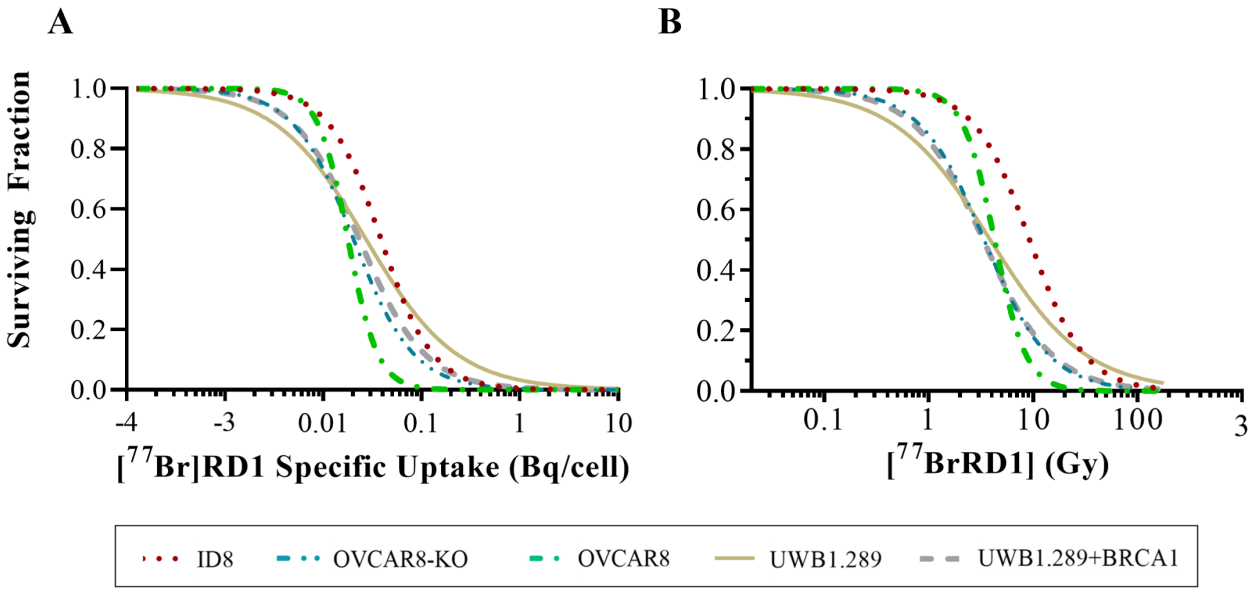

Figure 4.14: (**A**) Viability assays (Fig. 3.21D) conducted for several ovarian cancer cell lines, with cell survival plotted as a function of specific uptake (Bq/cell). (**B**) The specific uptake was converted to absorbed dose for ^{77}Br.

4.4 Discussion

While cellular size is relatively straightforward to characterize (Fig. 4.6, Table 4.2), it does significantly impact the dose to the nucleus with 12 µm cell radius cells seeing 39% lower nuclear self-dose compared with 8 µm radius cells (Fig. 4.10). It is the size of the nucleus and the cell that becomes a critical factor in determining the overall cytotoxicity of the radiopharmaceutical, with the self-dose dropping almost 50% between a 10 µm cell radius and a 12 µm cell radius when 62.5% of the activity is in the nucleus (Fig. 4.10) making the overall cellular response highly sensitive to variations in cell size and morphology.

The activity distribution is another critical variable to consider, particularly for ^{77}Br, where the dose to the nucleus is over 99% due to MAe^{-}, causing a greater than 99% self-dose contribution (Fig. 4.11). When the amount of radiopharmaceutical in the nucleus is decreased (e.g. 62.5% for PARP1(+) compared to 44.3% for PARP1(-)), dose to the nucleus decreases 32±1% (Fig. 4.10, Table 4.5). For ^{76}Br and ^{80m}Br, the nuclear dose decreases 28±2% and 23±3%, respectively. If the activity is 100% localized in the nucleus, for ^{76}Br, ^{77}Br and ^{80m}Br, the dose increases 40±2%,

45±2% and 33±4%, respectively. If the activity is located 100% in the cytoplasm, the nuclear dose decreases by a factor of 5.9, 16.7 and 3.1 for ^{76}Br, ^{77}Br and ^{80m}Br, respectively. As the nucleus is intimately related to cellular function and survival, this highlights the importance of accurately quantifying the dose delivered to this region. The extremely short range of the electrons emitted by ^{77}Br results in a high self-dose, as the electrons deposit most of their energy where they are directly distributed. Although modeling the neighboring cells was difficult due to the exponential growth of the cells directly opposed to the cytotoxicity of the radiopharmaceutical inhibiting or arresting cell reproduction, the neighboring cross-dose had less of an effect when compared to the activity distribution and cell geometry for ^{77}Br. Furthermore, the activity distribution was measured using a nuclear fractionation assay that required washing the cells between steps. From Chapter 3, it was evident that the radioligand binding was not irreversible, i.e., the radioligand could be washed out of the cells when the molar concentration of the media changed. Although it would be expected that the activity distribution would decrease with each progressive step, it can be assumed that the measured activity distribution may not be entirely accurate.

For ^{76}Br and ^{80m}Br, cross-dose played a much larger role due to the larger range of the β^+ and internal conversion electrons (IE) (4.12B,C). The contribution in dose from these particles to the nucleus was 30±8% and 58±2%, for ^{76}Br and ^{80m}Br, respectively (Fig. 4.11A). This causes an increase in the cross-dose contribution to the nucleus to 13±11% and 10±5%, for ^{76}Br and ^{80m}Br, respectively, compared to the less than 1% cross-dose contribution for ^{77}Br.

Quantifying the nuclear dose as a function of neighboring cells was done and the results are summarized in Figure 4.12, with ^{77}Br having at most an error 1.6±0.2% for all test cases compared to the reference geometry (200 cells each spaced 400 μm apart). From Figure 4.11, it is apparent the dose is localized to the location of the radiopharmaceutical, with cross-dose being minimal. For 145-cell colonies, the percent difference is 18±1% and 26±1% for ^{76}Br and ^{80m}Br, respectively. However, for the two cell lines ID8 and OVCAR8 with the same cell size but different colony sizes (145 vs 9 cells), the activity to dose conversion curves (Fig. 4.13) were virtually the same, indicating that the number of neighboring cells is not as influential as the cell and nucleus size and the activity

distribution.

Assuming the colony size variability causes virtually negligible differences in dose, when comparing UWB1-289 to ID8, which have two different cell and nucleus size nucleus, a difference in the nuclear dose as a function of specific uptake (Fig. 4.13 is observed. From these results, it can be concluded that the highest-impact variables are the activity distribution and the cell and nucleus size.

The *in vitro* viability experiments described in Chapter 3.3.4.1 were performed by plating 200 cells into a 6.4 mm diameter well of a 96-well plate. If the cells are assumed to be perfectly mixed in a single-cell suspension, this would result in 200 cells each resting 400 μm apart. At this distance, the cross-dose was calculated as virtually zero for ^{76}Br, ^{77}Br and ^{80m}Br. As these individual cells start to grow into individual colonies, the cross-dose contribution increases, especially for ^{76}Br and ^{80m}Br. Calculating the number of neighbors is difficult because as the radiation dose is being deposited into the cells over the course of multiple days after plating and dosing, the doubling time is dependent on the activity concentration. For a smaller activity concentration, the doubling time will be closer to the cell line's doubling time in optimal growing conditions. For higher activity concentrations, the doubling time approaches infinity due to cytotoxicity to the cells. For this reason, this work utilizes a colony size close to the half-way point for normal growing cells, knowing the difference from the reference geometry within this range is between 5–12% for ^{76}Br, 0.5–1.3% for ^{77}Br and 10–15% for ^{80m}Br. Assuming the reference geometry to be the actual geometry appears to be accurate at high concentrations. At low concentrations, assuming the actual geometry is similar to the growth at normal conditions appears to be accurate. Assuming a colony size similar to day 4 under normal growth conditions gives a geometry between the two extremes.

By converting the specific uptake to dose, the survival fractions can be plotted as a function of dose. Once the uptake-to-dose conversion factor is calculated, (Fig. 4.13), it can be applied to the [^{77}Br]RD1 cytotoxicity results discussed in Chapter 3.4.5.3, giving D_{50} values in terms of dose (Gy) (Table 4.6, column 3). The calculated D_{50} from the nonlinear regression fit can be compared to the EBRT D_{50} (Table 4.6, column 2) from Chapter 3.4.5.2. These gave RBE values between

0.41±0.09–0.78±0.17 (Table 4.6, column 4).

The D_{50} values ranged from 3.3±0.4 Gy to 9.2±1.0 Gy for all the cell lines for cells treated with [^{77}Br]RD1. Compared to cells treated with structurally analogous, MAe^{-}-emitting ^{125}I-KX1, these D_{50} values were 3.1, 2.7 and 1.7× larger for OVCAR8, OVCAR8 PARP1-KO and UWB1.289, respectively, and in agreement for UWB1.289+BRCA [93]. Comparing the D_{50} values reported by Riad et al [93] to the EBRT-measured D_{50} values in this work, the ^{125}I-KX1 RBEs were 1.3±0.6 for OVCAR8, 1.1±0.2 for OVCAR8 PARP1-KO, 1.1±0.6 for UWB1.238, and 0.5±0.1 for UWB1.238+BRCA1. In the work published by Lee et al., treatment with EBRT and ^{125}I-KX1 gave D_{50} values of 3.7 and 2.0 Gy, respectively, giving a RBE of 1.9 for the NLF neuroblastoma cell line.

The RBE is a measure of the effectiveness of one type of radiation compared with another type (often a standard, but which has to be specified) to produce the same outcome. In practice, the value for the RBE is often determined as the ratio of the doses for the two types of radiation resulting in the outcome. The RBE for a given type of radiation often varies with the outcome used for the evaluation. The cells were treated with [^{77}Br]RD1 over a relatively long amount of time, i.e., 7 days. This treatment time could play a role in the RBE being less than one. Having a long treatment time increases the time allowed for DNA repair processes, which thus requires more dose for the same biological effect. In comparison, the EBRT treatment was delivered in a single fraction in less than 3 minutes.

4.5 Conclusion

In this study, MIRDcell was utilized to calculate the dose to ovarian cancer cell lines taking into consideration their specific characteristics such as nuclear and cell size, activity cell distribution, and number of neighboring cells based on the cell's doubling time. The calculations were conducted using positron emitter ^{76}Br and MAe^{-} emitters ^{77}Br and ^{80m}Br. Doses as a function of specific uptake were obtained for each ovarian cell line, which were then used to convert activity uptake survival curves into dose survival curves. Although the calculated RBE was found to be less than one when compared with external beam, cellular dosimetry calculated showed minimal cross-dose

to the nucleus for activity distributed outside the nucleus. Further dosimetric studies are needed to investigate the toxicity in normal tissue of [^{77}Br]RD1.

CHAPTER 5
PET IMAGING POTENTIAL OF RADIOBROMINATED PARP1 INHIBITOR AND MURINE BIODISTRIBUTION STUDIES

This chapter summarizes *in vivo* imaging and murine/human dosimetry calculations with the radiobrominated PARP inhibitor [$^{76/77}$Br]RD1. This work utilizes PET imaging and *ex vivo* radioactivity biodistribution measurements to evaluate the *in vivo* pharmacokinetics of [^{76}Br]RD1 in mice. It attempts to perform PET imaging in murine models of ovarian cancer. The [^{76}Br]RD1 pharmacokinetic results were utilized in Monte Carlo simulations to estimate the organ-level dosimetry following [$^{76/77}$Br]RD1 administration in mice and humans.

5.1 Tumor Models

Murine tumor models are important for developing and investigating preclinical cancer therapies [148], but it is crucial to select the appropriate model for human care due to the limitations of animal models [149]. To effectively mimic human disease, the model must be carefully chosen. Xenograft models, where human cells are implanted into another species, allow for a model with human disease. However, for xenograft models to work in mice, they must be immunocompromised so they do not reject the cells. This may not allow for an effective model, as studies on immunocompromised mice may not give the same immune responses to the cancer or therapy.

Syngeneic models, unlike xenografts, are implanted with cells that match the host species and strain. In the case of mice, this means using murine cancer cells for tumor injection. Because the cancer is murine, the immunologically compatible material allows the use of immunocompetent mice. A major advantage in using this type of model is that with an intact immune system, the tumor environment can more closely replicate the tumor environment in an immunocompetent human [150]. Additionally, mice have a lower risk of infection compared to the immunocompromised mice. This allows for a model at a lower cost with high reproducibility, compared to the more expensive

immunocompromised mice necessary for human xenograft models. However, care must be taken in comparing murine cancer response in the syngeneic model compared to a model that uses human cancer cell lines. For our study, the use of a murine ovarian cancer cell line to show *in vivo* and *ex vivo* biodistribution was found to be appropriate.

Metastatic ovarian cancer presents in the peritoneal cavity [151]. Transported ovarian cancer cells can disseminate by the peritoneal fluid within the peritoneum and can be associated with ascites. Metastatic tumors can be found in the liver, lung parenchyma, pancreas, stomach, small intestine and large intestine [152]. Orthotopic models, or models that mimic the naturally occurring tumor growth environment, can be made by injecting ID8 murine ovarian cancer cells in the intraperitoneal (IP) cavity of C57BL6 mice [130, 153–155]. The IP injection would allow for the cells to disseminate in the peritoneal fluid, causing small, metastatic tumors. With metastatic ovarian cancer orthotopically located in the abdomen, imaging of metastatic tumors when drug clearance is done through the liver and intestines poses problems. With subcutaneous injections, the cancer cells can be injected in a controlled location, like the flank. These heterotopic models, or models that have the disease occurring in an abnormal place, can allow for easy observation of tumor progression and assurance of the tumor location in imaging studies before euthanizing the mouse.

In this work, a syngeneic strategy for ovarian cancer models was investigated, employing both a heterotopic and orthotopic model. The murine ID8 ovarian cancer cell line was gifted by Dr. Katherine Roby (University of Kansas, KS) [130], known to cause peritoneal tumors and ascites following IP injection [130, 153–155] and heterotopic tumor following subcutaneous injection [156–160]. Table 5.1 summarizes publications with orthotopic and heterotopic models with ID8 cells in female C57B6/J mice.

5.2 Positron Emission Tomography

Positron emission tomography (PET) utilizes β^+-emitting isotopes for imaging. The isotopes produce 511 keV photon pairs emitted in opposing directions when the positron annihilates with an electron. Detectors on opposing sides of a circular gamma-ray detection array collect these

Table 5.1: Procedure information for inoculation of ID8-based ovarian cancer cell lines in C57B6/J mice from literature. These studies informed the orthotopic and heterotopic inoculation scheduling in our study.

Orthotopic	**Cell Line**	**Inoculation Number**	**Volume (µL)**	**Endpoint**	**Ascites Progression**	**Tumor Growth**
Roby, *et al.* [130]	ID8	5×10^6	200	16 weeks	∼13–15	
Leinster, *et al.* [153]	ID8	1×10^7	300	∼12 weeks	6–8 weeks	
Chambers, *et al.* [154]	ID8-luc	5×10^6	300	8.5 weeks	3 weeks at	
	ID8-VEGF	5×10^6		8.5 weeks		
Chiriva-Internati, *et al.* [155]	ID8	1×10^5				17 weeks
		5×10^5				13 weeks
		1×10^6				8.5 weeks
		2×10^6		7–9 weeks	∼6 weeks	∼6 weeks
Heterotopic						
Zhang, *et al.*, [156]	ID8, GFP, VEGF/GFP	5×10^6	500		Flank	2 weeks
Jeanne, *et al.* [157]	ID8	5×10^6	300	4 weeks		
Su, *et al.* [158]	ID8	5×10^6		5 week	Flank	
Zhang, *et al.* [159]	ID8	1 or 5×10^6	100	3 weeks	Flank	
Janát-Amsbury, *et al.* [160]	ID8	5×10^6	500	5 weeks	Flank	

photons within a coincidence timing window to indicate that they are coming from the same positron annihilation event. The origin of this annihilation event is then localized along a line-of-response between the two detectors. Collecting millions of photons allows for the reconstruction of 3-dimensional images, using iterative reconstruction methods such as ordered-subset expectation maximization (OSEM) that can compensate for photon scatter [161].

The gold standard of PET imaging radionuclides is ^{18}F ($t_{1/2}$=1.8 h, 96.7% β^+). However, ^{76}Br ($t_{1/2}$=16.2 h, 55.6% β^+) has the potential for PET imaging capabilities as a chemically matched diagnostic to ^{77}Br therapeutics and a longer half-life to allow for imaging at later time points. ^{76}Br does have challenges related to the higher positron energy, shown in Table 5.2. This affects the positron range and thus the PET resolution [162], which is important to characterize. This is further addressed in the methods section.

The positron range is the distance between the point at which the isotope decays and the point at which the β^+ particle annihilates. The average positron range for ^{76}Br is 5.3 mm, compared to ^{18}F which has a maximum range of 2.3 mm. The positron range leads to partial volume (PV) and spillover effects that limit the resolution of PET scanners, which can be corrected with PV corrections [163].

5.3 RAPID and OLINDA Dosimetry Platforms

The Radiopharmaceutical Assessment Platform for Internal Dosimetry (RAPID) was developed at UW–Madison for patient-specific internal dosimetry calculations [165]. The software allows users to input serial PET/CT or SPECT/CT images after injection of a radiopharmaceutical to use for Monte Carlo dose calculations.

The PET/SPECT images are used for quantification of the activity distribution, and the CT images are used for the geometry to be used for Monte Carlo calculations. Contouring ROIs allows for organ- or tumor-specific calculations. To accurately calculate this, coregistration is an important step. PET/SPECT images are coregistered to their corresponding CT scans, and then eventually each scan will be coregistered over all time points to a chosen reference scan. All registrations occur

Table 5.2: Listed energies and their associated characteristics of β^+ particles emitted from ^{76}Br and ^{18}F for comparison [78, 105, 164].

^{76}Br

Avg Energy (keV)	End-point energy (keV)	Intensity (%)	Dose (MeV/Bq-s)	Range (mm)
146 *7*	337 *9*	0.03 *10*	4.4×10^5 *15*	0.26
166 *7*	385 *9*	0.04 *10*	6.6×10^5 *17*	0.32
207 *7*	482 *9*	0.13 *3*	0.00027 *6*	0.46
253 *7*	589 *9*	0.92 *11*	0.0023 *3*	0.64
336 *7*	781 *9*	1.44 *13*	0.0048 *4*	1.00
375 *7*	871 *9*	6.3 *6*	0.0236 *23*	1.18
427 *7*	990 *9*	5.2 *4*	0.0222 *17*	1.44
551 *7*	1271 *9*	1.24 *13*	0.0068 *7*	2.09
558 *7*	1285 *9*	0.2 *9*	0.0011 *5*	2.13
569 *7*	1310 *9*	0.3 *17*	0.0017 *10*	2.19
621 *7*	1426 *9*	0.35 *14*	0.0022 *9*	2.48
659 *7*	1512 *9*	0.5 *5*	0.003 *3*	2.69
797 *7*	1814 *9*	0.05 *5*	0.0004 *4*	3.49
953 *7*	2153 *9*	1 *4*	0.01 *4*	4.41
1022 *7*	2252 *9*	0.4 *4*	0.004 *4*	4.81
1221 *7*	2725 *9*	2.8 *13*	0.034 *16*	5.98
1265 *7*	2819 *9*	2.1 *7*	0.027 *9*	6.24
1532 *8*	3382 *9*	25.8 *19*	0.4 *3*	7.76
1800 *8*	3941 *9*	6 *10*	0.108 *18*	9.22
^{18}F				
249.8 *3*	633.5 *6*	96.73 *4*	0.2416 *3*	0.62

through affine transformation over 12-degrees of freedom, including 3 rotational, 3 translational, 3 scaling and 3 shearing, with the temporal coregistrations occurring to the reference CT using the CT scans. For cases with severe setup variations between scans, locally applied affine coregistration using the manually drawn ROIs can be used instead.

The PET/SPECT and CT pair are then used for Monte Carlo dose calculations performed with Geant4 v9.6 [166]. The Monte Carlo dose calculations were performed using the slice parallelization method, in which the dose deposition is calculated over a slice instead of a whole 3D volume [165]. The CT scan defines the material composition and mass density using the Hounsfield units (HU). The PET/SPECT images are used to define the activity for each voxel. The dose rate is modeled using a piecewise linear trapezoidal fit until the last time point, which is then modeled by exponential decay.

If a therapeutic radionuclide does not match the imaging radionuclide, the measured activity in the images with the imaging radionuclide is converted to the therapeutic radionuclide assuming the same injection activity. The RAPID software will account for the differences in the half life of the two radionuclides. The cumulated activity is established through the time-integrated activity distribution and sampled uniformly in each voxel. A single absorbed dose distribution is modeled using the G4RadioactiveDecay module [167] which uses decay information from the ENSDF database [168]. The output provides organ absorbed doses calculated in units of Gy/MBq of activity administered.

OLINDA (Organ Level INternal Dose Assessment) is another software platform used for estimating the internal radiation dose to organs and tissues resulting from the administration of radiopharmaceuticals. OLINDA utilizes reference phantoms to represent the human body and its organs [169]. The software uses data on the physical properties of radiopharmaceuticals and their biological distribution in the body to simulate the radiation transport and energy deposition in the organs and tissues of interest [126].

OLINDA allows users to input information such as patient characteristics, administered activity of radiopharmaceuticals, and imaging or measurement data, to estimate the absorbed dose in organs

and tissues. It also gives organ-level and whole body equivalent doses and effective doses in Sv/MBq. The software has been validated and is widely accepted in the field of nuclear medicine for its accuracy and reliability in estimating the absorbed dose in patients.

5.4 Methods

5.4.1 Radiopharmaceutical Production

Bromine-76 was produced by proton irradiation of enriched $Co^{76}Se$ according to published methods [116] and summarized in Chapter 3.3.1. For *in vivo* studies, ^{76}Br was produced by the UW–Madison GE PETtrace cyclotron irradiating $Co^{76}Se$ on niobium backings (35–40 μA, 12.5 MeV protons) for 1–2 hours. The radiobromine was collected via thermal chromatographic distillation and the contents trapped and released on a pre-equilibrated QMA light cartridge as described in Chapter 3.3.1. [^{76}Br]RD1 was synthesized via copper-mediated radiobromodeborylation chemistry according to published procedures [138] and outlined in Chapter 3.3.1.2. Radioactivity was measured using Capintec CRC 15R (Pittsburgh, PA) with a setting of #690÷2. Injections of [^{76}Br]RD1 on aHPLC were used to measure the molar concentration as described in Chapter 3.3.1.3.

5.4.2 Radiobromine PET Calibration

The Inveon microPET scanner (Siemens Medical Solutions) was calibrated with a flood-type phantom that was approximately 6 cm in diameter with 8 cm length. The phantom was filled with 500 mL of [^{76}Br]RD1 in water at an activity concentration of $(1.42\pm0.06)\times10^5$ Bq/mL and scanned for 16 hours within an energy window of 350–650 keV and a timing window of 3.432 ns. This energy and timing window were used for all subsequent images taken with ^{76}Br. Images were reconstructed with ordered-subset expectation maximization of 3 dimensions, followed by the maximum a posteriori algorithm [170] and attenuation correction applied. A normalization image and header file were produced and used for future scans with the ^{76}Br isotope.

Bromine-76 PET images were acquired with two different Derenzo pattern phantoms (Phantech, WI) with hole sizes between 1.0–1.5 mm with 0.1 mm increments and 1.6–2.6 mm with 0.2 mm

increments. Static PET scans were taken of the phantoms filled with 7.1 MBq/mL [^{76}Br]RD1 in aqueous solution for 500 million counts.

Partial volume (PV) effects, in which the finite spatial resolution of an imaging system causes the loss of activity signal in small objects, were measured for the microPET with a PVC27 phantom (Phantech, WI). PV corrections can be applied to correct for PV effects by measuring the signal loss in known objects of varying sizes. The PVC27 phantom has seven spheres with varying diameters interconnected between 2.5–12 mm and was filled with [^{76}Br]RD1 at an activity concentration of $(1.42\pm0.06)\times10^5$ Bq/mL. A static PET scan was acquired on an Inveon microPET scanner for 80 million counts. Images were reconstructed with OSEM of 3 dimensions, followed by the maximum a posteriori algorithm. PET/CT images were manually coregistered and analyzed using Inveon Research Workplace 4.2 (Siemens Medical Solutions). A region of interest (ROI) the same volume as the corresponding sphere was used to measure the PET signal in each sphere. An ROI with a diameter of 9 mm was placed inside the 12 mm diameter sphere and used as the 100% signal measurement. The signal measurement of each sphere was then normalized to the 100% signal measurement to get the recovery coefficient (RC).

5.4.3 Animal Cancer Cell Inoculation

All animal studies were approved by the Institutional Animal Care and Use Committee at University of Wisconsin–Madison. A total of 18 adult female C57BL/6 mice (Jackson Laboratory, ME) acquired in 3 cohorts at various ages were used for *in vivo* and *ex vivo* studies. Figure 5.1 summarizes the study design for the cohorts of mice. For the first cohort, four mice aged 12 weeks were used as the control group. They received no ID8 cell inoculation. PET/CT imaging and biodistribution studies were performed with [^{76}Br]RD1.

Murine ID8 ovarian cancer cells were maintained in Dulbecco's modified Eagle's medium supplemented with 5% fetal bovine serum (FBS, Corning), 1% penicillin-streptomycin (Corning) and 0.2% 500X insulin-transferrin-selenium (ITS) supplement (Biowhittiker) in a 5% CO_2 atmosphere at 37°C, as described in Chapter 3.3.2.1.

Four mice aged 13 weeks received a subcutaneous (SQ) injection of $(4.3\pm1.1)\times10^6$ ID8 cells in 120 µL of 1:1 PBS:Matrigel (BD Biosciences) in the lower right flank for a heterotopic tumor model of murine ovarian cancer. Tumor or mass growth in the heterotopic models was monitored once a week by caliper measurement of the mass length and width. The volume was calculated using equation Eq. 5.1:

$$V = \frac{1}{2}(l \cdot w^2), \tag{Eq. 5.1}$$

where l is the maximum length and w is the width perpendicular to the length. At 6 weeks post-SQ injection, imaging and biodistribution studies were performed with [^{76}Br]RD1. An assumed skin thickness of 0.5 mm [171] was subtracted from the caliper measurements before calculating the volume.

Ten mice aged 7 weeks received an intraperitoneal (IP) injection of $(3.0\pm0.6)\times10^6$ ID8 cells in 250 µL of PBS for an orthotopic model of murine metastatic ovarian cancer. The orthotopic models had their mass monitored weekly after 4 weeks post-injection and were observed for development of ascites. They were also imaged every 2–4 weeks with transabdominal ultrasound (TAUS) starting at 4 weeks post-injection. At 12 weeks post injection (p.i.), imaging and biodistribution studies were performed with [^{76}Br]RD1 on the 8 mice with the highest tumor burden as demonstrated on TAUS.

5.4.4 Imaging

5.4.4.1 Ultrasound

Starting at 4 weeks post-injection of ID8 ovarian cancer cells, orthotopically diseased mice were monitored for disease progression and tumor staging with transabdominal ultrasound (TAUS) on the Vevo 2100-LAZR PA-ultrasonic imaging system (FUJIFILM VisualSonics, Inc., Toronto, CA). TAUS was performed every 2–4 weeks, depending on observed disease progression until the study endpoint at 81 days p.i. of cancer cells. The TAUS imaging timeline is shown in Figure 5.2.

Mice were placed in an induction chamber with 3–5% isoflurane at 1–2 L/min of oxygen. Abdomen hair was shaved and removed with depilatory cream (Nair, Church & Dwight Co.,

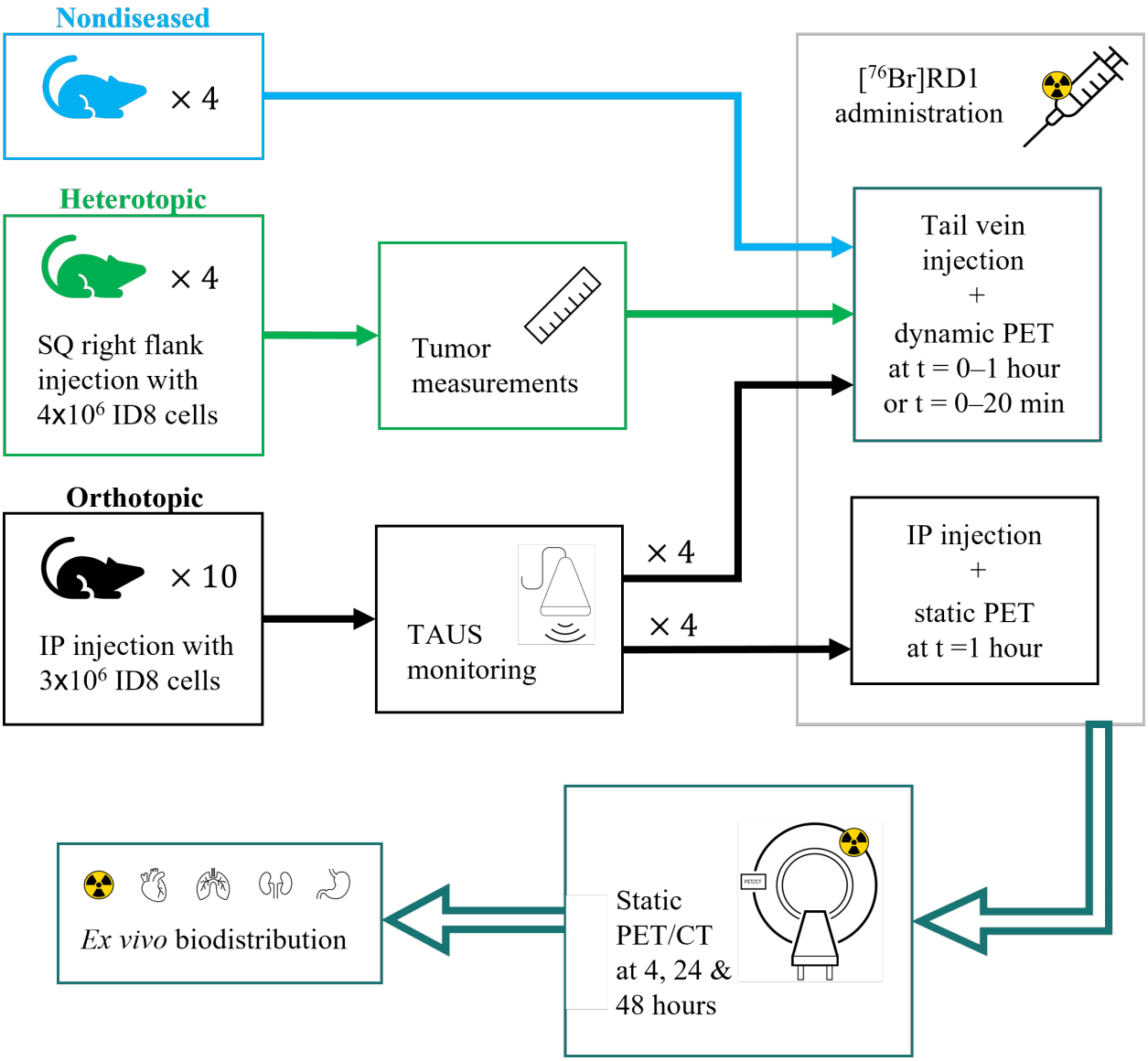

Figure 5.1: Study design for control (blue), heterotopic (green) and orthotopic (black) models. Orthotopic models underwent transabdominal ultrasound (TAUS) monitoring for disease progression and staging. The mice were ranked for disease burden based on TAUS imaging and the 8 mice with the highest burden were chosen for PET/CT and biodistribution studies. For intravenous drug administration, control models had a 1-hour dynamic scan and heterotopic and orthotopic models had a 20-minute dynamic scan. For IP drug administration in orthotopic models, a static microPET/CT was conducted at 1 hour.

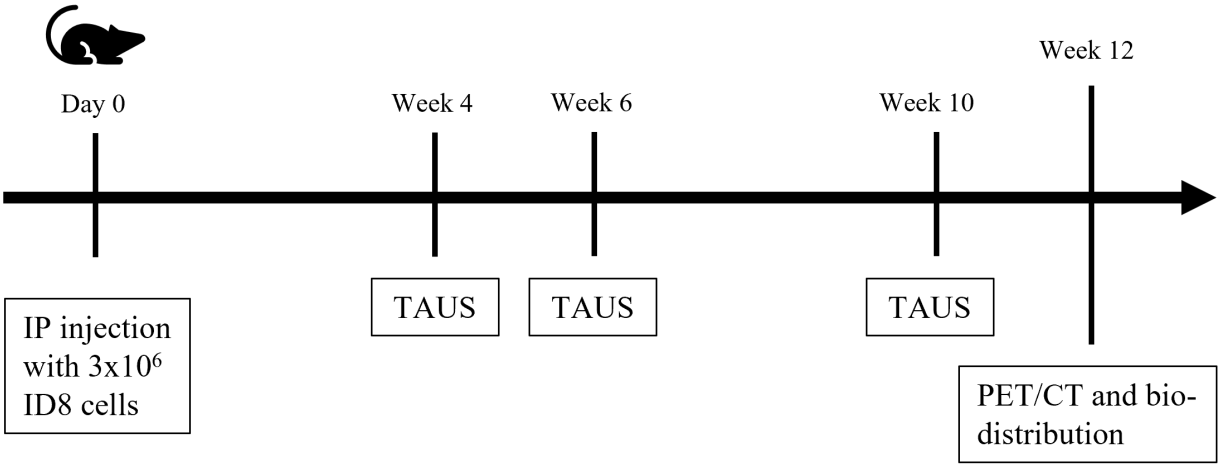

Figure 5.2: Study timeline for orthotopically diseased mice with ID8 ovarian cancer.

NJ) and mice were placed on a heated platform in the supine position under anesthesia with 1.5–3.5% isoflurane administered via nose cone. The system utilizes physiological monitoring system electrodes to measure the electrocardiogram (ECG) and respiratory signals during ultrasound scanning. Spectra 360 electrode gel (Parker Labs, NJ) was applied on the electrodes to ensure optimal contact with each paw that was subsequently taped down. Isoflurane was titrated to maintain a heart rate between 310–340 beats per minute (bpm) during scanning. Respiratory gating was used for B-mode cine loop image acquisition during exhalation.

The MS400 transducer with 30 MHz center frequency was used for data collection. An image sweep from vagina and pelvic bridge to lungs was collected using the 3D stepper motor with a step-size of 0.2 mm in two sections, a left and right side. Additional 3D scans were taken if a region of interest (ROI) was found to be in the peripherals of the initial image sweep. Tumors were detected by observing anomalous increases in brightness with irregular borders in unexpected areas during each tumor staging assessment. The tumor location were recorded and monitored for future scans.

The mass of the mice were measured weekly to assess for weight gain or loss from changes in appetite or the onset of ascites. After TAUS imaging at week 4 and 6 when no apparent tumors were observed in the images, the mass of the mice were used to indicate disease burden and inform the

next TAUS imaging study. A mass increase of 1 g compared to the previous week's mass was used to schedule the next TAUS study.

At the final TAUS imaging session at 10 weeks, mice were ranked in order of disease burden. The mouse ranked 1st had the highest disease burden, and two mice tied for rank 9 with no apparent disease burden as captured by TAUS. Mice ranked 1, 3, 5 and 7 were relegated to drug administration through tail vein injection. Mice ranked 2, 4, 6 and 8 were relegated to drug administration through IP injection. The two mice tied for rank 9 were omitted from the PET/CT and biodistribution study.

5.4.4.2 MicroPET/CT In Vivo Biodistribution

Mice were imaged on the Inveon microPET/CT scanner (Siemens Medical Solutions). Mice were anesthetized in an induction chamber with 3–5% isoflurane at a rate of 1–2 L/min of oxygen. They were placed on the scanning bed in the prone position and administered 1.5–3.5% isoflurane via nose cone.

CT imaging lasted 10 minutes, followed by PET image acquisition (20 million counts/scan at 48 hours and 50 million counts/scan for all other time points). Control mice received 5.11±0.13 MBq (138.0±3.4 μCi, 220 pmol) of [^{76}Br]RD1 via tail vein injections on the table, prompting the start of a 1-hour dynamic PET scan. Diseased mice received 9.191±0.474 MBq (248.4±12.8 μCi, 20 pmol) [^{76}Br]RD1 either by tail vein (IV) or IP injection. For the diseased IV administered group, a PET dynamic scan of 20 minutes was performed starting immediately at the end of radiopharmaceutical injection. For the IP administered group, a static PET scan at 1 hour p.i. was performed. For dynamic scans, images were histogrammed into 1 minute bins between 1–5 minutes p.i., 5 minute bins between 5–30 minutes p.i., and 10 minute bins between 30–60 minutes p.i. For all cohorts, static PET scans were performed at 4 hours, 24 hours and 48 hours p.i. This workflow is summarized in Figure 5.1. PET acquisition settings were the same as described in Section 5.4.2. Static PET scans were histogrammed into one frame. PET images for static and dynamic scans were reconstructed using ordered-subset expectation maximization of 3 dimensions. This was followed by the maximum a posteriori algorithm (18 iterations and 16 subsets) as described in Section 5.4.2.

The corresponding CT was used for attenuation corrections. The organs were contoured (Sec. 5.4.4.3) and the mean percentage injected dose per volume (%ID/g) measured after decay-correcting to time of injection.

5.4.4.3 Regions of Interest and Organ Contouring

PET/CT images were automatically coregistered and analyzed using Inveon Research Workplace 4.2 (Siemens Medical Solutions) using rigid and affine registrations methods as needed. Normal tissues were contoured using both anatomical and functional images. The gallbladder was contoured using PET images, with an average volume of 7.4±3.8 mm^3 and a range between 2.5–14.0 mm^3. All other normal tissues were contoured using the CT images. The contours of the liver, bone and muscle will be further described.

Whole liver contours, with an average volume of 601±178 mm^3, were estimated from the CT images. An additional "liver section" ellipsoid contour, with an average volume of 65.0±27.5 mm^3, was placed within the liver anatomy and used as a comparison. This ellipsoid was placed in a section of the liver away from the gallbladder contour and clearly within the liver margins.

The entire skeleton of the mouse was contoured for the bone measurements. The muscle contour was drawn in the left quadriceps muscle in the nondiseased cohort. For the heterotopic disease model, preference for the contralateral quadriceps muscle was given except in cases where a hot-spot in the abdomen had signal spill into the quadriceps region. In those instances, the muscle contour was drawn in the triceps muscle. For orthotopic models, the muscle contour was drawn in the triceps muscle to standardize the contour location for all mice instead of using signal spill as a deciding factor.

Masses at the subcutaneous tumor injection site (TIS) were easily delineated for heterotopic models in the axial plane of CT scans. For orthotopic models, TAUS and autopsy informed the tumor location on CT images. An additional control volume with the same volume as the TIS contour was drawn on the contralateral side of the mouse at the same location as the tumor. This was labeled the contralateral-to-tumor control volume (CTCV) and was used for measurement

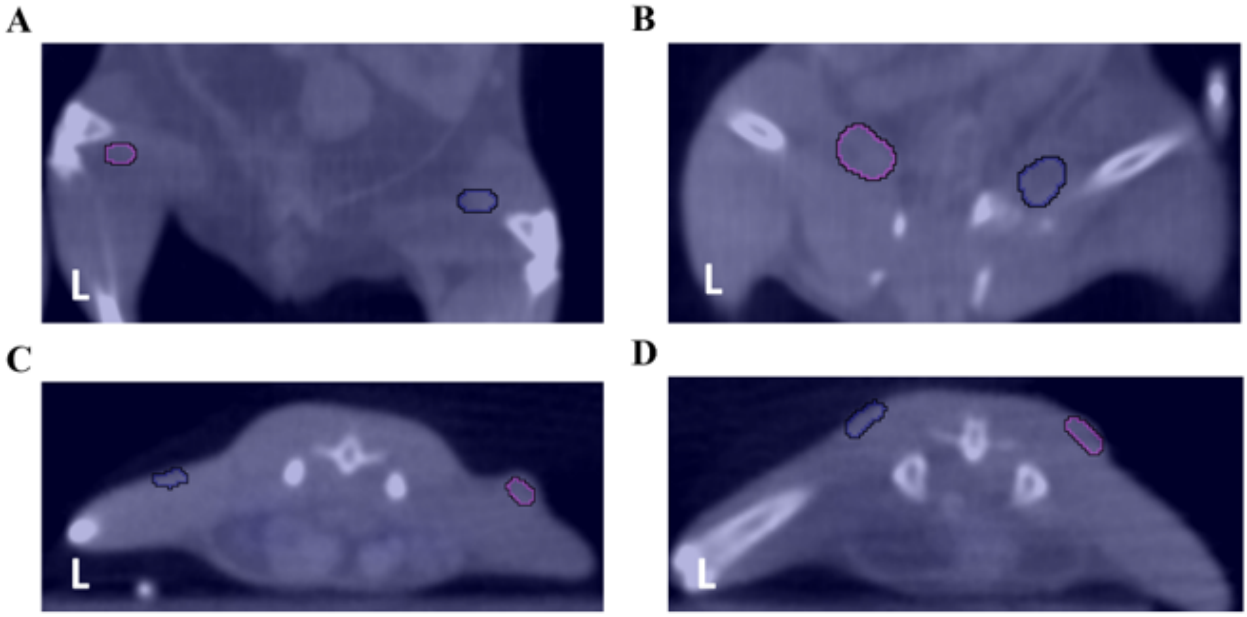

Figure 5.3: X-ray CT images showing contours of masses at tumor-injection-sites (TIS, in pink) and contralateral-to-tumor control volumes (CTCV, in navy) in (**A-B**) two orthotopic models shown here in the coronal plane and (**C-D**) two heterotopic models shown in the axial plane. Mice were imaged in the prone position.

comparisons to the TIS since the tumor was difficult to delineate in the orthotopic models, using a TIS-to-CTCV ratio (T:CTCV) calculation. The CTCV was drawn on the heterotopic models for validation. Examples of the TIS and CTCV contours are shown in Fig. 5.3 for two orthotopic and heterotopic models.

5.4.5 *Ex Vivo* Biodistribution

After the final PET/CT image at 48 hours, mice were euthanized via CO_2 asphyxiation followed by exsanguination. Blood, heart, lungs, pancreas, spleen, kidneys, liver, gallbladder, large intestine, small intestine, stomach, femur bone, quadriceps muscle, enteric contents (combined contents of stomach, small intestine and large intestine), and TIS tissue were harvested and weighed. The radioactivity was measured using an automated calibrated gamma counter (PerkinElmer) described in Chapter 3.3.1.6, with a calibration factor of 1.85 Bq/CPS for ^{76}Br. Each individual mouse's injected dose was background- and decay-corrected to time of injection to calculate the %ID/g. TIS-tissue-to-muscle ratios were calculated from the measurements.

5.4.6 Statistics

Differences in [^{76}Br]RD1 longitudinal PET uptake and end-point biodistribution of cohorts with groups of 4–16 mice were compared for statistical significance (RStudio 2022.2.2). The variables were tested for normality using the Shapiro-Wilk test [172]. In this study, mice were not paired based on similar characteristics and placed in separate groups, resulting in unmatched groups. For comparing two means in unmatched groups, Welch's two-sample t-test [173] was used, while Kruskal-Wallis was performed when there were more than two means in an unmatched group [174]. Mean values were reported as mean ± standard error of the mean (SEM), and statistical significance was determined as a P value less than 0.05.

5.4.7 Dosimetry

The PET/CT scans acquired from Section 5.4.4.2 were used for dosimetry calculations using the Radiopharmaceutical Assessment Platform for Internal Dosimetry (RAPID). PET images were coregistered to CT images on the Inveon Research Workplace v4.2 (Siemens Medical Solutions) automatically and checked manually. Each organ was contoured as described in 5.4.4.3 on the CT scan with the addition of an intestinal contour in nondiseased mice. Small and large intestine could not be delineated from each other and so one contour was made. All organs were contoured using anatomical images, except for intestinal contours. Those contours were made using CT scans and then after registration, PET images were used to complete the contour. Due to tumor growth issues, tumor dose calculation analysis is only reported in the appendix. Images and contours were exported to Amira v5.3.3 (Mercury Computer Systems, Germany) for RAPID analysis. An additional body contour was added so that the voxels outside the body contour were not used for computations.

Image coregistration was re-performed in Amira by affine transformation as described in Section 5.3. The images acquired at the first time point were used for reference, including the images at t= 4 h for IV administered mice and t= 1 h for the IP administered mice. The [^{76}Br]RD1 biodistribution at each scan time point was used for Geant4 simulations. Dose per MBq of injected activity was calculated for ^{76}Br without the Meitner-Auger cascade option (ARMflag) and for ^{77}Br with and

without the Meitner-Auger cascade option [175]. CT data were transformed from Hounsfield units into mass density using a CT scanner-specific calibration curve. Evaluated Nuclear Structure Data Files (ENSDF, Brookhaven National Laboratory) data, which includes all MAe^- ($<$1 keV), β, and γ radiation emitted per decay, were used to calculate the source decay sampled uniformly in a voxel. The energy deposition was tracked to create a 3D cumulative dose distribution, with the PET contours defining organ regions to calculate organ-specific dose. To calculate the dose distribution for [^{77}Br]RD1, the PET images acquired with [^{76}Br]RD1 were corrected for physical decay differences between the two radionuclides.

The PET quantified [^{76}Br]RD1 organ %ID/g uptake in mice was used to estimate the human organ dose using OLINDA/EXM v1.1 [126] as described previously [176]. In this method, the mouse biodistribution was assumed to be equal to human biodistribution. The mouse organ [^{76}Br]RD1 uptakes (%ID/g) were multiplied by the ratio of the average mouse mass in the study to the average human woman mass to get the estimated human organ %ID/g uptakes:

$$\left(\frac{\%\mathrm{ID}}{m_{\mathrm{organ}}}\right)_{\mathrm{human}} = \left(\frac{\%\mathrm{ID}}{m_{\mathrm{organ}}}\right)_{\mathrm{mouse}} \times \left[\frac{(m_{\mathrm{whole\ body}})_{\mathrm{mouse}}}{(m_{\mathrm{whole\ body}})_{\mathrm{human}}}\right], \qquad \text{(Eq. 5.2)}$$

where m is the mass of the region. The organ uptake in humans (%ID/g) was then multiplied by average human organ masses [177] to obtain organ-specific %ID in human. These values were calculated at each time point and then input into OLINDA/EXM, using the 3 exponential term modeling process to calculate the number of disintegrations in each organ. The organ-level equivalent dose was then calculated.

5.5 Results

5.5.1 Radiopharmaceutical Production

For ^{76}Br production, the average physical yield was 58±3 MBq/μAh, producing 2,000±40 MBq of ^{76}Br (n=2) at end of bombardment with a distillation yield of 54±6%. The non-decay corrected [^{76}Br]RD1 radiochemical yield was 4.8% and 73% for each production, with a molar activity of 22

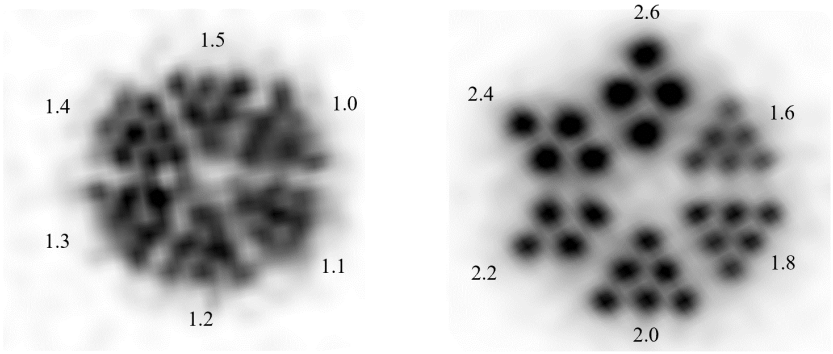

Figure 5.4: Derenzo phantoms with 1.0–1.5 mm and 1.6–2.6 mm sized rods filled with ^{76}Br. Images were acquired on a Siemens Inveon microPET.

GBq/nmol and 740 GBq/nmol for each production, respectively. Nondiseased animal scans used the radiopharmaceutical from the first production, and diseased models used the product from the second production.

5.5.2 Radiobromine PET Calibrations

The axial images of the Derenzo phantom are shown in Figure 5.4 with a resolution for ^{76}Br between 1.3–1.4 mm. The maximum intensity projection (MIP) of the PVC phantom is shown in Figure 5.5A and the resulting PET recovery coefficients are summarized in Figures 5.5B-C as a function of the sphere volume and diameter.

5.5.3 Tumor Models

During ultrasound, neither ascites nor metastatic tumor burden were observed. At autopsy, only two of ten mice were observed with metastatic tumors—one with 10–20 metastatic lung cancer nodules and the second with approximately 7 nodules on the pancreas. In all but one mouse, large primary type tumors next to the site of IP injection within the left gracillis or adductor (Fig. 5.6) and lateral to the sciatic lymph node [178] were palpated. At autopsy, they measured approximately 2–5 mm in diameter and were easily identified, informing the contours on CT.

Heterotopic mouse models had their tumors measured by caliper the day of the first scan. The average measured length was 4.6±0.7 mm before skin subtraction. Assuming a skin thickness of

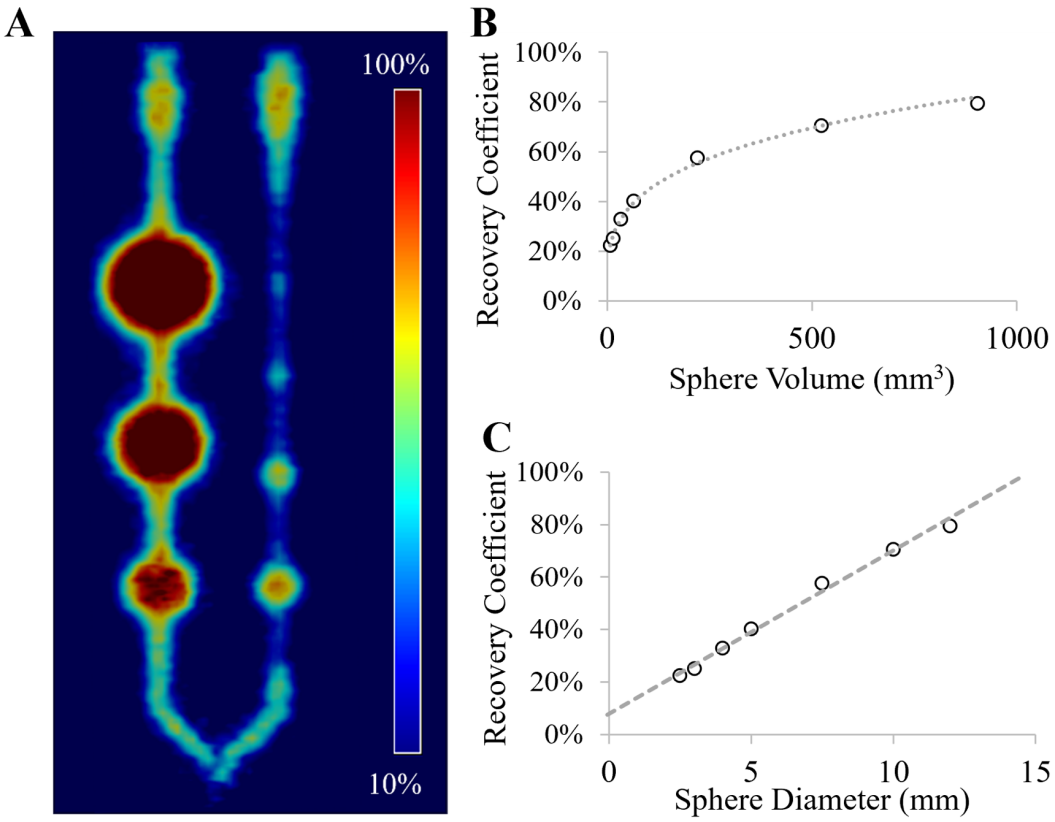

Figure 5.5: (**A**) The computed maximum intensity projection (MIP) for a partial volume (PV) correction phantom injected with ^{76}Br. The recovery coefficient (RC) (**B**) as a function of sphere volume and (**C**) as a function of sphere diameter.

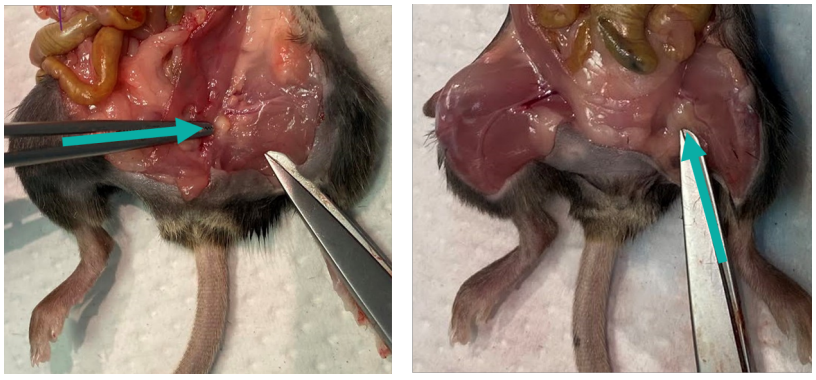

Figure 5.6: Tumors located on the left gracillis or adductor muscle on the left side of the mice. Intraperitoneal (IP) injection occurred in the lower left quadrant of the abdomen, approximately 0.5–1 cm superior to these two tumors.

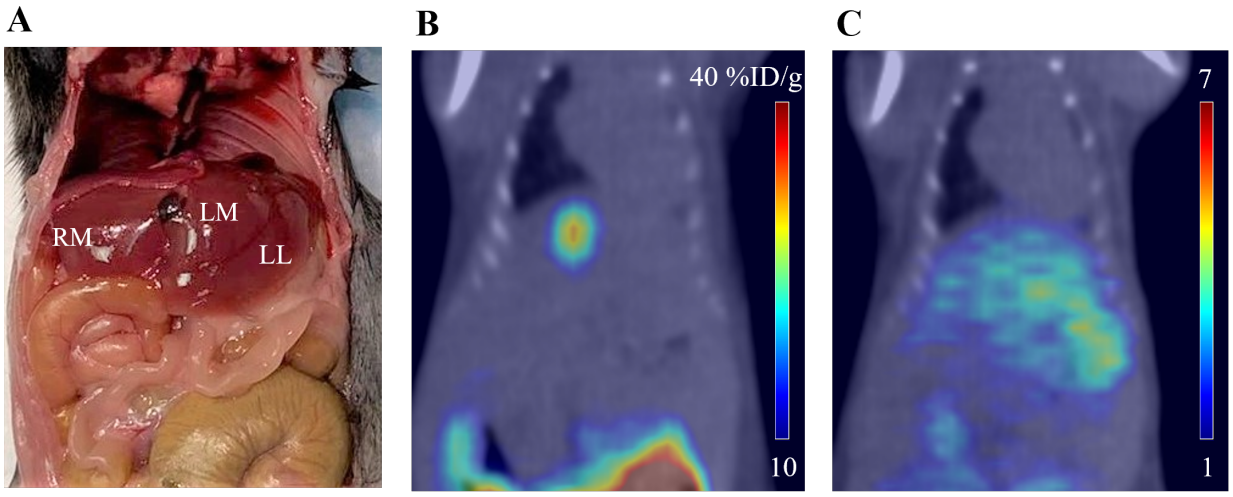

Figure 5.7: (**A**) Anatomy of mouse liver, including right medial (RM) lobe, left medial (LM) lobe, and left lateral (LL) lobe. The gallbladder is located posterior and between the RM and LM lobes. (**B**) Registered PET/CT image at 4 h post injection (p.i.) showing gallbladder uptake. (**C**) Registered PET/CT image at 24 h p.i. showing liver uptake.

0.5 mm [171], 1 mm was subtracted from the measurements to calculate an average volume size of 20±9 mm^3 with Eq. 5.1.

5.5.4 MicroPET/CT Imaging

For CT contours, the liver inferior margins and the gallbladder margins were difficult to detect. Moreover, the gallbladder, which posteriorly abuts the right and left medial lobe of the liver (Figure 5.7A), was indistinguishable in CT. PET images were used for the gallbladder contour (Figure 5.7B). Due to the liver/gallbladder boundary being difficult to distinguish, an enlarged margin of approximately 0.5–1 mm around the gallbladder contour was used to not overlap with the liver contour. This was done so the spread signal due to PV effects caused by the small volume of the gallbladder was not erroneously measured as liver uptake. The gallbladder average *in vivo* measured ROI volume was 7.4±3.8 mm^3 at 4 h. The *ex vivo* average measured mass was 11.9±0.7 mg at post 48 h injection. Assuming a density of 1 g/cm^3, the discrepancy between the *in vivo* and *ex vivo* measurement could be due to the amount of bile in the gallbladder at the time of measurement.

A representative mouse model was chosen to summarize the biodistribution *in vivo* over 48 p.i.

Table 5.3: *In vivo* [^{76}Br]RD1 uptake for the liver and liver section ROI. The difference between each ROI for each scan was measured and averaged. Percent difference between the liver section and liver is included.

	[^{76}Br]RD1 Uptake (%ID/g)				
	1–20 min	**1 h**	**4 h**	**24 h**	**48 h**
Liver	11.3±2.8	8.7±0.7	4.5±1.1	1.8±0.4	0.9±0.2
Liver Section	12.8±3.4	8.5±0.5	4.4±1.0	1.9±0.3	1.0±0.3
Difference	1.4±0.9	-0.2±0.4	-0.1±0.4	0.1±0.2	0.2±0.1
Difference (%)	11	-3	-2	7	15

of the radiopharmaceutical. Figure 5.8 shows the organ uptake for each time point of a heterotopic model mouse. MIP images of all the mice are shown in the supplemental materials in the appendix (Fig. B.3–B.5).

PET/CT registration using manual and automatic rigid and conformal registration was always manually checked for quality assurance. The majority of the time, the registration was lined up to the superior portion of the liver of the mouse since the PET image provided clear margins on the liver/lung interface to match to the CT scan. Since the tumor uptake was not visible on PET, registration to the tumor was not possible. Figure 5.9 shows an axial slice of two heterotopic model mice 4 h p.i. The %ID/g range on the PET scan was saturated to increase the signal at the tumor location for viewing purposes.

The liver ROI and liver section ROI were compared in terms of uptake. The average volume of the liver contour among all mice was 600±180 mm^3, while the liver section ROI had an average volume of 66±28 mm^3. Table 5.3 summarizes the uptake for each ROI and the average difference between the two for each scan at all time points. This comparison was conducted due to the difficulties in accurately assessing the inferior margins of the liver and the heterogeneity of the liver uptake. Although the liver section ROI would be within the liver organ, its measurement might not be accurate if located in a hot or cold region.

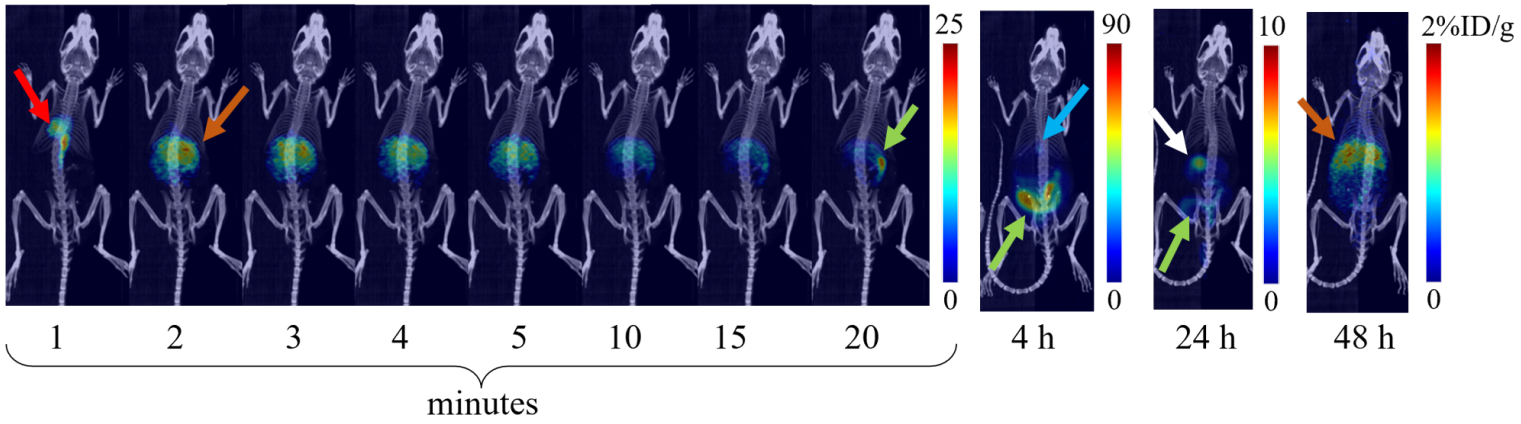

Figure 5.8: PET MIP images of a representative heterotopic mouse injected intravenously with [^{76}Br]RD1. Red arrow: heart; brown arrow: liver; green arrow: intestines; blue arrow: gallbladder; white arrow: stomach contents.

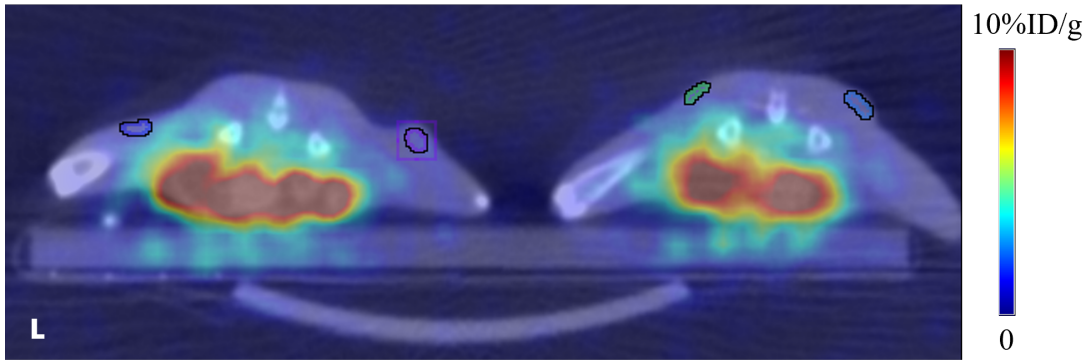

Figure 5.9: PET/CT axial slice at 4 h p.i. of two heterotopic mouse models with masses at the tumorinjection-site (TIS) on the right flank and corresponding CTCV on the left side.

Table 5.4: *In vivo* and *ex vivo* [^{76}Br]RD1 organ uptake measurements in all animal models at 48 p.i. (n=16).

Organ Type	***In Vivo* (%ID/g)**	***Ex Vivo* (%ID/g)**	***P* Values**[†]
Blood[a]		0.4±0.1	<0.001**
Heart	0.24±0.06	0.11±0.03	<0.001**
Lungs	0.22±0.06	0.27±0.08	0.056
Kidneys	0.37±0.11	0.55±0.12	<0.001**
Liver	1.0±0.2	2.3±0.4	<0.001**
Enteric Contents[b]		1.0±0.5	0.13
Stomach	0.82±0.24	0.21±0.07	<0.001**
Bone	0.08±0.03	0.11±0.05	0.048*
Muscle	0.09±0.03	0.05±0.02	<0.001**
Brain	0.08±0.03	0.05±0.02	0.021*
Pancreas		0.13±0.05	
Spleen		0.19±0.06	

[†]Welch's two-sample t-test.

[a]Blood uptake *ex vivo* was compared to heart *in vivo* to calculate the *P* value.

[b]Enteric contents uptake *ex vivo* were compared to stomach *in vivo* to calculate the *P* value.

5.5.5 Biodistribution

Figure 5.10 and appendix Tables B.4–B.3 summarize the [^{76}Br]RD1 uptake in diseased mice (n=12) measured at time points 1, 4, 24 and 48 h *in vivo* and the in the *ex vivo* radioactivity measurement. The 48 h p.i. *in vivo* and *ex vivo* [^{76}Br]RD1 organ and tumor uptake for all mice (n=16), are summarized in Figure 5.11 and Table 5.4. The Welch's two-sample t-test was used to calculate significant differences between corresponding *in vivo* and *ex vivo* measurements. Organs that also have contents, like the heart and stomach, had their *ex vivo* organ and contents compared to their organ *in vivo* percent uptake and tested for significance.

The mice were further divided into cohorts (n=4) and the [^{76}Br]RD1 organ uptake *in vivo* (Fig. 5.12, Table B.5–B.7) and *ex vivo* (Fig. 5.13, Table B.8–B.10) were graphed. The mice were divided by disease burden, [^{76}Br]RD1 administration route, and animal model. When two averages were compared, statistical significance was measured using Welch's t-test. When three averages were compared, the Kruskal-Wallis test was used.

The time activity curves (TAC) of [^{76}Br]RD1 for all measured organs are shown in Figure 5.14.

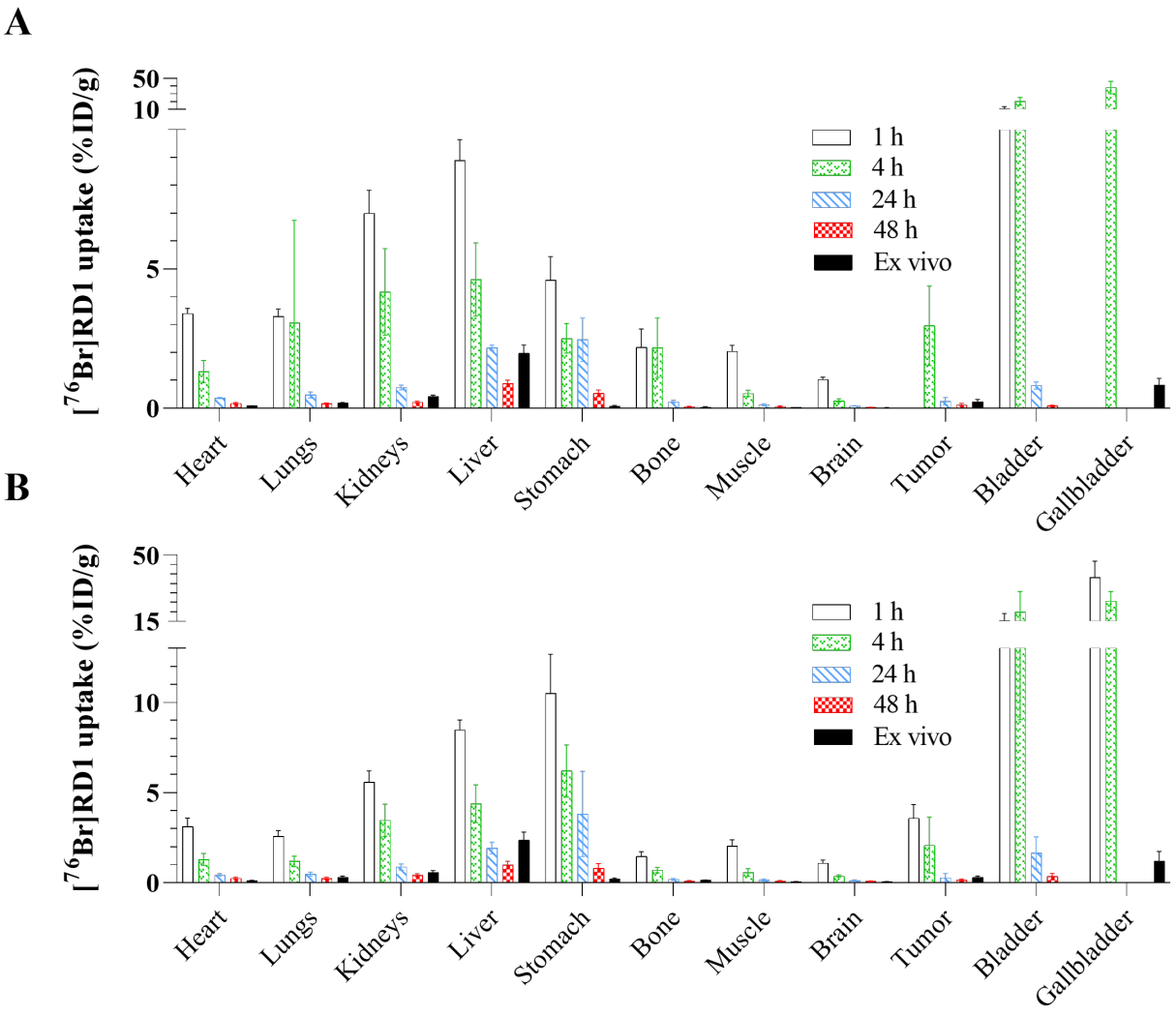

Figure 5.10: The *in vivo* [^{76}Br]RD1 organ uptakes at 4 time points p.i. and the *ex vivo* measurement in the (**A**) nondiseased models (n=4) and (**B**) diseased models (n=12).

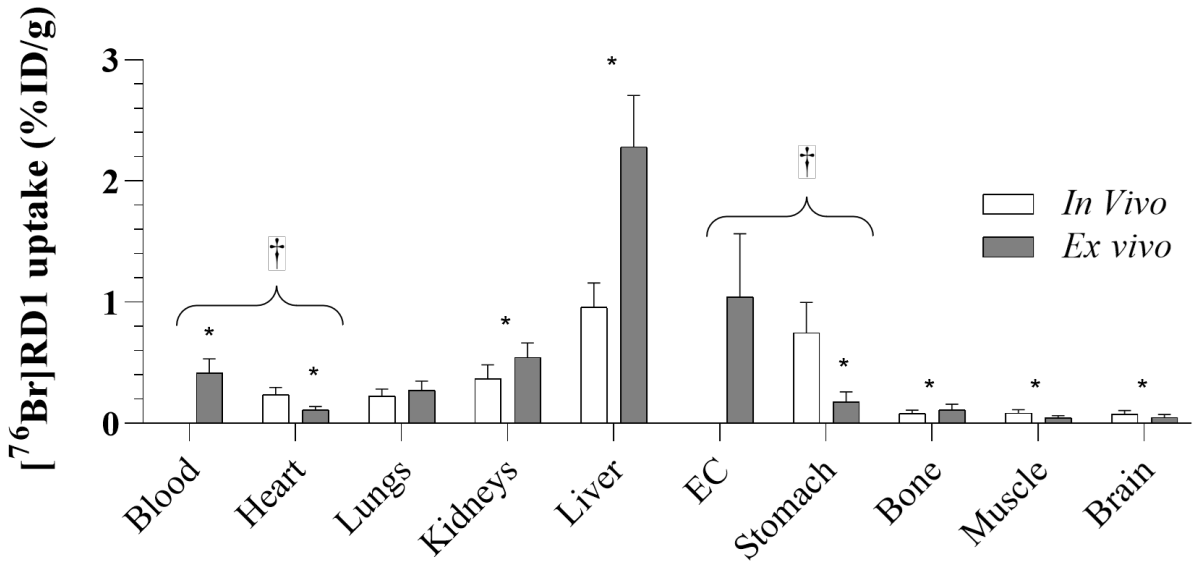

Figure 5.11: *In vivo* and *ex vivo* [^{76}Br]RD1 organ uptake measurements 48 h p.i. (n=16). †*In vivo* organ contour compared to *ex vivo* organ and organ contents separately, i.e., blood for heart, and enteric contents (EC) for stomach. $^{*}P<0.05$.

The TAC based on animal model types and clearance organs, including the liver, heart, bladder and kidney are summarized in Figure 5.15A. The TIS and CTCV are summarized in Figure 5.15B. The *in vivo* heart uptake was used to measure the biphasic blood clearance, which was assessed with nonlinear regression analysis (GraphPad Prism v9.3.1) using a two-phase decay model. In nondiseased mice, the α-phase half-life ($t_{1/2,\alpha}$) was 1.5 min (95% CI: 1.2–1.9 min) and the β-phase half-life ($t_{1/2,\beta}$) was 86 min (95% CI: 67–107 min). The weighted half-life $t_{1/2}$ was calculated using:

$$t_{1/2} = t_{1/2,\alpha} \cdot F_{\alpha} + t_{1/2,\beta} \cdot F_{\beta} \qquad \text{(Eq. 5.3)}$$

where F_{α} and F_{β} are the fractional clearances during the α- and β-phases, respectively. From the nonlinear regression analysis, the values were calculated as 69.9% and 30.1%, respectively. The weighted half-life was calculated as 32 min. For diseased mice, the $t_{1/2,\alpha}$ was 42 s (95% CI: 22–69 s) and the $t_{1/2,\beta}$ was 41 min (95% CI: 18 min to an unstable maximum). The F_{α} was 78%, which gave a weighted half-life of 9.6 min.

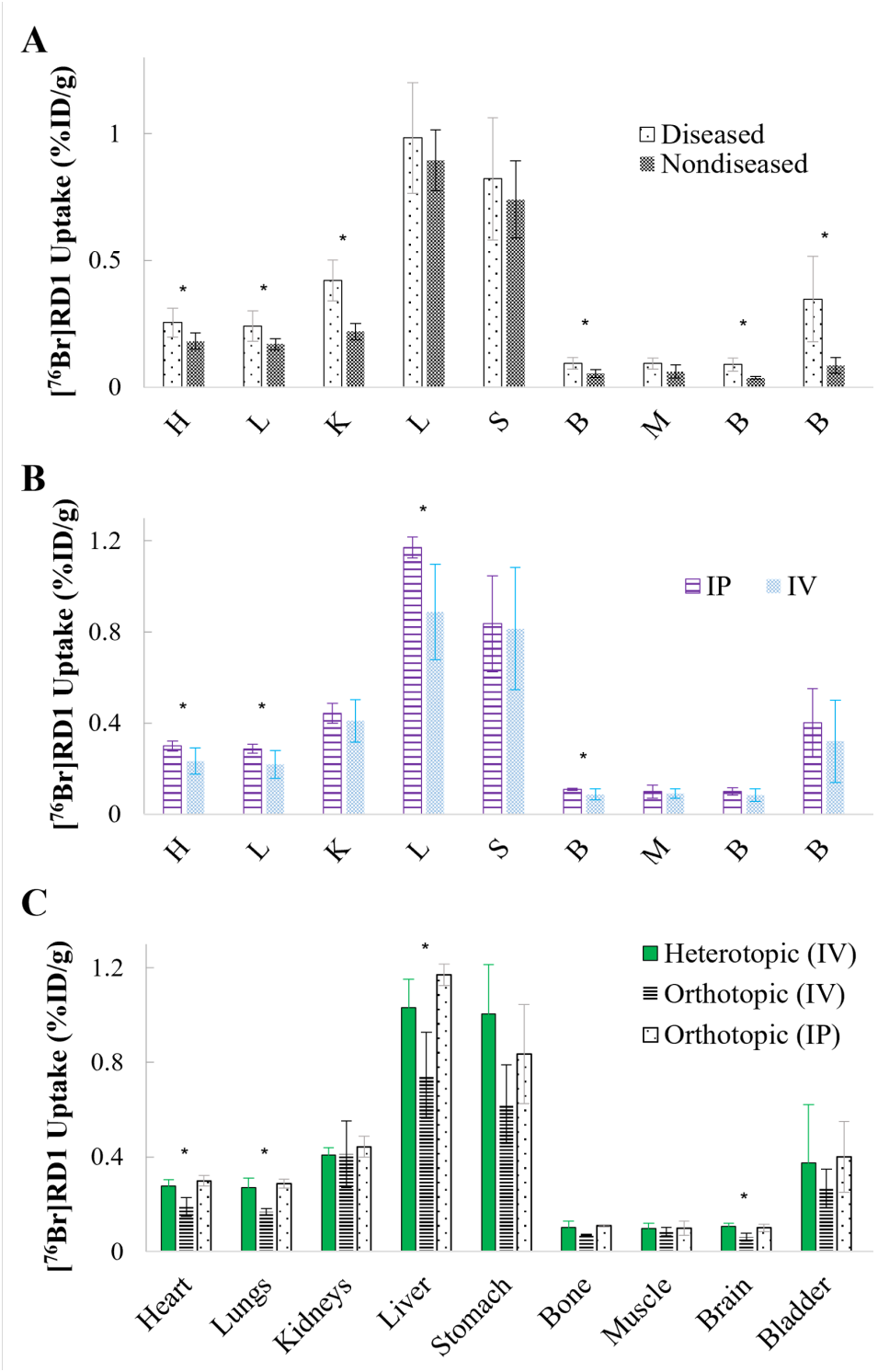

Figure 5.12: The [^{76}Br]RD1 uptake *in vivo* at 48 h of the 16 mice grouped into various cohorts. (**A**) Diseased (n=12) vs nondiseased (n=4), (**B**) IP injected (n=4) vs IV injected (n=8) in diseased models and (**C**) the diseased mice split into disease models and injection method (n=4 for all). $^{*}P<0.05$. CTCV:Contralateral-to-tumor control volume.

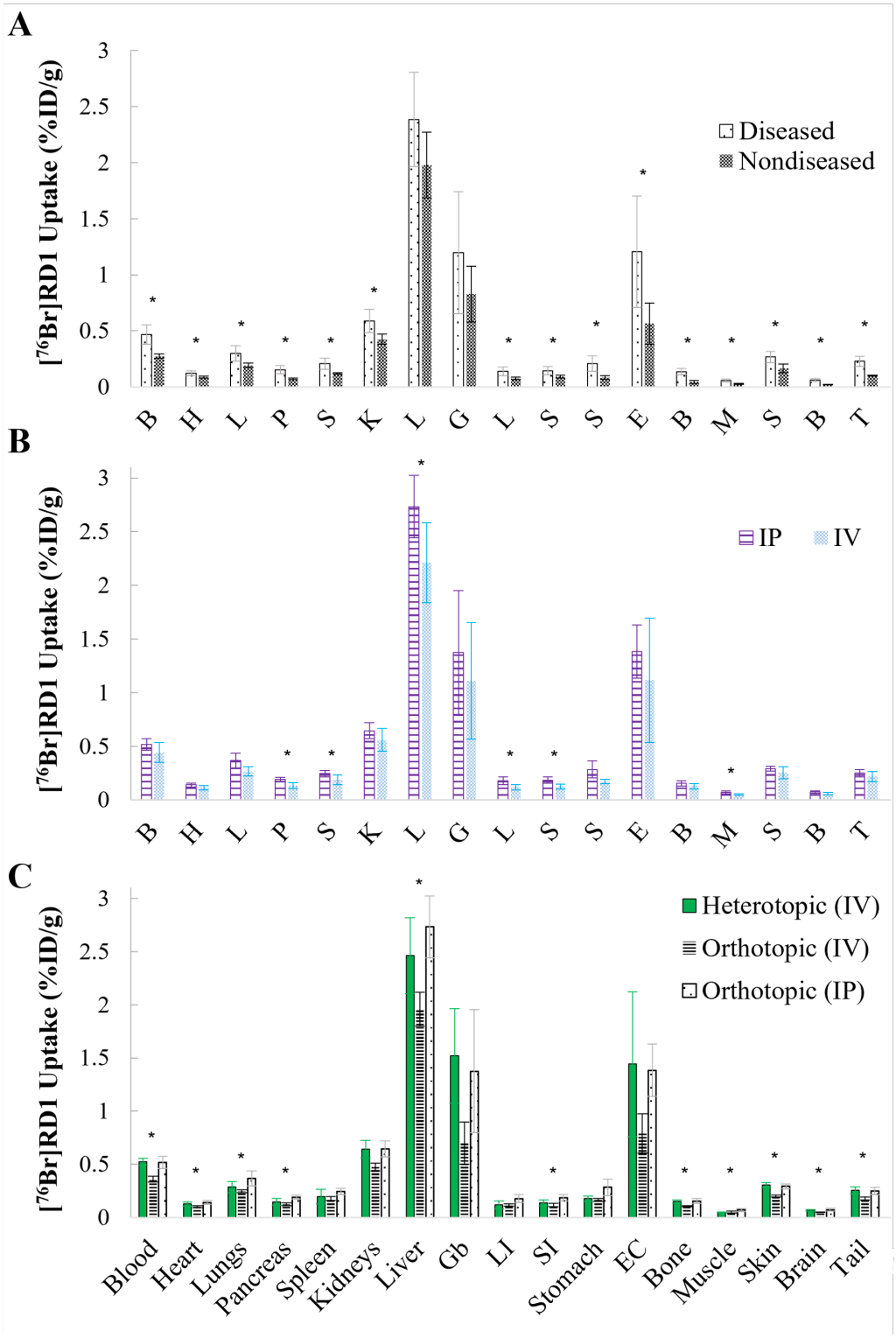

Figure 5.13: The *ex vivo* biodistribution of the 16 mice grouped into various cohorts. (**A**) Diseased (n=12) vs nondiseased (n=4), (**B**) IP injected (n=4) vs IV injected (n=8) in diseased models and (**C**) the diseased mice split into disease models and injection method (n=4 for all). $^{*}P<0.05$. Gb=gallbladder, LI=large intestine, SI=small intestine, EC=enteric contents.

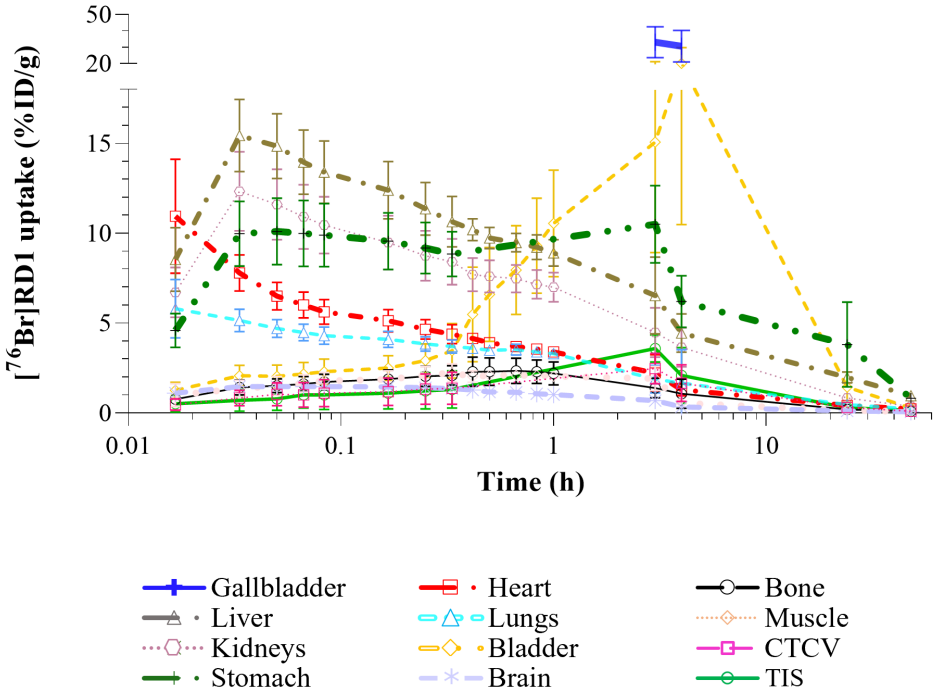

Figure 5.14: Timed uptake of [^{76}Br]RD1 in all the mice (n=16) for various organs measured *in vivo*. TIS: tumor-injection-site

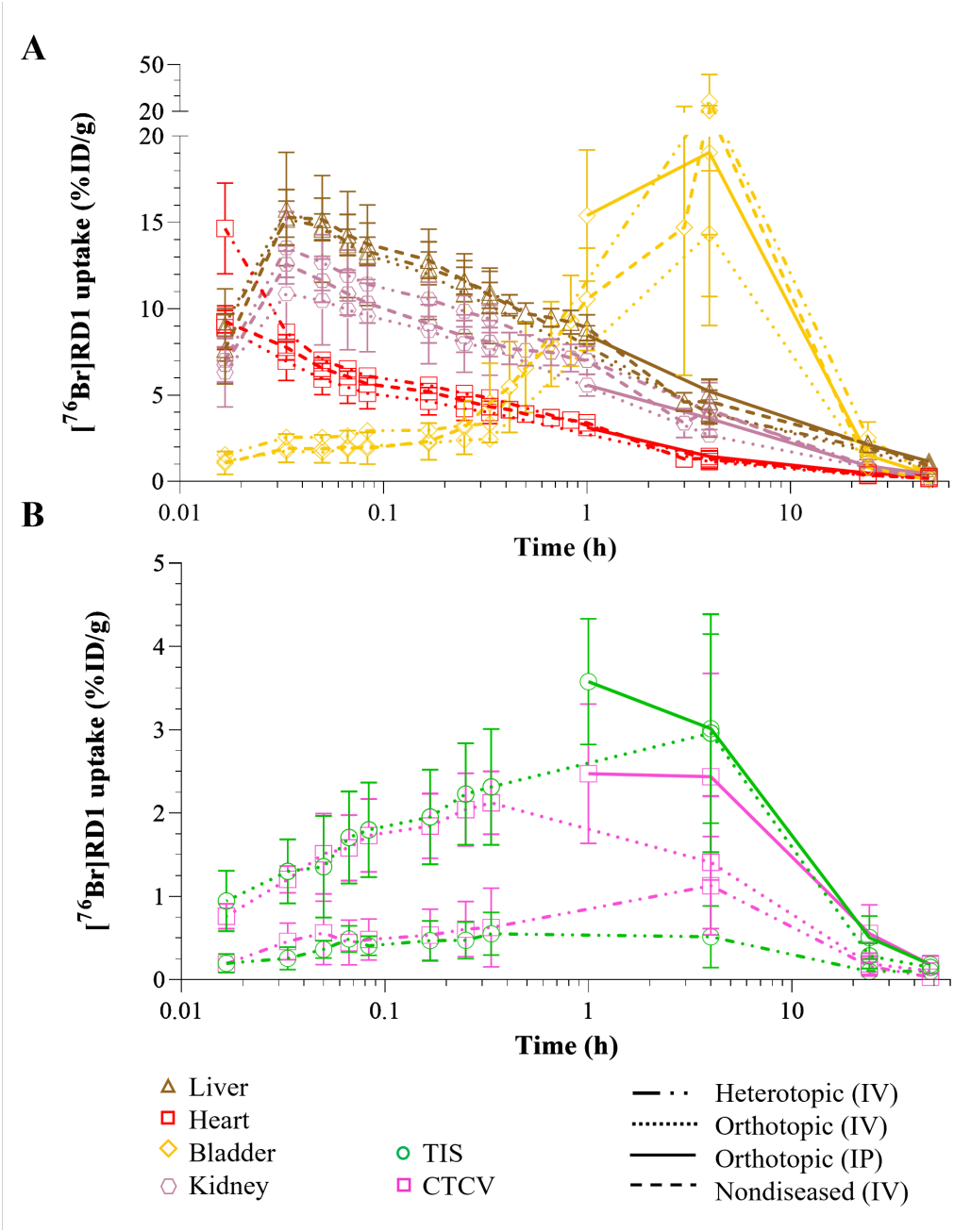

Figure 5.15: Timed activity curves of [^{76}Br]RD1 in the (**A**) normal tissues liver, heart bladder, kidney, (**B**) tumor-injection-site (TIS) and contralateral-to-tumor control volume (CTCV) for each model measured *in vivo* (n=4).

5.5.6 Dosimetry

The dose per activity calculated for ^{77}Br with the Meitner-Auger cascade option showed an increase of 1.6±0.1 times compared to the calculations without it. The following results will be the reported dose per activity when the Meitner-Auger cascade option is utilized for ^{77}Br results.

Using the values reported in Figure 5.10 for dosimetry inputs, the organ dose per activity was calculated for each disease model for ^{77}Br (Fig. 5.16A). The organ dose per activity was calculated for ^{77}Br and ^{76}Br for all diseased models (Fig. 5.16B). These calculations were repeated for the nondiseased mice (Fig. 5.16C, Table B.12). The equivalent organ dose estimates are summarized in Figure 5.16D and Table B.12.

5.6 Discussion

The tumor models did not exhibit the anticipated growth from the ID8 cancer cells, as shown in Table 5.1 for several references. In both models, the cancer grew at a considerably slower rate than expected. In the orthotopic models, ascites were expected to develop within 6–8 weeks, but only minimal bloating in two mice and ascites in only one mouse was observed at week 11, with no ultrasound confirmation of tumors or metastatic nodules upon autopsy. Ultrasound confirmed the absence of ascites at weeks 4 and 6, after which the ultrasound was delayed by 2 weeks in anticipation of visual or weight-based detection of ascites progression. However, no additional significant progression of ascites or tumor burden was observed.

At 8 weeks p.i. of the ID8 cells in the orthotopic models, it was clear the tumor burden was not high enough to warrant radiopharmaceutical production and imaging resources. The imaging and biodistribution studies were delayed to allow further development of the orthotopic model. During the week 10 ultrasound, the primary tumors were large enough to palpate and started to impede range of motion in one mouse. By week 11, two mice had range of motion impediment, and euthanization was suggested by the Small Animal Imaging and Radiotherapy Facility.

Heterotopic model animals were expected to have tumor sizes of approximately 200 mm^3

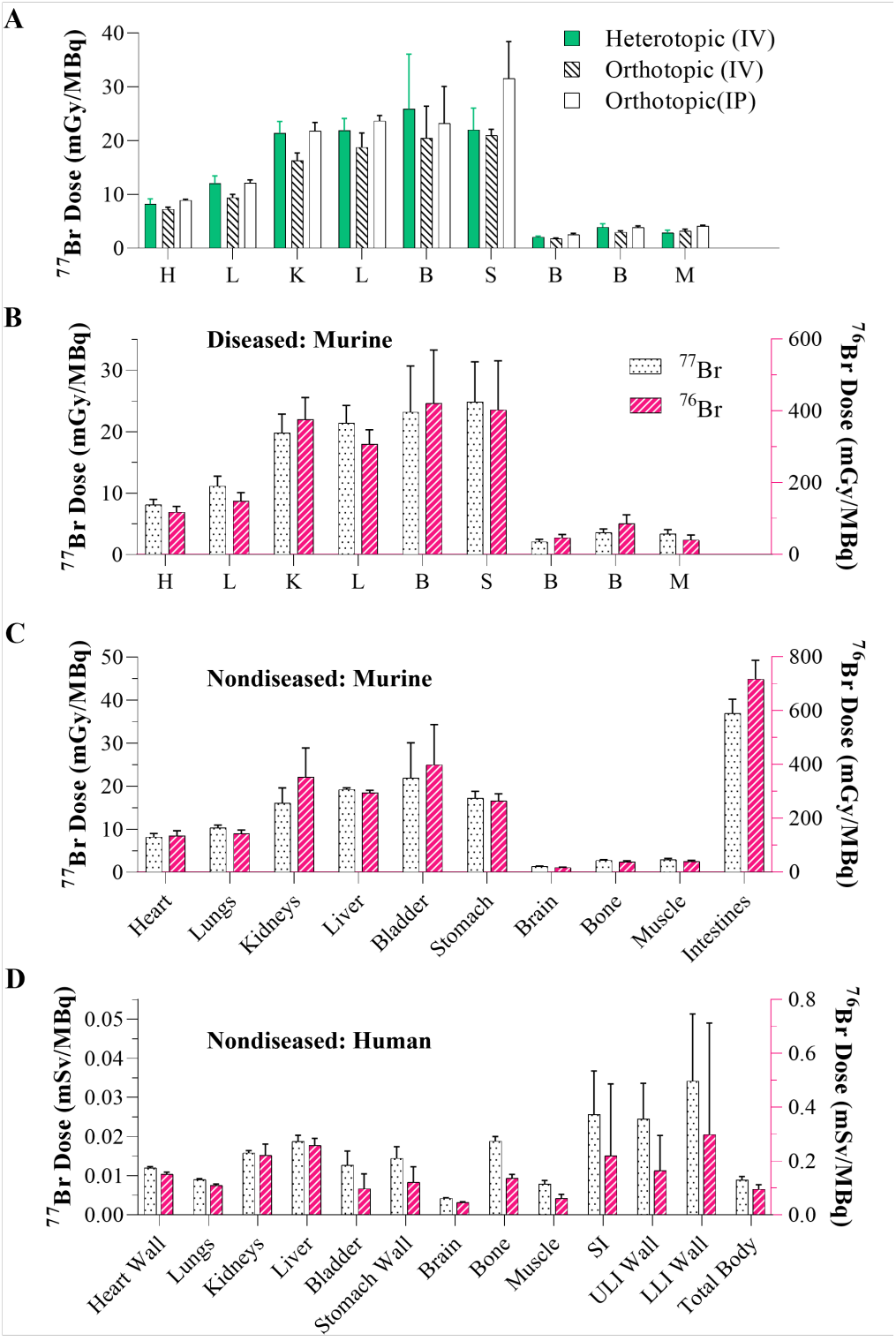

Figure 5.16: Dosimetry analysis showing estimated integrated organ-level absorbed doses following [^{76}Br]RD1 administration for (**A**) each disease model using RAPID, (**B**) all diseased mice using RAPID, (**C**) in nondiseased mice using RAPID and (**D**) equivalent dose in female humans using OLINDA. SI: small intestine; ULI: upper large intestine; LLI: lower large intestine.

[156–158] at 5 weeks p.i. of ID8 cells. Not accounting for skin thickness, tumors only measured 33±15 mm^3 this time point. At week 6, tumor size increased to 45±19 mm^3, at which point the orthotopic models had matured to a point where mice needed to be euthanized. Heterotopic and orthotopic mice were imaged at the same time, resulting in the heterotopic models being imaged at week 6 p.i. of ID8 cells. Further investigation into this model type has shown inconsistent or differing growth expectations, with expected volumes of 50 mm^3 at 3 weeks [156, 160], and even shrinkage of the tumor between 3–5 weeks [160].

At autopsy, one orthotopic disease model mouse had approximately 7 metastatic nodules on the pancreas. Another had 10–20 metastatic nodules on the lungs. No other metastatic disease was observed in the other mice. However, 7 of 8 mice had a primary tumor close to the IP injection site. This may be due to user error during the tumor cell IP injection. Perhaps the peritoneum was not properly punctured during injection, leaving the cells in the extraperitoneal space between the skin and peritoneum. Due to observed tumor growth issues, tumor assessment *in vivo* and *ex vivo* could not be properly conducted. Furthermore, immunohistological studies should have been conducted to validate the tumor cells.

Orthotopic tumors were contoured on the CT images using information from ultrasound and autopsy. Looking at the CT scans, it appeared that the margins of the tumor could be delineated. However, confidence in delineating tumor as opposed to normal tissues like lymph nodes or ovaries was low. Mouse atlases were used, but from slice to slice, it was difficult to assess accuracy.

The CTCV was a control volume that was meant to address the user contour error. If there were errors in the drawn TIS contours, then the CTCV would give similar results to the drawn TIS ROI %ID/g. Quality assurance of this method using the CTCV in the heterotopic model was done since the subcutaneous TIS masses were clearly delineated by CT in the heterotopic model. In comparison, the CTCV in the heterotopic model mice were in the muscle and skin areas on the contralateral side. However, it is apparent in Figure 5.9 that the shine from the abdomen does not allow for the accurate %ID/g measurement of the TIS or CTCV. Apart from the shine, it is also apparent that an error in the registration of the PET to the CT at the tumor location would cause

inaccurate measurements. Since the signal was so small at the TIS location, registering the PET to the TIS was not feasible. The registration occurred with the liver, which was approximately 2.5 cm superior to the TIS.

The subcutaneous tumors were measured and their volumes calculated. Comparing the calculated volume from caliper measurements (45±19 mm^3) to the contour volume (11±9) showed large discrepancies. Although contours were made conservatively, i.e., not contouring outside any perceived margin, this discrepancy seemed too large. Mouse skin thickness and fur in caliper measurements were not initially considered. After correcting for skin thickness, assuming 0.5 mm thickness [171], the volume was calculated as 20±9 mm^3, which more closely matched the CT-measured TIS contour. Furthermore, the average positron range of ^{76}Br is 5.3 mm. The length and width of the tumors on the heterotopic models were 5.1±1.2 mm and 4.1±0.4 mm, respectively, as measured by calipers. The diameter of the TIS contour of the orthotopic models from CT scans were 2.7±0.7 mm, although this may not be the accurate size of the orthotopic tumors (for future studies, it would be important to fully excise the tumors to accurately measure the mass to then apply an RC correction value). All of these dimensions are on the same order of magnitude as the positron range.

In the orthotopic model, the tumors were located in the abdomen, suggesting that shine from the abdomen was equal for both. In the orthotopic models, the TIS:CTCV and TIS:Muscle ratios showed no significant difference from unity (Appx. Table B.11, P=0.677 and 0.288 for the IV and IP administration, respectively). Although the T:M values were above 1, this may be due to the signal from clearance from the small or large intestine in the abdomen. In conclusion, *in vivo* TIS:Muscle measurements were inconclusive. The absence of vascularization in the tumors may have contributed to this observation. Conducting immunohistochemical studies could have shed light on the tumors' condition.

The error in the TIS measurements were also confirmed from the CTCV measurements. The CTCV measurements were the same magnitude as the TIS measurements (Fig. 5.14B). In fact, for the heterotopic models, the CTCV "uptake" was higher than the TIS uptake. The TIS location

was easily discerned in the heterotopic models, so an incorrect contouring of the tumor on the heterotopic model was not an issue. However, registering the PET scans so that the TIS PET signal was accurately registered to the TIS found on the CT image would be extremely difficult, especially with the size of the TIS contour and the positron range. Figure 5.9 shows how there is no PET signal where the TIS is located, but the high signal from the abdomen located close to the CTCV is adding signal to the CTCV measurement. As mentioned previously, it is also possible the tumor was not vascularized. Immunohistological studies could have illuminated whether this was the case.

Hepatic, renal and biliary excretion pathways were observed for [^{76}Br]RD1 (Fig. 5.10). These clearance pathways were similar to those observed for other rucaparib derived PARP inhibitors [63, 92, 179]. The weighted half-lives of a radioiodinated rucaparib derivative and fluorinated rucaparib radiopharmaceutical were reported as 1.7 min (95% CI: 1.2–2.8 min) and 4.3 min, respectively [179]. The half-life reported by phase was not reported. The $t_{1/2,\alpha}$ (1.5 min and 95% CI: 1.2–1.9 min) was on the same order as these values. Although the values reported by Destro et al. are from SPECT measurements at 2 and 24 h p.i. [179], it is unclear why there is such a large discrepancy between their measurements and ours. Further investigation is warranted.

Gallbladder excretion was measured using PET scans and was not measurable at 24 or 48 h. *In vivo* small and large intestinal organ [^{76}Br]RD1 were not measured separately due to the inability to accurately assess the margins of the organs and the large heterogeneity of the [^{76}Br]RD1 uptake as seen in the PET images. However, in the MIP images, it is clear there is uptake in either these organs, their contents, or both (Figs. 5.8). This may be through gastrointestinal excretion. However, with the gallbladder having such a high uptake, it is most likely bile released from the gallbladder into the small intestine and making its way through the large intestine.

The stomach uptake was 10±2%ID/g by 2 minutes before decreasing after 24 h, with high heterogeneity within the ROI. The stomach [^{76}Br]RD1 uptake could be explained in several ways. The first explanation would be that [^{76}Br]RD1 is targeting the stomach. However, in the *ex vivo* measurement, the uptake was significantly lower compared to the 48 h p.i. *in vivo* measurement, 0.21±0.07%ID/g vs. 0.82±0.24%ID/g ($P<0.001$), respectively, with the [^{76}Br]RD1 uptake in the

enteric contents more closely matching the measurement of the stomach, indicating the *in vivo* stomach uptake is from the contents in the stomach (Fig. 5.11).

Another explanation could be from ingestion of materials in the cage that have been contaminated by bladder excretion. However, from the TAC (Fig. 5.14), *in vivo* measured stomach uptake is at 10±2%ID/g at 2 minutes p.i and decreases between 4–48 h p.i. If it were from ingestion, higher uptake would be expected after the mice had been returned to their cages, at the 4, 24 and 48 hour mark.

It is unclear what the mechanism for stomach uptake would be. It appears that the actual stomach does not have uptake, and that it is the contents of the stomach. However, if not through oral ingestion and it is not absorption of excretions produced by the stomach wall, it is unclear what it is from. Gallbladder releases bile into the duodenum connected to the stomach, but unless there is an abnormality, bile contents in the duodenum do not usually reflux into the stomach. Further investigation into this may be warranted, and stomach contents should be collected separately from the small and large intestine contents for *ex vivo* measurements to better assess the stomach biodistribution.

Comparison of [^{76}Br]RD1 organ uptake *in vivo* and *ex vivo* at 48 h shows good agreement within standard deviations for lungs, kidneys and bone (Fig. 5.4). The liver, heart, stomach, muscle, brain and tumor uptake showed significant differences when comparing *in vivo* and *ex vivo* at 48 h (n=16 for normal tissues). The discrepancy between *in vivo* and *ex vivo* liver measurements may be characterized by the inhomogeneous distribution of [^{76}Br]RD1 in the liver, as shown in Figure 5.7C. The right medial lobe (247±36 mg) was measured for all *ex vivo* liver measurements to have a 2.3±0.4%ID/g uptake. The *in vivo* liver measurements were done with both a liver contour and a liver section contour. For the dynamic scan, the liver section had an 11% increase in the measured [^{76}Br]RD1 uptake. This may have been due to the hepatobiliary clearance and not being able to decipher between liver and gallbladder uptake at that time point. At 1 and 4 h, the liver section contour is 2-3% lower than the liver ROI. However, at 24 and 48 h, the difference in the measurements starts to increase. This may be due to an increase in the heterogeneity of [^{76}Br]RD1

uptake in the liver (Fig. 5.7C), in which the liver section measures a 15% higher uptake. If the right medial lobe has a higher uptake than the rest of the liver, this may be why the *in vivo* measurements disagrees with the *ex vivo* measurement.

The *in vivo* [^{76}Br]RD1 uptake in the heart was compared to the *ex vivo* blood and heart uptake to calculate the *P* value. Neither the blood nor heart *ex vivo* measurements are a one-to-one comparison to the heart *in vivo* measurement, since the heart contains only a fraction of the blood during PET scans. For both comparisons, a significant difference was observed. This is most likely due to this faulty comparison. However, the blood had a mean %ID/g closer to the *in vivo* %ID/g compared to the *ex vivo* heart measurement. Using a weighted average of the blood and heart *ex vivo* uptake measurement, and assuming a mass of 20 mg[1] in the heart, the *ex vivo* measured heart+blood is 0.2±0.1%ID/g, compared to the *in vivo* heart uptake of 0.26±0.06%ID/g.

A similar comparison was performed between the stomach and enteric contents. The *in vivo* [^{76}Br]RD1 uptake in the stomach was compared to the *ex vivo* stomach and enteric contents to calculate the *P* value, showing significance when compared to the empty organ. This is expected due to the activity measured in the enteric contents. Unfortunately, the stomach, small intestine and large intestine enteric contents were combined, so the stomach contents could not be compared to the *in vivo* stomach uptake for a more accurate comparison. However, it can be assumed that the *in vivo* stomach uptake measurement are from the contents rather than the organ itself due to the ROI including the contents. Furthermore, no significance was calculated between the enteric contents and the *in vivo* stomach uptake. This is similar to the heart, in which the contents of the organ more closely match the *in vivo* measured organ uptake.

Brain and muscle also showed significant differences between *in vivo* and *ex vivo* [^{76}Br]RD1 uptake, with absolute differences of 0.04±0.02%ID/g and 0.05±0.02%ID/g for the brain and muscle, respectively. The brain mass had an average mass of 450±30 mg. Assuming a blood mass of 19 mg in the brain [180] with a blood activity concentration of 0.47±0.09%ID/g, this could account for the discrepancy in the *in vivo* and *ex vivo* uptake measurements. The brain blood accounts for

[1]This was calculated by taking the average volume of the heart *in vivo* (125±35 mm^3), assuming a density of 1 g/cm^3, and subtracting the average heart mass measured *ex vivo* (102±7 mg).

approximately 4% of the mass, but the blood has 10× higher activity concentration. Losing even a small amount of brain blood during the exsanguination or excision process could play an outsized role in causing an underestimation of the brain %ID/g via *ex vivo* compared to PET.

At 48 h, [^{76}Br]RD1 resides mainly in the liver region. This prolonged retention of [^{77}Br]RD1 may cause toxicity in the liver, with dose estimates of 19.3±0.3 mGy/MBq and 19±2 mSv/GBq in mice and humans, respectively (Fig. 5.16, Table B.12). However, liver uptake of an olaparib-based fluorescent PARP inhibitor was observed to be cytoplasmic, significantly decreasing the equivalent dose to liver cell DNA compared to the nuclear uptake observed in tumor cells [64]. In mice, stomach and intestinal absorbed doses were 270±30 and 720±70 mGy/MBq, respectively, for [^{76}Br]RD1. However, as mentioned above, the ex vivo and in vivo differences indicate that most of the activity and thus dose is in the contents of the organ. Human dose estimates were compared to organ dose reported for ^{18}F-FTT [54]. All [^{76}Br]RD1 human equivalent organ dose estimates were 7±2 times larger compared to PARP-targeted imaging agent, ^{18}F-FTT, except for the lower large intestine (20 times larger).

5.7 Conclusion

Mice were inoculated with ID8 ovarian cancer in orthotopic and heterotopic models. Orthotopic models saw primary tumor growth instead of metastatic growth. Tumor uptake of [^{76}Br]RD1 *in vivo* was difficult to assess, both due to minimal tumor burden and radiopharmaceutical uptake in the small and large intestine. Heterotopic models had slow-growing tumors that also proved difficult to assess the [^{76}Br]RD1 uptake *in vivo*. To evaluate the diagnostic potential of [^{76}Br]RD1, further development of animal models and immunohistochemistry studies of the tumors are necessary.

The *in vivo* pharmacokinetics of [^{76}Br]RD1 in healthy and ovarian cancer model mice were measured, revealing hepatobiliary and renal clearance patterns consistent with other MAe^{-} labeled PARP inhibitors. Murine dose calculations and human dose equivalent estimates were performed using RAPID and OLINDA software. Despite the challenges encountered in developing cancer models, further investigation is warranted due to the observed cytoplasmic or nuclear uptake of the radiophar-

maceutical, which is dependent on cell type. Additionally, PET scans of [$^{76/77}$Br]RD1 can be used as a basis for dosimetric calculations following both diagnostic and therapeutic administrations.

CHAPTER 6
CONCLUSIONS AND FUTURE WORK

6.1 Conclusions

This work describes preclinical experiments used to characterize a MAe$^-$ and PET emitting theranostic pair bound to a PARPi. Future work investigating a MAe$^-$ emitting radiopharmaceuticals could use this work to inform experimental design, and further contribute to the understanding of MAe$^-$ as a potential therapeutic for the treatment of metastatic disease.

This work provided instructions and rationale for future experiments aimed at investigating the fundamental radiation biology of targeted radionuclide therapeutic agents, taking into account the uncertainties associated with *in vitro* and *in vivo* assays.

We measured the pharmacokinetics of [^{77}Br]RD1 in various ovarian cancer cell lines with and without expression of PARP1 and BRCA1. Our observations revealed that the uptake of [^{77}Br]RD1 in human and murine ovarian cancer cells was specific to PARP expression. In addition, we evaluated the cytotoxicity of the radiopharmaceutical and found that it was potent at concentrations 2–4 orders of magnitude lower than those of chemotherapeutic agents. The efficacy of the treatment was PARP-dependent and BRCA-agnostic in cell lines, indicating its potential for treating BRCA-positive ovarian cancer, which is currently difficult to treat with approved PARP inhibitors. These preclinical studies highlight the translational potential of MAe$^-$ emitters and provide valuable insights into fundamental radiation biology.

This study utilized MIRDcell to determine the dose to ovarian cancer cell lines by factoring in their unique characteristics such as cell size, nuclear size, activity cell distribution, and neighboring cells based on cell doubling time. The dose calculations were performed using ^{76}Br positron emitter and MAe-emitters ^{77}Br and ^{80m}Br. Specific uptake of each ovarian cell line was used to convert activity uptake survival curves into dose survival curves. Although the calculated RBE was lower

than that of external beam, cellular dosimetry showed minimal cross-dose to the nucleus for activity distributed outside the nucleus. Further dosimetric studies are necessary to evaluate the toxicity in normal tissue of [^{77}Br]RD1.

Inoculation of ID8 ovarian cancer in mice were intended to provide both orthotopic and heterotopic models. Orthotopic models displayed primary tumor growth instead of metastatic growth. However, the assessment of tumor uptake of [^{76}Br]RD1 *in vivo* was challenging due to minimal tumor burden and radiopharmaceutical uptake in the small and large intestine. Heterotopic models had slow-growing tumors, which also made it difficult to evaluate the [^{76}Br]RD1 uptake *in vivo*. This may have been further exacerbated by a lack of vascularization in the tumors. Thus, further development of animal models is necessary to accurately determine the diagnostic potential of [^{76}Br]RD1. Despite these challenges, our observations of the pharmacokinetics of [^{76}Br]RD1 in nondiseased and diseased mice demonstrated hepatobiliary and renal clearance similar to other MAe^{-} labeled PARPis. The cell type dependent cytoplasmic or nuclear uptake of the radiopharmaceutical further underscores the need for additional research.

For animal models, RAPID was employed with PET/CT scans using radiopharmaceutical [^{76}Br]RD1 to determine the dose obtained in the biodistribution studies. Organ dose per injected activity was calculated from organ contours for ^{77}Br and ^{76}Br. Measured organ uptake was also used to measure the equivalent dose in humans using OLINDA. Additionally, PET scans of [^{76}Br]RD1 can facilitate dosimetric calculations.

6.2 Recommendations For Future Work

The work provided in this thesis could be used to measure the cytotoxocity and biodistribution of PARPi alternatives to rucaparib. Although the radiochemistry of radiobromination with PARPi is outside the scope of this work, once those radiopharmaceuticals have been developed, this work could instruct *in vitro* and *in vivo* imaging and biodistribution of the $^{76/77}$Br-PARPi.

Geant4-DNA is an extension of the Geant4 toolkit designed to simulate interaction of radiation with biological matter on a nano scale, modeling the nanodosimetry for further dosimetric studies

[181]. Benchmark studies comparing the Geant4-DNA calculated S-values of ^{77}Br and ^{76}Br to the MIRD calculations can be done. The PARP1 and PARPi complex bound to DNA geometry, published by the Protein Data Bank (PDB), allows for accurate geometry at the molecular level. It can model the double- and single- strand DNA breaks caused from MAe**-** by tracking particles at the subcellular level. Future work could include DNA damage assessment of MAe^{-} PARPis in ovarian cancer and compare the dosimetry calculations from MIRDcell to Geant4-DNA. Additionally, these calculations could be validated with DNA strand break assays like comet or γ-H2AX assays.

Orthotopic models with tumors in the abdomen proved difficult to image when drug clearance through the small and large intestine occurred. Heterotopic models with subcutaneous injection on the hind leg developed only relatively small masses at the tumor-injection site (TIS) even after growing for 4 weeks. Allowing more time for the tumors to grow in the subcutaneous injection did not seem to work. Investigation into subcutaneous tumors is warranted. It may be necessary to use a different cancer cell line for subcutaneous injection, and if it is a human line, then it would require immunocompromised mice.

The ^{77}Br isotope exhibits potential diagnostic versatility due to its SPECT imaging capabilities. While our studies utilized PET imaging, SPECT imaging could be a more accessible substitute, and exploring the radiopharmaceutical's efficacy with SPECT could enhance the viability of radiobrominated PARPi in clinical settings that lack PET imaging technology. Utilizing SPECT imaging for dosimetric purposes would be a more cost-effective alternative to PET imaging.

If PET/SPECT imaging turns out to be unsatisfactory in terms of diagnostic capabilities even at a preclinical level, and immunocompetent tumor models are preferred over immunocomprimised mice, ID8-luciferase could be used [182]. This allows for bioluminscence imaging (BLI) which detects the light emitted from enzyme-catalyzed reactions to monitor and report molecular-level activity. This technology has high sensitivity, which is ideal for small metastatic lesions in mice. It is also a cost-effective, non-invasive imaging technique that offers real-time imaging with high-throughput capabilities. Developing this model could add a robust workflow to future studies, including therapeutic studies looking at tumor burden and response. With the high sensitivity,

after developing a metastatic model, BLI could offer images that have the capabilities of assessing tumor shrinkage [183] without worrying about shine from other organs due to radiopharmaceutical clearance.

The cytotoxicity and therapeutic efficacy of ^{77}Br-PARPi in mice could be investigated. Although the heterotopic model could be improved, as mentioned above, by using different ovarian cell lines or immunocompromised mice, the orthotopic model may provide a robust, albeit a slow-growing model, provided the disease is validated. With a robust model, maximum tolerated doses could be investigated. From the dosimetry studies, the dose to liver appears to be concerning. However, Pirovano et al. [89] mention that the liver uptake of PARPis is mostly in the cytoplasm. Studies investigating specific organ uptake and cytotoxicity through organoid tissue engineering or veterinary histopathology could elucidate liver and other organ toxicity and maximum tolerated doses.

Appendices

APPENDIX A
PROTOCOLS

A.1 Cell Line Handling

The following procedures are for the adherent cell lines summarized in Table A.1. The procedures are for a T75 flask (75 cm^2). The procedures for different plates require scaling up or down in volume. Six-well plates have an area of 9.5 cm^2 and usually a volume of 3–5 mL while 10 cm diameter plates will have a volume of 7–10 mL. For an explanation of seeding ratio, please see section A.1.2 list item 5. A biosafety cabinet with level 2 capabilities should be used and aseptic technique practiced.

Table A.1: Cancer cell line plating characteristics and specific media. Seeding ratio is from an approximately 80% confluent plate. Doubling time for both UWB1.289 is from the ATCC website. Roby, *et al.* reported them as 15 h and 20 h for UWB1.289 and UWB1.289+BRCA1, respectively [130].

Name	Doubling Time	Passage Rate	Seeding Ratio	Medium
ID8	13 h	2–3 days	1:5–1:10	• DMEM (4.5 g/L D–glucose, 0.11 g/L sodium pyruvate) • 4% FBS • 1% Pen/Strep • 5 µg/mL insulin, transferrin + 5 ng/mL sodium selenite (1x ITS)
OVCAR8	24 h	3–4 days	1:3–1:6	• RPMI–1640 • 10% FBS • 1% Pen/Strep
OVCAR8 PARP1–KO		3–4 days	1:3–1:5	• OVCAR8 media • 2 µg/mL puromycin
UWB1.289	56 h	3–4 days	1:2–1:5	• 44.5% RPMI–1640 • 44.5% MEGM • 10% FBS • 1% Pen/Strep
UWB1.289+BRCA1	36 h	2–4 days	1:4–1:6	• UWB1.289 media • 200 µg/mL G-418

A.1.1 Thawing

To ensure the highest level of viability, thaw the cells immediately upon receipt from the vendor. If they are brought up from liquid nitrogen (LN), store on dry ice for less than 30 minutes until the

thaw procedure.

1. Warm medium to 37°C and gather sterile 1 mL pipette tips and 15 mL polystyrene conical tubes and place in the BSC.
2. Gently agitate the vial of frozen cells in a 37°C water bath. Do not submerge the cap to protect the cells from contamination.
3. When a sliver of ice is left in vial, remove contents from water bath and spray with 70% EtOH to keep aseptic conditions.
4. Transfer tube to the BSC. Add 1 mL of 37°C medium drop-wise to the vial. Gently transfer the contents of the vial by pipette (do not pour cells to avoid contamination) to a 15 mL polystyrene conical tube.
5. Add another 1 mL of medium drop-wise and an additional 7 mL medium and spin at approximately 125 g for 5 minutes.
6. Discard medium and resuspend the cell pellet in 3 mL of medium, gently breaking up the pellet to avoid clumping and creating a homogeneous mixture.
7. Place this in the plate size of choice. If using T75 plates, can usually split 1 vial into 1 T75 plate with a passage rate of 6–36 h. Add 7 mL medium for a total volume of 10 mL.
   (a) The ID8 cells grow quickly. If using one T75 flask, they should be thawed in the morning and checked at the end of the day for passing or thawed at the end of the day and passed first thing in the morning to avoid reaching 100% confluency. Otherwise, use 2 T75 flasks.
8. Incubate the plate at 37°C with 5% CO_2 and humid conditions.

A.1.2 Subculturing

Follow the subculturing procedure when cells are 70–90% confluent. The following procedure is for a T75 flask.

1. Remove and discard the culture medium.
2. Rinse the cell layer with room temperature PBS and discard, approximately 5 mL.
3. Add 2 mL of trypsin-EDTA solution to the flask to detach the adherent cells for 2–5 minutes at 37°C.
   (a) Use 0.25% (w/v) trypsin–EDTA for ID8, UWB1.289 and UWB1.289+BRCA1 cells.
   (b) Use 0.05% (w/v) trypsin–EDTA for OVCAR8 and OVCAR8 PARP1–KO. If cells are not detaching, use 1.5 mL of 0.05% trypsin–EDTA and 0.5 mL of 0.25% trypsin–EDTA. Increase the amount of 0.25% trypsin–EDTA as necessary to detach the cells.
4. Add 4 mL of medium to neutralize the trypsin and gently pipette to disperse the cells.

   (a) If plating the cells at a concentration equal to or less than 1:6 in a T75, the cells can be plated at the desired concentration and incubated at 37°C in 5% CO_2. The final neutralized trypsin concentration will be less than 5%.
   (b) If more than 1 mL of the trypsin–EDTA/medium mixture will be used in a T75 or if plating the cells in a volume where the neutralized trypsin volume will be larger than 5%, centrifuge the cell suspension at 125 g for 5 minutes. Discard supernatant and resuspend in fresh medium.

5. Aliquot the cell suspension in the desired seeding ratio as shown in table A.1. For a T75, a final medium volume of 8–12 mL is appropriate.

   - A 1:6 seeding ratio means that from a confluent plate, it was split 6 ways. So if a confluent plate is dispersed in 6 mL of volume (2 mL of trypsin + 4 mL of medium), a 1:6 seeded plate will have 1 mL of this volume with the appropriate amount of fresh medium (8–11 mL). If the seeding ratio is 1:12, it was split 12 ways, so it will use 0.5 mL of the cell+medium and 8–11.5 mL of fresh medium.

6. Incubate cultures at 37°C in 5% CO_2 and humid conditions. Label plate with passage number.

A.1.3 Freezing

One T75 80–90% confluent plate should go into one frozen vial. Cells can be grown in several T75 plates to freeze several vials at a time or to have an extra plate full of cells in case the T75 plates do not reach 80–90% the day of cryopreservation. The cells from the extra plate can be divided into the other quantities to supplement the cell count.

1. Use a freezing container with an ability to cool at a rate of -1ºC/minute all the way to -80ºC (Mr. Frosty Freezing Container, Thermo Scientific). Fill it with 100% isopropyl alcohol between room temperature and 4°C. Make sure to replace the alcohol after every 5th use.
2. Label sterile 2 mL cryogenic storage vials with the cell type, date, passage number, and scientist's initials.
3. Make cryopreservation medium with complete growth medium supplemented with DMSO.
   (a) 10% (v/v) DMSO for ID8. Alternatively, can use 90% FBS with 10% DMSO.
   (b) 5% (v/v) DMSO for OVCAR8, OVCAR8 PARP1–KO, UWB1.289 and UWB1.289+/-BRCA1.
4. Follow subculture protocol through step 4.
5. Centrifuge cells at 250 g for 5 min. Discard supernatant.
6. Depending on number of 80–90% confluent T75 plates, add the appropriate volume of cryopreservation medium so that each cryogenic storage vial has $\sim$1–1.5 mL.
7. Place each storage vial in the freezing container and place in a -80°C freezer. If necessary, you can place it in a -20°C freezer short term before transferring it to -80ºC.
8. After 24 h, transfer tubes to liquid nitrogen.

A.2 Preparing Concentration Stock Vials

An Excel spreadsheet has been made to assist with calculating the volume needed for cytotoxic and/or uptake studies. One cyclotron production of [^{77}Br]RD1 can yield 1–2 cytotoxicity studies and 1–3 uptake studies. Cytotoxicity studies require a much higher concentration of the radiopharmaceutical compared to the uptake studies. Uptake studies can be diluted in cold BrRD1 to keep the molar concentration high without using all the radiopharmaceutical product. The activity is still high enough to have a sufficient signal when measuring via gamma counter.

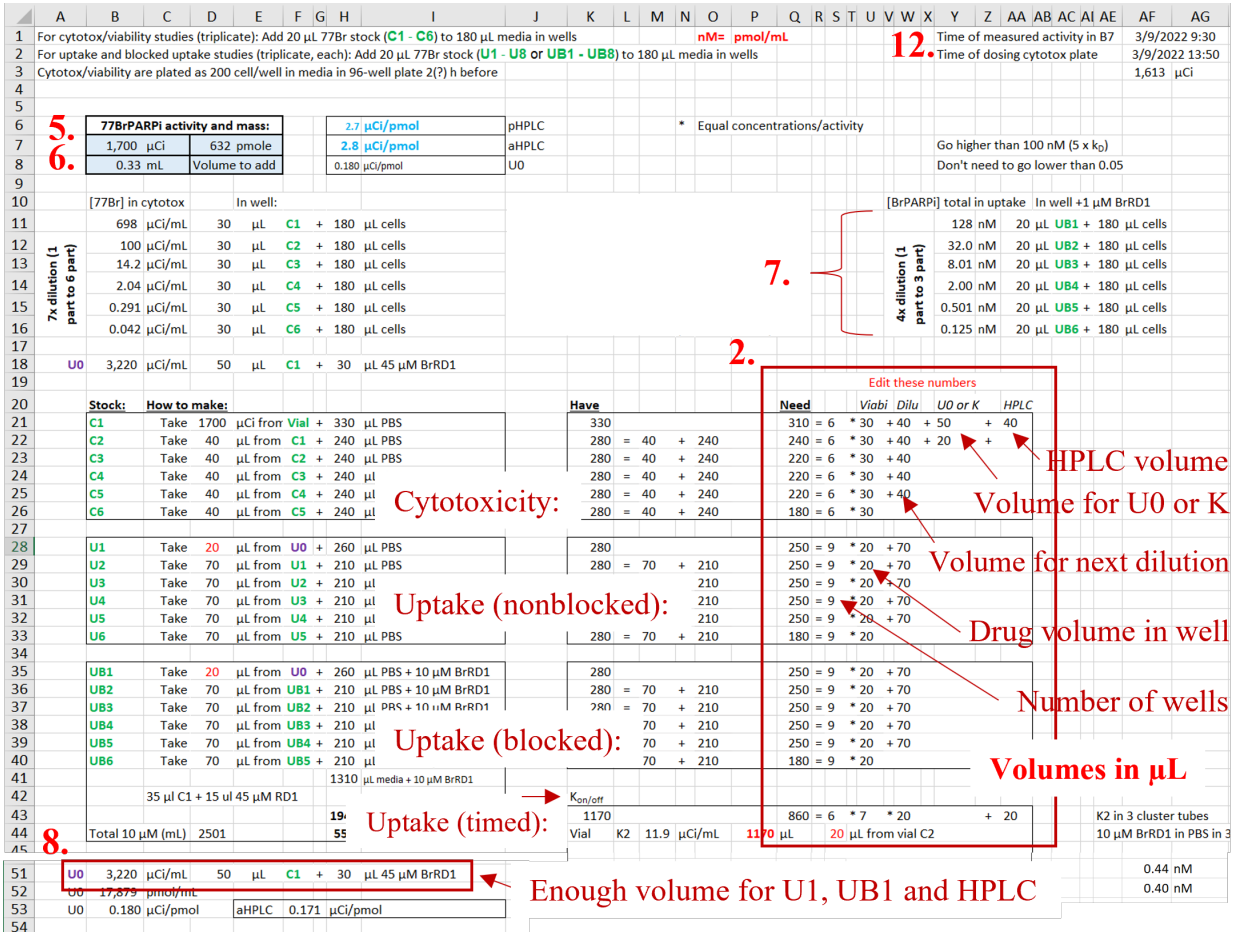

Figure A.1: Excel spreadsheet to calculate volumes and concentrations depending on type and number of assays to perform after production of [^{77}Br]RD1.

1. Use the [$^{76/77}$Br]RD1CellStudy_StockMixing Excel spreadsheet to calculate the volume needed at each concentration level for the number of studies conducted.

2. The box in red is where the user can put in the information based on the number of studies and plates.

    - Column S is for the number of wells to be dosed at that specific concentration. Each study should be done in triplicate, so 2 plates in triplicate would be 6 wells.

- Column U is for the volume of drug in each well. This is usually 20 μL administered in a well with 180 μL of media.
- Column W is the volume needed for the next serial dilution. Cytotoxic studies had 1/7th serial dilutions and uptake studies had 1/4th serial dilutions.
- Column Y is for the volume taken for non-serial dilutions. An amount from the cytotoxic 1 concentration (C1) vial is used to make the uptake concentration vial (U0) that will be used for the non-blocked uptake concentration vial (U1) and the blocked uptake concentration vial (UB1).
- Column AA accounts for the volume required to measure the molar concentration via analytical HPLC for 20 μL injections. In this case, it allows for 2 injections.

3. Have the [^{77}Br]RD1 transferred to a mass-measured, sterile cluster tube preceding the dry-down step.
4. Measure the activity and volume of the dried down [^{77}Br]RD1 in the cluster tube.
5. User can input the activity in B7 and the assumed moles in D7 based off the molar activity as measured by the preparative HPLC.
6. The dried down [^{77}Br]RD1 will usually be approximately 10-60 μL, so add the amount of PBS required to bring the volume to at least the volume needed as calculated in Q21. Make sure to include some extra volume to account for losses in tubes and pipette tips. That is why B8 (0.33 mL, the total volume) is 20 μL larger than Q21 (0.31 mL).
7. For uptake studies, the molar concentration should be above 5× k_D, i.e., 100 nM, and no lower than 0.05 nM.
    - Nonblocked uptake serial dilutions are done in PBS.
    - Blocked uptake serial dilutions are done in PBS + 10 μM BrRD1. This will give 1 μM BrRD1 in the well with volume 200 μL.
    - Excel cell Y11–16 will calculate the molar concentration in the 96-well plate wells.
8. Change the amount of volume needed from C1 and the volume of 45 μM BrRD1 to get the amount needed, both in volume and concentration value, for the uptake studies.
    - Nonblocked (U1–6) and blocked (UB1–6) concentrations should match each other.
9. After dosing plates, a known mass should be taken from each concentration vial.
10. This known mass should be measured via gamma counter.
    - User can compare U1–6 to UB1–6 vials to make sure the activity concentration matches.
    - Can also double-check that dilutions were seven-fold and four-fold for cytotoxicity and uptake concentration vials, respectively.
11. The measured activity concentration can be compared to the calculated activity concentration as a quality check.

12. Decay correction at the time of dosing plates is necessary for the cytotoxicity studies which use activity concentration. Cell AF1–3 allows for entering the time between measuring the activity of vial C1 and the time of dosing cytotoxicity plate. The equation in cell B11 uses the decayed measurement to calculate the activity concentration.

A.3 Total, Nonspecific and Specific Binding

1. Plate cells 24 hours before the study at a high density but below confluence on the day of the study.
    - Plating 24 hours allows for the cells to settle and enter different phases of the growth cycle.
    - You can also plate at a lower amount knowing that the cell density will increase the next day, meaning you will need fewer cells to begin with.
    - Plating anywhere from 20,000–60,000 cells/well depending on the doubling time.
    - Plate cells in triplicate for 6 dose concentration levels and a control. In one plate, can seed both the nonblocked and blocked triplicate wells, to plate 7 columns for 2 studies in triplicate, or 42 wells.
    - Plate wells in a volume of 180 µL.
    - Add 200 µL PBS in surrounding wells to avoid edge effects on dosed wells caused by evaporation on the outer wells.
2. Follow the instructions from A.2 for the uptake vials, including the nonblocked and blocked sections.
3. Add 20 µL of the correct concentration of [^{77}Br]RD1 in triplicate (U1-6 series) or 20 µL [^{77}Br]RD1+10 µM BrRD1 in triplicate (UB1-6 series. For the control wells, add 20 µL of PBS. Use Fig. A.2A for reference.
4. Let the plate sit for 2 hours after adding the radiopharmaceutical at 37ºC in CO_2.
5. After 2 hours, remove the media+radiopharmaceutical and place in corresponding cluster tubes for each well. Label the cluster tubes with the corresponding radiopharmaceutical concentration and a–f.
6. Rinse the empty wells with 100 µL PBS.
    - Work in batches so that the cells are only ever contacted with PBS for no more than $\sim$10 seconds.
7. Collect the 100 µL of PBS and place in the corresponding cluster tube.
8. Add 100 µL of warmed 0.5% EDTA+trypsin and let sit on cells for greater than 10 minutes at 37ºC.
    - Dissociating the adherent cells from the plate is more important than keeping the cell walls intact, hence why trypsinizing for longer than recommended is fine in this instance.
9. After trypsinization, use pipettes to mix the contents in each well. Any cells that are still adhered to the plate can be dislodged from the mechanical motion of the contents being collected and ejected from the pipette. Do this for at least 20 seconds.

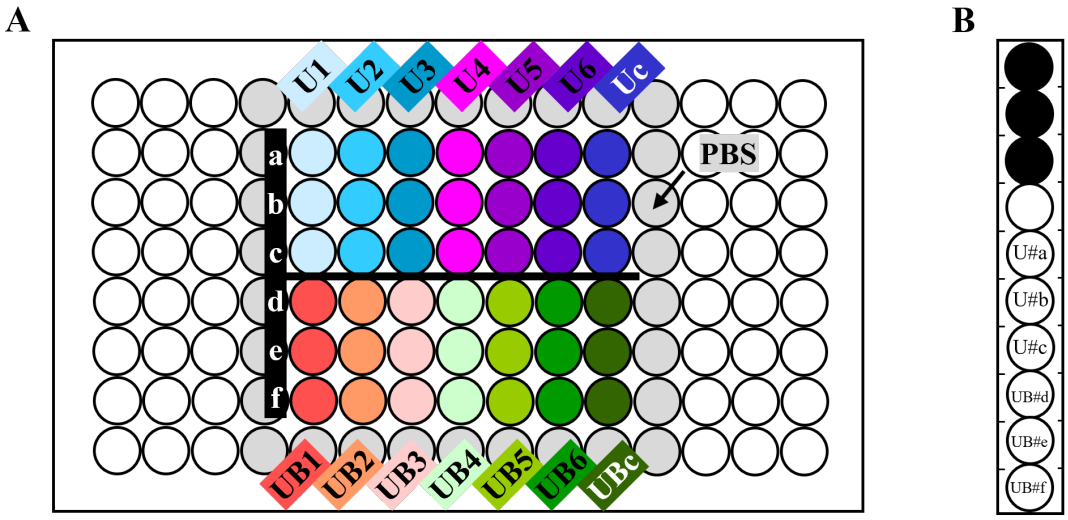

Figure A.2: (**A**) Radiopharmaceutical concentration orientation of wells. Series Uc and UBc are the control wells with no radiopharmaceutical added, just 20 µL of PBS. Wells with cells and radiopharmaceutical are surrounded by wells with 200 µL of PBS to avoid edge effects on dosed wells. (**B**) A ten-sample rack orientation for the gamma counter. The first 3 slots are empty, the 4th slot has an empty sample holder for a rack background count, and the next 6 slots have samples from the same radiopharmaceutical concentration level.

10. Collect the trypsin+cells and place the contents of each well into new cluster tubes, except for the Uc and UBc series.

11. Use a hemocytometer to count the number of cells in each well for all 6 wells of the U/UBc series.

    - Add 100 µL of PBS to the U/UBc wells for a total volume of 200 µL.
    - Assuming all wells have the same seeding density, calculate the average and standard deviation of the number of cells/well.

12. Rinse the empty wells with 100 µL of PBS vigorously using a pipette. You can do this by collecting and ejecting the contents in the well with a pipette.

13. Collect the 100 µL of PBS and place in the corresponding cluster tube.

14. Check the contents of the plate under a microscope to make sure all cells have been collected. If not, repeat adding trypsin and placing in the incubator.

15. Place the trypsin+cells containing cluster tubes in the gamma counter racks from the highest activity concentration to the lowest, as shown in A.2B.

    - Use the racks with 10 slots per rack.
    - Keep the first 3 slots empty and add sample holders to the next 7 slots.

- Add no sample to the first sample holder (for background count), then add the U and UB series of the same radiopharmaceutical concentration to each sample holder, e.g., U1a, U1b, U1c, UB1d, UB1e, UB1f for rack 1, U2a, U2b, U2c, UB2d, UB2e, UB2f for rack 2, etc.

16. Place the media containing cluster tubes in gamma counter racks from the highest activity concentration to the lowest, as shown in A.2B.

    - The vials containing media will have a higher activity than the vials containing cells. You can wait 1-3 days (depending on the activity) to count the contents of the media so that you do not have a high dead time on the gamma counter.

17. Use the gamma counter on the [^{77}Br] setting and count each vial for at least 1 minute.

18. Check that the background (empty) sample is no more than 10% of any of the other samples in the same rack. If it is, remeasure the entire rack, either in one rack or split up into multiple racks.

19. Check that none of the samples (excluding background samples) have a dead time over +10%. If it does, remeasure the sample.

20. Convert gamma counts (CPM) to decay corrected activity (to the time of contact with radiopharmaceutical).

21. Divide the activity counted for each vial by the number of cells/well to get the activity per cell.

22. Divide activity/cell by the molar activity of U1 and UB1 as measured by the aHPLC to get the attomol/cell.

23. Plot the total binding (U series) and nonspecific binding (UB series) in units of amol/cell as a function of molar concentration (nM).

24. Subtract the average nonspecific binding at a certain concentration level from the average total binding at the same concentration level to get the specific binding.

25. Plot the specific binding (amol/cell) as a function of molar concentration (nM).

A.4 Timed Uptake Studies

1. Plate cells 24 hours before the study at a high density but below confluence on the day of the study in a volume of 180 µL. For 9 time points in triplicate, plate cells in 56 wells. Add 200 µL of PBS to surrounding wells to avoid edge effects on wells with cells.

2. Prepare the radiopharmaceutical vial to have a final concentration in wells of at least 37 kBq/mL (1 µCi/mL). Use the Stock Mixing Excel file to help with calculating the appropriate volume and dilution from C1 or C2, depending on the number of time points and number of studies.

3. Create a 10 µM BrRD1 in PBS solution to add 20 µL to each well for the dissociation (k_{off}) portion. That is 27 wells for 9 time points in triplicate.

4. An hour before beginning the time point series, add 20 µL of the radiopharmaceutical to all k_{off} wells. See Fig. A.3A for reference of a plate orientation that you can use.

    - Adding the radiopharmaceutical an hour before the time point series allows for simultaneous plate workup of the association and dissociation assay instead of having to do it sequentially.

5. When dosing the cells, keep the cells warm by using a hot pad at 37ºC. Transfer the plate to the incubator between time points if there is enough time.

6. Fig. A.3A shows numbers (in minutes) on the left-hand side that will correspond to the eventual time point that you will use to graph the data for k_{on}, and after adding 60 minutes, the time points for k_{off}. In chronological order, you will:

    - At t=0 min, add radiopharmaceutical to all k_{off} wells.
    - At t=60 min, add radiopharmaceutical (20µL) to the top row (labeled 60) of k_{on} wells and antagonist (20 µL of 10 µM BrRD1) to k_{off} wells.
    - At t=75 min, add radiopharmaceutical to the next row (labeled 45) of k_{on} wells and antagonist (10 µM BrRD1) to k_{off} wells.
    - You will repeat adding radiopharmaceutical to the k_{on} wells and antagonist to the k_{off} wells for each subsequent row labeled 30, 15, 10, 5, 3, 2 and 1 at t=90, 105, 110, 115, 117, 118 and 119 minutes, respectively.
    - At t=120 min, you will remove all the media, starting with the bottom row and working backwards, and place it in corresponding cluster tubes.

7. After collecting the media, rinse each row one at a time with 100 µL of PBS. Do not let the PBS sit for more than 5 seconds on the cells.

8. Transfer the rinse to the corresponding cluster tubes with the media. Label the cluster tubes.

9. Add 100 µL of 0.5% EDTA+trypsin to each well. Incubate at 37ºC for at least 10 minutes.

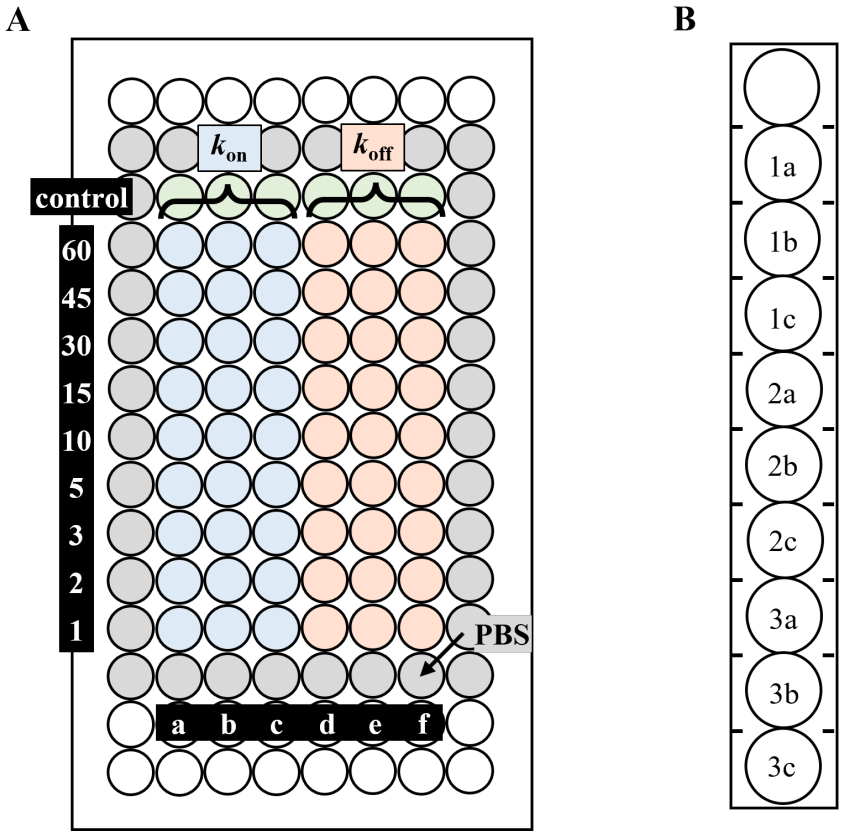

Figure A.3: (**A**) Timed uptake orientation of wells. The k_{off} series had the radiopharmaceutical added to it 60 minutes before beginning the timed series. The labels on the left-hand side corresponds to the plotted time in minutes (add 60 to each label for the k_{off} data). At each time point, starting at time point labeled 60 minutes, radiopharmaceutical was added to the k_{on} series and antagonist was added to the k_{off} series. This was repeated for subsequent rows at the corresponding time. (**B**) A ten-sample rack orientation for gamma counter measurements. The first slot has an empty sample holder for a background count, and the next 9 slots have samples with increasing activity levels, starting with k_{on} at time point label 1. Repeat the same order for the k_{off} vials.

10. After trypsinization, use pipettes to mix the contents in each well. Any cells that are still adhered to the plate can be dislodged from the mechanical motion of the contents being collected and ejected from the pipette. Do this for at least 20 seconds.

11. Collect the trypsin+cells and place the contents of each well into new cluster tubes, except for the control wells.

12. Use a hemocytometer to count the number of cells in each well for all 6 wells of the control row.

    - Add 100 µL of PBS to the control wells for a total volume of 200 µL.
    - Assuming all wells have the same seeding density, calculate the average and standard deviation of the number of cells/well.

- When repeating this procedure, aim for the same number of cells in each well.

13. Rinse the empty wells with 100 μL of PBS vigorously using a pipette. You can do this by collecting and ejecting the contents in the well with a pipette.

14. Collect the 100 μL of PBS and place in the corresponding cluster tube.

15. Check the contents of the plate under a microscope to make sure all cells have been collected. If not, repeat adding trypsin and placing in the incubator.

16. Add the cluster tubes containing the cells to gamma counter racks. You can use the 10-sample racks and use the order shown in Fig. A.3B.

    - Fig. A.3B shows the first rack with the k_{on} vials. Continue the second rack with vials from rows labeled 5, 10, 15, 30, 45 and 60, respectively.
    - Clear the racks from the scanner. Add the k_{off} vials to the racks in the same order, starting with the last row labeled 1.

17. Add the cluster tubes containing the media to the gamma counter racks in the same order as the cell containing vials. You can wait 1-2 days for the activity to decay away so you do not have a high dead time on the gamma counter.

18. Use the gamma counter on the [^{77}Br] setting and count each vial for at least 1 minute.

19. Check that the background (empty) sample is no more than 10% of any of the other samples in the same rack. If it is, remeasure the entire rack, either in one rack or split up into multiple racks.

20. Check that none of the samples (excluding background samples) have a dead time over +10%. If it does, remeasure the sample.

21. Convert gamma counts (CPM) to decay corrected activity (to the time row labeled 60 was dosed).

22. Add the activities of the corresponding vials of media with the vials of cells for each well.

23. Divide the activity measured from the vials of cells from the corresponding activity total of that well to get the percent uptake.

24. Plot the percent uptake as a function of time (the labeled numbers for k_{on} and the labeled numbers+60 for k_{off}).

A.5 Luminescence Assay

1. Store CellTiter-Glo 2.0 reagent in 1-2 mL aliquots at -80°C.
2. Thaw the appropriate volume of CellTiter-Glo 2.0 reagent at 4°C overnight.
3. Before use, equilibrate reagent to room temperature on the bench-top for ∼30 minutes. Do not use temperatures above 25°C.
4. Equilibrate medium to room temperature.
5. Mix room temperature medium and reagent in equal parts for a volume equal to 50–100 µL per well in a 96-well plate.
    - Make an extra 0.5–1 mL of medium/reagent mixture to account for losses from pipettes and the reservoir.
6. Place medium/reagent mixture in a reagent reservoir to quickly add contents to wells in a 96-well plate.
7. Remove media from 96-well plate and add medium/reagent mixture to each well of interest.
    - Make sure to add the same amount to all wells to ensure a consistent luminescence signal.
8. Mix the contents for 2 minutes on an orbital shaker to induce cell lysis. Shaking the plate manually to simulate an orbital shaker can also be done.
9. Allow the plate to incubate at room temperature for 10 minutes to stabilize the luminescent signal.
10. Record luminescence and normalize the treated well readings to the control readings.

A.6 Clonogenic Assay

A.6.1 Cell Plating and Staining

1. Follow the subculturing procedure in section A.1.2 through step 4.
2. Use a hemocytometer to count the number of cells.
   (a) Fill both sides of the hemocytometer with 10 µL each.
   (b) Count the number of cells found in the highlighted 1.0×1.0 mm^2 corner boxes as shown in Fig. A.4 for both sides of the hemocytometer. At least four of the 1.0×1.0 mm^2 box's cell contents should be counted.
   (c) Chose two sides of the 1.0×1.0 mm^2 box and only count cells that straddle the line on those two edges and exclude cells that straddle the line on the other two edges.
   (d) Average the number of cells counted per 1.0×1.0 mm^2 box. Multiply this number by 1×10^4 to calculate the number of cells per mL.

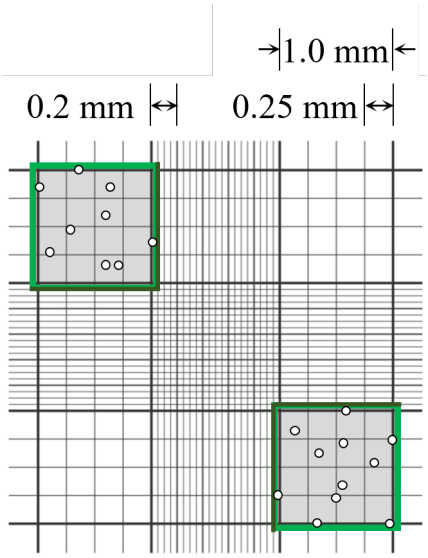

Figure A.4: Hemocytometer dimensions and example. If counting the 1.0×1.0 mm^2 boxes marked in green and choosing to count the outside edges of the hemocytometer, the upper left-hand corner has 8 cells, the lower corner has 9 cells, and the average count is 8.5×10^4 cells/mL.

3. Dilute the cell suspension into the desired seeding concentration and place in plates.
   - For most protocols found in this thesis, this will be a 6-well plate. Other plates commonly used are 10 cm or 35 mm diameter plates.
   - The seeding concentration will depend on the cell type and treatment dose. The control wells will be seeded at a lower density than the highest dosed plates to get good counting statistics for the highest dosed plates.
   - The diluted concentrations made after counting the density with the hemocytometer are assumed to be perfect.

4. Let cells adhere for 2 hours before treatment. Incubate at 37°C in 5% CO_2 and humid conditions.

5. Dose the cells. Handle control plates in the same way as dosed plates (remove from incubator for the same amount of time, etc.).

6. After treatment dose, place dishes in incubator and leave them there until cells in the control dishes have formed sufficiently large colonies. This can take 5-14 days depending on the seeding concentration and cell type.

7. Remove the medium from the plates.

8. Rinse the plates with room temperature PBS. For a 6-well plate, use $\sim$2.5 mL. Discard the PBS.

9. Add 2 mL of a 6.0% glutaraldehyde and 0.5% crystal violet mix to fix and stain the colonies.

10. Leave the solution on the cells for at least 30 min.

11. Fill a tub with tap water. After removing the stain from the plates, carefully submerge the plates into the water to rinse the stain off.

12. Repeat the rinsing step if the water becomes sufficiently stained and there is still stained water in the plates (rather than clear water).

13. Leave the dishes to dry upside down for at least 24 hours.

14. Count the number of colonies found on the plates. An easy way to take pictures is by using a light-box in a dark room. A white computer screen can work as a light-box.

    - If the light-box creates a Moiré-pattern artifact, move the plate away from the light-box until it disappears. A distance of 1 m from the light-box should suffice to get the artifacts to disappear on a digital camera.

15. Use the ColonyArea plugin for ImageJ to quickly count the number of colonies.

16. Calculate the plating efficiency (PE) by using the ratio between the number of colonies counted in the control to the number of cells seeded, as shown in Eq. A.1:

$$\mathrm{PE} = \frac{\#\text{ of control colonies}}{\#\text{ of cells seeded}}, \qquad \text{(Eq. A.1)}$$

    which can then be used to calculate the surviving fraction (SF) for the treated plates using Eq. A.2:

$$\mathrm{SF} = \frac{\#\text{ of colonies}}{\#\text{ of cells seeded} \times \mathrm{PE}}. \qquad \text{(Eq. A.2)}$$

A.6.2 ImageJ Colony Counting

This plugin can be downloaded at http://www.btk.fi/research/research-groups/abankwa/downloads/. It will require the latest version of ImageJ to function properly. These instructions have been modified from the ColonyArea User Manual [184]. The below instructions are for colony forming cells. For lawn forming colonies, follow the extra step in A.6.2.1.

1. Take pictures of your plates with a light box so there are no shadows. This will allow the plugins to accurately assess colonies or cells correctly. I used a computer screen in a dark room, held up the plate 1 m away and took a picture with my smartphone.
2. For images that do not have the wells in a straight line:
   - Go to Image →Transform →Rotate
   - Set the angle to 0º. An error of 1–1.5º is tolerable. Click OK.
3. Use the *Rectangular Selection* tool from the toolbar to make a ROI containing all the wells to be processed. The ROI should touch the outer walls of the wells, as shown in Fig. A.5.
4. Go to Plugins →ColonyArea →Colony area
5. Create a folder for the processed pictures to be saved to.
6. Chose the correct input for the type of plate you are processing, and then the correct number of rows and columns for said plate.
7. The wells will be converted into two cropped ROI gray scale (8-bit) image stacks (with the option of clicking through the stack to see a different well). One stack contains the gray scale images, and the other stack contains the same images with pixel values converted to an intensity used from a lookup table (LUT) as described in Chapter 3.3.4.3.
8. An additional window with the threshold of each of the wells will pop up.
9. Use the *Straight* line tool from the toolbar and place it along the diameter of the well.
10. Go to Analyze →Set Scale... and place the known diameter of the well into the *Known distance* box (35 mm for a 6-well plate). Add the unit of length as mm.
11. Go to Image →Adjust →Threshold to convert the image into a black and white picture.
    - You can use the Threshold popup as a guide for the maximum value.
    - The purpose is to have all pixels associated with colonies as black and all pixels associated with shadows or the well as white.
12. Go to Analyze →Analyze Particles and change the size and circularity threshold as necessary.
    - Adding a minimum to the size parameter will exclude colonies of too small a size.
    - Changing the minimum of the circularity parameter may help exclude counting anything that isn't a round colony.

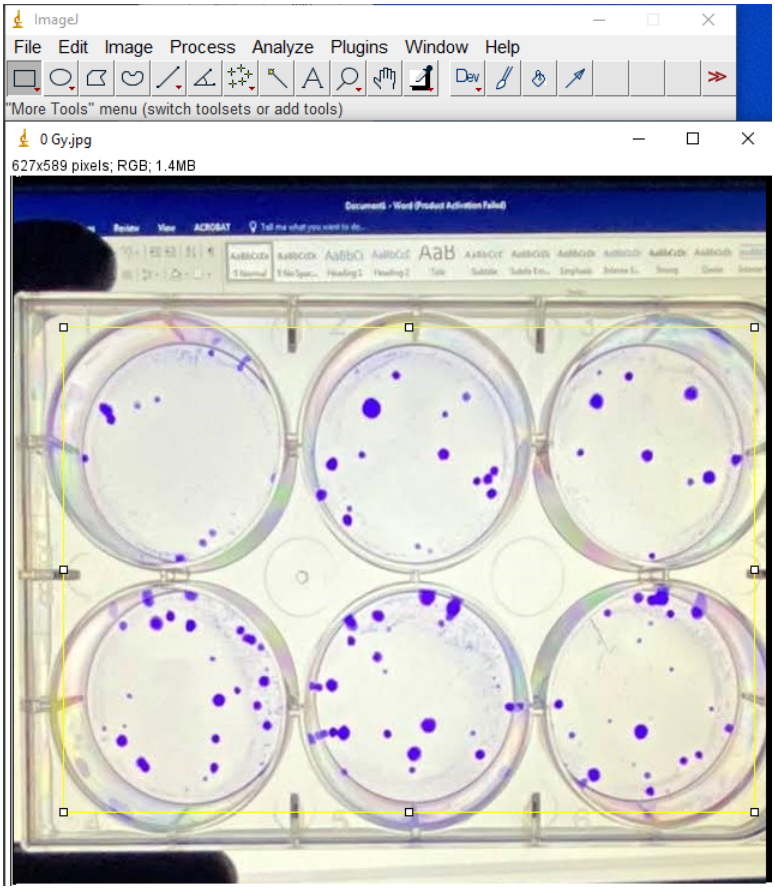

Figure A.5: Use the rectangle selection tool to outline the wells to analyze. The box should encompass the wells themselves (yellow line) instead of the edges of the well as to not throw an error. You can see here that I used a blank page of Word to have the computer screen fill with white to get a clean picture of my plate.

- Using *Overlay* or a different option from the *Show* dropdown menu allows you to see which colonies the Analyze Particles feature counted. Make sure the *Overlay* box is checked for it to appear (as shown in Fig. A.6) to validate whether the correct colonies are counted.

13. Check the boxes *Display results* and *Summarize*. The Results box will summarize the area of each colony. The Summary box will summarize the colony count of each well along with the average size of each colony and the % area of the well covered in cells.

14. Click OK and click Yes to process all 6 images. Double check that the colonies you want to count are included and those that you don't want are excluded.

15. Record the number of colonies per plate. Find the average value and standard deviation at each dose level. Normalize the values to the control plate and plot the surviving fraction as a function of dose.

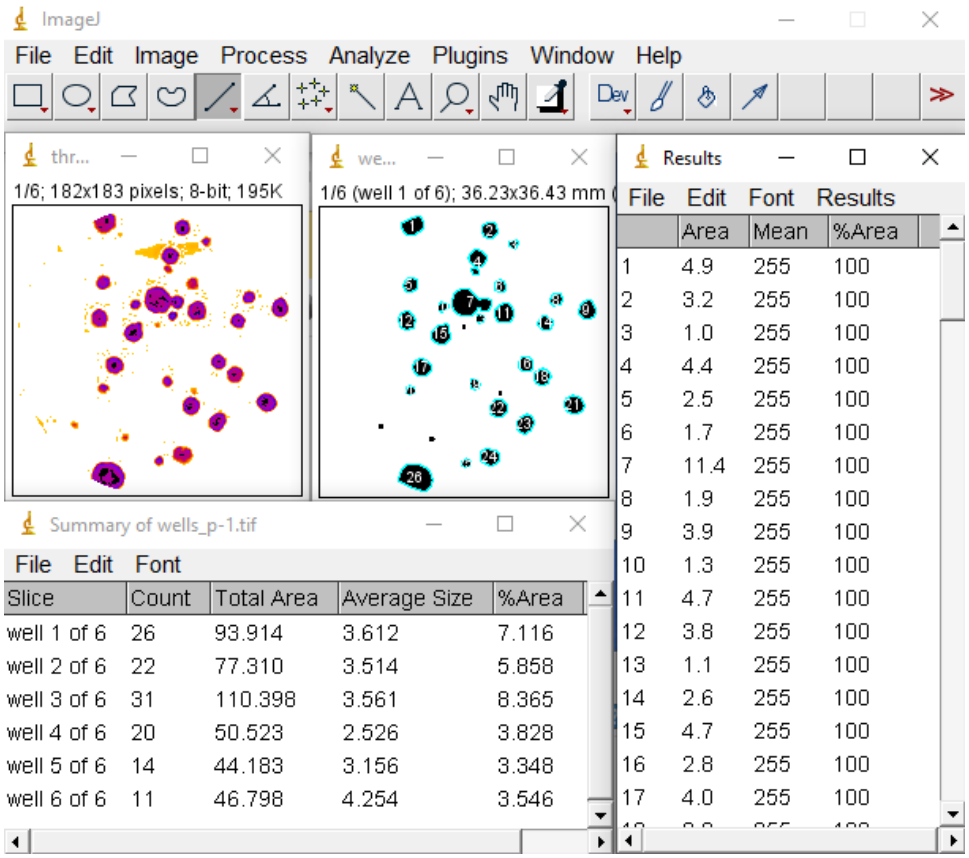

Figure A.6: The LUT image stack is shown in the top right (showing well 1 of 6). The gray scale images processed into binary images are shown in the middle box. It also has the Overlay (shown in blue) from Analyze Particles and a count marker over each counted colony. The Results box summarizing the characteristics of each colony is shown on the right, and the Summary box for all images in the stack is shown in the lower left box.

A.6.2.1 Lawn Forming Cells

1. Follow the instructions above. Before step 12, use the *Oval* selection tool to draw an ROI over an individual colony.

2. Go to Analyze →Measure to measure the area of an individual colony. Repeat this 8 times for different colonies to get the average size and standard deviation of a colony.

    - The Area reading is the size of the ROI. Use the % Area multiplied by the Area to get the colony size in mm^2. This will be the unit if you followed step 10 in section A.6.2 to set the scale of the image.

3. Use the *Oval* selection tool to draw an ROI over the entire well. Use the Measure tool to measure the ROI size and the % Area covered in cells. Fig. A.7 shows how the ROI selection tool is used to make measurements for the colonies and the wells.

4. Multiply the Area and % Area to get the area of the plate covered in cells. Divide this by the average size of a colony that you obtained in step 2. Repeat this for each well.

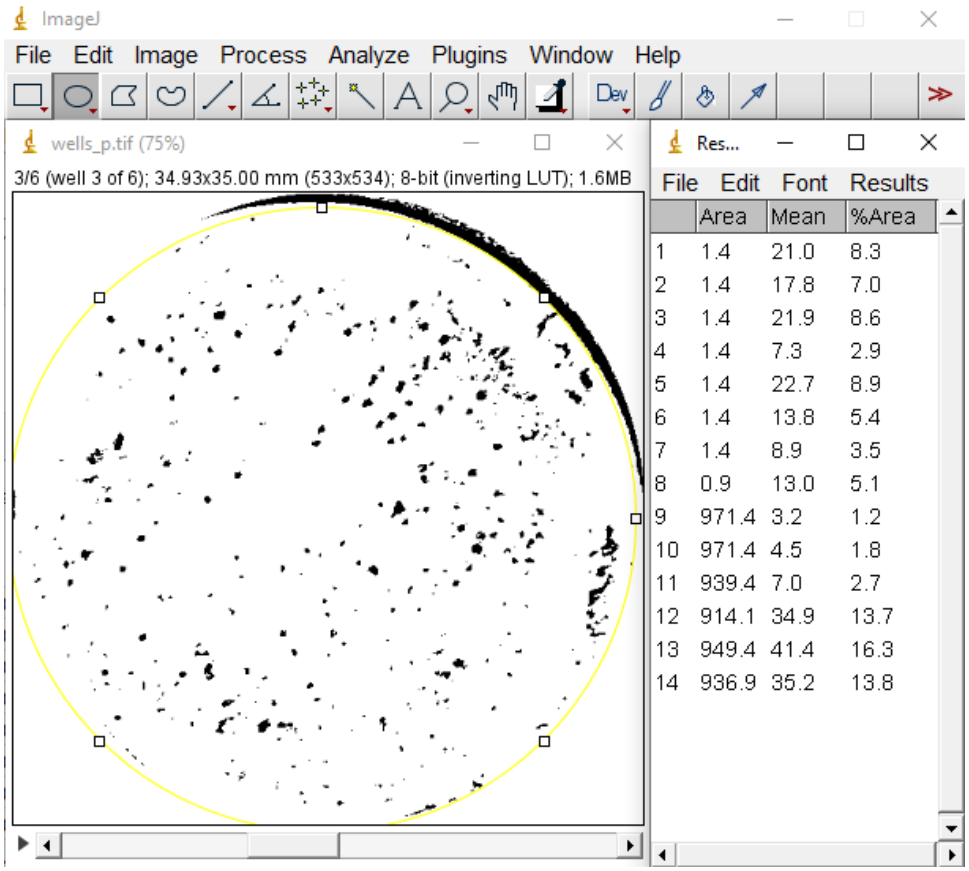

Figure A.7: The left image is after converting the image stack to binary images. The *Oval* selection was used to place an ROI over the well. The shadow from the well edge is excluded from the ROI selection. The Results box on the right shows measurements for individual colonies as the first 8 entries. The final six measurements are of the entire well.

5. Record the number of colonies per plate. Find the average value and standard deviation at each dose level. Normalize the values to the control plate and plot the surviving fraction as a function of dose.

A.7 External Beam Radiotherapy Treatment

1. Follow plating procedures for specific cell lines. For various assays, follow the cell density plating procedure corresponding to that assay.
2. Let cells adhere to the bottom of the plate for 2 hours after plating.
    - Six-well plates can be used. They allow for two seeding densities in triplicate for each dose. If colonies form for both seeding densities, you will have results in sextuplicate.
    - If the seeding density is too high (colonies start to grow into each other and form a lawn), or a seeding density is too low (0–1 colonies grow leading to large errors), then hopefully you will still have results in triplicate with the other seeding density.
3. When transporting cells from the incubator to the irradiator room, cells should be kept as close to 37°C as possible.
    - If the room has an incubator, use that while individual plates are being irradiated.
    - Use either heat packs that have been warmed to 37°C or a heating pad set to 37°C in a styrofoam box big enough for all the plates to fit for transport.
4. Choose a focal source distance (FSD) that will have a field size (FS) big enough to irradiate plates. This will probably be FSD=30 cm with FS diameter=19 cm for 2 plates.
    - If using only 1 plate, can use FSD=20 cm, FS diameter=12 cm.
    - Consider beam on time. If the dose corresponds to a time less than approximately 10 s, consider increasing the FSD.
5. Irradiate plates at desired dose. This is done by setting the time. Xstrahl CIX3 Cabinet Irradiator has a dose rate of 3.27 Gy/min at FSD=30 cm.
6. Transfer plates back to an incubator at 37°C at 5% CO_2 and humid conditions.
7. Let the plates sit for the allotted time specified in that specific assay protocol, e.g., clonogenic, luminescence, etc.

A.8 Nuclear Extraction

The nuclear extraction is done in triplicate. Each plate will have its contents collected individually. Each plate will require 3 scintillation vials to collect the media, PBS rinse and PBS supernatant (SN) (Table A.2). Each plate will also require 6 centrifuge tubes to collect the SN after step 10 and 12, the cytoplasmic faction, the nuclear extraction, the protein fraction (nuclear membrane) and the initial vial the pellet was collected in for each step. The protocol is derived from the Nuclear Extraction Kit protocol provided from Chemicon Internation (Cat. No. 2900).

1. Grow the cells to 70–90% confluency in a T75 flask or a 10 cm plate[1] in triplicate.
2. Bring 1× PBS to ice-cold temperatures. Bring Beckman Coulter Microfuge 22R to 4ºC.
3. Prepare media with a concentration of 30–50 kBq/mL (0.02–5 nM) [^{77}Br]RD1 for a volume of at least 7 mL per T75 flask or 5 mL per 10 cm plate.
4. Remove old media from the T75 flask and add radioactive media. Dose the cells for at least 2 h.
5. Prepare the cytoplasmic lysis buffer (CLB), protease inhibitor cocktail (PIC) and nuclear extraction buffer (NEB).
   - 0.05 M DTT:
     5 µL of 1 M DTT in 95 µL dH_2O.
   - ½₀× PIC:
     5 µL of 1× PIC in 95 µL dH_2O.
   - 1× CLB:
     120 µL 10× CLB
     + 12 µL 0.05 M DTT
     + 24 µL ½₀× PIC
     + 1044 µL dH_2O
   - NEB:
     970 µL 1× NEB
     + 20 µL ½₀× PIC
     + 10 µL 0.05 M DTT
6. After the treatment time, collect the media and wash the cells with 3 mL of ice-cold PBS solution. Collect the PBS rinse.
7. Use a cell scraper (Nunc) to scrape up the cells. Add 5 mL of PBS to collect all the cells from the plate. Place in a 15 mL polypropylene centrifuge tube.
8. Centrifuge at room temperature at 250 rcf on the VWR Benchtop Centrifuge. Collect the PBS SN.

[1] The large number of cells grown in a T75 flask may not be necessary. I would recommend a 10 cm plate unless you have a very slow-growing cell line and not enough time before the experiment to allow them to come to above 70% confluency.

9. Add 800 µL of ice-cold PBS to the tube and transfer the contents to a 1.5 mL centrifuge tube.
10. Centrifuge at 4ºC and 1,500 rpm on the Beckman Coulter centrifuge. Collect the SN.
11. Add 70 µL of the CLB solution. Use a 1 mL glass syringe with a blunted metal tip (26 gauge) to stir and break up the pellet. Let chill on ice for 15 min.
12. Centrifuge tube for 5 min at 4ºC at 1,500 rpm. Collect the SN.
13. Add 50 µL CLB to the pellet and mix the contents with the metal tip of the 1 mL glass syringe. Centrifuge at 8,000 rcf for 20 min at 4ºC. Collect the SN. This is the cytosolic fraction.
14. Add 50 µL of NEB. Disrupt the pellet with the metal tip. Place the centrifuge tubes on ice and place on an orbital shaker at 300 rpm for 30 minutes.
15. Centrifuge at 16,000 rcf for 5 min at 4ºC. Collect the SN. This is the nuclear extract.
16. Transfer the pellet to a fresh centrifuge tube. This is the nuclear membrane.

Table A.2: The step in the protocol when each fraction is collected and the container used for gamma counting. SCV: scintillation vial; SN: supernatant.

Step	Fraction	Container
6	Media	SCV
6	PBS rinse	SCV
8	PBS SN	SCV
10	SN1	Centrifuge tube
12	SN2	Centrifuge tube
13	Cytosolic	Centrifuge tube
15	Nuclear extract	Centrifuge tube
16	Nuclear membrane	Centrifuge tube
16	Empty[a]	Centrifuge tube

[a]This vial was the initial centrifuge tube used. After transferring the final pellet into a fresh tube, this should have only any leftover activity stuck to the vial.

A.9 Subcutaneous Injections

Matrigel can be used for subcutaneous injections to provide a scaffold for cells to grow and interact with. It mimics the extracellular matrix and can help promote cell survival, proliferation and differentiation in order to produce a tumor. Matrigel is stored at -20º or -70ºC and is thawed at 4ºC overnight. At that temperature, it is a liquid, but becomes solid at 37ºC. It is important to keep pipette tips and any materials coming into contact with the matrigel at ice-cold temperatures so that it does not solidify while you are working with it. Keep pipette tips, syringes, needles, tubes and cells on ice before injection into mice.

For each mouse, an injection with 5×10^6 of ovarian cancer cells is desired. This is approximately one T75 flask at 70-90% confluency. For 4 mice, 5 plates should be sufficient, but make sure to check the growth and number of cells in a confluent plate for the cell line you are working with. The below directions are for injection in 4 mice.

1. Grow cells in T75 plates in normal growth conditions. Remove media and rinse with 3 mL PBS.

2. Use trypsin EDTA (at a concentration suggested for the specific cell line, Appx. A.1.2, Step 3) for 3–5 min or a cell scraper to detach the cells.

   - If using trypsin, use an amount of media to neutralize the trypsin (2×). Will probably have used 1.5–2 mL of trypsin and 3–4 mL of media, giving a max of 6 mL of volume per plate.
   - If using a cell scraper, use PBS to collect the cells. Approximately 5 mL per plate should be sufficient.

   Use a 5 or 10 mL pipette to break up cell clusters by gently pipetting the mixture several times.

3. Collect all the cells from all the plates into a 50 mL centrifuge tubes and centrifuge at 500 g for 5 min. Remove the supernatant (SN).

4. Add 10 mL of PBS and mix pellet to form a uniform mixture. Add 40 mL of PBS and thoroughly mix.

5. Count the number of cells using a hemocytometer in the 50 mL volume.

6. Repeat centrifugation. Remove SN.

7. Add 10 mL of PBS and mix pellet in volume. Add 40 mL of PBS and thoroughly mix.

8. Repeat centrifugation. Remove SN.

9. Calculate a volume needed for 5×10^6 in 60 µL. Add that amount of ice-cold PBS to the cells. Place cells on ice.

10. Add equal parts of ice-cold liquid matrigel to the cell volume.[2] Place cell+matrigel solution on ice.
11. Place sterile 1 mL syringes and sterile 25 guauge needles on ice.
12. Prepare mice for subcutaneous injection. Injections can be administered to mice under anesthesia or while they are conscious. If using immunocompetent mice, it is best to shave the area of injection in order to view the injection site.
13. Draw 120 µL[3] of the cell+matrigel mix for injection.
14. Insert the needle obliquely.[4] After insertion, lift the needle to form a tent of the skin. This will indicate that you are not injecting into the muscle.
15. Inject 120 µL of the cell+matrigel mix. Hold the needle depth and twist the syringe. Slowly pull the needle back to avoid the mix leaking from the injection site.
16. If the contents leak, collect them with a needless syringe to note the volume. Subtract this from the expected injected volume and calculate the subsequent number of cells injected.

Example calculation:

Hemocytometer calculation:

$$88+98+95+71 \text{ (cells per } 0.2\times0.2 \text{ square)} \implies 88\times10^4 \text{ cells/mL}$$

$$50 \text{ mL} \cdot 88\times10^4 \text{ cells/mL} = 4.4\times10^7 \text{ cells}$$

$$\frac{4.4 \times 10^7 \text{ cells/mL}}{5 \times 10^6 \text{ cells/mL}} = 8.8 \text{ inoculations}$$

Inoculation Volume:

$$8.8 \text{ inoculations} \cdot 60 \text{ µL of PBS} = 528 \text{ µL of PBS}$$

[2] If the volume of the cells is larger than 500 µL, split the contents in order to not overflow the centrifuge tube after adding the matrigel. This volume can also be used as a final check of the number of cells injected with a hemocytometer after injection

[3] This volume was recommended by the Hernandez Lab, but the ID8 tumors resulting from this volume and cell number gave very small tumors. Perhaps a larger volume should be used instead.

[4] Needles may become dull after 2–4 injections and should be replaced.

Pellet:

Add a small amount, like 100 µL, of ice-cold PBS to pellet in 50 mL tube. Measure and transfer contents to a 1.5 mL centrifuge tube.

$$\text{Volume}_{\text{pellet}} + 100\ \mu\text{L} = 245\ \mu\text{L}$$

After measuing the volume, assuming a pellet volume of 145 µL, calculate the amount of additional PBS required to have a concentration of 10×10^5 cells/mL that was calculated during the inoculation volume step.

$$528\ \mu\text{L} - 245\ \mu\text{L} = 283\ \mu\text{L additional PBS}$$

Add an addiontional 283 µL of PBS to the centrifuge tube with the cells. Assuming an inoculation of 4 mice, we have extra cells in this centrifuge tube. Additionally, adding an equal volume of matrigel to this 1.5 mL tube increases the odds of spilling since it will have a volume of approximately 1.1 mL.

Instead, transfer 6.5× inoculation amount to a new 1.5 mL centrifuge tube. The additional amount is to account for pipette losses and potential spilling during inoculation.

$$6.5 \times 60\ \mu\text{L} = 390\ \mu\text{L}$$

Transfer 390 µL of cells in PBS to new centrifuge. Then add 390 µL of ice-cold matrigel. The leftover cells in PBS can be used as an additional check on the cell density with a hemocytometer.[5]

[5]Make sure to dilute this volume to a reasonable amount in order to count the cells and note that this is twice the density.

APPENDIX B

SUPPLEMENTAL DATA

B.1 Chapter 3: Cellular Pharmacokinetics and Cytotoxicity Studies with Radiobrominated PARP1 Inhibitor

To determine the BrRD1 mass response of the UV absorbance detector, 0.05–50 µM radioinert BrRD1 standard solutions in 5% acetonitrile were assayed in triplicate. The quantification of the area under the BrRD1 peak, measured in milli-absorbance units (mAU), was done for each molar concentration and used to establish a calibration curve (Fig. B.1). A least squares regression line was fitted to the data, and the resulting equation was utilized to convert the analytical HPLC areas under the peaks to BrRD1 mass (pmol). The slope and intercept values of the calibration curve were determined to be 0.3694±0.0003 pmol/mAU and -0.58±0.41 pmol, respectively.

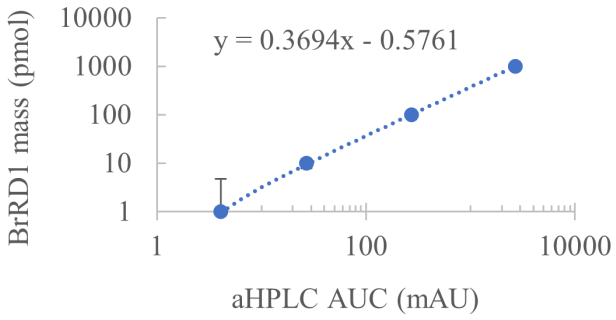

Figure B.1: Calibration curve of radioinert BrRD1 on analytical high-performance liquid chromatography (aHPLC).

Table B.1: Mass of the radioinert BrRD1 and the corresponding area under the curve (AUC) of the milli absorbance unit measured at 8.86 min.

BrRD1 mass (pmol)	**aHPLC AUC (mAU @ 8.86 min)**	
	Avg	**Error**
1	4.08	3.70
10	27.0	2.2
100	274.3	8.2
1000	2708	34

B.2 Chapter 4: Preclinical Dosimetric Investigation of a Radiobromine PARP1 Inhibitor

B.2.1 Radiopharmaceutical Cellular Distribution

As described in Chapter 4, the radiopharmaceutical cellular distribution was measured using a nuclear extraction kit as described in Section 4.2.1.2. In Chapter 4, the fractions of interest were the cytoplasm, nucleus and nuclear membrane. However, many more fractions were collected and measured. Their results are summarized in Fig. B.2 and Table B.2.

The amount of time the cells were in contact with the radiopharmaceutical did not seem to affect the amount of radiopharmaceutical found in the cytosolic fraction, nuclear extract or nuclear membrane. The OVCAR8 PARP1-KO cell line with a 90% reduction in PARP1 protein expression [135] had significantly lower cellular uptake of [^{77}Br]RD1 compared to the OVCAR8 cell line. The media contained a higher percentage of the radiopharmaceutical compared to the media of the OVCAR8 cells, perhaps due to fewer sites for the radiopharmaceutical to bind to. Less of the radiopharmaceutical was found in the cell contents of the knockout line, with only 0.23±0.06% found in the cell compared to 3.3% found in the OVCAR8 cells.

For the blocked arm of the OVCAR8 PARP1-KO cell line, measurements were so small they could not be measured above background with the gamma counter, and the majority of the activity was found in the media and the first wash. If this study were to be repeated, using the OVCAR8 cell line with a higher expression of PARP1 protein would be a better choice of cell line for the blocking study.

If only the cellular contents are considered, in the OVCAR8 cell line, radiopharmaceutical uptake is higher in the nucleus compared to the cytosolic fraction, with 89±4% in the nucleus (including the membrane) compared to 11±4% in the cytosolic fraction. This is in agreement with PARPi binding to the PARP protein and binding to DNA complexes in the nucleus. The knockout line showed higher uptake in the nucleus, with 62±1% in the nucleus compared to 38±1% in the cytosolic fraction, although not as high as that shown in the OVCAR8 line, and as mentioned before, with much lower uptake overall compared to the OVCAR8 cell line.

The radiopharmaceutical stuck to the vial in the OVCAR8 24 h at a much higher percentage of the final pellet, the nuclear membrane, compared to the OVCAR8 PARP1-KO nonblocked. The blocked arm didn't have any measured counts for the final pellet or the vial and the OVCAR8 2 h arm didn't have a unique vial measurement. It was noted that the pellet was much larger for the OVCAR8 24 h arm, which saw the pellet smear along a larger length of the Eppendorf tube during centrifuge steps compared to the other extraction experiments. Perhaps this caused inadequate retrieval of the entire pellet when resuspending it in small volumes of the detergent or buffer solutions, which caused radiopharmaceutical to end up on the vial after the final step. Since two measurements of the vial gave such different values, it is difficult to subtract a background from the OVCAR8 2 h nuclear membrane measurement to account for the radiopharmaceutical stuck to the vial. However, the values are in agreement with the OVCAR8 24 h readings, perhaps indicating that not much of the radiopharmaceutical was stuck to the vial.

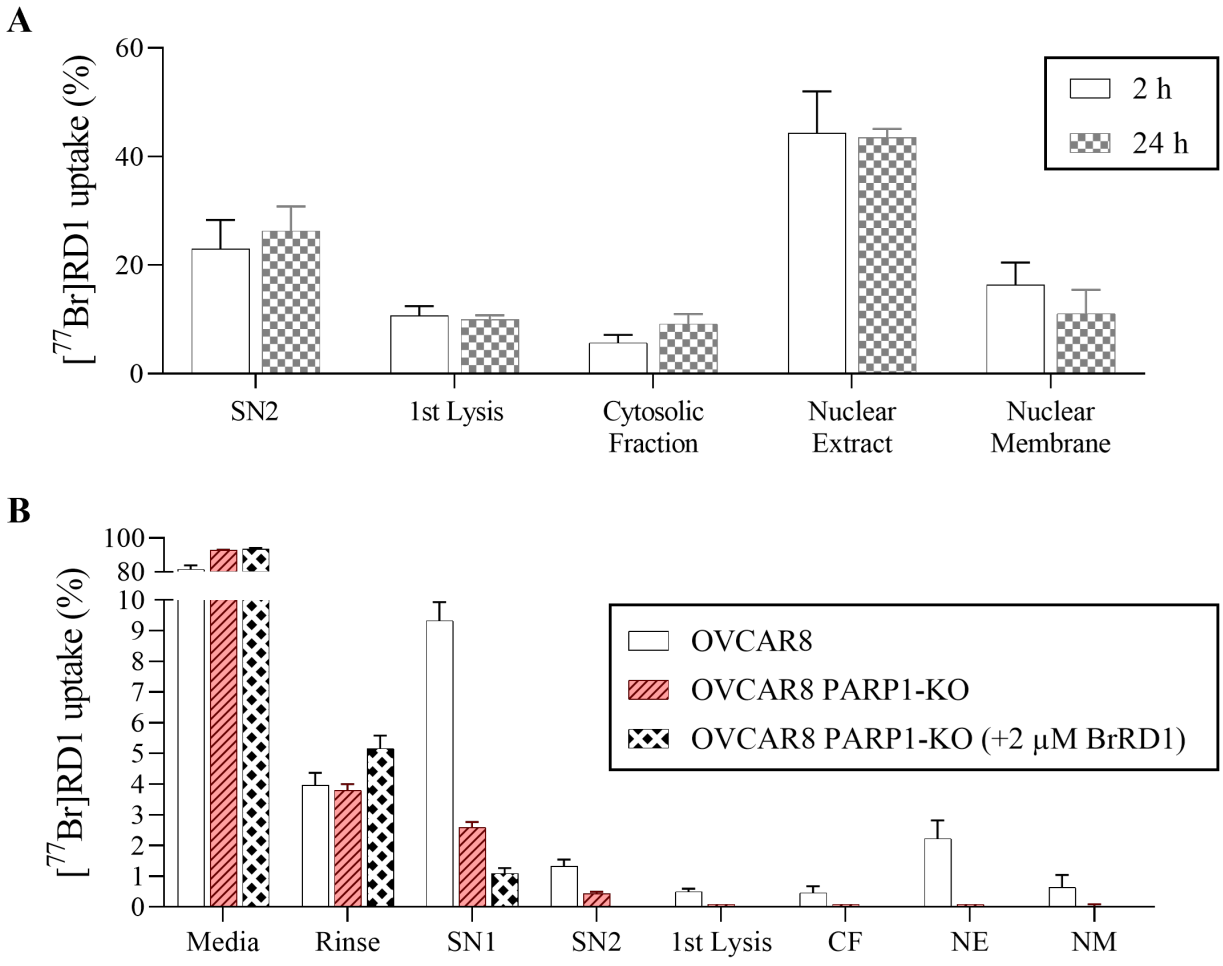

Figure B.2: (**A**) Comparison between radiopharmaceutical distribution when OVCAR8 cells are dosed for 2 h or 24 h. (**B**) Comparison between radiopharmaceutical distribution of OVCAR8 and OVCAR8 PARP1-KO ovarian cancer cells with and without a blocking dose (2 μM radioinert BrRD1) was added to the OVCAR8 PARP1-KO cell lines to see effects of radiopharmaceutical cellular distribution. SN: supernatant; CF: cytosolic fraction; NE: nuclear extract; NM: nuclear membrane.

Table B.2: Radiopharmaceutical [^{77}Br]RD1 activity measured for each fraction and the corresponding percent uptake. OVCAR8 PARP1-KO cells were dosed with the radiopharmaceutical with 2 μM radioinert BrRD1 (blocked) or without (nonblocked).

	OVCAR8					**OVCAR8 PARP1-KO**			
	2 h		**24 h**			**Nonblocked**		**Blocked**	
Fraction	**(Bq)**	**(%)**	**(Bq)**		**(%[a])**	**(Bq)**	**(%)**	**(Bq)**	**(%)**
Media	-	-	223,200±6,500	-	81.5±2.2	97,800±2,700	92.8±0.2	102,000±1,000	93.7±0.4
Rinse	-	-	10,900±1,100	-	4.0±0.4	4,010±330	3.8±0.2	5,670±510	5.2±0.4
Supernatant 1	-	-	25,500±1,470	-	9.3±0.6	2,730±130	2.6±0.2	1,210±170	1.1±0.2
Supernatant 2	2,970±190	22.9±5.4	3,640±560	26.3±4.5	1.3±0.2	461±29	0.4±0.1	15.3±3.1	0
1st Lysis	1,450±520	10.6±1.8	1,400±280	10.0±0.8	0.50±0.10	131±12	0.10±0	2.3±1.5	0
Cytosolic Fraction	780±350	5.7±1.4	1,320±550	9.1±1.9	0.47±0.21	91.0±14.0	0.10±0	0.33±0.58	0
Nuclear Extract	6,100±2,260	44.3±7.7	6,150±1,610	43.5±1.6	2.2±0.6	106±15	0.10±0	0.33±0.58	0
Nuclear Membrane	2,110±110[†]	16.4±4.1[†]	1,680±1,140	11.0±4.4	0.63±0.42	43.7±16.2	0.03±0.06	0±0	0
Vial[b]	-	-	8,380±700	-	-	9.5±1.7	-	0±0	-

[a] Two sets of data to compare to the OVCAR8 2 h fractions and OVCAR8 PARP1-KO cells as a percentage of the fractions indicated.

[b] Not included in the percentage total.

[†] Activity from the nuclear membrane fraction and the activity left on the vial.

B.3 Chapter 5: PET Imaging Potential of Radiobrominated PARP1 Inhibitor and Murine Biodistribution Studies

Table B.3: The *ex vivo* and *in vivo* [^{76}Br]RD1 organ uptake (%ID/g) at 4 time points p.i. in the nondiseased models (n=4).

Organ Type	1 h	4 h	24 h	48 h	Ex Vivo
Heart	3.4±0.2	1.3±0.4	0.37±0.02	0.18±0.03	0.11±0.03
Lungs	3.3±0.3	3±4	0.5±0.1	0.17±0.02	0.3±0.1
Kidneys	7.0±0.8	4±2	0.7±0.1	0.22±0.03	0.5±0.1
Liver	8.9±0.7	5±1	2.2±0.1	0.9±0.1	2.3±0.4
Gallbladder	-	38±8	-	-	0.8±0.2
Stomach	10±2	6±1	4±2	0.8±0.2	0.2±0.1
Brain	1.0±0.1	0.3±0.1	0.083±0.004	0.04±0.01	0.05±0.02
Bone	2.2±0.6	2±1	0.24±0.05	0.05±0.02	0.11±0.05
Muscle	2.1±0.2	0.5±0.1	0.13±0.03	0.06±0.03	0.05±0.02
Bladder	11±3	21±5	0.8±0.1	0.09±0.03	-
Intestines	11±1	14±2	1.8±0.4	0.20±0.02	0.24±0.06

Table B.4: The *ex vivo* and *in vivo* [^{76}Br]RD1 organ uptake (%ID/g) at 4 time points p.i. in the diseased models (n=12).

Organ Type	1 h	4 h	24 h	48 h	*Ex vivo*
Heart	3.1±0.4	1.3±0.3	0.43±0.08	0.26±0.06	0.12±0.02
Lungs	2.6±0.3	1.2±0.3	0.5±0.1	0.24±0.06	0.30±0.07
Kidneys	5.6±0.6	3.5±0.9	0.9±0.2	0.42±0.08	0.59±0.10
Liver	8.5±0.5	4.4±1.0	1.9±0.3	1.0±0.2	2.4±0.4
Gallbladder	38±9	26±5	-	-	1.2±0.5
Stomach	10±2	6.2±1.4	3.8±2.4	0.8±0.2	0.21±0.07
Bone	1.5±0.2	0.7±0.2	0.19±0.04	0.09±0.02	0.13±0.03
Muscle	2.0±0.3	0.6±0.2	0.15±0.06	0.09±0.02	0.056±0.012
Brain	1.1±0.2	0.37±0.07	0.12±0.03	0.09±0.03	0.062±0.013
Bladder	15±4	20±11	1.6±0.9	0.3±0.2	-
Tumor	3.6±0.8	2.1±1.5	0.3±0.2	0.14±0.06	0.30±0.08

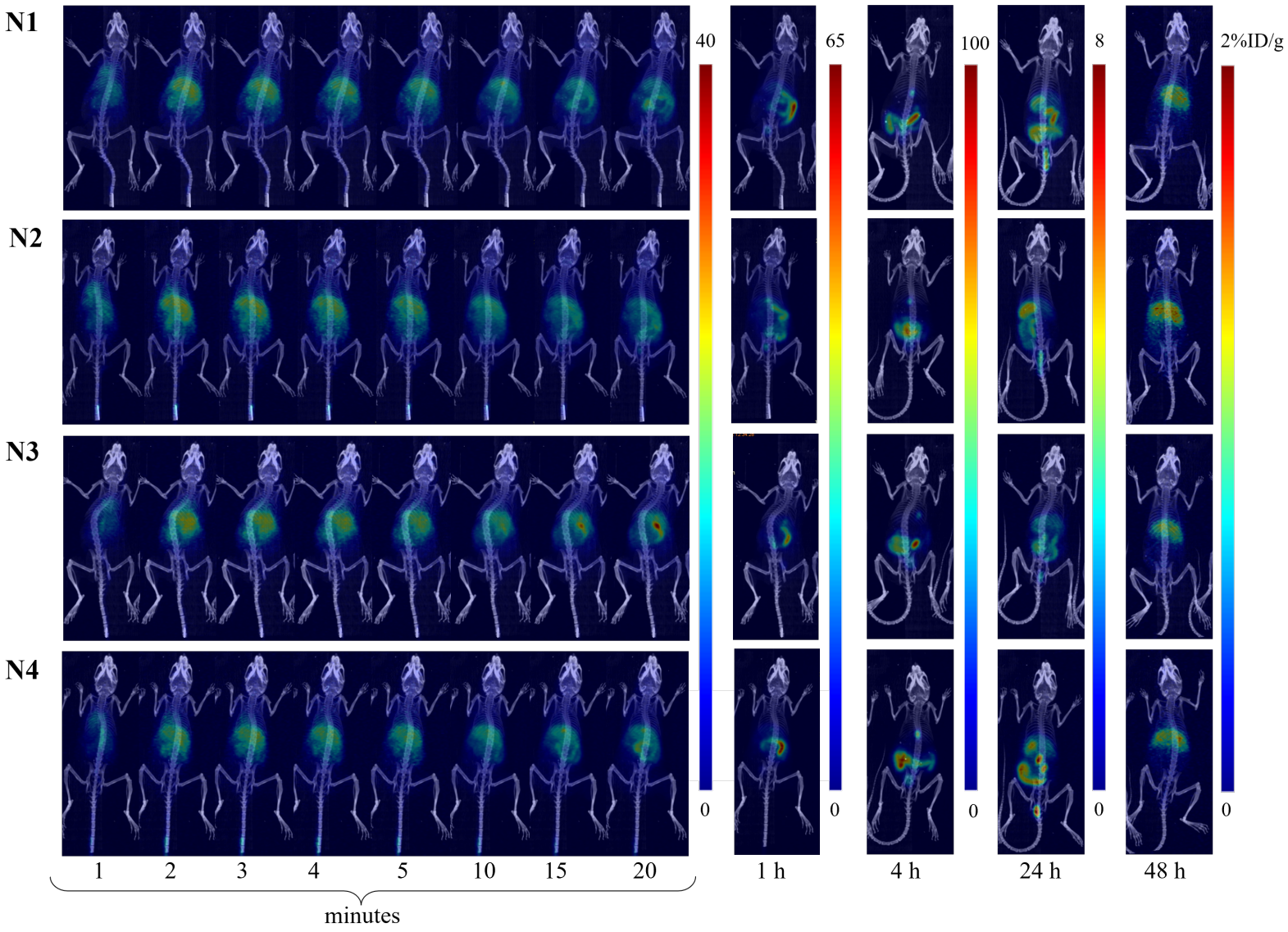

Figure B.3: Serial maximum intensity projection (MIP) PET/CT images of nondiseased models (mice labeled N1-N4) IV injected with [^{76}Br]RD1. Dynamic scans were acquired at t=0–60 minutes in 1 minute bins from 0–5 minutes, 5 minute bins between 5–20 minutes, and a 10 minute bin from 50–60 min. Static scans were acquired at t=4, 24 and 48 h. Scales are in %ID/g.

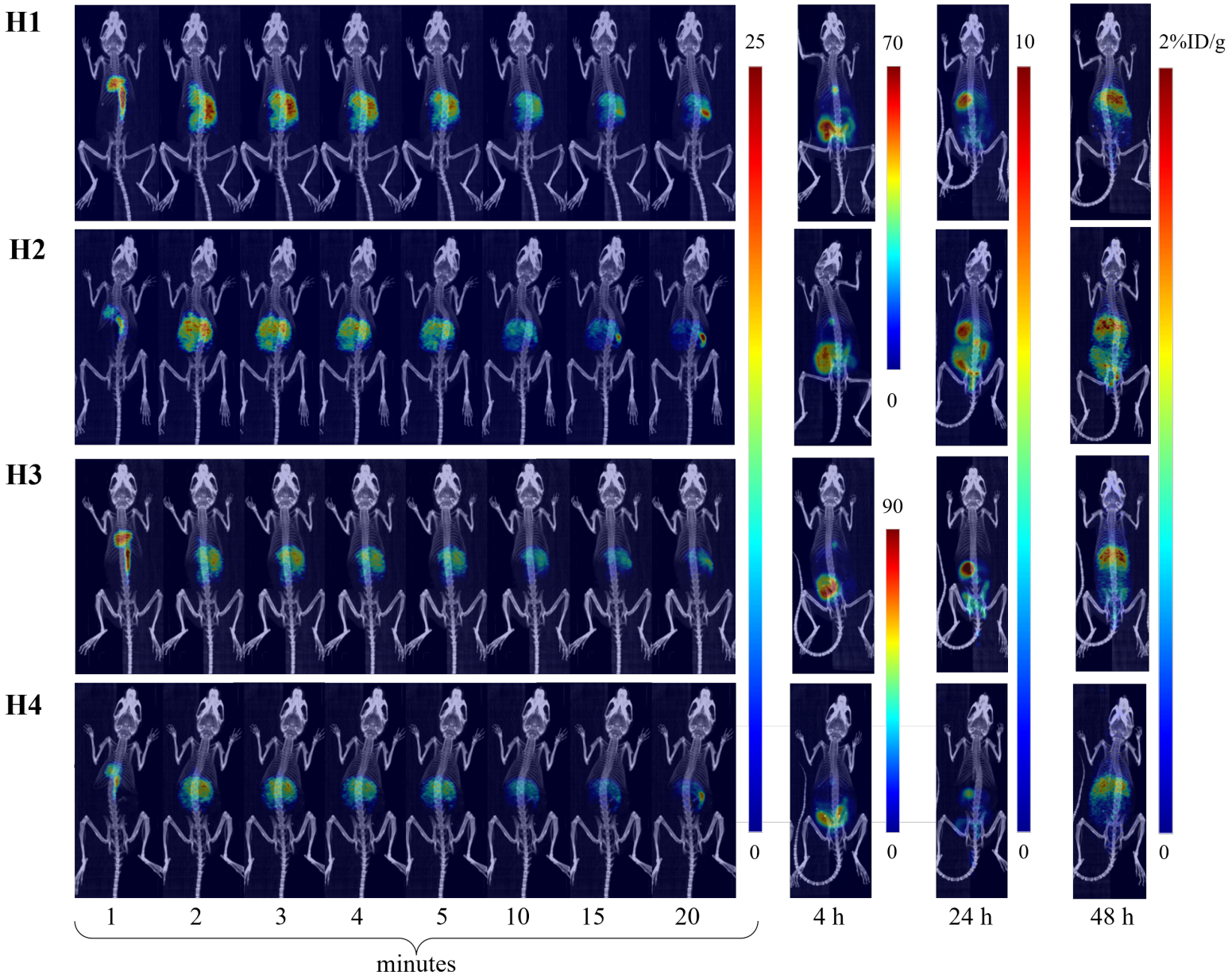

Figure B.4: Serial maximum intensity projection (MIP) PET/CT images of heterotopic models (mice labeled H1-H4) IV injected with [^{76}Br]RD1. Dynamic scans were acquired at t=0–20 minutes in 1 minute bins from 0–5 minutes and 5 minute bins between 5–20 minutes. Static scans were acquired at t=4, 24 and 48 h. Scales are in %ID/g.

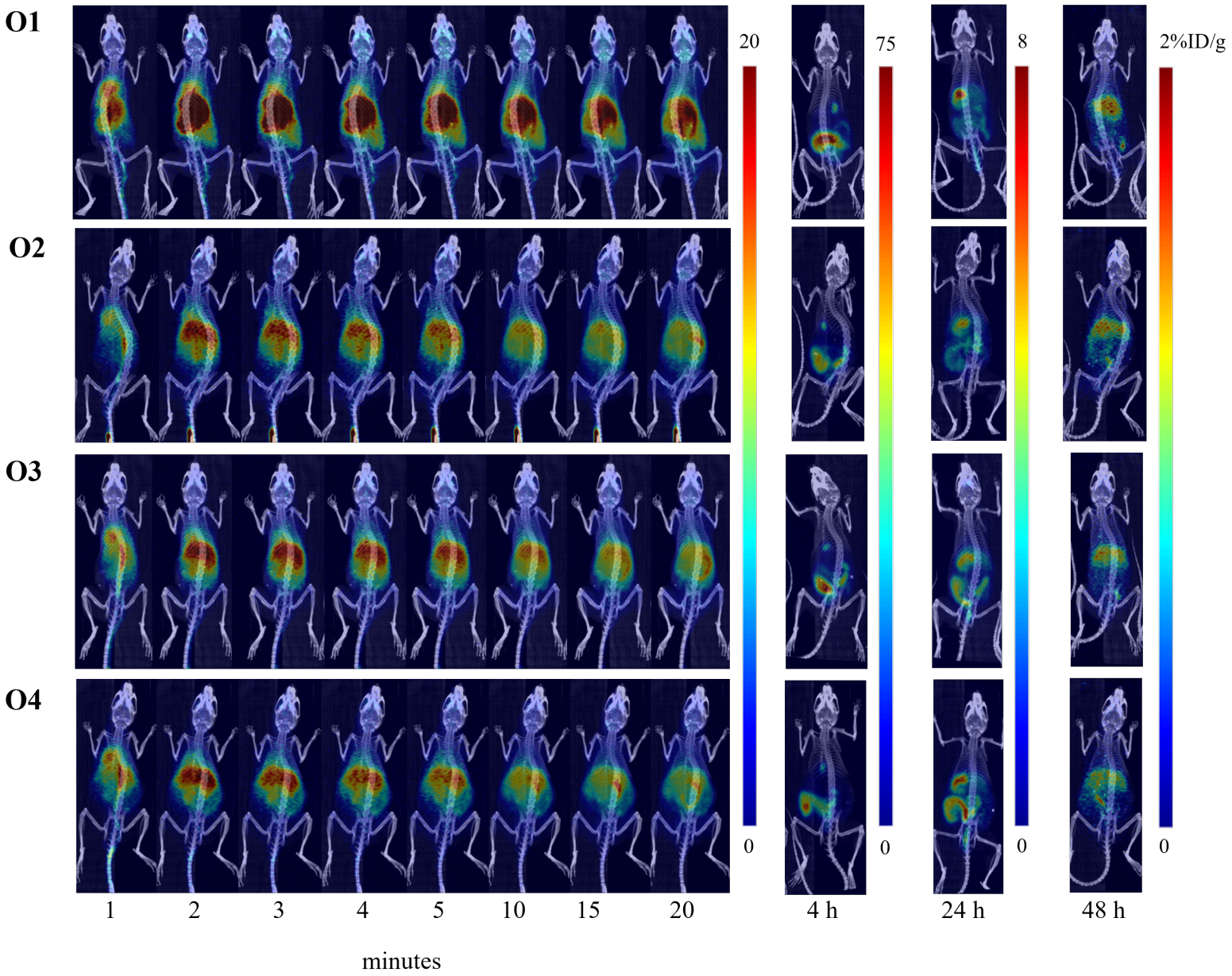

Figure B.5: Serial maximum intensity projection (MIP) PET/CT images of orthotopic models (mice labeled O1-O4) injected with [^{76}Br]RD1 via IV administration. Dynamic scans were acquired at t=0–20 minutes in 1 minute bins from 0–5 minutes and 5 minute bins between 5–20 minutes. Static scans were acquired at t=4, 24 and 48 h. Scales are in %ID/g.

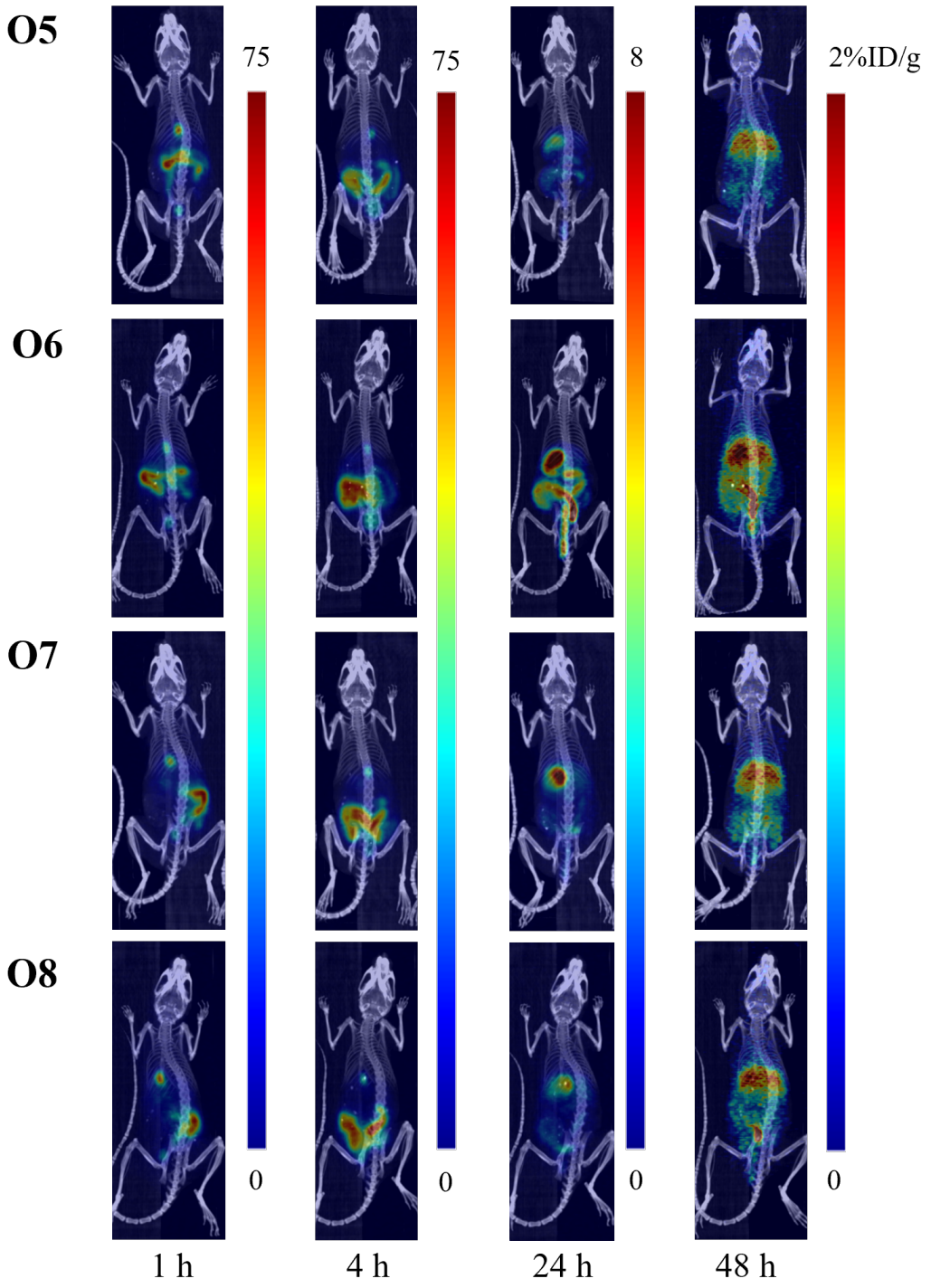

Figure B.6: Serial maximum intensity projection (MIP) PET/CT images of orthotopic models (mice labeled O5-O8) injected with [^{76}Br]RD1 via IP administration. Static scans were acquired at t= 1, 4, 24 and 48 h. Scales are in %ID/g.

Table B.5: The [^{76}Br]RD1 organ uptake 48 post injection (p.i.) of the diseased and nondiseased models measured *in vivo* with microPET/CT.

Organ Type	Diseased (%ID/g)	Nondiseased (%ID/g)	*P* Value[†]
Heart	0.255±0.057	0.182±0.032	0.010*
Lungs	0.242±0.060	0.170±0.022	0.004*
Kidneys	0.421±0.080	0.219±0.031	<0.001**
Liver	0.982±0.219	0.894±0.119	0.334
Bone	0.094±0.023	0.054±0.016	0.005*
Muscle	0.093±0.022	0.061±0.026	0.084
Brain	0.089±0.025	0.037±0.005	<0.001**
Bladder	0.347±0.169	0.086±0.031	<0.001**

[†]Welch's two-sample t-test.

Table B.6: The [^{76}Br]RD1 organ uptake in the diseased models measured *in vivo* with microPET/CT 48 h p.i. grouped by radiopharmaceutical administration method.

Organ Type	IP Injection (%ID/g)	IV Injection (%ID/g)	*P* Value[†]
Heart	0.299±0.022	0.233±0.057	0.017*
Lungs	0.287±0.019	0.219±0.061	0.017*
Kidneys	0.443±0.044	0.410±0.094	0.420
Liver	1.171±0.046	0.888±0.209	0.006*
Stomach	0.836±0.210	0.814±0.268	0.881
Bone	0.109±0.004	0.086±0.024	0.033*
Muscle	0.099±0.029	0.090±0.020	0.625
Brain	0.100±0.016	0.084±0.028	0.228
Bladder	0.401±0.150	0.320±0.180	0.438
CTCV	0.182±0.108	0.068±0.047	0.124
Tumor	0.182±0.080	0.122±0.034	0.239

[†]Welch's two-sample t-test.

Table B.7: The [^{76}Br]RD1 organ uptake in the diseased models measured *in vivo* with microPET/CT 48 h p.i. grouped by tumor model with administration method.

Organ Type	Heterotopic (IV) (%ID/g)	Orthotopic (IV) (%ID/g)	Orthotopic (IP) (%ID/g)	*P* Value[†]
Heart	0.278±0.027	0.189±0.039	0.299±0.022	0.018*
Lungs	0.269±0.041	0.168±0.014	0.287±0.019	0.023*
Kidneys	0.408±0.032	0.411±0.140	0.443±0.044	0.472
Liver	1.031±0.121	0.745±0.182	1.171±0.046	0.010*
Stomach	1.005±0.209	0.624±0.167	0.836±0.210	0.092
Bone	0.103±0.026	0.070±0.002	0.109±0.004	0.084
Muscle	0.098±0.022	0.083±0.018	0.099±0.029	0.668
Brain	0.106±0.014	0.061±0.017	0.100±0.016	0.023*
Bladder	0.374±0.248	0.266±0.082	0.401±0.150	0.390
CTCV	0.030±0.014	0.106±0.035	0.182±0.108	0.015*
Tumor	0.103±0.026	0.149±0.025	0.182±0.080	0.227

[†]Kruskal-Wallis test.

Table B.8: The [^{76}Br]RD1 organ uptake measured *ex vivo* of the diseased and nondiseased models.

Organ Type	Diseased (%ID/g)	Nondiseased (%ID/g)	*P* Value[†]
Blood	0.467±0.087	0.274±0.019	<0.001**
Heart	0.123±0.023	0.087±0.009	<0.001**
Lungs	0.300±0.070	0.192±0.020	<0.001**
Pancreas	0.154±0.036	0.072±0.007	<0.001**
Spleen	0.207±0.049	0.120±0.005	<0.001**
Kidneys	0.588±0.103	0.426±0.044	<0.001**
Liver	2.385±0.420	1.977±0.293	0.066
Gallbladder	1.198±0.543	0.828±0.247	0.088
Large Intestine	0.139±0.040	0.076±0.010	<0.001**
Small Intestine	0.146±0.037	0.093±0.013	<0.001**
Stomach	0.209±0.071	0.084±0.016	<0.001**
Enteric Contents	1.206±0.497	0.565±0.185	0.002*
Bone	0.136±0.028	0.043±0.013	<0.001**
Muscle	0.056±0.013	0.027±0.005	<0.001**
Skin	0.267±0.051	0.167±0.039	0.005*
Brain	0.063±0.013	0.021±0.003	<0.001**
Tail	0.228±0.044	0.101±0.004	<0.001**
Tumor	0.300±0.081		

[†]Welch's two-sample t-test.

Table B.9: The [^{76}Br]RD1 organ uptake in the diseased models measured *ex vivo* grouped by radiopharmaceutical administration method.

Organ Type	**IP Injection (%ID/g)**	**IV Injection (%ID/g)**	***P* Value**[†]
Blood	0.518±0.055	0.442±0.091	0.108
Heart	0.141±0.018	0.114±0.020	0.053
Lungs	0.366±0.070	0.266±0.042	0.056
Pancreas	0.191±0.019	0.136±0.027	0.003*
Spleen	0.244±0.028	0.188±0.046	0.027*
Kidneys	0.645±0.074	0.560±0.108	0.144
Liver	2.733±0.292	2.211±0.371	0.030*
Gallbladder	1.375±0.578	1.110±0.543	0.474
Large Intestine	0.178±0.036	0.120±0.025	0.038*
Small Intestine	0.185±0.029	0.126±0.023	0.017*
Stomach	0.284±0.078	0.171±0.020	0.061
Enteric Contents	1.384±0.247	1.116±0.579	0.288
Bone	0.154±0.023	0.127±0.026	0.111
Muscle	0.070±0.013	0.049±0.006	0.046*
Skin	0.293±0.022	0.254±0.058	0.120
Brain	0.073±0.012	0.058±0.011	0.078
Tail	0.249±0.035	0.218±0.047	0.228
Tumor	0.318±0.099	0.279±0.072	0.517

[†]Welch's two-sample t-test.

Table B.10: The [^{76}Br]RD1 organ uptake in the diseased models measured *ex vivo*, grouped by tumor model with administration method.

Organ Type	Heterotopic (IV) (%ID/g)	Orthotopic (IV) (%ID/g)	Orthotopic (IP) (%ID/g)	*P* Value[†]
Blood	0.523±0.033	0.360±0.027	0.518±0.055	0.025*
Heart	0.126±0.021	0.101±0.008	0.141±0.018	0.044*
Lungs	0.286±0.054	0.246±0.015	0.366±0.070	0.030*
Pancreas	0.147±0.034	0.125±0.015	0.191±0.019	0.026*
Spleen	0.198±0.067	0.178±0.017	0.244±0.028	0.092
Kidneys	0.644±0.083	0.476±0.037	0.645±0.074	0.023*
Liver	2.462±0.356	1.960±0.159	2.733±0.292	0.037*
Gallbladder	1.520±0.445	0.699±0.199	1.375±0.578	0.058
Large Intestine	0.121±0.036	0.119±0.012	0.178±0.036	0.055
Small Intestine	0.136±0.026	0.116±0.015	0.185±0.029	0.037*
Stomach	0.176±0.026	0.166±0.013	0.284±0.078	0.105
Enteric Contents	1.442±0.682	0.790±0.183	1.384±0.247	0.058
Bone	0.150±0.016	0.105±0.006	0.154±0.023	0.025*
Muscle	0.048±0.003	0.050±0.009	0.070±0.013	0.037*
Skin	0.306±0.022	0.202±0.010	0.293±0.022	0.023*
Brain	0.067±0.005	0.048±0.004	0.073±0.012	0.021*
Tail	0.256±0.032	0.180±0.013	0.249±0.035	0.024*
Tumor	0.325±0.047	0.217±0.048	0.318±0.099	0.087

[†]Kruskal-Wallis test.

Table B.11: The tumor-to-muscle ratio (T:M) and tumor-to-contralateral-to-tumor control volume ratio (T:CTCV) for the three disease models measured *in vivo* at 48 h p.i.

Model	T:M	T:CTCV	*P* Value[a]
Heterotopic (IV)	1.1±0.4	4.0±2.3	0.081
Orthotopic (IV)	1.9±0.6	1.7±0.7	0.677
Orthotopic (IP)	2.1±1.5	1.1±0.4	0.288
***P* Value[b]**	0.208	0.029*	

[a]Welch's two-sample t-test.

[b]Kruskal-Wallis test.

The subsequent "tumor" at the tumor-injection-site (TIS) was used to calculate tumor-to-organ ratio (T:M). These values were calculated for each disease model *in vivo* at various time points p.i. and compared to the *ex vivo* T:M (Fig. B.7A). Box-plots summarizing the T:M for the heterotopic models were calculated. The recovery coefficient (RC) was applied to the tumor %ID/g measurement using the caliper measurements of the heterotopic tumors. The tumor-to-organ ratios for the organs measured *ex vivo* are summarized in Figure B.7C. From the tumor-to-CTCV (contralateral-to-tumor control volume) ratios (T:CTCV), it is apparent that the PET imaging of the tumor may not be accurate. Further investigation deemed it may be due to the tumor not actually being malignant or vascularized. The data is presented here, but these points should be kept in mind.

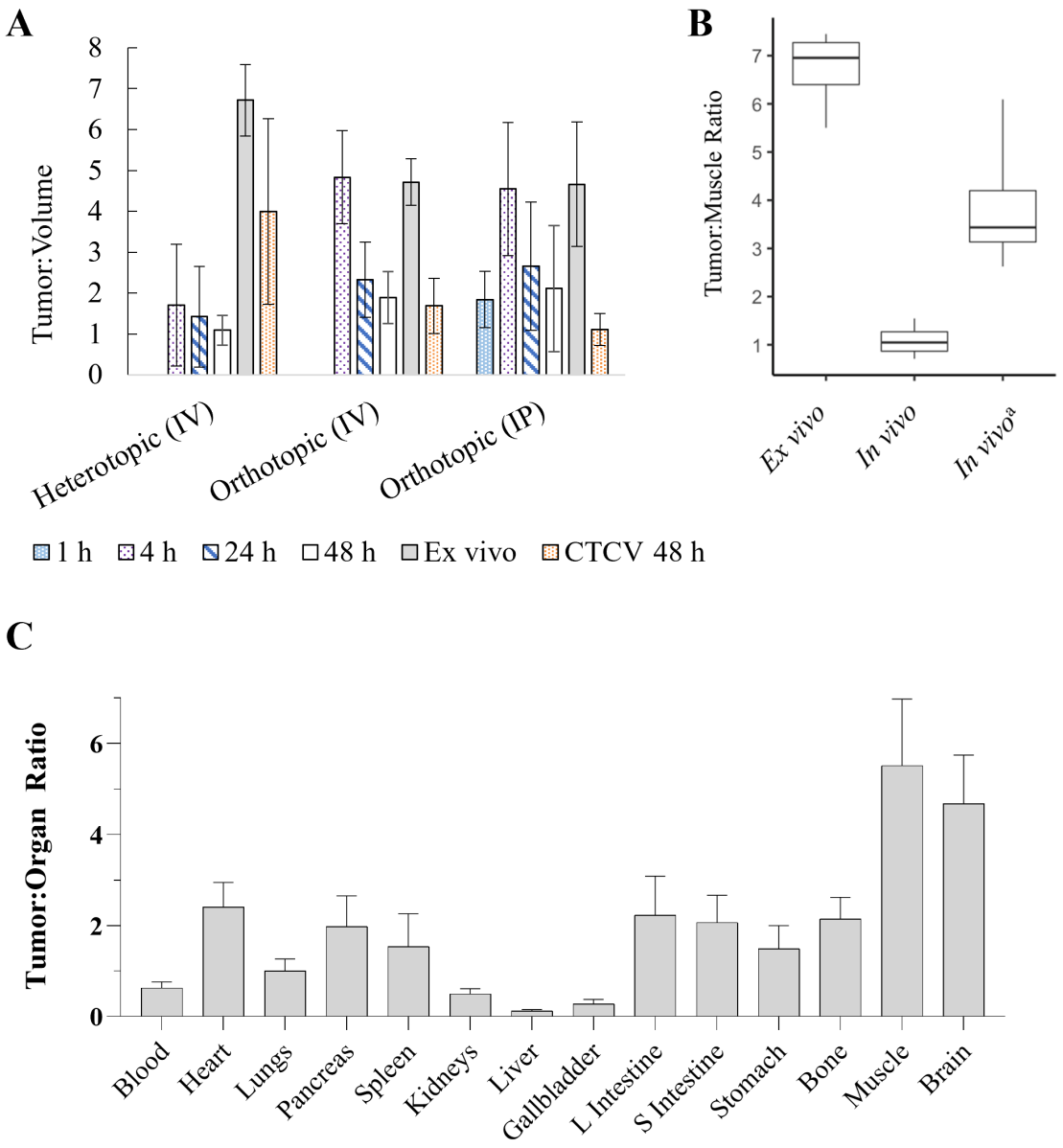

Figure B.7: (**A**) Tumor-to-muscle ratios (T:M) *in vivo* at various time points compared to the *ex vivo* and tumor-to-contralateral-to-tumor control volume ratios (T:CTCV) *in vivo* at 48 h p.i. of 9.2 MBq (250 μCi) [^{76}Br]RD1 in the various diseased models (heterotopic, orthotopic (IV or IP)) in tumor-bearing mice. (**B**) Heterotopic T:M *ex vivo*, *in vivo* and partial volume (PV) corrected using the recovery coefficient based off caliper measurements of the tumors before imaging at 48 h p.i. [a]Recovery coefficient (RC) corrected. (**C**) The tumor-to-organ ratios for the organs measured *ex vivo* after the 48 h p.i. PET scan for all diseased models.

Table B.12: The [$^{76/77}$Br]RD1 estimated organ dose from Monte Carlo calculations using RAPID for murines and OLINDA for humans.

	Mouse Organ Absorbed Dose (mGy/MBq)		**Adult Woman Equivalent Dose (mSv/GBq)**	
Organ	**^{76}Br**	**^{77}Br**	**^{76}Br**	**^{77}Br**
Heart*	130±20	8.2±0.8	151±7	12.0±0.4
Lungs	140±10	10.3±0.7	110±5	9.0±0.2
Kidneys	400±100	16±4	220±40	15.9±0.6
Liver	290±10	19.3±0.3	260±30	19±2
Stomach*	270±30	17±2	120±60	14±3
Brain	17.3±0.9	1.4±0.1	46±3	4.2±0.2
Bone	38±3	2.8±0.2	140±10	19±1
Muscle	39±4	3.0±0.2	60±20	7.9±0.9
Bladder*	400±100	22±8	100±50	13±4
Intestines	720±70	37±3		
Small Intestine			200±300	30±10
Upper Large Intestine			200±100	20±10
Lower Large Intestine			300±400	30±20
Total Body			100±20	8.9±0.9
Effective Dose			140±70	16±4
Effective Dose Equivalent			130±80	15±4

*Estimated organ wall equivalent dose for adult woman calculations.

REFERENCES

1. Siegel, R. L., Miller, K. D., Wagle, N. S. & Jemal, A. Cancer statistics, 2023. *CA: A Cancer Journal for Clinicians* **73,** 17–48 (2023).

2. Lengyel, E. Ovarian cancer development and metastasis. *American Journal of Pathology* **177,** 1053–1064 (2010).

3. Jemal, A., Thomas, A., Murray, T. & Thun, M. Cancer Statistics, 2002. *CA: A Cancer Journal for Clinicians* **52,** 23–47 (2002).

4. Torre, L. A., Trabert, B., DeSantis, C. E., Miller, K. D., Samimi, G., Runowicz, C. D., Gaudet, M. M., Jemal, A. & Siegel, R. L. Ovarian cancer statistics, 2018. *CA: A Cancer Journal for Clinicians* **68,** 284–296 (2018).

5. Vang, R., Ming Shih, I. & Kurman, R. J. Ovarian low-grade and high-grade serous carcinoma: Pathogenesis, clinicopathologic and molecular biologic features, and diagnostic problems. *Advances in Anatomic Pathology* **16,** 267–282 (2009).

6. Du Bois, A., Quinn, M., Thigpen, T., Vermorken, J., Avall-Lundqvist, E., Bookman, M., Bowtell, D., Brady, M., Casado, A., Cervantes, A., Eisenhauer, E., Friedlaender, M., *et al. 2004 consensus statements on the management of ovarian cancer: Final document of the 3rd International Gynecologic Cancer Intergroup Ovarian Cancer Consensus Conference (GCIG OCCC 2004)* in. **16** (2005).

7. Marth, C., Reimer, D. & Zeimet, A. G. Front-line therapy of advanced epithelial ovarian cancer: standard treatment. *Annals of Oncology* **28.** doi: 10.1093/annonc/mdx450, viii36–viii39 (2017).

8. Zhang, C., Xu, C., Gao, X. & Yao, Q. Platinum-based drugs for cancer therapy and anti-tumor strategies. *Theranostics* **12,** 2115–2132 (2022).

9. Colombo, P. E., Fabbro, M., Theillet, C., Bibeau, F., Rouanet, P. & Ray-Coquard, I. Sensitivity and resistance to treatment in the primary management of epithelial ovarian cancer. *Critical Reviews in Oncology/Hematology* **89,** 207–216 (2014).

10. The Cancer Genome Atlas Research Network. Integrated genomic analyses of ovarian carcinoma. *Nature* **474,** 609–615 (2011).

11. (Ed.) Hanaoka, F. & Sugasawa K. *DNA Replication, Recombination, and Repair Molecular Mechanisms and Pathology* 1st ed. (Springer, Japan, 2016).

12. Bhargava, R., Onyango, D. O. & Stark, J. M. Regulation of Single-Strand Annealing and its Role in Genome Maintenance. *Trends in Genetics* **32,** 566–575 (2016).

13. Sallmyr, A. & Tomkinson, A. E. Repair of DNA double-strand breaks by mammalian alternative end-joining pathways. *Journal of Biological Chemistry* **293,** 10536–10549 (2018).

14. Tarsounas, M. & Sung, P. The antitumorigenic roles of BRCA1–BARD1 in DNA repair and replication. *Nature Reviews Molecular Cell Biology* **21,** 284–299 (2020).

15. Prakash, R., Zhang, Y., Feng, W. & Jasin, M. Homologous recombination and human health: The roles of BRCA1, BRCA2, and associated proteins. *Cold Spring Harbor Perspectives in Biology* **7** (2015).

16. Yang, H., Jeffrey, P. D., Miller, J., Kinnucan, E., Sun, Y., Thomä, N. H., Zheng, N., Chen, P.-L., Lee, W.-H. & Pavletich, N. P. BRCA2 function in DNA binding and recombination from a BRCA2-DSS1-ssDNA structure. *Science* **297,** 1837–1848 (2002).

17. Neff, R. T., Senter, L. & Salani, R. BRCA mutation in ovarian cancer: Testing, implications and treatment considerations. *Therapeutic Advances in Medical Oncology* **9,** 519–531 (2017).

18. Futreal, P. A., Liu, Q., Shattuck-Eidens, D., Cochran, C., Harshman, K., Tavtigian, S., Bennett, L. M., Haugen-Strano, A., Swensen, J., Miki, Y., Eddington, K., McClure, M., *et al.* BRCA1 Mutations in Primary Breast and Ovarian Carcinomas. *Science* **266,** 120–122 (1994).

19. Petrucelli, N., Daly, M. B. & Feldman, G. L. Hereditary breast and ovarian cancer due to mutations in BRCA1 and BRCA2. *Genetics in Medicine* **12,** 245–259 (2010).

20. Cass, I., Baldwin, R. L., Varkey, T., Moslehi, R., Narod, S. A. & Karlan, B. Y. Improved survival in women with BRCA-associated ovarian carcinoma. *Cancer* **97,** 2187–2195 (2003).

21. Tan, D. S., Rothermundt, C., Thomas, K., Bancroft, E., Eeles, R., Shanley, S., Ardern-Jones, A., Norman, A., Kaye, S. B. & Gore, M. E. "BRCAness" syndrome in ovarian cancer: A case-control study describing the clinical features and outcome of patients with epithelial ovarian cancer associated with BRCA1 and BRCA2 mutations. *Journal of Clinical Oncology* **26,** 5530–5536 (2008).

22. Tutt, A., Robson, M., Garber, J. E., Domchek, S. M., Audeh, W., Rey, J., Weitzel, N., Friedlander, M., Arun, B., Loman, N., Schmutzler, R. K., Wardley, A., *et al.* Oral poly(ADP-ribose) polymerase inhibitor olaparib in patients with BRCA1 or BRCA2 mutations and advanced breast cancer: a proof-of-concept trial. *The Lancet* **376,** 235–244 (2010).

23. Fong, P. C., Yap, T. A., Boss, D. S., Carden, C. P., Mergui-Roelvink, M., Gourley, C., Greve, J. D., Lubinski, J., Shanley, S., Messiou, C., A'Hern, R., Tutt, A., *et al.* Poly(ADP)-

ribose polymerase inhibition: Frequent durable responses in BRCA carrier ovarian cancer correlating with platinum-free interval. *Journal of Clinical Oncology* **28,** 2512–2519 (2010).

24. Lee, J. M., Ledermann, J. A. & Kohn, E. C. PARP inhibitors for BRCA1/2 mutation-associated and BRCA-like malignancies. *Annals of Oncology* **25,** 32–40 (2014).

25. Chaudhuri, A. R. & Nussenzweig, A. The multifaceted roles of PARP1 in DNA repair and chromatin remodelling. *Nature Reviews Molecular Cell Biology* **18,** 610–621 (2017).

26. Harter, P., Mouret-Reynier, M. A., Pignata, S., Cropet, C., González-Martín, A., Bogner, G., Fujiwara, K., Vergote, I., Colombo, N., Jakobi Nøttrup, T., Floquet, A., El-Balat, A., *et al.* Efficacy of maintenance olaparib plus bevacizumab according to clinical risk in patients with newly diagnosed, advanced ovarian cancer in the phase III PAOLA-1/ENGOT-ov25 trial. *Gynecologic Oncology* **164,** 254–264 (2022).

27. McMullen, M., Madariaga, A. & Lheureux, S. New approaches for targeting platinum-resistant ovarian cancer. *Seminars in Cancer Biology* **77,** 167–181 (2021).

28. Sonnenblick, A., de Azambuja, E., Azim, Jr, H. A. & Piccart, M. An update on PARP inhibitors—moving to the adjuvant setting. *Nature Reviews Clinical Oncology* **12,** 27–41 (2015).

29. Tikhe, J. G., Webber, S. E., Hostomsky, Z., Maegley, K. A., Ekkers, A., Li, J., Yu, X.-H., Almassy, R. J., Kumpf, R. A., Boritzki, T. J., Zhang, C., Calabrese, C. R., *et al.* Design, synthesis, and evaluation of 3,4-dihydro-2H-[1,4]diazepino[6,7,1-hi]indol-1-ones as inhibitors of poly(ADP-ribose) polymerase. *Journal of Medicinal Chemistry* **47.** doi: 10.1021/jm030513r, 5467–5481 (2004).

30. Menear, K. A., Adcock, C., Boulter, R., Cockcroft, X.-l., Copsey, L., Cranston, A., Dillon, K. J., Drzewiecki, J., Garman, S., Gomez, S., Javaid, H., Kerrigan, F., *et al.* 4-[3-(4-cyclopropanecarbonylpiperazine-1-carbonyl)-4-fluorobenzyl]-2H-phthalazin-1-one: A novel bioavailable inhibitor of poly(ADP-ribose) polymerase-1. *Journal of Medicinal Chemistry* **51.** doi: 10.1021/jm8001263, 6581–6591 (2008).

31. Lee, E. K. & Matulonis, U. A. PARP inhibitor resistance mechanisms and implications for post-progression combination therapies. *Cancers* **12,** 1–25 (2020).

32. Shall, S. & de Murcia, G. Poly(ADP-ribose) polymerase-1: what have we learned from the deficient mouse model? *Mutation Research/DNA Repair* **460,** 1–15 (2000).

33. Farmer, H., McCabe, H., Lord, C. J., Tutt, A. H., Johnson, D. A., Richardson, T. B., Santarosa, M., Dillon, K. J., Hickson, I., Knights, C., Martin, N. M., Jackson, S. P., *et al.* Targeting the DNA repair defect in BRCA mutant cells as a therapeutic strategy. *Nature* **434,** 917–921 (2005).

34. Murai, J., Huang, S.-y. N., Das, B. B., Renaud, A., Zhang, Y., Doroshow, J. H., Ji, J., Takeda, S. & Pommier, Y. Trapping of PARP1 and PARP2 by clinical PARP inhibitors. *Cancer Research* **72,** 5588–5599 (2012).

35. Murai, J., Huang, S.-Y. N., Renaud, A., Zhang, Y., Ji, J., Takeda, S., Morris, J., Teicher, B., Doroshow, J. H. & Pommier, Y. Stereospecific PARP trapping by BMN 673 and comparison with olaparib and rucaparib. *Molecular Cancer Therapeutics* **13,** 433–443 (2014).

36. Langelier, M. F., Planck, J. L., Roy, S. & Pascal, J. M. Structural basis for DNA damage-dependent poly(ADP-ribosyl)ation by human PARP-1. *Science* **336,** 728–732 (2012).

37. Eustermann, S., Wu, W. F., Langelier, M. F., Yang, J. C., Easton, L. E., Riccio, A. A., Pascal, J. M. & Neuhaus, D. Structural Basis of Detection and Signaling of DNA Single-Strand Breaks by Human PARP-1. *Molecular Cell* **60,** 742–754 (2015).

38. Zandarashvili, L., Langelier, M. F., Velagapudi, U. K., Hancock, M. A., Steffen, J. D., Billur, R., Hannan, Z. M., Wicks, A. J., Krastev, D. B., Pettitt, S. J., Lord, C. J., Talele, T. T., *et al.* Structural basis for allosteric PARP-1 retention on DNA breaks. *Science* **368** (2020).

39. U.S. Food and Drug Administration. *FDA Approves Olaparib Tablets for Maintenance Treatment in Ovarian Cancer* `https://www.fda.gov/drugs/resources-information-approved-drugs/fda-approves-olaparib-tablets-maintenance-treatment-ovarian-cancer`. Accessed on January 23, 2023. 2017.

40. Tattersall, A., Ryan, N., Wiggans, A. J., Rogozińska, E. & Morrison, J. Poly(ADP-ribose) polymerase (PARP) inhibitors for the treatment of ovarian cancer. *Cochrane Database of Systematic Reviews* (ed Library, C.) (2022).

41. Jiang, Y., Zhao, J., Zhang, L., Tian, S., Yang, T., Wang, L., Zhao, M., Yang, Q., Wang, Y. & Yang, X. Evaluation of the Efficacy and Safety of PARP Inhibitors in Advanced-Stage Epithelial Ovarian Cancer. *Frontiers in Oncology* **10** (2020).

42. Kern, K. A., Zhang, S., Shalinsky, D. R. & Wang, D. D. Comparative PARP enzyme inhibition of PF-01367338, olaparib, and MK-4827. *Journal of Clinical Oncology* **29,** e13552–e13552 (2011).

43. Murray, J., Thomas, H., Berry, P., Kyle, S., Patterson, M., Jones, C., Los, G., Hostomsky, Z., Plummer, E. R., Boddy, A. V. & Curtin, N. J. Tumour cell retention of rucaparib, sustained PARP inhibition and efficacy of weekly as well as daily schedules. *British journal of cancer* **110,** 1977–1984 (2014).

44. Drew, Y., Mulligan, E. A., Vong, W.-T., Thomas, H. D., Kahn, S., Kyle, S., Mukhopadhyay, A., Los, G., Hostomsky, Z., Plummer, E. R., Edmondson, R. J. & Curtin, N. J. Therapeutic Potential of Poly(ADP-ribose) Polymerase Inhibitor AG014699 in Human Cancers With

Mutated or Methylated BRCA1 or BRCA2. *JNCI: Journal of the National Cancer Institute* **103,** 334–346 (2011).

45. Ihnen, M., zu Eulenburg, C., Kolarova, T., Qi, J. W., Manivong, K., Chalukya, M., Dering, J., Anderson, L., Ginther, C., Meuter, A., Winterhoff, B., Jones, S., *et al.* Therapeutic Potential of the Poly(ADP-ribose) Polymerase Inhibitor Rucaparib for the Treatment of Sporadic Human Ovarian Cancer. *Molecular Cancer Therapeutics* **12,** 1002–1015 (2013).

46. Swisher, E. M., Lin, K. K., Oza, A. M., Scott, C. L., Giordano, H., Sun, J., Konecny, G. E., Coleman, R. L., Tinker, A. V., O'Malley, D. M., Kristeleit, R. S., Ma, L., *et al.* Rucaparib in relapsed, platinum-sensitive high-grade ovarian carcinoma (ARIEL2 Part 1): an international, multicentre, open-label, phase 2 trial. *The Lancet Oncology* **18,** 75–87 (2017).

47. Kristeleit, R., Shapiro, G. I., Burris, H. A., Oza, A. M., LoRusso, P., Patel, M. R., Domchek, S. M., Balmaña, J., Drew, Y., Chen, L. M., Safra, T., Montes, A., *et al.* A phase I–II study of the oral PARP inhibitor rucaparib in patients with germline BRCA1/2-mutated ovarian carcinoma or other solid tumors. *Clinical Cancer Research* **23,** 4095–4106 (2017).

48. Coleman, R. L., Oza, A. M., Lorusso, D., Aghajanian, C., Oaknin, A., Dean, A., Colombo, N., Weberpals, J. I., Clamp, A., Scambia, G., Leary, A., Holloway, R. W., *et al.* Rucaparib maintenance treatment for recurrent ovarian carcinoma after response to platinum therapy (ARIEL3): a randomised, double-blind, placebo-controlled, phase 3 trial. *The Lancet* **390,** 1949–1961 (2017).

49. Kristeleit, R., Lisyanskaya, A., Fedenko, A., Dvorkin, M., de Melo, A. C., Shparyk, Y., Rakhmatullina, I., Bondarenko, I., Colombo, N., Svintsitskiy, V., Biela, L., Nechaeva, M., *et al.* Rucaparib versus standard-of-care chemotherapy in patients with relapsed ovarian cancer and a deleterious BRCA1 or BRCA2 mutation (ARIEL4): an international, open-label, randomised, phase 3 trial. *The Lancet Oncology* **23,** 465–478 (2022).

50. Sankaranarayanan, R. A., Kossatz, S., Weber, W., Beheshti, M., Morgenroth, A. & Mottaghy, F. M. Advancements in PARP1 targeted nuclear imaging and theranostic probes. *Journal of Clinical Medicine* **9** (2020).

51. Zhou, D., Zhou, H., Jenks, C. C., Lewis, J. S., Katzenellenbogen, J. A. & Welch, M. J. Bromination from the macroscopic level to the tracer radiochemical level: ^{76}Br radiolabeling of aromatic compounds via electrophilic substitution. *Bioconjugate Chemistry* **20,** 808–816 (2009).

52. Michel, L. S., Dyroff, S., Brooks, F. J., Spayd, K. J., Lim, S., Engle, J. T., Phillips, S., Tan, B., Wang-Gillam, A., Bognar, C., Chu, W., Zhou, D., *et al.* PET of poly (ADP-ribose) polymerase activity in cancer: Preclinical assessment and first in-human studies. *Radiology* **282,** 453–463 (2017).

53. McDonald, E. S., Doot, R. K., Pantel, A. R., Farwell, M. D., Mach, R. H., Maxwell, K. N. & Mankoff, D. A. Positron emission tomography imaging of poly-(adenosine diphosphate-ribose) polymerase 1 expression in breast cancer: A nonrandomized clinical trial. *JAMA Oncology* **6,** 921–923 (2020).

54. Puentes, L. N., Makvandi, M. & Mach, R. H. Molecular imaging: PARP-1 and beyond. *Journal of Nuclear Medicine* **62,** 765–770 (2021).

55. McDonald, E. S., Pantel, A. R., Shah, P. D., Farwell, M. D., Clark, A. S., Doot, R. K., Pryma, D. A. & Carlin, S. D. In vivo visualization of PARP inhibitor pharmacodynamics. *JCI Insight* **6** (2021).

56. Carney, B., Carlucci, G., Salinas, B., Gialleonardo, V. D., Kossatz, S., Vansteene, A., Longo, V. A., Bolaender, A., Chiosis, G., Keshari, K. R., Weber, W. A. & Reiner, T. Non-invasive PET imaging of PARP1 expression in glioblastoma models. *Molecular Imaging and Biology* **18,** 386–392 (2016).

57. Young, R. J., França, P. D. D. S. D. S., Pirovano, G., Piotrowski, A. F., Nicklin, P. J., Riedl, C. C., Schwartz, J., Bale, T. A., Donabedian, P. L., Kossatz, S., Burnazi, E. M., Roberts, S., *et al.* Preclinical and first-in-human-brain-cancer applications of [^{18}F]poly (ADP-ribose) polymerase inhibitor PET/MR. *Neuro-Oncology Advances* **2** (2020).

58. Chan, C. Y., Tan, K. V. & Cornelissen, B. PARP inhibitors in cancer diagnosis and therapy. *Clinical Cancer Research* **27,** 1585–1594 (2021).

59. Chen, Z., Destro, G., Guibbal, F., Chan, C. Y., Cornelissen, B. & Gouverneur, V. Copper-mediated radiosynthesis of [^{18}F]rucaparib. *Organic Letters* **23.** doi: 10.1021/acs.orglett.1c02770, 7290–7294 (2021).

60. Chan, C. Y., Chen, Z., Destro, G., Veal, M., Lau, D., O'Neill, E., Dias, G., Mosley, M., Kersemans, V., Guibbal, F., Gouverneur, V. & Cornelissen, B. Imaging PARP with [18F]rucaparib in pancreatic cancer models. *European Journal of Nuclear Medicine and Molecular Imaging* **49,** 3668–3678 (2022).

61. Bowden, G. D., Stotz, S., Kinzler, J., Geibel, C., Lämmerhofer, M., Pichler, B. J. & Maurer, A. DoE optimization empowers the automated preparation of enantiomerically pure [^{18}F]talazoparib and its in vivo evaluation as a PARP radiotracer. *Journal of Medicinal Chemistry* **64.** doi: 10.1021/acs.jmedchem.1c00903, 15690–15701 (2021).

62. Zhou, D., Chen, H., Mpoy, C., Afrin, S., Rogers, B. E., Garbow, J. R., Katzenellenbogen, J. A. & Xu, J. Radiosynthesis and evaluation of talazoparib and its derivatives as PARP-1-targeting agents. *Biomedicines* **9** (2021).

63. Wilson, T., Pirovano, G., Xiao, G., Samuels, Z., Roberts, S., Viray, T., Guru, N., Zanzonico, P., Gollub, M., Pillarsetty, N. V. K., Reiner, T. & Bargonetti, J. PARP-Targeted Auger Therapy

in p53 Mutant Colon Cancer Xenograft Mouse Models. *Molecular Pharmaceutics* **18,** 3418–3428 (2021).

64. Guibbal, F., Isenegger, P. G., Wilson, T. C., Pacelli, A., Mahaut, D., Sap, J. B. I., Taylor, N. J., Verhoog, S., Preshlock, S., Hueting, R., Cornelissen, B. & Gouverneur, V. Manual and automated Cu-mediated radiosynthesis of the PARP inhibitor [^{18}F]olaparib. *Nature Protocols* **15,** 1525–1541 (2020).

65. Cabanillas, M. E., McFadden, D. G. & Durante, C. Thyroid cancer. *The Lancet* **388,** 2783–2795 (2016).

66. Rizzieri, D. Zevalin® (ibritumomab tiuxetan): After more than a decade of treatment experience, what have we learned? *Critical Reviews in Oncology/Hematology* **105,** 5–17 (2016).

67. Hennrich, U. & Kopka, K. Lutathera®: The first FDA-and EMA-approved radiopharmaceutical for peptide receptor radionuclide therapy. *Pharmaceuticals* **12** (2019).

68. U.S. Food and Drug Administration. *FDA Letter of approval for NETSPOT™* `https://www.accessdata.fda.gov/drugsatfda_docs/appletter/2016/208547Orig1s000ltr.pdf`. Accessed on April 23, 2023. 2016.

69. Hennrich, U. & Benešová, M. [^{68}Ga]Ga-DOTA-TOC: The first FDA-approved ^{68}Ga-radiopharmaceutical for PET imaging. *Pharmaceuticals* **13** (2020).

70. Hennrich, U. & Eder, M. [^{177}Lu]Lu-PSMA-617 (Pluvicto™): The first FDA-approved radiotherapeutical for treatment of prostate cancer. *Pharmaceuticals* **15** (2022).

71. Bařinka, C., Rojas, C., Slusher, B. & Pomper, M. Glutamate carboxypeptidase II in diagnosis and treatment of neurologic disorders and prostate cancer. *Current Medicinal Chemistry* **19,** 856 (2012).

72. Hennrich, U. & Eder, M. [^{68}Ga]Ga-PSMA-11: The first FDA-approved ^{68}Ga-radiopharmaceutical for PET imaging of prostate cancer. *Pharmaceuticals* **14** (2021).

73. Ku, A., Facca, V. J., Cai, Z. & Reilly, R. M. Auger electrons for cancer therapy – a review. *EJNMMI Radiopharmacy and Chemistry* **4** (2019).

74. Meitner, L. Über die Entstehung der β-Strahl-Spektren radioaktiver Substanzen. *Zeitschrift für Physik* **9,** 131–144 (1922).

75. Meitner, L. Das β-Strahlenspektrum von UX1 und seine Deutung. *Zeitschrift für Physik* **17,** 54–66 (1923).

76. Auger, P. Sur les rayons β secondaires produits dans un gaz par des rayons X. *Comptes rendus de l'Académie des Sciences* **177,** 169 (1923).

77. Matsakis, D., Coster, A., Laster, B. & Sime, R. A renaming proposal: "The Auger–Meitner effect". *Physics Today* **72,** 10–11 (2019).

78. Berger, M. J., Coursey, J. S., Zucker, M. A. & Chang, J. *ESTAR, PSTAR, and ASTAR: Computer Programs for Calculating Stopping-power and Range Tables for Electrons, Protons, and Helium Ions (Version 1.2.3)* (National Institute of Standards and Technology, Gaithersburg, MD, 2005).

79. Lammerding, J. in *Comprehensive Physiology* 783–807 (John Wiley & Sons, Ltd, 2011). ISBN: 9780470650714.

80. Mothersill, C., Rusin, A., Fernandez-Palomo, C. & Seymour, C. History of bystander effects research 1905-present; what is in a name? *International Journal of Radiation Biology* **94,** 696–707 (2018).

81. Kassis, A. I., Fayad, F., Kinsey, B. M., Sastry, K. S. R., Taube, R. A., Adelstein, S. J., Kinsey, F., Sastry, B. M. & Radiotoxicity, S. J. Radiotoxicity of ^{125}I in mammalian cells. *Radiation Research* **111,** 305–318 (1987).

82. Desombre, E. R., Harper, P. V., Hughes, A., Mease, R. C., Gatley, S. J., Dejesus, O. T., Schwartz, J. L., Institute, B. M. & Institute, F. M. Bromine-80m radiotoxicity and the potential for estrogen receptor-directed therapy with Auger electrons. *Cancer Research* **48,** 5805–5809 (1988).

83. Faraggi, M., Gardin, I., de Labriolle-Vaylet, C., Moretti, J.-L. & Bok, B. D. The influence of tracer localization on the electron dose rate delivered to the cell nucleus. *Journal of Nuclear Medicine* **35,** 113 (1994).

84. Balagurumoorthy, P., Xu, X., Wang, K., Adelstein, S. J. & Kassis, A. I. Effect of distance between decaying ^{125}I and DNA on Auger-electron induced double-strand break yield. *International Journal of Radiation Biology* **88,** 998–1008 (2012).

85. Freudenberg, R., Runge, R., Maucksch, U., Berger, V. & Kotzerke, J. On the dose calculation at the cellular level and its implications for the RBE of 99mTc and 123I. *Medical Physics* **41** (2014).

86. Pouget, J. P., Santoro, L., Raymond, L., Chouin, N., Bardiès, M., Bascoul-Mollevi, C., Huguet, H., Azria, D., Kotzki, P. O., Pèlegrin, M., Vivès, E. & Pèlegrin, A. Cell membrane is a more sensitive target than cytoplasm to dense ionization produced by auger electrons. *Radiation Research* **170,** 192–200 (2008).

87. Paillas, S., Ladjohounlou, R., Lozza, C., Pichard, A., Boudousq, V., Jarlier, M., Sevestre, S., Blay, M. L., Deshayes, E., Sosabowski, J., Chardès, T., Navarro-Teulon, I., *et al.* Localized irradiation of cell membrane by Auger electrons is cytotoxic through oxidative stress-mediated nontargeted effects. *Antioxidants and Redox Signaling* **25,** 467–484 (2016).

88. Jannetti, S. A., Carlucci, G., Carney, B., Kossatz, S., Shenker, L., Carter, L. M., Salinas, B., Brand, C., Sadique, A., Donabedian, P. L., Cunanan, K. M., Gönen, M., *et al.* PARP-1-targeted radiotherapy in mouse models of glioblastoma. *Journal of Nuclear Medicine* **59,** 1225–1233 (2018).

89. Pirovano, G., Jannetti, S. A., Carter, L. M., Sadique, A., Kossatz, S., Guru, N., de Souza França, P. D., Maeda, M., Zeglis, B. M., Lewis, J. S., Humm, J. L. & Reiner, T. Targeted brain tumor radiotherapy using an auger emitter. *Clinical Cancer Research* **26,** 2871–2881 (2020).

90. Lee, H., Riad, A., Martorano, P., Mansfield, A., Samanta, M., Batra, V., Mach, R. H., Maris, J. M., Pryma, D. A. & Makvandi, M. PARP-1-targeted Auger emitters display high-LET cytotoxic properties in vitro but show limited therapeutic utility in solid tumor models of human neuroblastoma. *Journal of Nuclear Medicine* **61,** 850–856 (2020).

91. Sankaranarayanan, R. A., Peil, J., Vogg, A. T., Bolm, C., Terhorst, S., Classen, A., Bauwens, M., Maurer, J., Mottaghy, F. & Morgenroth, A. Auger emitter conjugated PARP inhibitor for therapy in triple negative breast cancers: A comparative in-vitro study. *Cancers* **14** (2022).

92. Sreekumar, S., Zhou, D., Mpoy, C., Schenk, E., Scott, J., Arbeit, J. M., Xu, J. & Rogers, B. E. Preclinical efficacy of a PARP-1 targeted Auger-emitting radionuclide in prostate cancer. *International Journal of Molecular Sciences* **24** (2022).

93. Riad, A., Gitto, S. B., Lee, H., Winters, H. D., Martorano, P. M., Hsieh, C. J., Xu, K., Omran, D. K., Powell, D. J., Mach, R. H. & Makvandi, M. PARP Theranostic Auger Emitters Are Cytotoxic in BRCA Mutant Ovarian Cancer and Viable Tumors from Ovarian Cancer Patients Enable Ex-Vivo Screening of Tumor Response. *Molecules* **25** (2020).

94. Wilbur, D. S. & Adam, M. J. Radiobromine and radioiodine for medical applications. *Radiochimica Acta* (2019).

95. Winogrodzka, A., Bergmans, P., Booij, J., van Royen, E. A., Janssen, A. G. M. & Wolters, E. C. [123I]FP-CIT SPECT is a useful method to monitor the rate of dopaminergic degeneration in early-stage Parkinson's disease. *Journal of Neural Transmission* **108,** 1011–1019 (2001).

96. Chin, B. B., Kronauge, J. F., Femia, F. J., Chen, J., Maresca, K. P., Hillier, S., Petry, N. A., James, O. G., Oldan, J. D., Armor, T., Stubbs, J. B., Stabin, M. G., *et al.* Phase-1 Clinical Trial Results of High-Specific-Activity Carrier-Free 123I-Iobenguane. *Journal of Nuclear Medicine* **55,** 765–771 (2014).

97. Stöcklin, G. Bromine-77 and iodine-123 radiopharmaceuticals. *International Journal of Applied Radiation and Isotopes* **28,** 131–147 (1977).

98. Rowland, D. J., McCarthy, T. J. & Welch, M. J. *Handbook of Radiopharmaceuticals: Ch. 14 Radiobromine for imaging and therapy* 441–465 (John Wiley & Sons, Ltd, 2005).

99. Zhou, D., Kim, S. H., Chu, W., Voller, T. & Katzenellenbogen, J. A. Evaluation of aromatic radiobromination by nucleophilic substitution using diaryliodonium salt precursors. *Journal of Labelled Compounds and Radiopharmaceuticals* **60,** 450–456 (2017).

100. Zhou, D., Chu, W., Voller, T. & Katzenellenbogen, J. A. Copper-mediated nucleophilic radiobromination of aryl boron precursors: Convenient preparation of a radiobrominated PARP-1 inhibitor. *Tetrahedron Letters* **59,** 1963–1967 (2018).

101. Halpern, A. & Stocklin, G. A radiation chemical resonance effect in solid 5-bromodeoxyuridine; Chemical Consequences of the Auger Effect. *Radiation Research* **58,** 329–337 (1974).

102. Ellison, P., Murali, D., Barnhart, T., Hoffman, S., Graves, S., Nickles, R., DeJesus, O., Speer, T. & Thomadsen, B. *In vitro* characterization of a novel prostate cancer therapeutic radiopharmaceutical. *Journal of Nuclear Medicine* **57,** 83 (2016).

103. Dunford, C. L. & Burrows, T. W. Online Nuclear Data Service, Report IAEA-NDS-150. *NNDC Informal Report* **(NNDC/ONL-95/10),** Rev. 95/10, International Atomic Energy Agency, Vienna, Austria (1995).

104. Eckerman, K. & Endo, A. Nuclear decay data for dosimetric calculations. ICRP Publication 107. *Annals ICRP* **38,** 1–123 (2008).

105. Singh, B. & Viggars, D. A. Nuclear Data Sheets for A = 76. *Nuclear Data Sheets* **42,** 233–368 (1984).

106. Singh, B. & Nica, N. Nuclear Data Sheets for A = 77. *Nuclear Data Sheets* **113,** 1115–1314 (2012).

107. Koning, A. J., Rochman, D., Sublet, J.-C., Dzysiuk, N., Fleming, M. & van der Marck, S. TENDL: Complete Nuclear Data Library for Innovative Nuclear Science and Technology. *Nuclear Data Sheets* **155,** 1–55 (2019).

108. Tárkányi, F. T., Ignatyuk, A. V., Hermanne, A., Capote, R., Carlson, B. V., Engle, J. W., Kellett, M. A., Kibédi, T., Kim, G. N., Kondev, F. G., Hussain, M., Lebeda, O., *et al.* Recommended nuclear data for medical radioisotope production: diagnostic positron emitters. *Journal of Radioanalytical and Nuclear Chemistry* **319,** 533–666 (2019).

109. Barcharts, Inc. *Periodic Table Advanced* ISBN: 9781423224310 (Barcharts, Inc., 2014).

110. Vaalburg, W., Paans, A., Terpstra, J., Wiegman, T., Dekens, K., Rijskamp, A. & Woldring, M. Fast recovery by dry distillation of ^{75}Br induced in reusable metal selenide targets via the

^{76}Se(p,2n)^{75}Br reaction. *The International Journal of Applied Radiation and Isotopes* **36,** 961–964 (1985).

111. Tolmachev, V., Lundqvist, A., Einarsson, L., Schultz, J. & Lundqvist, H. Production of ^{76}Br by a low-energy cyclotron. *Applied Radiation and Isotopes* **49,** 1537–1540 (1998).

112. Tang, L. Radionuclide production and yields at Washington University School of Medicine. *The Quarterly Journal of Nuclear Medicine and Molecular Imaging* **52,** 121–33 (2008).

113. Breunig, K., Spahn, I., Spellerberg, S. & Coenen, H. H. Production of no-carrier-added radiobromine: new nickel selenide target and optimized separation by dry distillation. *Radiochimica Acta* **103** (2015).

114. Ellison, P. A., Graves, S. A., Murali, D., De Jesus, O. T., Barnhart, T. E., Thomadsen, B. R., Speer, T. & Nickles, R. J. Radiobromine production, isolation and radiosynthesis for the development of a novel prostate cancer radiotherapeutic agent. *AIP Conference Proceedings* **1845,** 020007 (2017).

115. Hassan, H. E., El-Azony, K. M., Azzam, A. & Qaim, S. M. Investigation of selenium compounds as targets for ^{76,77}Br production using protons of energies up to 34 MeV. *Radiochimica Acta* **105,** 841–850 (2017).

116. Ellison, P. A., Olson, A. P., Barnhart, T. E., Hoffman, S. L., Reilly, S. W., Makvandi, M., Bartels, J. L., Murali, D., DeJesus, O. T., Lapi, S. E., Bednarz, B., Nickles, R. J., *et al.* Improved production of ^{76}Br, ^{77}Br and ^{80m}Br via CoSe cyclotron targets and vertical dry distillation. *Nuclear Medicine and Biology* **80,** 32–36 (2020).

117. ICRU report no. 67: absorbed-dose specification in nuclear medicine. *Journal ICRU,* 3–110 (2002).

118. Loevinger, R., Budinger, T. F., Watson, E. E. & Committee, M. *MIRD Primer for Absorbed Dose Calculations* 128. ISBN: 9780932004383 (Society of Nuclear Medicine, 1991).

119. Carter, L. L. & Cashwell, E. D. Particle-transport simulation with the Monte Carlo method (1975).

120. Vassiliev, O. N. *Monte Carlo Methods for Radiation Transport: Fundamentals and Advanced Topics* (Springer, 2017).

121. Seco, J. & Verhaegen, F. *Monte Carlo Techniques in Radiation Therapy* ISBN: 9781466507944 (Taylor & Francis Group, 2013).

122. Jia, X., Ziegenhein, P. & Jiang, S. B. GPU-based high-performance computing for radiation therapy. *Physics in Medicine and Biology* **59,** R151–R182 (2014).

123. Agostinelli, S., Allison, J., Amako, K., Apostolakis, J., Araujo, H., Arce, P., Asai, M., Axen, D., Banerjee, S., Barrand, G., Behner, F., Bellagamba, L., *et al.* GEANT4 - A simulation toolkit. *Nuclear Instruments and Methods in Physics Research, Section A: Accelerators, Spectrometers, Detectors and Associated Equipment* **506,** 250–303 (2003).

124. Forster, R. A. & Godfrey, T. N. K. MCNP - a general Monte Carlo code for neutron and photon transport. *Monte-Carlo Methods and Applications in Neutronics, Photonics and Statistical Physics* (eds Robert, Arthur, F., Guy, L., Raymond, M. B. A. & Dautray) 33–55 (1985).

125. Kawrakow, I., Mainegra-Hing, E., Rogers, D. W., Tessier, F. & Walters, B. R. B. *The EGSnrc Code System: Monte Carlo Simulation of Electron and Photon Transport* 6th (2011).

126. Stabin, M. G., Sparks, R. B. & Crowe, E. OLINDA/EXM: The second-generation personal computer software for internal dose assessment in nuclear medicine. *Journal of Nuclear Medicine* **46,** 1023 (2005).

127. Vaziri, B., Wu, H., Dhawan, A. P., Du, P., Howell, R. W., Bolch, W. E., Brill, A. B., Dewaraja, Y. K., Dunphy, M. P., Fisher, D. R., Meredith, R. F., Sgouros, G., *et al.* MIRD pamphlet No. 25: MIRDcell V2.0 software tool for dosimetric analysis of biologic response of multicellular populations. *Journal of Nuclear Medicine* **55,** 1557–1564 (2014).

128. Goddu, S. M., Howell, R. W., Bouchet, L. G., Bolch, W. E. & Rao, D. V. *MIRD Cellular S Values: Self-absorbed Dose Per Unit Cumulated Activity for Selected Radionuclides and Monoenergetic Electron and Alpha Particle Emitters Incorporated Into Different Cell Compartments* (Society of Nuclear Medicine, 1997).

129. Tutt, A. N., Lord, C. J., McCabe, N., Farmer, H., Turner, N., Martin, N. M., Jackson, S. P., Smith, G. C. & Ashworth, A. Exploiting the DNA repair defect in BRCA mutant cells in the design of new therapeutic strategies for cancer. *Cold Spring Harbor Symposium Quantitative Biology* **70,** 139–48 (2005).

130. Roby, K. F., Taylor, C. C., Sweetwood, J. P., Cheng, Y., Pace, J. L., Tawfik, O., Persons, D. L., Smith, P. G. & Terranova, P. F. Development of a syngeneic mouse model for events related to ovarian cancer. *Carcinogenesis* **21,** 585–591 (2000).

131. Walton, J., Blagih, J., Ennis, D., Leung, E., Dowson, S., Farquharson, M., Tookman, L. A., Orange, C., Athineos, D., Mason, S., Stevenson, D., Blyth, K., *et al.* CRISPR/Cas9-mediated Trp53 and Brca2 knockout to generate improved murine models of ovarian high-grade serous carcinoma. *Cancer Research* **76,** 6118–6129 (2016).

132. Schilder, R. J., Hall, L., Monks, A., Jr., L. M. H., Fornace, A. J., Ozols, R. F., Fojo, A. T. & Hamilton, T. Metallothionein gene expression and resistance to cisplatin in human ovarian cancer. *International Journal of Cancer* **45,** 416–422 (1990).

133. Busschots, S., O'Toole, S., O'Leary, J. J. & Stordal, B. Carboplatin and taxol resistance develops more rapidly in functional BRCA1 compared to dysfunctional BRCA1 ovarian cancer cells. *Experimental Cell Research* **336,** 1–14 (2015).

134. Stordal, B., Timms, K., Farrelly, A., Gallagher, D., Busschots, S., Renaud, M., Thery, J., Williams, D., Potter, J., Tran, T., Korpanty, G., Cremona, M., *et al.* BRCA1/2 mutation analysis in 41 ovarian cell lines reveals only one functionally deleterious BRCA1 mutation. *Molecular Oncology* **7,** 567–579 (2013).

135. Makvandi, M., Pantel, A., Schwartz, L., Schubert, E., Xu, K., Hsieh, C. J., Hou, C., Kim, H., Weng, C. C., Winters, H., Doot, R., Farwell, M. D., *et al.* A PET imaging agent for evaluating PARP-1 expression in ovarian cancer. *Journal of Clinical Investigation* **128,** 2116–2126 (2018).

136. DelloRusso, C., Welcsh, P. L., Wang, W., Garcia, R. L., King, M. C. & Swisher, E. M. Functional characterization of a novel BRCA1-null ovarian cancer cell line in response to ionizing radiation. *Molecular Cancer Research* **5,** 35–45 (2007).

137. Franken, N. A., Rodermond, H. M., Stap, J., Haveman, J. & van Bree, C. Clonogenic assay of cells in vitro. *Nature Protocols* **1,** 2315–2319 (2006).

138. Mixdorf, J. C., Hoffman, S. L., Aluicio-Sarduy, E., Barnhart, T. E., Engle, J. W. & Ellison, P. A. Copper-mediated radiobromination of (hetero)aryl boronic pinacol esters. *Journal of Organic Chemistry* **88,** 2089–2094 (2023).

139. Promega Corporation. *CellTiter-Glo® 2.0 Assay Instructions for Use of Products G9241, G9242 and G9243* (2018).

140. Gomi, K. & Kajiyama, N. Oxyluciferin, a Luminescence Product of Firefly Luciferase, is Enzymatically Regenerated into Luciferin. *Journal of Biological Chemistry* **276,** 36508–36513 (2001).

141. Guzmán, C., Bagga, M., Kaur, A., Westermarck, J. & Abankwa, D. ColonyArea: An ImageJ Plugin to Automatically Quantify Colony Formation in Clonogenic Assays. *PLOS ONE* **9,** 1–9 (2014).

142. Fassy, F., Dureuil, C., Lamberton, A., Mathieu, M., Michot, N., Ronan, B. & Pasquier, B. in *Molecular Characterization of Autophagic Responses, Part A* (eds Galluzzi, L., Pedro, J. M. B.-S. & Kroemer, G.) 447–464 (Academic Press, 2017). ISBN: 9780128096758.

143. *Cochrane Handbook for Systematic Reviews of Interventions* version 6.3 (eds Higgins, J. P. T., Thomas, J., Chandler, J., Cumpston, M., Li, T., Page, M. J. & Welch, V. A.) (Cochrane, 2022).

144. Makvandi, M., Xu, K., Lieberman, B. P., Anderson, R. C., Effron, S. S., Winters, H. D., Zeng, C., McDonald, E. S., Pryma, D. A., Greenberg, R. A. & Mach, R. H. A radiotracer strategy to quantify PARP-1 expression in vivo provides a biomarker that can enable patient selection for PARP inhibitor therapy. *Cancer Research* **76,** 4516–4524 (2016).

145. Milanese, C., Bombardieri, C. R., Sepe, S., Barnhoorn, S., Payán-Goméz, C., Caruso, D., Audano, M., Pedretti, S., Vermeij, W. P., Brandt, R. M. C., Gyenis, A., Wamelink, M. M., *et al.* DNA damage and transcription stress cause ATP-mediated redesign of metabolism and potentiation of anti-oxidant buffering. *Nature Communication* **10,** 1–16 (2019).

146. Eckerman, K. F. & Endo, A. *MIRD: Radionuclide Data and Decay Schemes* ISBN: 0932004806 (Society of Nuclear Med, Reston, VA, 2008).

147. Baguley, B. C., Marshall, E. S., Whittaker, J. R., Mccrystal, M. C. M. R., Finlay, G. J., Matthews, J. H. L., Dotchin, P. V. Z., Nixon, J. & Holdaway, K. M. Resistance mechanisms determining the in vitro sensitivity to paclitaxel of tumour cells cultured from patients with ovarian cancer. *European Journal of Cancer* **31,** 230–237 (1995).

148. Olson, B., Li, Y., Lin, Y., Liu, E. T. & Patnaik, A. Mouse models for cancer immunotherapy research. *Cancer Discovery* **8,** 1358–1365 (2018).

149. Guerin, M. V., Finisguerra, V., den Eynde, B. J. V., Bercovici, N. & Trautmann, A. Preclinical murine tumor models: A structural and functional perspective. *eLife* **9** (2020).

150. Coffelt, S. B. & de Visser, K. E. Immune-mediated mechanisms influencing the efficacy of anticancer therapies. *Trends in Immunology* **36,** 198–216 (2015).

151. Lengyel, E. Ovarian cancer development and metastasis. *American Journal of Pathology* **177,** 1053–1064 (2010).

152. Bian, C., Yao, K., Li, L., Yi, T. & Zhao, X. Primary debulking surgery vs. neoadjuvant chemotherapy followed by interval debulking surgery for patients with advanced ovarian cancer. *Archives of Gynecology and Obstetrics* **293,** 163–168 (2016).

153. Leinster, D. A., Kulbe, H., Everitt, G., Thompson, R., Perretti, M., Gavins, F. N. E., Cooper, D., Gould, D., Ennis, D. P., Lockley, M., McNeish, I. A., Nourshargh, S., *et al.* The peritoneal tumour microenvironment of high-grade serous ovarian cancer. *The Journal of Pathology* **227,** 136–145 (2012).

154. Chambers, L. M., Esakov, E., Braley, C., AlHilli, M., Michener, C. & Reizes, O. Use of Transabdominal Ultrasound for the detection of intra-peritoneal tumor engraftment and growth in mouse xenografts of epithelial ovarian cancer. *PLOS ONE* **15,** e0228511– (2020).

155. Chiriva-Internati, M., Yu, Y., Mirandola, L., Jenkins, M. R., Chapman, C., Cannon, M., Cobos, E. & Kast, W. M. Cancer Testis Antigen Vaccination Affords Long-Term Protection in a Murine Model of Ovarian Cancer. *PLOS ONE* **5,** e10471– (2010).

156. Zhang, L., Yang, N., Garcia, J. R. C., Mohamed, A., Benencia, F., Rubin, S. C., Allman, D. & Coukos, G. Generation of a Syngeneic Mouse Model to Study the Effects of Vascular Endothelial Growth Factor in Ovarian Carcinoma. *The American Journal of Pathology* **161,** 2295–2309 (2002).

157. Jeanne, A., Sarazin, T., Charlé, M., Moali, C., Fichel, C., Boulagnon-Rombi, C., Callewaert, M., Andry, M.-C., Diesis, E., Delolme, F., Rioult, D. & Dedieu, S. Targeting ovarian carcinoma with TSP-1:CD47 antagonist TAX2 activates anti-tumor immunity. *Cancers* **13** (2021).

158. Su, F., Kozak, K. R., Imaizumi, S., Gao, F., Amneus, M. W., Grijalva, V., Ng, C., Wagner, A., Hough, G., Farias-Eisner, G., Anantharamaiah, G. M., Lenten, B. J. V., *et al.* Apolipoprotein A-I (apoA-I) and apoA-I mimetic peptides inhibit tumor development in a mouse model of ovarian cancer. *Proceedings of the National Academy of Sciences* **107,** 19997–20002 (2010).

159. Zhang, Y., Yang, S., Yang, Y. & Liu, T. Resveratrol induces immunogenic cell death of human and murine ovarian carcinoma cells. *Infectious Agents and Cancer* **14,** 27 (2019).

160. Janát-Amsbury, M., Yockman, J., Anderson, M., Kieback, D. & Kim, S. Comparison of ID8 MOSE and VEGF-modified ID8 cell lines in an immunocompetent animal model for human ovarian cancer. *Anticancer Research* **26,** 2785–2789 (2006).

161. Hudson, H. & Larkin, R. Accelerated image reconstruction using ordered subsets of projection data. *IEEE Transactions on Medical Imaging* **13,** 601–609 (1994).

162. Ribeiro, M. J., Almeida, P., Strul, D., Ferreira, N., Loc'h, C., Brulon, V., Trébossen, R., Mazière, B. & Bendriem, B. Comparison of fluorine-18 and bromine-76 imaging in positron emission tomography. *European Journal of Nuclear Medicine* **26** (1999).

163. Levin, C. S. & Hoffman, E. J. Calculation of positron range and its effect on the fundamental limit of positron emission tomography system spatial resolution. *Physics in Medicine and Biology* **44,** 781–799 (1999).

164. Tilley, D., Weller, H., Cheves, C. & Chasteler, R. Energy levels of light nuclei A=18–19. *Nuclear Physics A* **595,** 1–170 (1995).

165. Besemer, A. E., Yang, Y. M., Grudzinski, J. J., Hall, L. T. & Bednarz, B. P. Development and validation of RAPID: A patient-specific Monte Carlo three-dimensional internal dosimetry platform. *Cancer Biotherapy and Radiopharmaceuticals* **33,** 155–165 (2018).

166. Agostinelli, S., Allison, J., Amako, K., Apostolakis, J., Araujo, H., Arce, P., Asai, M., Axen, D., Banerjee, S., Barrand, G., Behner, F., Bellagamba, L., *et al.* GEANT4 - A simulation toolkit. *Nuclear Instruments and Methods in Physics Research, Section A: Accelerators, Spectrometers, Detectors and Associated Equipment* **506,** 250–303 (2003).

167. Hauf, S., Kuster, M., Batič, M., Bell, Z. W., Hoffmann, D. H. H., Lang, P. M., Neff, S., Pia, M. G., Weidenspointner, G. & Zoglauer, A. Radioactive Decays in Geant4. *IEEE Transactions on Nuclear Science* **60,** 2966–2983 (2013).

168. Bhat, M. R. *Evaluated Nuclear Structure Data File (ENSDF)* in (ed Qaim, S. M.) (Springer Berlin Heidelberg, 1992), 817–821. ISBN: 978-3-642-58113-7.

169. Stabin, M. G. & Siegel, J. A. Physical models and dose factors for use in internal dose assessment. *Health Physics* **85,** 294–310 (2003).

170. Yao, R., Seidel, J., Johnson, C. A., Daube-Witherspoon, M. E., Green, M. V. & Carson, R. E. Performance characteristics of the 3-D OSEM algorithm in the reconstruction of small animal PET images. *IEEE Transactions on Medical Imaging* **19,** 798–804 (2000).

171. Wei, J. C. J., Edwards, G. A., Martin, D. J., Huang, H., Crichton, M. L. & Kendall, M. A. F. Allometric scaling of skin thickness, elasticity, viscoelasticity to mass for micro-medical device translation: from mice, rats, rabbits, pigs to humans. *Scientific Reports* **7,** 15885 (2017).

172. Shapiro, S. S. & Wilk, M. B. An analysis of variance test for normality (complete samples). *Biometrika* **52,** 591–611 (1965).

173. Welch, B. L. The generalization of 'student's' problem when several different population varlances are involved. *Biometrika* **34,** 28–35 (1947).

174. Kruskal, W. H. & Wallis, W. A. Use of Ranks in One-Criterion Variance Analysis. *Journal of the American Statistical Association* **47,** 583–621 (1952).

175. Perkins, S. T., Cullen, D. E., Chen, M. H., Rathkopf, J., Scofield, J. & Hubbell, J. H. Tables and graphs of atomic subshell and relaxation data derived from the LLNL Evaluated Atomic Data Library (EADL), Z = 1–100 (1991).

176. Marsh, I. R., Grudzinski, J., Baiu, D. C., Besemer, A., Hernandez, R., Jeffery, J. J., Weichert, J. P., Otto, M. & Bednarz, B. P. Preclinical pharmacokinetics and dosimetry studies of ^{124}I/^{131}I-CLR1404 for treatment of pediatric solid tumors in murine xenograft models. *Journal of Nuclear Medicine* **60,** 1414–1420 (2019).

177. Valentin, J. Basic anatomical and physiological data for use in radiological protection: reference values: ICRP Publication 89. *Annals of the ICRP* **32,** 1–277 (2002).

178. Kodama Lab, Tohoku University. *News: Lymph nodes in mice.* `https://web.tohoku.ac.jp/kodama/en/news/940/`. Accessed March 8, 2023. 2021.

179. Destro, G., Chen, Z., Chan, C. Y., Fraser, C., Dias, G., Mosley, M., Guibbal, F., Gouverneur, V. & Cornelissen, B. A radioiodinated rucaparib analogue as an Auger electron emitter for cancer therapy. *Nuclear Medicine and Biology* **116-117,** 108312 (2023).

180. Chugh, B. P., Lerch, J. P., Yu, L. X., Pienkowski, M., Harrison, R. V., Henkelman, R. M. & Sled, J. G. Measurement of cerebral blood volume in mouse brain regions using micro-computed tomography. *NeuroImage* **47,** 1312–1318 (2009).

181. Incerti, S., Baldacchino, G., Bernal, M., Capra, R., Champion, C., Francis, Z., Guatelli, S., Guèye, P., Mantero, A., Mascialino, B., Moretto, P., Nieminen, P., *et al.* The Geant4-DNA Project. *International Journal of Modeling, Simulation and Scientific Computing* **1,** 157–178 (2010).

182. Liao, J. B., Ovenell, K. J., Curtis, E. E. M., Cecil, D. L., Koehnlein, M. R., Rastetter, L. R., Gad, E. A. & Disis, M. L. Preservation of tumor-host immune interactions with luciferase-tagged imaging in a murine model of ovarian cancer. *Journal for immunotherapy of cancer* **3,** 16 (2015).

183. Sim, H., Bibee, K., Wickline, S. & Sept, D. Pharmacokinetic Modeling of Tumor Bioluminescence Implicates Efflux, and Not Influx, as the Bigger Hurdle in Cancer Drug Therapy. *Cancer Research* **71,** 686–692 (2011).

184. Bagga, M., Guzmán, C. & Abankwa, D. *User Manual for the ImageJ plugin: ColonyArea* (2014).